EFFECTS OF SITE IMPROVEMENT TECHNIQUE ON SEISMIC PERFORMANCE OF GEOTECHNICAL STRUCTURES

by

Bilge Sultan Demirtaş

B.S., Civil Engineering, Yıldız Technical University, 2016

Submitted to Kandilli Observatory and Earthquake Research Institute

in partial fulfillment of requirements for the degree of

Master of Science

Graduate Program in Earthquake Engineering

Boğaziçi University

2022

EFFECTS OF SITE IMPROVEMENT TECHNIQUE ON SEISMIC PERFORMANCE OF GEOTECHNICAL STRUCTURES

APPROVED BY:

Prof. Dr. Ayşe Edinçliler …….
(Thesis Supervisor)

Prof. Dr. Ali Pınar …….

Prof. Dr. Musaffa Ayşen Lav …….
(İstanbul Technical University)

DATE OF APPROVAL: 31.10.2022

ACKNOWLEDGEMENTS

I would like to express my thanks to my thesis supervisor, Prof. Dr. Ayşe Edinçliler, who has always supported me throughout my graduate studies and thesis stage. I am extremely grateful for her invaluable advice, continuous guidance, and patience. Her immense knowledge and plentiful experience have encouraged me all the time in my academic research and daily life.

I would also like to thank my committee members, Prof. Dr. Ali Pınar and Prof. Dr. Musaffa Ayşen Lav, for their contributions.

I would like to thank the technicians who helped me during my experiments in Prof. Dr. Mustafa Erdik Shake Table Laboratory, Kandilli Observatory and Earthquake Research Institute of Boğaziçi University.

I would like to thank Maccaferri Corporate for their financial support for the manufacturing of the aluminum wall model used in this thesis.

Finally, I would like to express my deepest gratitude to my parents and my twin sister, Ezgi Demirtaş. I also appreciate all the support I received from my dearest friends and colleagues. Without their tremendous understanding and encouragement over the past few years, it would be impossible for me to complete my study.

ABSTRACT

EFFECTS OF SITE IMPROVEMENT TECHNIQUE ON SEISMIC PERFORMANCE OF GEOTECHNICAL STRUCTURES

Earth-retaining structures are widely used in the man-made environment and compose the significant constituents of infrastructural systems worldwide. Besides, they have been constructed broadly in seismically active regions. Earthquakes can cause a lot of damage to geotechnical structures. The prevention of failures in these structures is an important issue. Cost-effective remedies can be applied to retaining structures in order to prevent them from failing under seismic loading. The use of lightweight materials behind the wall as a cushion layer is one of the methods to improve the seismic performance of the retaining system. The objective of this thesis is to investigate the effects of cushion type on the seismic performance of retaining walls by performing shake table tests. The experiments were carried out with a 1/25 scaled retaining wall model with or without a cushion layer. In the experimental study, the cushions were considered as EPS geofoam and a mixture of tire crumb and sand. Additionally, various parameters, such as cushion thicknesses, EPS geofoam densities, mixture ratios of sand-tire crumb mixture, and input characteristics, are also evaluated. The results were examined by comparing the cases having a cushion layer with the case without a cushion layer depending on mentioned parameters. The evaluation of the results indicates that the seismic performance of the retaining wall is very sensitive to cushion type. It is observed that the EPS cushions are more effective than the sand-tire crumb mixtures to improve the seismic performance of the wall. Additionally, the use of cushion layer with higher thickness can be an effective solution to improve the seismic performance of the retaining wall, prevent the future failure of the retaining structure, and mitigate earthquake hazards.

ÖZET

ZEMİN İYİLEŞTİRME TEKNİĞİNİN GEOTEKNİK YAPILARIN SİSMİK PERFORMANSI ÜZERİNDEKİ ETKİLERİ

İstinat duvarları, yaygın olarak kullanılan ve dünya çapında altyapı sistemlerinin önemli bileşenlerini oluşturan yapılardır. Yaygın olarak deprem bölgelerinde de inşa edilirler. Depremler bu geoteknik yapılarında çok fazla hasara neden olabilir. Bu yapılardaki hasarların önlenmesi önemli bir konudur. Dinamik yüklemeler altında göçmelerini önlemek için istinat yapılarına uygun maliyetli çözümler uygulanmalıdır. Hafif malzemelerin duvarın arkasında yastık tabakası olarak kullanılması, istinat duvar sisteminin sismik performansını iyileştirme yöntemlerinden bir tanesidir. Bu tezin amacı, farklı tip yastık malzemelerinin istinat duvarlarının sismik performansı üzerindeki etkilerini sarsma masası testleri yardımıyla araştırmaktır. Deneyler, 1/25 ölçekli istinat duvarı modeli ile yastık tabakası yerleştirilmeden ve yerleştirilerek gerçekleştirilmiştir. Deneysel çalışmada, yastık tabakası EPS geofoam ile lastik parçası ve kum karışımından oluşmaktadır. Deneyler, farklı yastık kalınlıkları, farklı EPS geofoam yoğunlukları, farklı kum-lastik parçası karışım oranları ve farklı yer hareketi özellikleri ile gerçekleştirilmiştir. Bahsedilen parametrelere bağlı olarak, yastık katmanı olan deney düzenekleri yastık yerleştirilmeden oluşturulan deney düzeneği ile karşılaştırılarak sonuçlar değerlendirilmiştir. Sonuçların yorumlanması, istinat duvarının sismik performansının yastık tipine hassas olduğunu göstermiştir. EPS geofoam içeren yastık tabakası duvarın sismik performansını iyileştirmede kum-lastik parçası içeren yastık tabakasına göre daha etkili olduğu gözlemlenmiştir. Ek olarak, daha kalın bir yastık tabakasının kullanılması, istinat duvarı sisteminin sismik performansını iyileştirilmesi, istinat yapısındaki hasarlarının önlenmesi ve deprem tehlikesini azaltılması için etkili bir çözüm olabilir.

TABLE OF CONTENTS

LIST OF FIGURES

LIST OF TABLES

LIST OF SYMBOLS

H	Height of the wall
σ'_h	Lateral earth pressure acting on the retaining wall
ΔH	Amount of wall movement
σ'_a	Active earth pressure
σ'_p	Passive earth pressure
W	Weight of the soil wedge
φ	Friction angle of the backfill soil
β	Angle of the inclined back face of the wall
i	Slope of the backfill surface relative to the horizontal
δ	Angle of the wall friction
γ	Unit weight of the backfill soil
α	Angle of the inclined surface of the backfill soil
θ	Angle of the failure surface
R	The resultant force
c	Cohesion of backfill soil
z_0	Depth of the tensile crack
P_a	Active force per unit length
K_{AE}	Coefficients of active earth pressure under seismic loading
K_{PE}	Coefficients of passive earth pressure under seismic loading
P_{AE}	Total active earth pressure under seismic loading
P_{PE}	Total passive earth pressure under seismic loading
ΔP_{AE}, ΔP_{PE}	Additional component of dynamic lateral force due to earthquake
K_A	Coefficients of static active pressure
K_P	Coefficients of static passive pressure
ΔK_{AE}	Coefficients of dynamic pressure increments for active condition
ΔK_{PE}	Coefficients of dynamic pressure increments for passive condition
a_h	Horizontal acceleration of the earthquake

a_v	Vertical acceleration of the earthquake
k_h	Factor of horizontal acceleration
k_v	Factor of vertical acceleration
g	Acceleration due to gravity
$\bar{H}$	Acting point of total earth force
H_c	Depth of tension cracks
q	Surcharge loading
V_s	Shear wave velocity
G	Shear modulus of the backfill soil
ρ	Density of the backfill soil
ν	Poisson's ratio
ω_1	Fundamental frequency of the system
a_{max}	Maximum ground acceleration
v_{max}	Maximum ground velocity
E	Young's modulus
ρ_s	Density of soil
ρ_{dmin}	Minimum dry density
ρ_{dmax}	Maximum dry density
e_{min}	Void ratio of the soil in the densest state
e_{max}	Void ratio of the soil in the loosest state
D_{50}	Mean diameter of soil particles
C_u	Coefficient of uniformity
C_c	Coefficient of curvature
t_m	Thickness of the model wall,
t_p	Thickness of the prototype wall,
E_m	Young's modulus of the model wall,
E_p	Young's modulus of the prototype wall.
f_{11}	Fundamental frequency
f_l	Frequency of infinitely long and uniform soil (1D approach)
B	Width of the backfill

LIST OF ACRONYMS/ABBREVIATIONS

sf	sand fraction
EPS	Expanded Polystyrene
XPS	Extruded Polystyrene
FLAC	Fast Lagrangian Analysis of Continua
2D	Two dimensional
SAFETY	Stability and flexibility of structures during earthquake using tyres
M-O	Mononobe-Okabe method
FS	Factor of safety
GF	Geometric factor
USCS	United Soil Classification System
SP	Poorly graded sand
TC	Tire crumb and sand mixture
A	Accelerometers
D	Displacement sensors
İzmit-F	The far-field recording of Kocaeli Earthquake
İzmit-N	The near-field recording of Kocaeli Earthquake
İzmir-F	The far-field recording of İzmir Earthquake
PGA	Peak ground acceleration
Hz	Hertz
ATH	Acceleration-time histories
FAS	Fourier amplitude spectra
SA	Spectral acceleration
DTH	Displacement-time histories
NS	North-South component of earthquake recording

1. INTRODUCTION

1.1. General

Retaining structures are a crucial element of infrastructural and transportation systems worldwide, including seismically active regions. Therefore, the design process of these structures should be implemented carefully.

The design of retaining structures includes determining the static and dynamic forces against the retaining wall. However, the determination of forces on the retaining structure is a pretty complicated process since the designer has to deal with various uncertainties, especially under dynamic conditions. Unfortunately, it is quite challenging to anticipate the seismic response of the retaining wall system and the nature of the earthquakes. Additionally, apart from the characteristics of the ground shaking, the behavior of the retaining wall system under an earthquake depends on many factors, such as the seismic response of the foundation and backfill soil of the retaining structure. In the literature, in order to calculate the static and dynamic forces, simplified methods have been proposed by many researchers by conducting numerical and experimental studies until today. The forces against the wall have been calculated using these methods, and the structures have been designed according to the determined forces.

During the design process, the retaining wall stability is controlled against overturning, sliding, and bearing capacity failure. Additionally, the stability of the retaining structure under seismic conditions is also checked. When stability is not satisfied under seismic conditions, remedies should be sought to prevent any possible future failures. The selection of solution is a serious issue to provide stability in retaining structure. One of the significant methods to mitigate the damage and improve the seismic performance of the wall is the installation of lightweight materials behind the retaining structures as a cushion layer.

In this thesis, the mentioned method is evaluated by placing the cushion layer consisting of EPS geofoam and sand-tire crumb mixture materials behind the retaining wall. In order to conduct an experimental study, a series of shaking table tests on a 1/25 scaled wall model is carried out. The aim of the study is to evaluate the effects of cushion type on the seismic performance of the retaining wall. Additionally, the influence of EPS geofoam density, the mixture ratio of sand and tire crumb, cushion thickness and input motion characteristics on the behavior of the retaining wall under seismic loading is also investigated in this thesis.

1.2. Problem Statement

Earth-retaining structures are widely used in the man-made environment and compose the significant constituents of infrastructural systems throughout the world. Besides, they have been constructed broadly in seismically active regions. In history, many earthquakes have caused damage that is sometimes negligibly small, sometimes quite significant, or even resulting in collapse. The substantial damage that happened to retaining structures has vital and economic consequences. Therefore, improvement methods have a significant role in the prevention or mitigation of any type of possible damage. One of these methods is the placement of various lightweight materials behind the wall as a cushion layer to enhance the seismic performance of retaining walls. Generally, cushion layers are composed of materials that have advantageous features, such as being lightweight, highly vibration absorbent, and compressible. The aim of this study is to investigate the change in the behavior of retaining walls under seismic conditions depending on the types of cushion layer by conducting a series of shaking table tests on the 1/25 scaled wall model. Moreover, the effects of the thickness and density of cushion layers, and input motion characteristics on the seismic performance of the retaining structure are evaluated.

1.3. Objective of Thesis

The objective of this thesis is to investigate the effects of a cushion type on the seismic behavior of the retaining wall system by installing the cushion behind the scaled wall model. In this study, two types of cushion material are utilized in the experiments in order to improve the

seismic performance of the wall model. These materials are EPS geofoam and a mixture of sand and tire crumb. The reason for the selection of mentioned materials is that they have advantageous characteristics, such as low unit weight, high compressibility, and high vibration absorption. By performing a series of shaking table tests, the change in seismic performance of the retaining wall is evaluated depending on the type of cushion. Accordingly, the cushions are designed with the same thicknesses. Additionally, in order to investigate the effects of cushion thickness, the cushion is placed behind the scaled model in thicknesses of 2 and 4 cm. Along with cushion types and thicknesses, the effects of the density of EPS geofoam, the mixture ratio of sand-tire crumb mixture, and input motion characteristics are evaluated. As a result of the shaking table tests performed on the 1/25 scaled model, the decrease in the displacement of the wall and transmitted acceleration in front of the wall is expected due to the inclusion of the cushion layer.

1.4. Organization of Thesis

This study includes an experimental study that investigates the effects of two different cushion types, EPS geofoam and tire waste-sand mixtures, on the seismic behavior of the retaining walls. For each cushion type, the effects of the thickness and density of the cushion material and the input motions were evaluated. Firstly, information on the stability of the retaining walls under static and seismic loadings is given. The literature review on the engineering properties of the cushion materials and the effects of cushion layers behind the retaining walls are summarized. By examining the results of the literature study, the parameters such as the thickness and density of cushion layers, and input motion affecting the seismic stability of the retaining wall were evaluated. Secondly, the design of shaking table tests setups, the materials, the instrumentation, and the selection of input motions are explained comprehensively. Then, the 1/25 scaled shaking table tests for eleven different cases were conducted, and the results of the models with cushions were compared with the model without cushion. Finally, the effectiveness of cushion materials and related parameters such as thickness, density, and input motions on the seismic behavior of the retaining wall were evaluated and discussed.

2. RETAINING STRUCTURES

2.1. Types of Retaining Structures

Earth retaining structures are mainly constructed in order to provide lateral support for slopes or excavations (illustrated in Figure 2.1) and, in some cases, in order to support vertical loads transferred from the structure above, such as bridge abutment and basement walls.

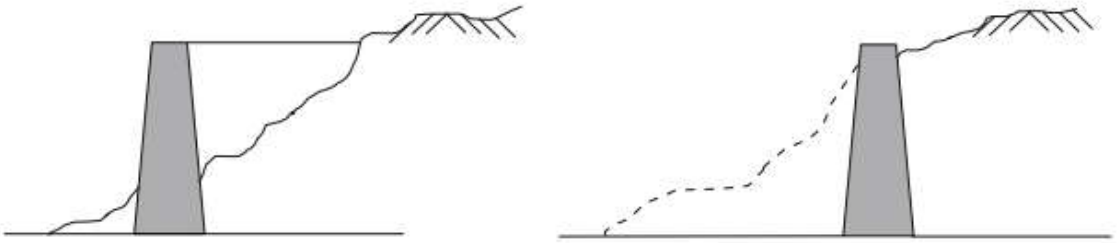

Figure 2.1. Retaining Structures [1].

Retaining structures are divided into two general categories. The first category is rigid walls, and the other is flexible walls. Whereas the former relies on the gravity of the wall to provide stability, the latter depends on passive soil resistance or anchored systems embedded into backfill soil [2]. The retaining structures used commonly are illustrated in Figures 2.2.

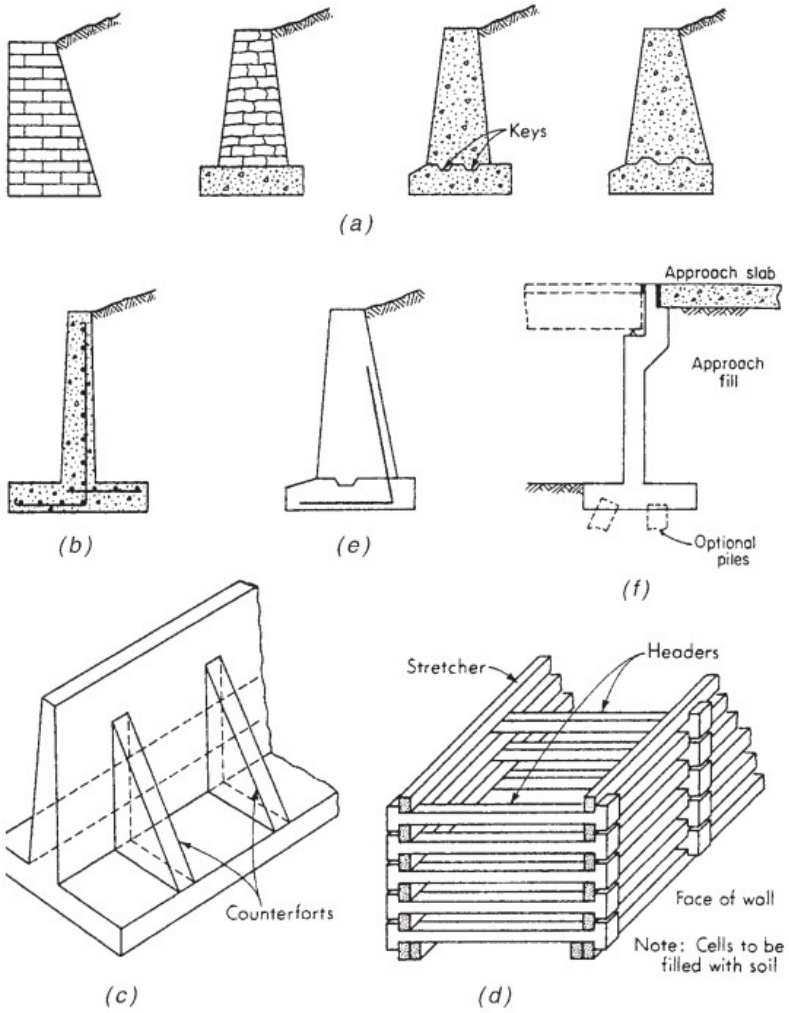

Figure 2.2. Common Types of Retaining Structures. (a) Gravity Wall; (b) Cantilever Wall; (c) Counterfort or Buttressed Wall; (d) Crib Wall; (e) Semigravity Wall; (f) Bridge Abutment [3].

The most common types of retaining walls encountered in construction projects are gravity walls, cantilever walls, and crib walls. Additionally, mechanically stabilized earth (MSE) walls which have gained popularity in recent years, are included in the common retaining structure types.

Gravity walls are generally built of mass concrete or stone masonry. The stability of these structures relies predominantly on their massive weight; that is, the dead weight of the wall provides support for the material behind the structure. As a result, the construction of

gravity walls is uneconomic for walls with high heights [4]. In some cases, so as to decrease the mass of concrete and to diminish the size of the walls, reinforcing steel with small amounts might be placed in the back of the gravity wall [4,5]. This type of wall is classified as a semi-gravity wall.

Cantilever retaining walls are constructed of reinforced concrete, and they are built in the shape of L, reverse L, or inverted T (in Figure 2.3). The wall comprises a stem with thin width and a base slab, in other words, a heel. In some cases, a shear key shown in Fig 6 may be used so as to increase sliding resistance. Additionally, this type of structure is economical to build walls with moderate heights (about 6 to 8 meters) because the weight of the backfill material resting on the base slab plays a crucial role in overall stability [5].

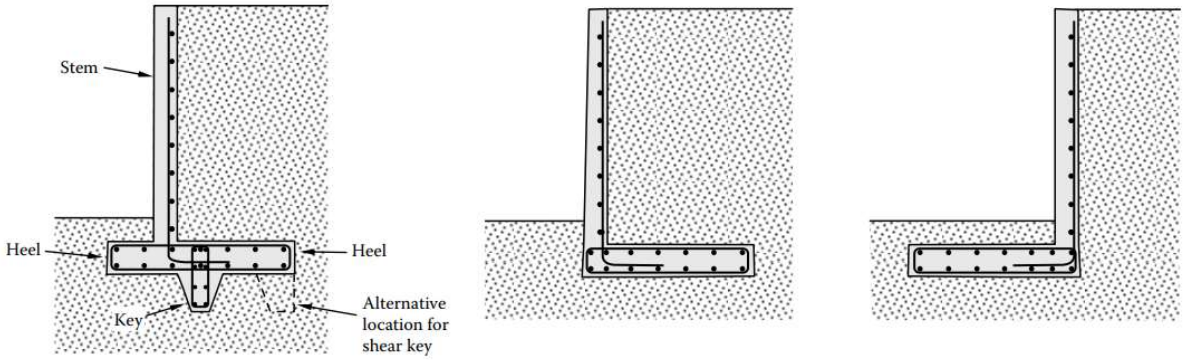

Figure 2.3. Cross-sections of the typical cantilever walls [6].

Moreover, a vertical bracket or rib connecting the stem and base of the wall might be necessary to construct walls with a height greater than 6 meters in order to lead to a decrease in bending moment and shear stresses in a wall stem and the base [6]. There are two types of brackets: counterfort and buttress. The difference between them is that counterforts are constructed at the back of the wall, which means that they are buried in the backfill material, while buttress is constructed at the front of the wall, as depicted in Figure 2.4.

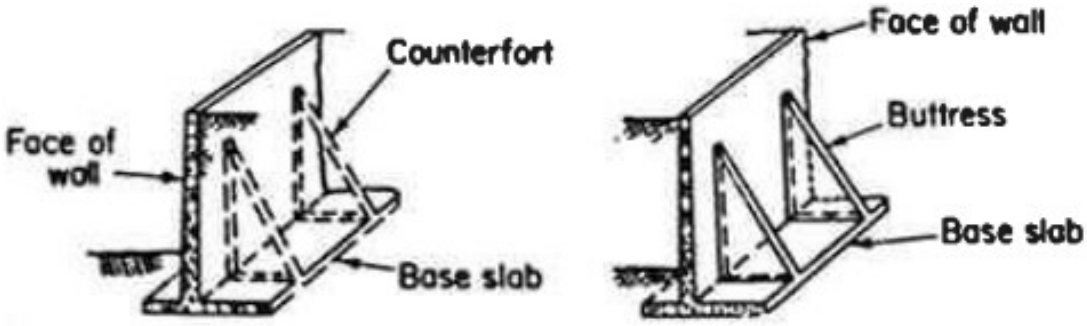

Figure 2.4. Counterfort and Buttressed [5].

Crib walls are another type of gravity wall. They consist of interlocking members with cells that are made of timber, precast concrete, or prefabricated steel, and compacted granular soil filled in the cells [5]. A wall with a height of about 6 to 9 meters subjected to moderate earth pressure may be built with cribs [6].

Lastly, using reinforcement materials, such as metal strips, geotextiles, or geogrids, in the design of retaining walls has gained popularity in recent years. These systems are identified as mechanically stabilized earth (MSE) walls, which have reinforced soil behind the wall, as depicted in Figure 2.5. The friction between the reinforcement material and the retained soil provides stability of the wall. Additionally, these flexible walls tolerate large displacements in lateral and vertical directions without significantly taking damage [4].

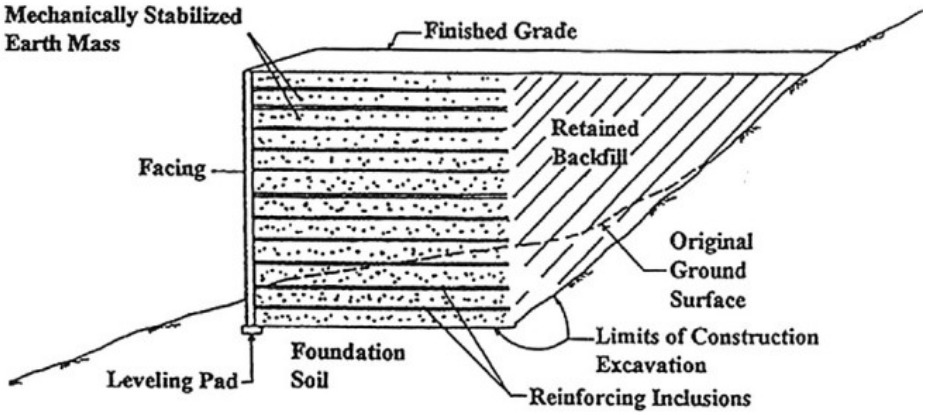

Figure 2.5. Cross-section and main elements of the MSE walls [7].

2.2. Failure of Retaining Walls

The failure is an undesirable situation because the retaining wall has a significant role in the transportation and infrastructural systems. Therefore, it is crucial to know what failure is, why and how it occurs, what are the indications of failure, and what are the remedies for possible failure. The failure of the retaining wall happens when it becomes unable to support the lateral forces created by the backfill soil. However, the phare of "failure" does not directly correspond to the total collapse of the soil-wall system. When total failure, which can be classified as overturning, sliding, loss of bearing capacity, excessive settlement, or deep-seated shear failure (Figure 2.6), occurs, the structure cannot be saved or rehabilitated. Total collapse happens rarely, but when it appears, the only solution is the reconstruction of the wall. However, the wall displays some indications before the possible future collapse, such as cracking, bulging, tilting, or deflection. If the reasons for these signs are determined by the professional evaluation, the possible failure can be prevented before it happens.

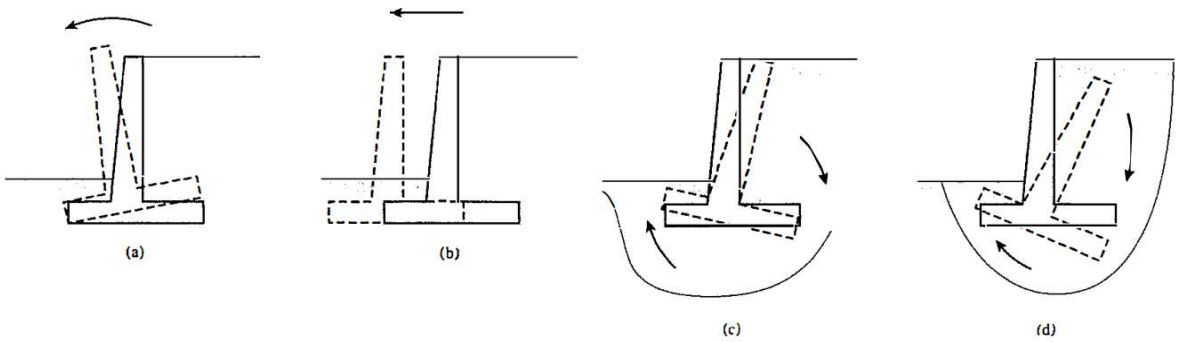

Figure 2.6. The failure mechanisms of retaining walls. (a) Overturning; (b) Sliding; (c) Bearing Capacity Failure; (d) Deep-seated Shear Failure [4].

The primary causes of failure/ failure indications can be listed as follows [8]:

1. Construction errors (such as placement of reinforcement at the wrong amount or position, or size)
2. Design errors (such as selection of insufficient wall type or size)

3. Making mistakes in calculation or using software, or detailing the project
4. The installation or design of an improper drainage system (which is not able to prevent surface water from accumulating within the backfill) or the clogged drainage holes due to a lack of filter layer
5. The selection of inappropriate backfill material (such as clay which can be swell and results in an increase in forces acting on the wall)
6. The foundation problems due to the absence of ground investigation on the construction site

Nevertheless, even if the retaining structures constructed in the seismic region are adequately designed under static conditions, both the internal forces generated during an earthquake and soil strength changing owing to a ground shaking might disturb the wall in the state of static equilibrium [9].

The following precautions are commonly used in order to preserve the wall stability against possible future failures [8]:

- Solving the surface drainage problems,
- Reduction of the wall height,
- Use of tie-backs,
- Extension of the footing size,
- Addition of the shear key,
- Removal and replacement of the backfill material with granular soils or lightweight materials,
- Use of reinforcement on the front of the wall

2.3. Case Studies of Retaining Wall Failure

The examples of failures or lateral movements of retaining walls due to various earthquakes were tabulated by Das and Ramana (2010), which are given in Table 2.1.

Table 2.1. The reported failures and movements of retaining walls [a] [10].

Earthquake	Date	M[e]	Harbor	Distance from Epicenter	Damage	Approximate Movement
Kitaizu	25 November 1930	7.1	Shimizu	48 km	Failure of gravity walls [b]	7.93 m
Shizuoka	11 July 1935		Shimizu	-	Retaining wall collapse [b]	4.88 m
Tonankai	7 December 1944	8.2	Shimizu	175 km	Sliding of retaining wall [b]	
			Nagoya	128 km	Outward movement of bulkhead with relieving platform [b]	3.05-3.96 m
			Yokkaichi	144 km	Outward movement of pile-supported deck [b]	3.66 m
Nankail	21 December 1946	8.1	Nagoya	200-304 km	Outward movement of bulkhead with relieving platform [b]	3.96 m
			Osaka	200-304 km	Failure of retaining wall above relieving platform [b]	4.27 m
			Yokkaichi	200-304 km	Outward movement of pile-supported deck [b]	3.66 m
			Uno	-	Outward movement of gravity wall [b]	0.61 m
Tokachioki	4 March 1952	7.8	Kushiro	144 km	Outward movement of gravity wall [b]	5.49 m
Chile	22 May 1960	8.4	Puerto Montt	112 km	Complete over-turning of gravity walls [c]	>4.57 m
					Outward movement of anchored bulkheads [c]	0.60-0.90 m
Niigata	16 June 1964	7.5	Niigata	51,2 km	Tilting of gravity wall [d]	3.05 m
					Outward movement of anchored bulkheads [d]	0.30-2.10 m

[a] After Seed and Whitman (1970)

[b] Reported by Amano, Azuma, and İshii (1956)

[c] Reported by Duke and Leeds (1963)

[d] Reported by Hayashi, Kubo, and Nakase (1966)

[e] Magnitude

Fang et al. (2003) examined three failure cases on the gravity-type retaining wall due to Chi-Chi Earthquake that happened in Taiwan on September 21, 1999. The first case was the failure of the retaining wall, which was constructed to withhold a steep excavation in Taiwan. The wall was built to consist of five blocks, and two of them fell down due to sliding along the construction joint during ground shaking, as shown in Figure 2.7.

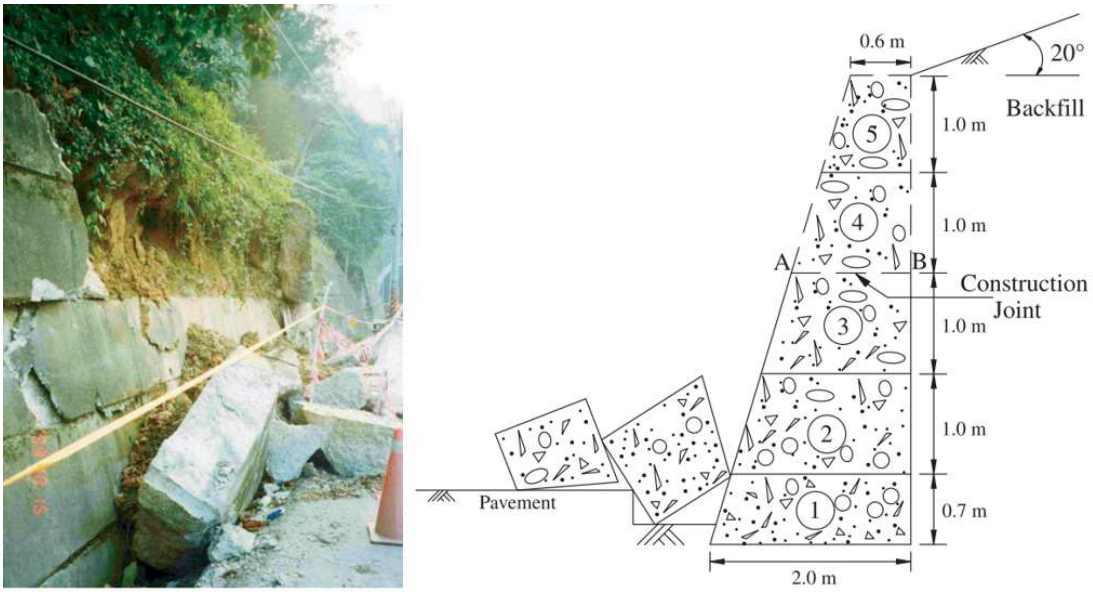

Figure 2.7. (a) The picture of the failed gravity wall, (b) The cross sections of failed wall [11].

The second case was the collapse of the gravity wall which was constructed with the aim of holding a steep slope. The wall turned about its toe after the earthquake due to bearing capacity failure, as shown in Figure 2.8.

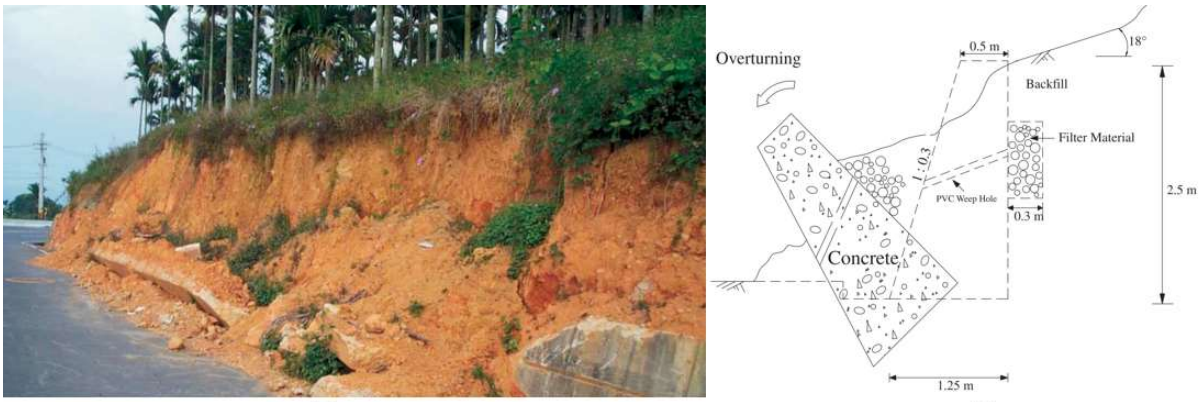

Figure 2.8. (a) The picture of the failed gravity wall, (b) The cross sections of failed wall [11].

The final case was the failure of the gravity wall occurred owing to excessive fault rupture. The gravity wall, which was built above a fault, overturned and slid during the earthquake, as shown in Figure 2.9.

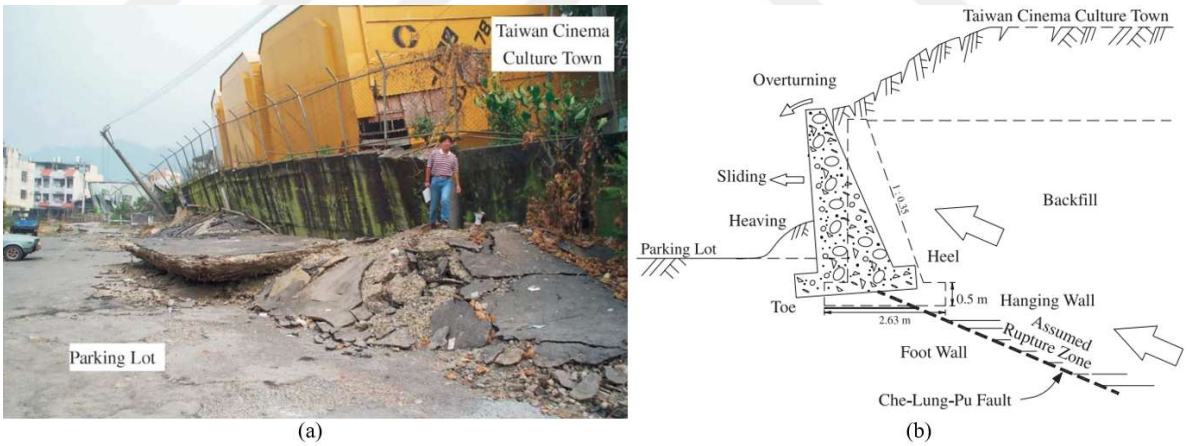

Figure 2.9. (a) The picture of the failed gravity wall, (b) The cross sections of failed wall [11].

Huang and Chen (2004) have examined two sites where the retaining walls constructed adjacent to the embankments failed during Chi-Chi Earthquake. The damaged walls displaced largely in both directions (horizontal and vertical) associated with tilting (comparably minor). The failure that occurred in the two investigated sites is depicted in Figures 2.11 and 2.12. As

can be seen in Figures 2.10 and 2.11, two failure mechanisms were observed in the incident sites. The first one is sliding along the base, and the other is bearing capacity failure.

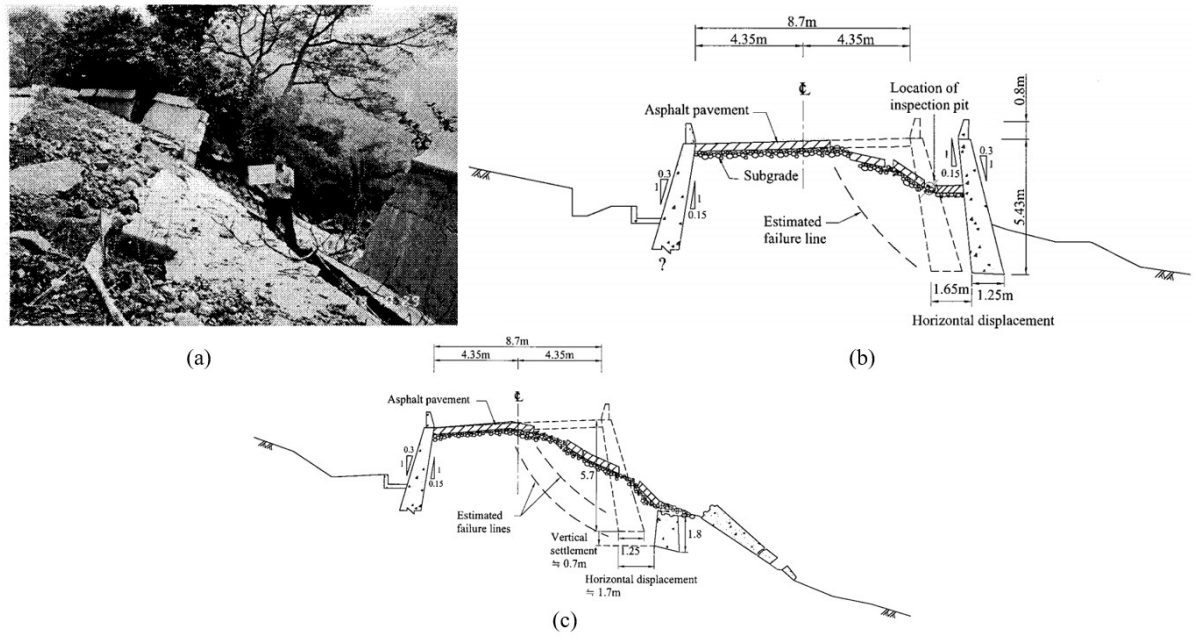

Figure 2.10. (a) The picture of the failed embankment and wall belonging to Case 1, (b) and (c) The cross sections of failed embankment and wall at different locations [12].

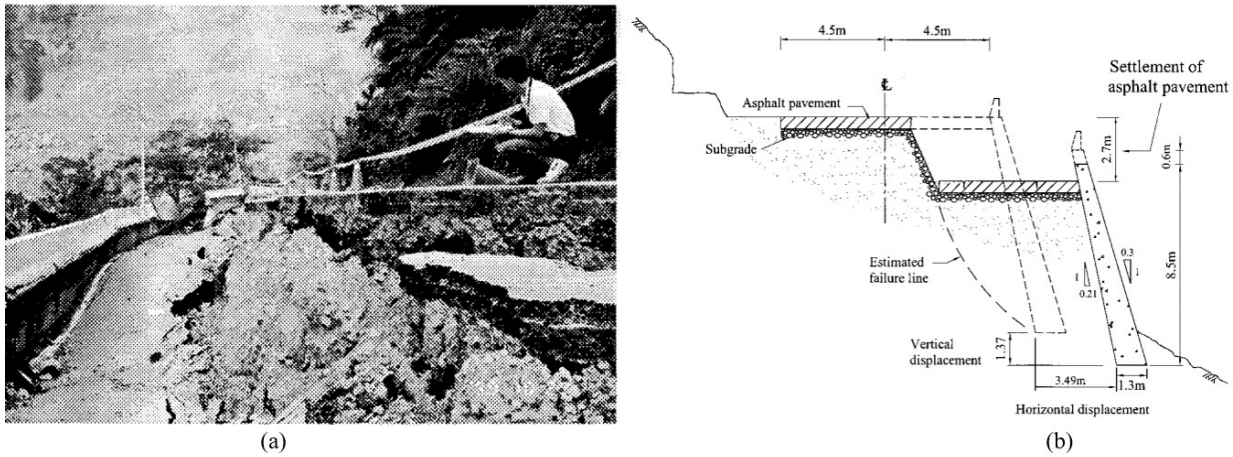

Figure 2.11. (a) The picture of the failed embankment and wall belonging to Case 2, (b) The cross-section of failed embankment and wall [12].

Binici et al. (2010) have studied a retaining wall damaged without showing any sign in Kahramanmaraş, Türkiye. The main reason for the failure was the fact that the pressure due to water was not considered during the design procedure. The heavy rainfall resulted in the accumulation of water behind the wall. Thus, the increase in hydrostatic pressure caused a drastic increase in lateral forces on the wall. Additionally, using an inappropriate type of aggregate and poor-quality concrete were other reasons for failure. The damaged wall is given in Figure 2.12.

Figure 2.12. The pictures of wall failure and collapsed wall [13].

Lim (2018) reviewed five different failure cases that occurred on retaining walls. Of the cases examined in this study, four cases stemmed from unloading problems, while one of them was a consequence of loading problems. The cases are tabulated in Table 2.2.

Table 2.2. The cases investigated by Lim (2018).

Case	Name	Location	Causes	Picture of Failure
1	The Nicoll Highway Excavation	Singapore	- Unloading due to excavation - Underestimation of diaphragm wall bending moment and displacement due to overestimation of undrained shear strength	 (a). Before collapse  (b).After collapse
2	Rebar Broadway Excavation	Taipei, Taiwan	- Unloading due to excavation - Failure of struts and diaphragm wall as well	

Table 2.2. The cases investigated by Lim (2018). (cont.)

3	Shipai Excavation	Taipei, Taiwan	- Unloading due to excavation - Failure of struts and diaphragm wall as well	
4	Case A Excavation	North Jakarta, Endonesia	- Unloading due to excavation - Absence of appropriate design of excavation	

Table 2.2. The cases investigated by Lim (2018). (cont.)

5	High Retaining Wall Failure	North Bandung, Endonesia	- Loading due to heavy rain - The usage of colluvium backfills where water can easily infiltrate	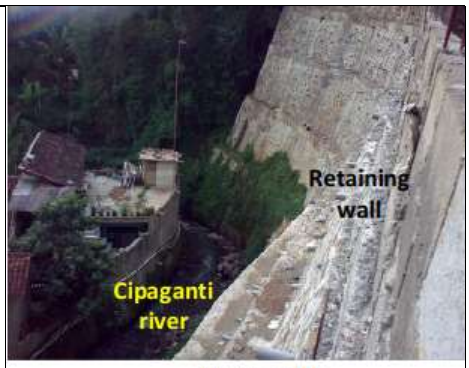 (a). Before failure  (b). After failure

3. STATIC AND DYNAMIC STABILITY OF THE RETAINING WALL

3.1. Introduction

The design of the retaining wall under static and seismic conditions has always been a significant subject in geotechnical engineering. In order to design and construct them adequately, detailed information about the lateral earth pressure that acts between the structure and the backfill soil has great importance. Moreover, so as to understand the seismic behavior of the retaining wall, the static earth pressure against the wall prior to ground shaking and the dynamic earth pressure occurring temporarily during the earthquake should be investigated [9]. Accordingly, in this section, the calculation of static and dynamic pressures on retaining walls will be explained in order to understand the static and seismic behavior of retaining walls.

3.2. Analytical Methods for Calculation of Static Earth Pressure

The magnitude and distribution of lateral earth pressure under static loading are functions of the following factors [4]:

- the unit weight of retained soil,
- the shear strength parameters of backfill soil,
- the type and amount of wall displacement,
- the drainage conditions within retained soil.

However, the wall movement largely affects the static earth pressure. When the wall tilt is constrained, the corresponding earth pressure is referred to as at-rest earth pressure (Figure 3.1a). In addition, active earth pressure occurs when the wall deflects away from the backfill soil (Figure 3.1b), whereas passive earth pressure occurs when the wall moves toward the backfill soil (Figure 3.1c) [4,9].

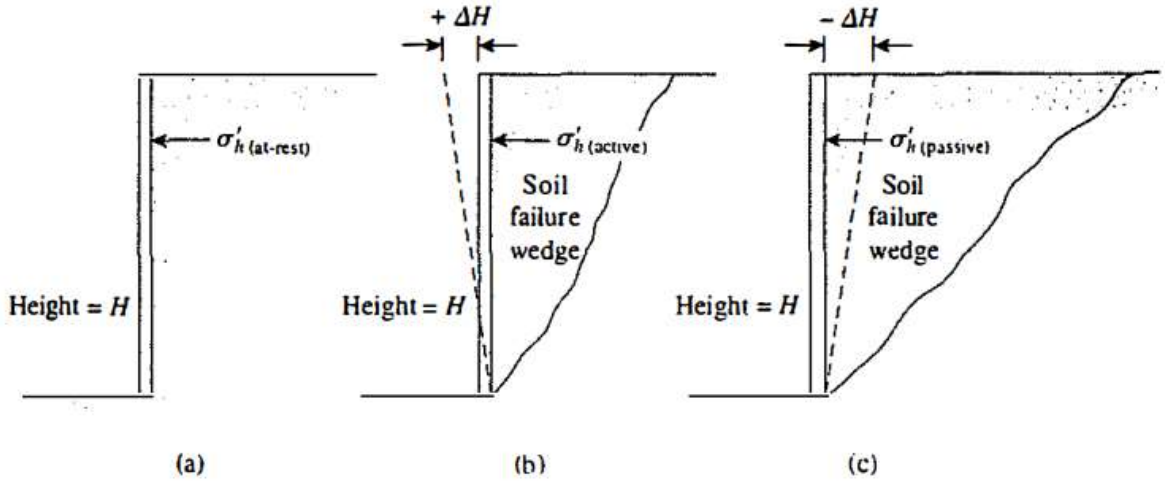

Figure 3.1. The lateral earth pressures on the retaining wall [4].

Reaching active and passive state needs a wall movement that relies on the type of backfill soil and the height of the wall, as shown in Table 3.1.

Table 3.1. The required wall movement for reaching active and passive states [15].

Soil Type	Horizontal Movement Required to Reach the Active Condition	Horizontal Movement Required to Reach the Passive Condition
Dense sand	0.001 H	0.020 H
Loose sand	0.004 H	0.060 H
Stiff clay	0.010 H	0.020 H
Soft clay	0.020 H	0.040 H

The horizontal pressure of the wall gradually increases under passive conditions, while the horizontal thrust gradually decreases under active conditions. The change in lateral earth pressure with wall displacement is demonstrated in Figure 3.2.

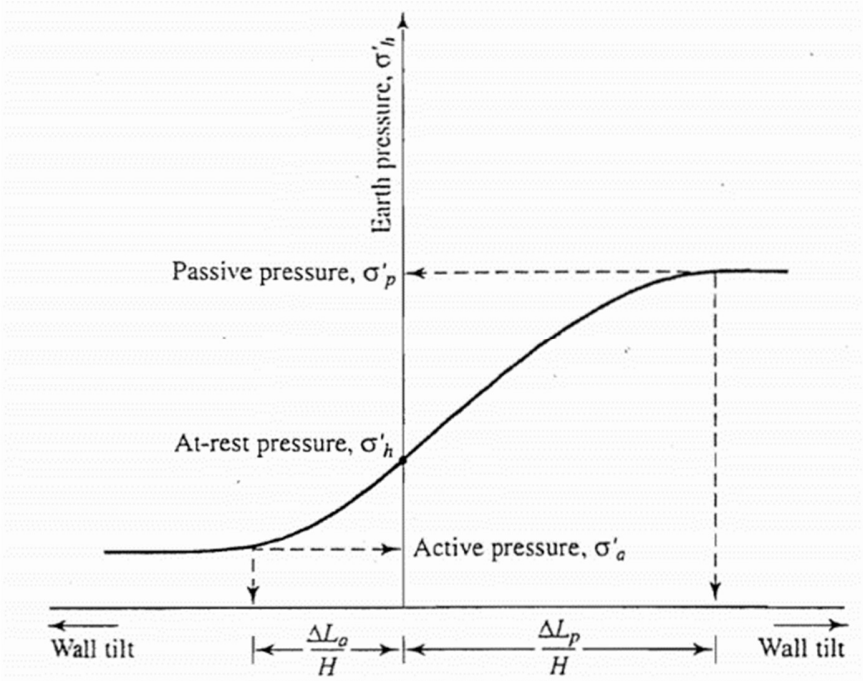

Figure 3.2. The change in lateral earth pressure with wall movement [16].

With the aim of designing earth-retaining structures, the estimation of lateral earth thrust was one of the first implementations of the scientific approach [15]. The pioneering theory for lateral earth pressure against the earth retaining wall was proposed by Charles Augustin Coulomb in 1776. In his work, the force equilibrium method was used as an approach to calculate the magnitude of lateral forces against the wall with cohesionless granular backfill soil having a constant friction angle and an infinite length [9,17]. Furthermore, the failure surface was postulated as a plane, and the friction between the structure and the retained soil was taken into consideration [16]. The critical failure surface on which the active pressure becomes maximum and the passive pressure becomes minimum was determined by analyzing several trial slip surfaces of failure [9,17]. In Figure 3.3, the prediction of the maximum active soil thrust generated on the critical failure plane by Coulomb's theory is depicted.

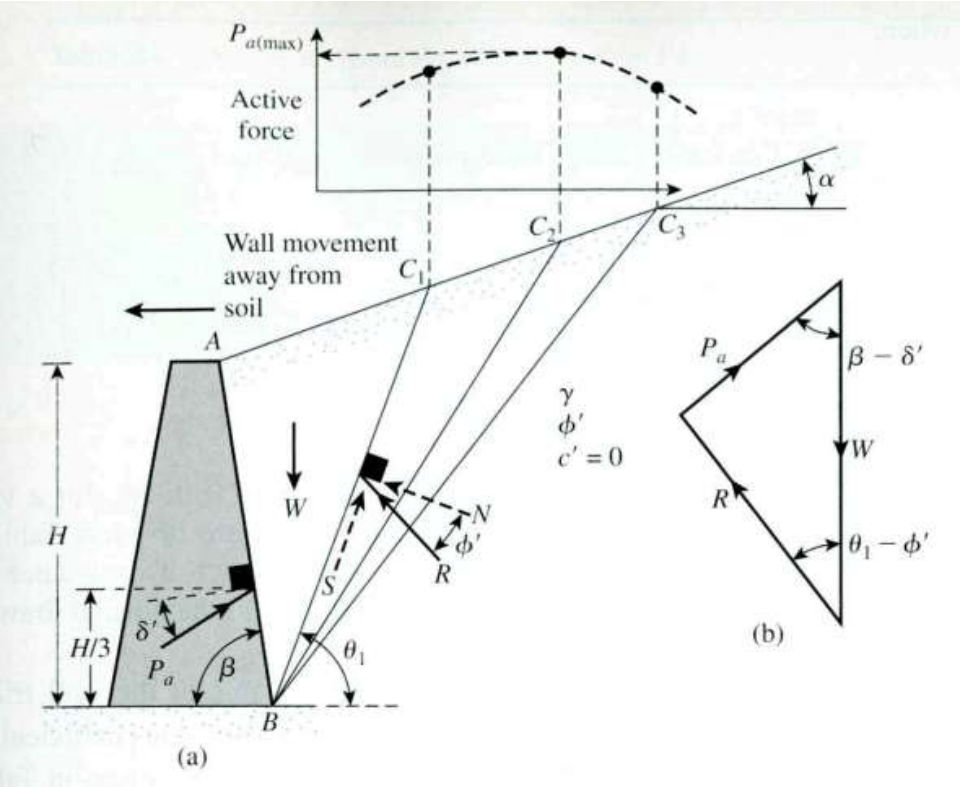

Figure 3.3. Coulomb's Active Earth Pressure, (a) Determination of the maximum active force per unit length (P_a) value, (b) The application of the force equilibrium method [4].

In 1857, William John Macqourn Rankine proposed a much simpler method to determine active and passive earth pressures acting on the wall [9]. Rankine's approach was based on the stress state of the soil. While developing this approach, Rankine made the following assumptions [2], [15], [17].

1. There is homogenous and cohesionless soil behind the wall with a plane surface.
2. The critical failure surface is planar.
3. The back of the wall is vertical.
4. There is no friction between the wall and the retained soil.
5. The wall has an infinite length to analyze it in two-direction and to avoid end effects (a plane strain condition).

By using these presumptions, the problem of lateral earth pressure became more certain, and the static earth pressures against the wall were able to be calculated directly (Kramer, 1996).

There are other researchers who worked on the lateral earth pressure problem and who contributed significantly to this issue. However, these works have their origins in the work of Coulomb and Rankine [15]. One of these researchers is Culmann (1975). He presented a graphic solution technique using Coulomb's theory which can be applied on the wall with any friction angle, not taking into consideration the irregularity of backfill and surcharges [16].

3.3. Analytical Methods for Calculation of Dynamic Earth Pressure

The determination of seismic behavior of even the simple form of retaining structure has considerable complexity because of the fact that the response of the soil, wall, and ground motion nature have an impact on the dynamic response of the wall. Moreover, owing to the variability and uncertainty of soil properties, the dynamic response of the retaining structure cannot be determined completely. In order to make his complicated problem simpler and easier to solve, the estimation of earthquake-induced lateral earth pressure behind the wall is made by a simplified method with various assumptions and approximations about soil, structure, and ground motion [9,18].

In this study, these methods will be briefly examined into two main categories. These categories are force-based and displacement-based methods.

3.3.1. Force-based Methods

The retaining wall is designed commonly by determining the loads acting on the wall during the ground shaking and by controlling whether the wall can remain stable without sliding, overturning, and bearing capacity failure. Dynamic earth pressure acting on the wall can be

calculated by simplified methods because of the complexity of original loading conditions during earthquake shaking [9,18].

3.3.1.1. Mononobe-Okabe Method. Okabe (1926) and Mononobe and Matsuo (1929) proposed a method to estimate earthquake-induced lateral earth pressure under active and passive conditions after the Great Kanto Earthquake of 1923. This method is broadly referred to as Mononobe-Okabe (M-O) method. The M-O method is a modified form of Coulomb's theory. Additionally, similar to Coulomb's theory, the M-O method utilizes the force equilibrium method and does not establish the dynamic earth pressure distribution with depth, which means that the total force and its acting point were evaluated [19]. Furthermore, this method considers the seismic forces as equivalent static forces acting on the soil wedge behind the structure (pseudo-static approach) [20,21]. The forces considered in this method are shown in Figure 3.4.

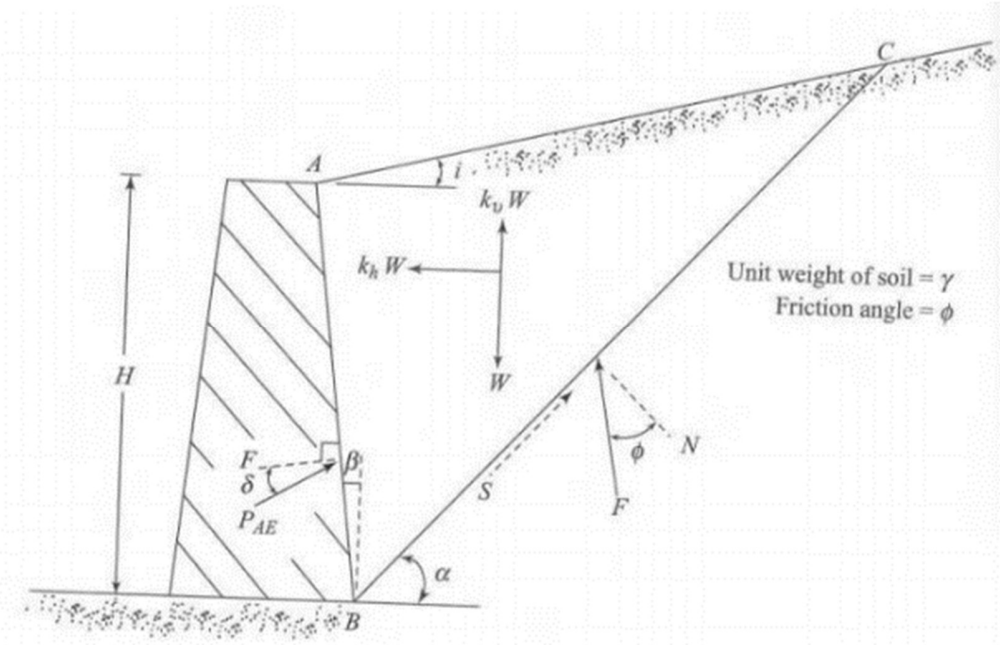

Figure 3.4. The forces against the wall evaluated by the Mononobe-Okabe [10].

This pseudo-static method was established for gravity walls with dry cohesionless backfill material, and the following assumptions were made [19]:

1. The wall movement is sufficient to generate minimum active pressure.
2. When the minimum active pressure is attained, a soil wedge behind the wall is at the point of incipient failure, and the maximum shear strength is mobilized along the potential sliding surface.
3. The backfill soil behaves as a rigid body so that the accelerations propagate uniformly within the soil mass.
4. The equivalent static forces of the earthquake motion can be expressed as k_h.W and k_v.W, where W, $a_h = k_h.g$, and $a_v = k_v.g$ are the weight of the soil wedge, horizontal and vertical components of the earthquake accelerations (g is the acceleration due to gravity), respectively.

The total active thrust (P_{AE}) and passive thrust (P_{PE}) per unit length of the wall calculated by force equilibrium is represented as

$$P_{AE} = \frac{1}{2}\gamma H^2(1-k_v)K_{AE} \tag{3.1}$$

$$P_{PE} = \frac{1}{2}\gamma H^2(1-k_v)K_{PE} \tag{3.2}$$

where γ is the unit weight of the backfill soil, H is the height of the wall, K_{AE} are K_{PE} are the coefficients of active and passive earth pressure under seismic loading, respectively. K_{AE} and K_{PE} are determined as

$$K_{AE} = \frac{\cos^2(\Phi-\theta-\beta)}{\cos\theta\cos^2\beta\cos(\delta+\beta+\theta)\left[1+\sqrt{\frac{\sin(\Phi+\delta)\sin(\Phi-\theta-i)}{\cos(i-\beta)\cos(\delta+\beta+\theta)}}\right]^2} \tag{3.3}$$

$$K_{PE} = \frac{\cos^2(\Phi-\theta+\beta)}{\cos^2\beta\cos(\delta-\beta+\theta)\left[1-\sqrt{\frac{\sin(\Phi-\delta)\sin(\Phi-\theta+i)}{\cos(i-\beta)\cos(\delta-\beta+\theta)}}\right]^2}, \tag{3.4}$$

in which φ is the internal friction angle of the backfill soil, δ is the angle of wall friction, i is the slope of the backfill surface relative to the horizontal, β is the slope of the wall back relative to the vertical, θ is calculated as $\tan^{-1}\left(\frac{k_h}{1-k_v}\right)$.

Arango (1969) has proposed a method to determine the value of K_{AE} using the standard charts for K_A which is the active earth pressure coefficient calculated by Coulomb's theory under static conditions. This procedure is applicable for any slope angle of the backfill surface

and the wall face, wall friction, internal friction of backfill soil, and earthquake acceleration [19].

Kapila (1962) developed a method for the determination of the dynamic active and passive earth pressure using graphical construction. This method was modified from Culmann's graphical method for static earth thrust [19].

Seed and Whitman (1970) have investigated the impacts of the wall friction angle, δ, the internal friction of the backfill soil, φ, the inclination of the ground surface behind the wall, i, and the vertical acceleration components of the earthquake, k_v, on the value of K_{AE}, as shown in Figure 3.5.

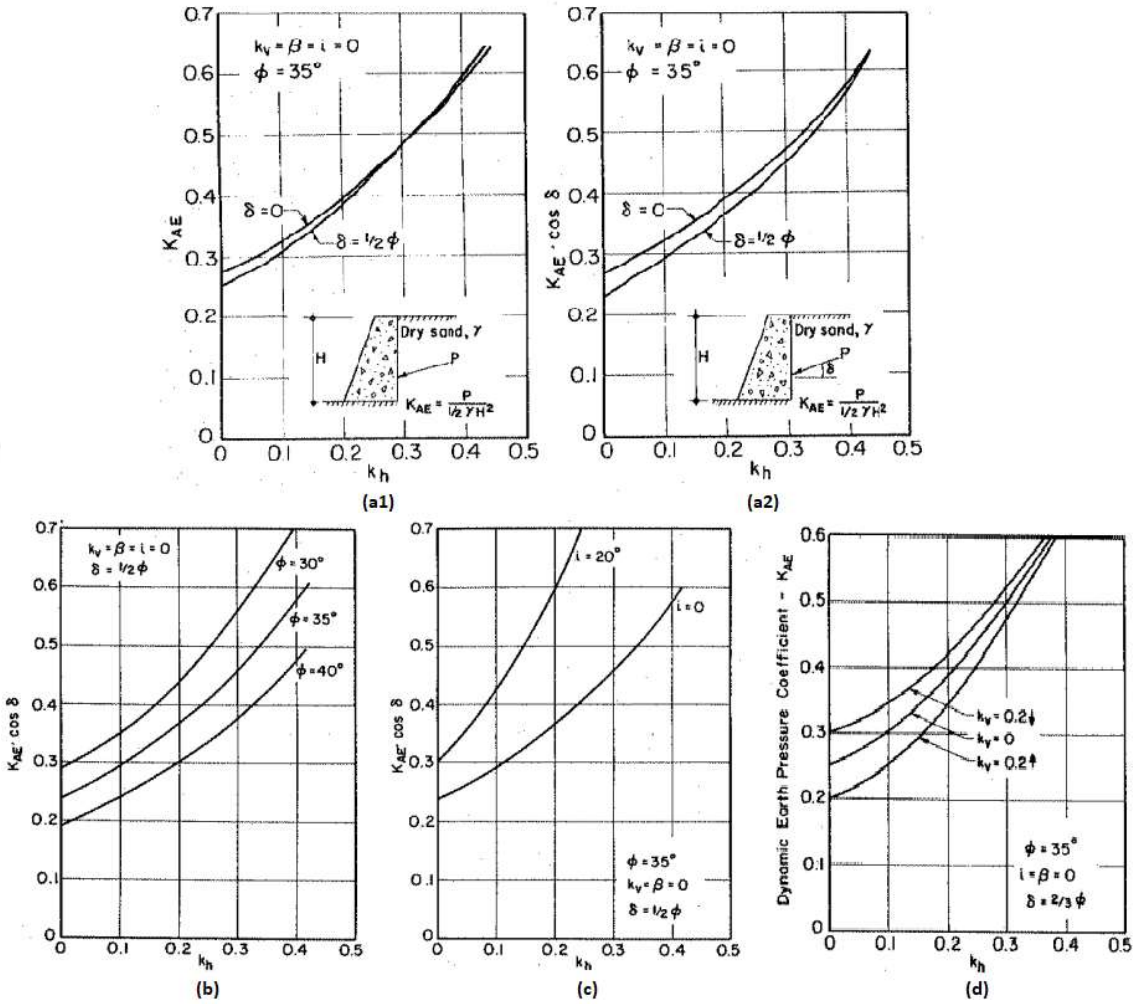

Figure 3.5. The effects of the angle of wall friction (a1 – a2), the friction angle of soil (b), the backfill inclination (c), and the vertical acceleration (d) on the coefficient of lateral earth pressure under seismic loading [19].

They noted that the total maximum earth pressure (P_{AE} or P_{PE}) could be divided into a static component (P_A or P_P) and an additional component of dynamic lateral force (ΔP_{AE} or ΔP_{PE}) due to an earthquake. Therefore, the dynamic increment of the active and passive thrust and the dynamic earth pressure coefficients for active and passive conditions could be expressed in a simpler manner as

$$\Delta P_{AE} = \frac{1}{2}\gamma H^2 \Delta K_{AE} \; ; \;\; K_{AE} = K_A + \Delta K_{AE} \tag{3.5}$$

$$\Delta P_{PE} = \frac{1}{2}\gamma H^2 \Delta K_{PE} \; ; \;\; K_{PE} = K_P + \Delta K_{PE} \; , \tag{3.6}$$

where K_A and K_P are the coefficients of static active and passive pressures calculated by Coulomb's theory, respectively, ΔK_{AE} and ΔK_{PE} are the the coefficients of dynamic pressure increments for active and passive conditions, respectively.

The changes in ΔK_{AE} with the horizontal acceleration (k_h.g) of the earthquake are depicted in Figure 3.6. This graph was plotted for a vertical wall with a horizontal backfill surface and a soil friction angle of 35° in the backfill soil. Considering Figure 3.6, the value of ΔK_{AE} could be equal to $2/3k_h$ for practical purposes.

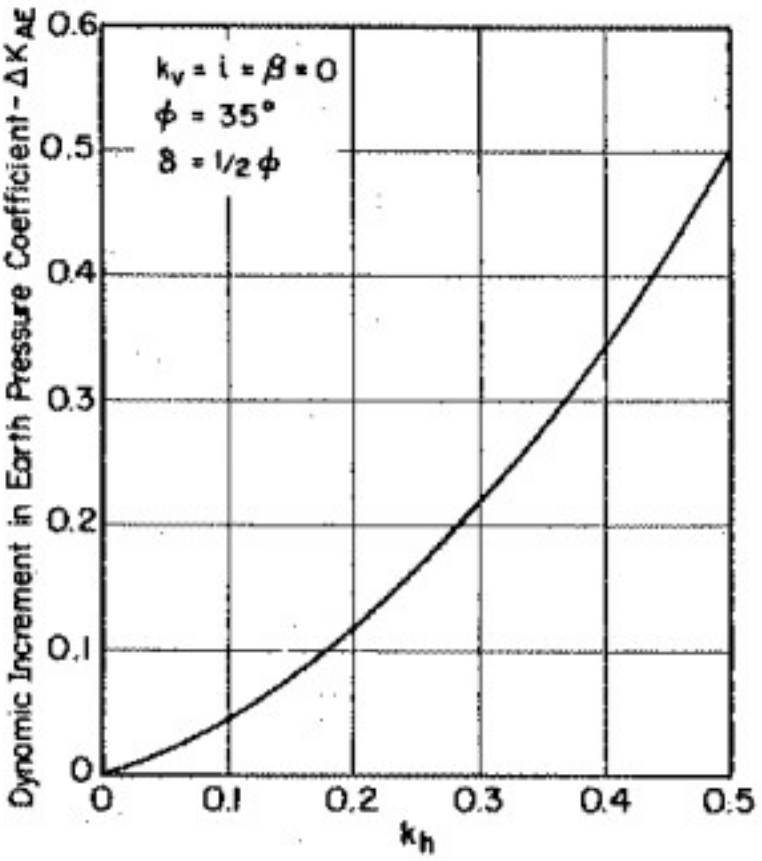

Figure 3.6. Dynamic increment in earth pressure coefficient, ΔK_{AE} [19].

Mononobe-Okabe (M-O) analysis suggested that the point of application of the dynamic active force should be at H/3 above the base of the wall of height, H, which is the same acting

point of the active thrust under static conditions. Nevertheless, laboratory tests carried out on retaining structures have demonstrated that the total dynamic earth force (P_{AE} or P_{PE}) was applied at a height greater than H/3 [1,10], as illustrated in Figure 3.7.

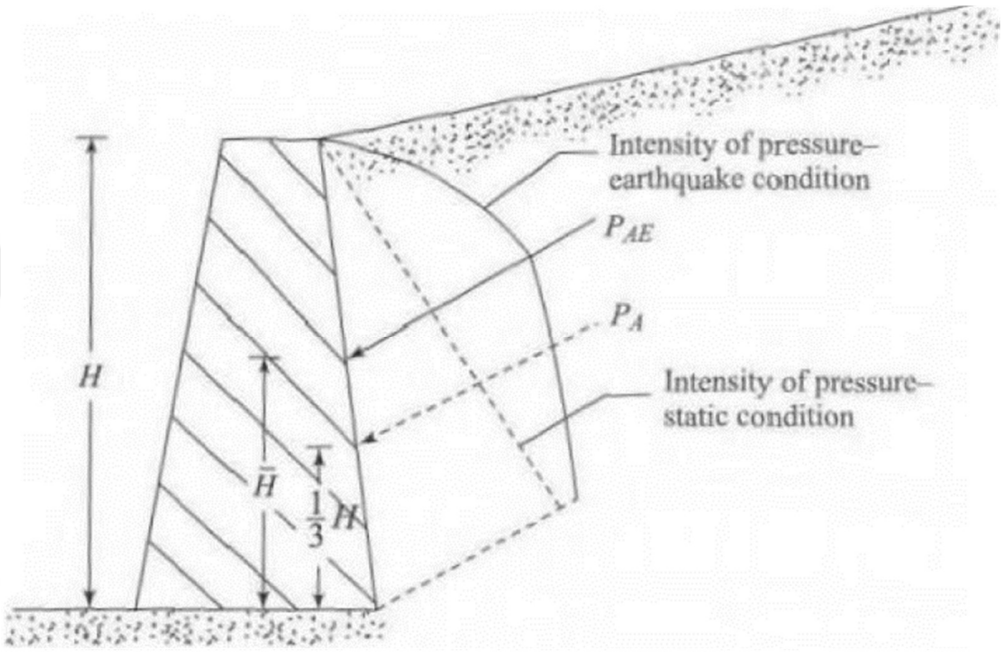

Figure 3.7. The application points of static and dynamic earth thrusts [10].

Prakash and Pasavanna (1969) have proposed a theoretical method to obtain the height of the acting point of total earth force which is calculated by the M-O method (Das and Ramana, 2010). The value of $\bar{H}$ is calculated as

$$\bar{H} = C_{ha} * H/3. \tag{3.7}$$

C_{ha} can be selected in Figure 3.8 as corresponding to the value of k_h on the basis of force and moment equilibrium conditions [10,19].

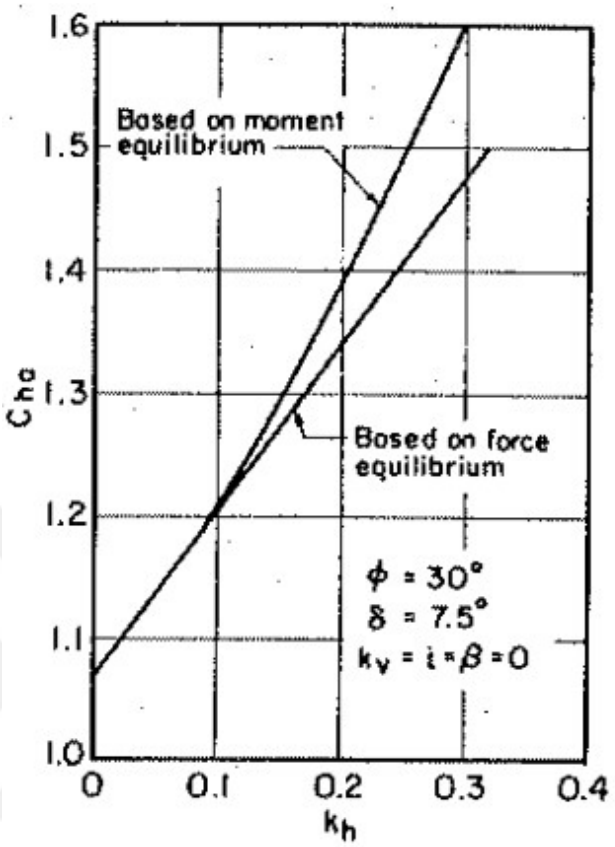

Figure 3.8. The values of C_{ha} based on moment and force equilibrium conditions [19].

The simple procedure for the determination of M-O earth pressure against a retaining wall which was proposed by Seed (1969) has suggested that the application point of the dynamic increment could be at 0.6H above the base of the wall, as illustrated in Figure 3.9. Thus, the value of $\overline{H}$ can be determined as [1], [10], [19]

$$\overline{H} = \frac{P_A(1/3H)+\Delta P_{AE}(0,6H)}{P_{AE}}. \quad (3.8)$$

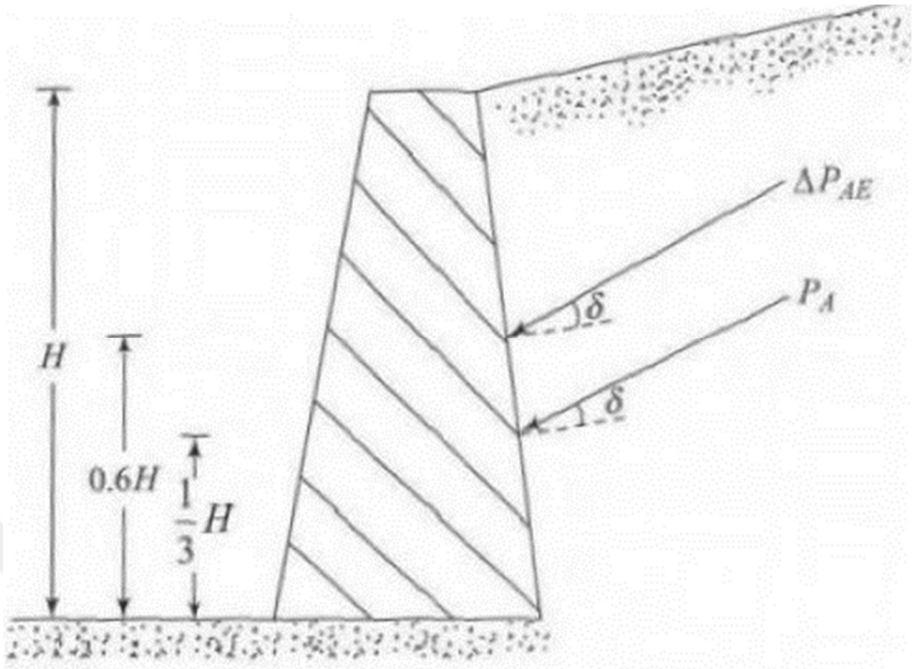

Figure 3.9. The acting point of a static component and an additional increment of dynamic forces, according to Seed (1969) [10].

Seed and Whitman (1970) reviewed experimental studies on retaining walls and indicated that the dynamic pressure increment (ΔP_{AE} or ΔP_{PE}) should act between 0,5H and 0,67H measured from the base of the unanchored retaining wall. Furthermore, the authors suggested that the effective acceleration leading to movement on the wall could be selected as about 85% of the peak acceleration since the duration of the PGA is not sufficient to result in significant movement, but the effective acceleration occurs several times and is smaller than the value of PGA. Additionally, they concluded that the retaining structure designed appropriately under static conditions would probably display a good performance experiencing dynamic loading.

Prakash and Saran (1966) and Saran and Prakash (1968) have developed a procedure to calculate the total lateral earth pressure (sum of dynamic and static pressures) acting on the wall holding c-φ soil with a horizontal surface, as depicted in Fig 3.10. This method was established based on the following assumptions [10], [20], [22]:

1. The effects of vertical acceleration of ground motion were ignored.
2. The adhesion along the soil-wall interface was assumed to equal the cohesion of the backfill.

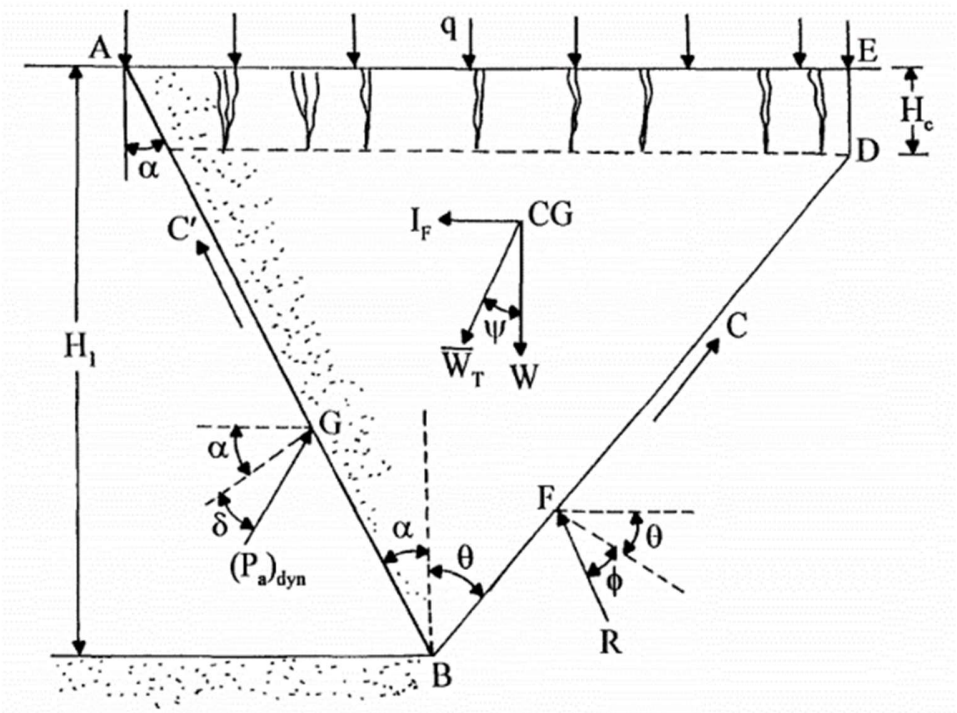

Figure 3.10. The forces against the wall evaluated by Prakash and Sarah (1966) [22].

Das and Puri (1996) have proposed a method modified from Coulomb's theory by considering the effects of cohesion (c), adhesion (c'), the inclination of the ground surface behind the wall (i), horizontal and vertical acceleration of the ground shaking (a_h and a_v), surcharge loading (q), the inclination of the wall (α), depth of tension cracks (H_c). Figure 3.11 demonstrates the aforementioned parameters, the soil wedge, and the acting forces on it.

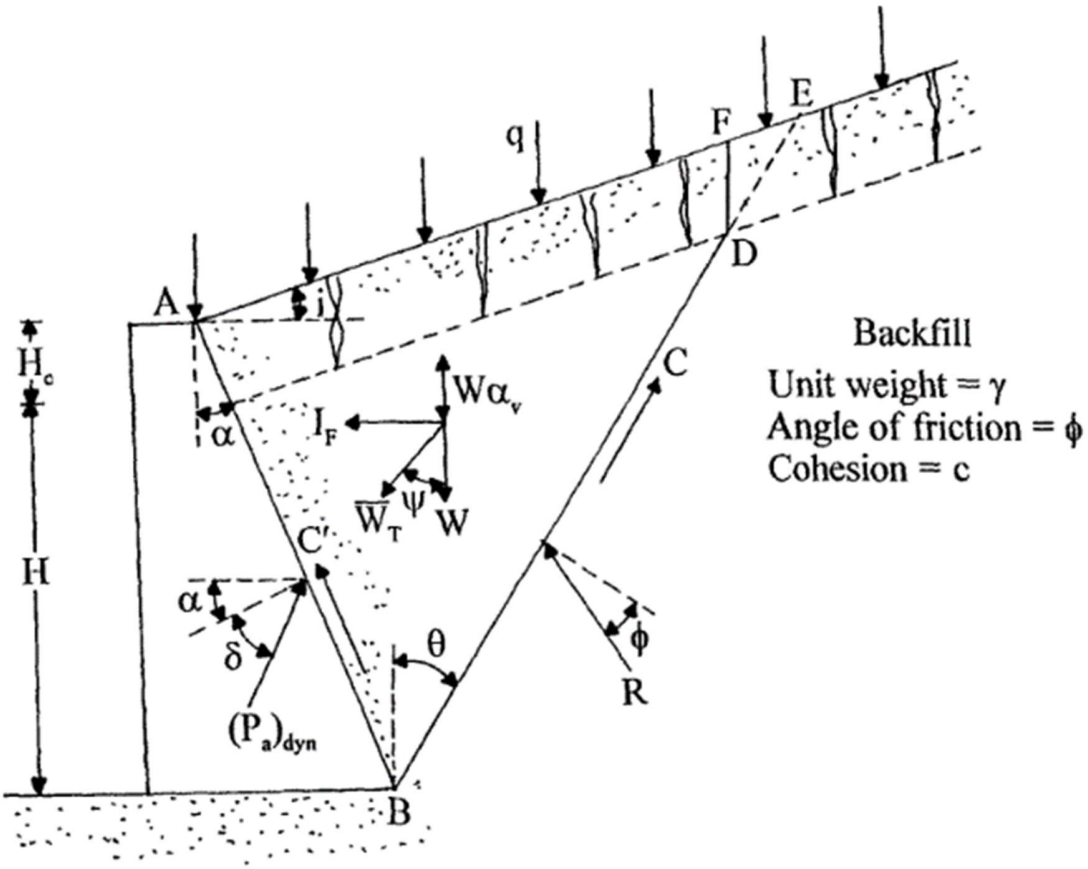

Figure 3.11. The forces against the wall evaluated by Das and Puri (1996) [22].

3.3.1.2. Steedman- Zeng Method. Pseudo-static analysis (M-O method) considers the dynamic nature of the earthquake in a very approximate manner, regardless of the effects of time and seismic waves, and it has been assumed that the acceleration is uniform within the soil mass retained by the wall. The assumption of uniform acceleration is only valid if the backfill soil behaves like a rigid body and the shear wave velocity is infinite. Furthermore, both the magnitude and the phase of the acceleration were presumed uniform [23,24]. With the aim of eliminating these limitations, Steedman and Zeng (1990) has developed a simple pseudo-dynamic analysis to estimate seismic earth pressure behind a fixed-base cantilever wall retaining dry backfill material, as shown in Figure 3.12.

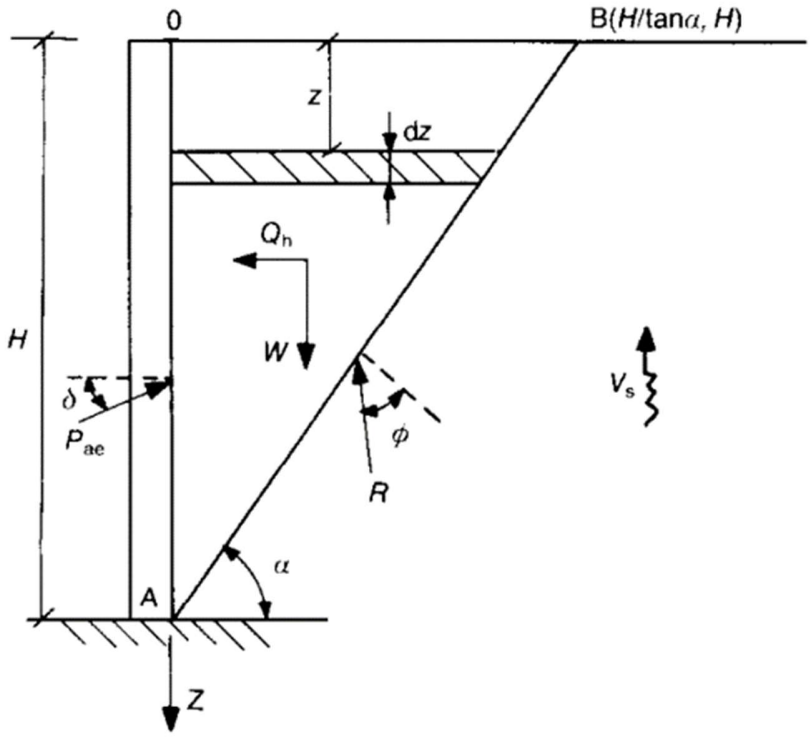

Figure 3.12. The forces evaluated by Steedman and Zeng (1990).

This simple but more realistic method took into consideration the time and phase difference owing to finite shear wave propagation within the backfill soil [9], [23], [25-26].

Steedman and Zeng (1990) proposed this pseudo-dynamic analysis based on the following assumptions [24,27]:

1. The shear modulus is constant with depth.
2. The magnitude does not change, whereas the phase of acceleration does.
3. The critical failure surface in the backfill soil is planar.

As seen in Figure 3.13, in order to simplify the problem, the wall and the ground surface of retained soil were assumed as vertical (i=0°) and horizontal (β=0°), respectively. In addition,

the period of lateral shaking was defined as T=2π/ω, where ω is the angular frequency. The acceleration of harmonic base shaking at a depth z and time t can be expressed as

$$a(z,t) = k_h g \sin\left[\omega\left(t - \frac{H-z}{V_s}\right)\right] = a_h \sin\left[\omega\left(t - \frac{H-z}{V_s}\right)\right], \quad (3.9)$$

in which

$a_h =$ the horizontal acceleration of the earthquake ($k_h g$),

H= the height of the wall,

$V_s = \left(\frac{G}{\rho}\right)^{1/2}$, the shear wave velocity (G and ρ are the shear modulus and density of the backfill soil, respectively.).

The mass of the horizontal element of depth z is determined as

$$m(z) = \rho\left(\frac{H-z}{\tan\alpha}\right)dz = \frac{\gamma}{g}\left(\frac{H-z}{\tan\alpha}\right)dz, \quad (3.10)$$

where γ is the unit weight of the backfill soil, α is the angle of the triangular soil wedge relative to the horizontal.

The total horizontal inertia force within the soil wedge can be expressed as

$$Q_h(t) = \int_0^H m(z)a(z,t)dz = \frac{\lambda\gamma k_h}{4\pi^2\tan\alpha}[2\pi H\cos\omega\zeta + \lambda(\sin\omega\zeta - \sin\omega t)] \quad (3.11)$$

in which λ is the shear wavelength propagating vertically which is calculated as $2\pi V_s/\omega = T/\omega$, ζ is determined as $t\text{-}H/V_s$.

If the limit of $Q_h(t)$ is solved as V_s approaches infinity due to the presumption of infinite shear wave velocity of the pseudo-static method, the equivalent static force in the horizontal direction assumed in the M-O method will be obtained as

$$\left(\lim_{V_s\to\infty} Q_h\right)_{max} = \frac{\gamma H^2 k_h}{2\tan\alpha} = \frac{1}{2}\frac{\gamma H^2}{\tan\alpha}k_h = Wk_h \quad (3.12)$$

where W is the weight of the soil wedge OAB shown in Figure 3.13.

When the forces acting on the soil wedge OAB were resolved by the limit equilibrium method, the total active soil thrust was determined as

$$P_{AE}(t) = \frac{Q_h(t)\cos(\alpha-\phi)+W\sin(\alpha-\phi)}{\cos(\delta-\alpha+\phi)}. \quad (3.13)$$

Moreover, the coefficient of dynamic, active earth pressure was expressed as

$$K_{AE}(t) = \frac{2P_{AE}(t)}{\gamma H^2}. \quad (3.14)$$

The derivation of $K_{AE}(t)$ can be obtained by substituting P_{AE} and Q_h in the above equation.

In a similar manner to Seed and Whitman (1970), Steedman and Zeng (1990) have separated the total active pressure (P_{AE}) into static (P_{as}) and dynamic (P_{ad}) components as

$$P_{AE}(t) = \frac{\partial P_{AE}(t)}{\partial z} = \frac{\gamma z}{\tan\alpha}\frac{\sin(\alpha-\phi)}{\cos(\delta-\alpha+\phi)} + \frac{k_h\gamma z}{\tan\alpha}\frac{\cos(\alpha-\phi)}{\cos(\delta-\alpha+\phi)}\sin\left[\omega\left(t-\frac{z}{V_s}\right)\right] = P_{as} + P_{ad}(t). \quad (3.15)$$

It can be observed that the dynamic earth pressure determined by the pseudo-dynamic method increases as a nonlinear function of depth, while that determined by the pseudo-static method increases linearly with depth. This comparison of dynamic earth pressure distributions is depicted in Figure 3.13.

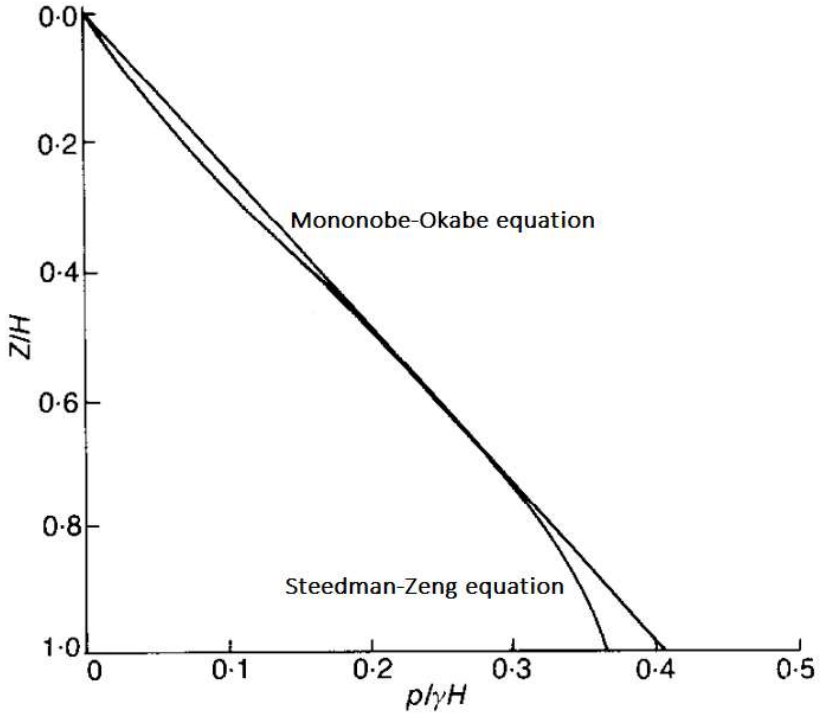

Figure 3.13. The comparison of dynamic earth pressure distributions determined from Mononobe-Okabe method and Steedman and Zeng method (for φ=33°, δ=16°, k_h=0.20, H/TV_s=0.30) [24].

The application point of the dynamic earth pressure can be determined by taking a moment about the bottom of the wall as

$$h_d = H - \frac{2\pi^2 H^2 \cos\omega\zeta + 2\pi\lambda H \sin\omega\zeta - {}^2(\cos\omega\zeta - \cos\omega t)}{2\pi H \cos\omega\zeta + \pi\lambda(\sin\omega\zeta - \sin\quad)}. \qquad (3.16)$$

Steedman and Zeng (1990) have simply considered the shear wave velocity and horizontal acceleration of the earthquake while developing the method [27]. Choudhury and Nimbalkar (2006) have modified this pseudo-dynamic method by taking into account the effect of several parameters such as primary wave velocity (V_p), vertical acceleration of the earthquake (a_v=k_vg), wall friction angle (δ), and soil friction angle (φ) in addition to those considered by Steedman and Zeng (1990). Furthermore, the authors have made similar assumptions to Steedman and Zeng (1990) to estimate dynamic earth pressure acting on the wall. The generated model is depicted in Figure 3.14.

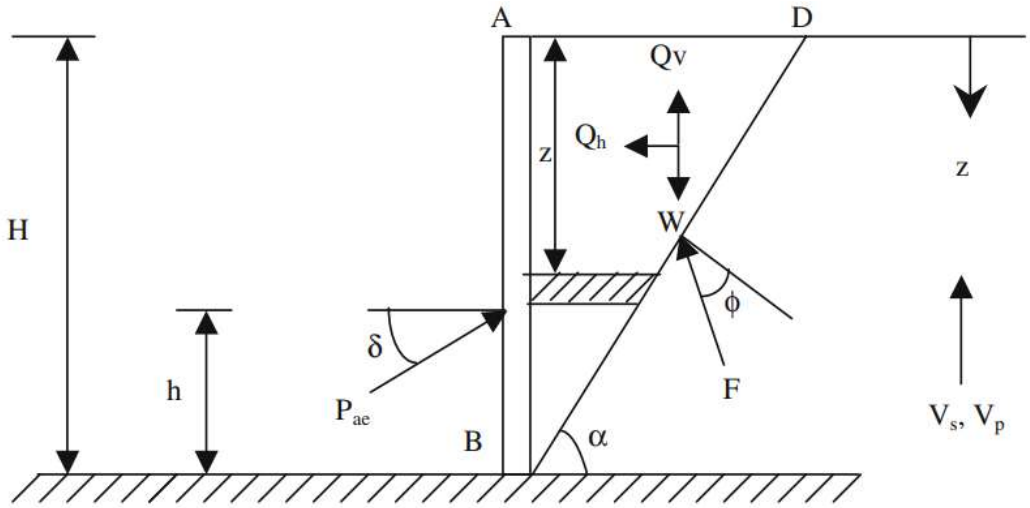

Figure 3.14. The forces evaluated by Choudhury and Nimbalkar (2006).

In their study, they claimed that the pseudo-dynamic method gave more realistic results on the nonlinear distribution of active earth pressure under seismic loading in comparison with the pseudo-static method. Additionally, they concluded that the seismic active earth thrust was influenced considerably by both horizontal and vertical components of the earthquake.

The pseudo-dynamic approach has been extended by researchers by considering the effects of various conditions or parameters. Ghosh (2010) proposed a solution, a modification of the method developed by Choudhury and Nimbalkar (2006), for a rigid and battered cantilever retaining wall supporting a backfill consisting of dry and cohesionless material. The model and the forces stated by Ghosh (2010) are given in Figure 3.15.

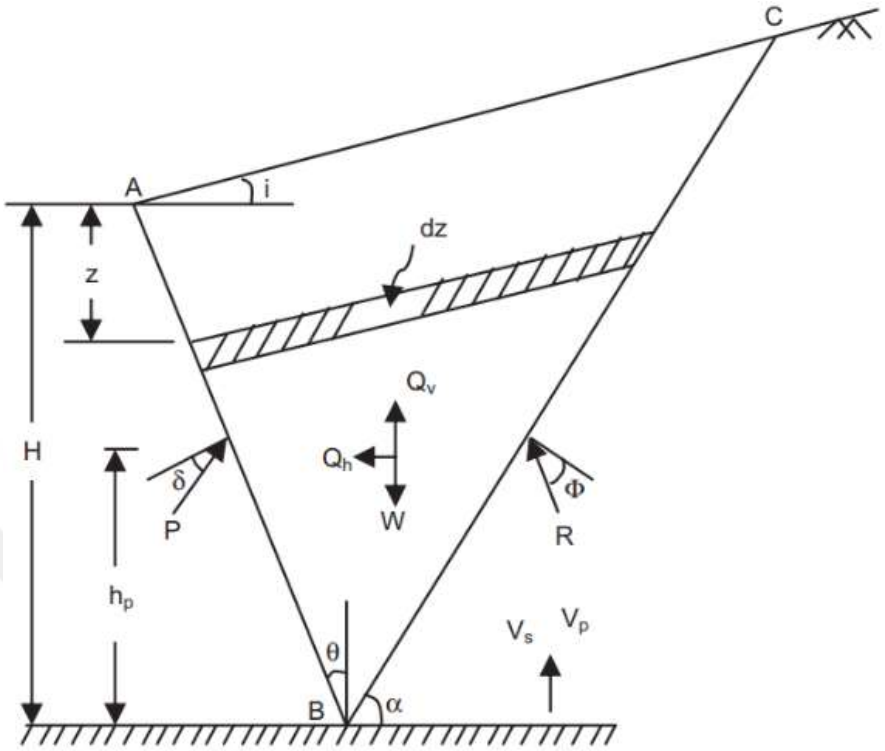

Figure 3.15. The forces evaluated by Ghosh (2010).

All aforementioned approaches assume that the failure surface within the backfill is planar. Yan et al. (2020) have assumed that the failure surface is curved, which was assumed as a logarithmic spiral and a straight line. They proposed a method on the basis of the pseudo-dynamic method and limit equilibrium theory to determine the total dynamic earth thrust by taking into account the effects of various parameters such as amplification factor, soil friction angle, wall friction angle, and horizontal and vertical components of earthquake acceleration. In Figure 3.16, the evaluated forces, the model, and the curved failure surface are illustrated.

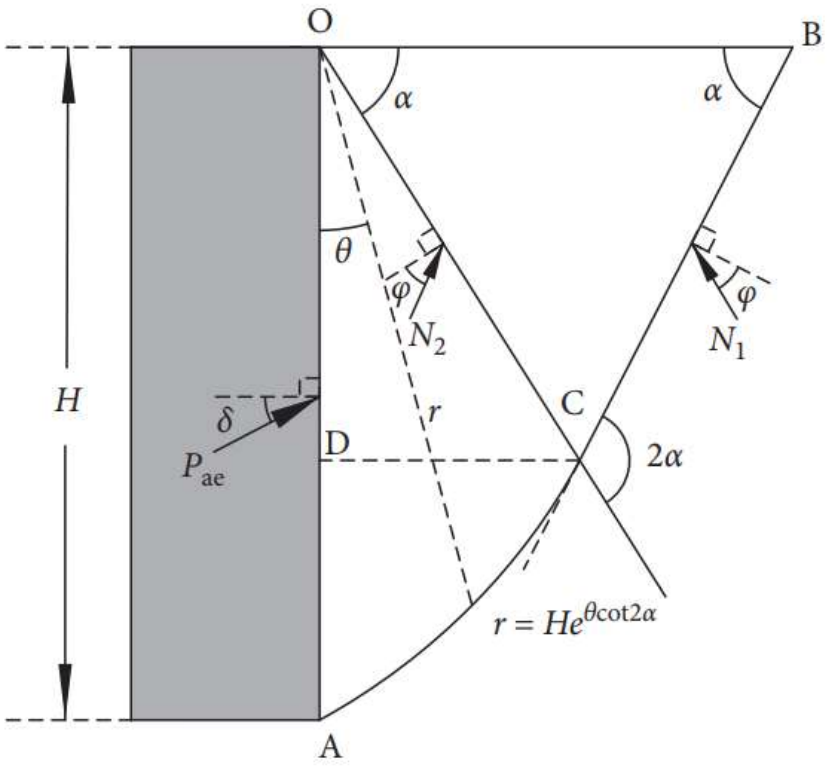

Figure 3.16. The forces evaluated by Yan et al. (2020).

3.3.1.3. Wood Method for Non-yielding Walls. Mononobe-Okabe method has been developed for the wall which is able to move sufficiently to produce minimum active or maximum passive earth pressure. This type of wall is generally named yielding walls. Wood (1973) claimed that the M-O method was not suitable for non-yielding walls (such as basement walls, building walls supporting soil, or other large structures constructed on firm soil or rock layer), and the method developed on the basis of the theory of elasticity would be more appropriate for non-yielding walls.

Wood (1973) proposed a study that investigated the dynamic earth pressure on a retaining wall. He made the following assumptions about ground motion and soil-wall system:

1. The earthquake motion can be selected arbitrarily as horizontal acceleration recordings changing as a function of time which act at the base of the wall.

2. There is no amplification, so the acceleration is constant and uniform throughout the soil.
3. The retained soil is dry, homogenous, and isotropic.
4. The wall behaves “truly” rigid, which means that the wall is constructed on a rigid base.
5. The wall is smooth, which means that there is no shear stress on vertical boundaries.
6. The soil-wall system has a linear elastic behavior.
7. The problem satisfies the plain-strain condition.

The idealized soil-wall system evaluated by using the above assumptions is illustrated in Figure 3.17.

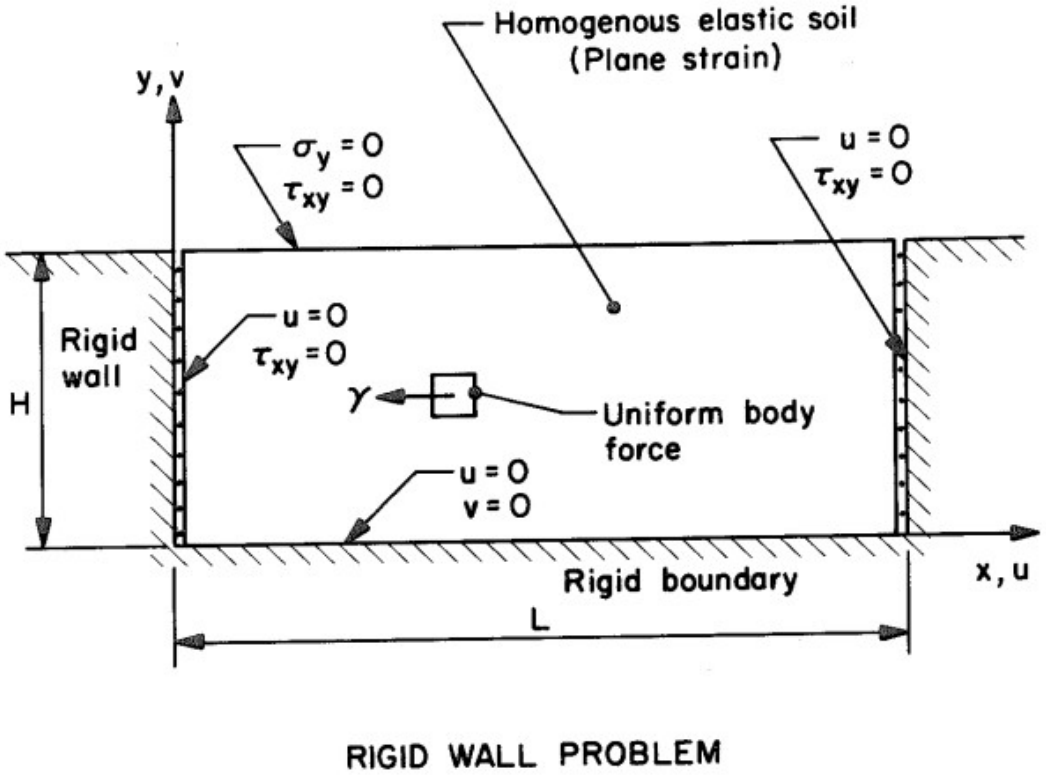

Figure 3.17. The soil-wall system evaluated by Wood (1973).

According to Wood (1973), the dynamic thrust (ΔP_E) and the dynamic overturning moment (ΔM_E) of the smooth rigid wall could be simply calculated as

$$\Delta P_E = \gamma H^2 \frac{a_h}{g} F_p = \gamma H^2 k_h F_p \tag{3.17}$$

$$\Delta M_E = \gamma H^3 \frac{a_h}{g} F_m = \gamma H^3 k_h F_m \,, \tag{3.18}$$

where F_p is the thrust factor, F_m is the moment factor.

The thrust and moment factors can be selected from Figure 3.18 with corresponding Poisson's ratio (ν) varying between 0.2 and 0.5 [9,29].

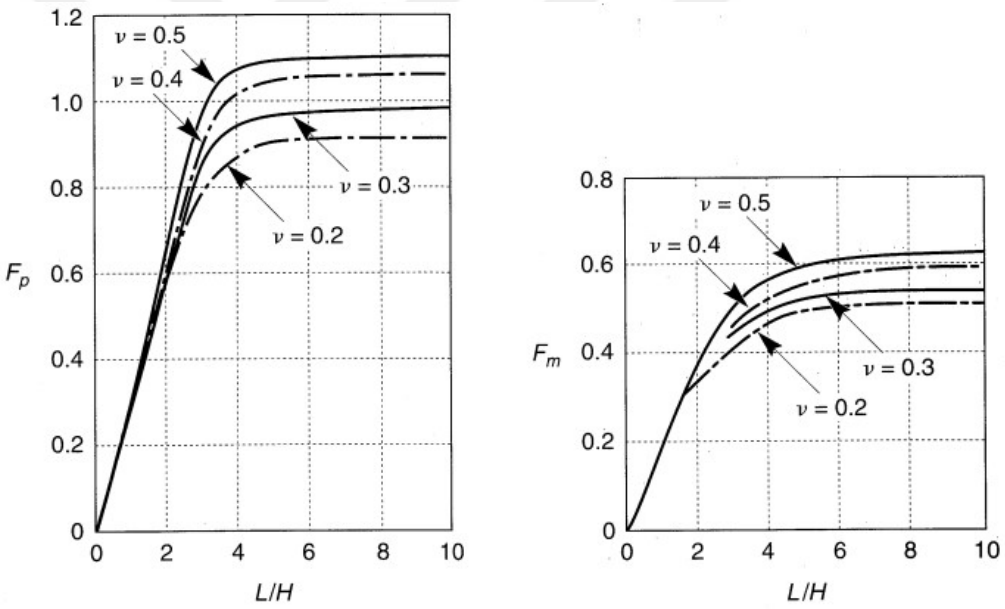

Figure 3.18. The dimensionless thrust and moment factors [9].

Moreover, the height where the dynamic pressure acts above the wall base was determined as

$$h_{eq} = \frac{\Delta M_E}{\Delta P_E} \tag{3.19}$$

The value of h_{eq} typically equals 0.63H, and the soil pressure distribution is nearly in parabolic shape [9,30].

In this study, static and dynamic solutions were evaluated by the use of analytical and numerical (finite element) methods in accordance with linear elastic theory. Wood (1973) found that there was a good agreement between the results obtained from the analytical method and the numerical method. Moreover, the total thrust determined by Wood's solution was estimated to be approximately 2-3 times greater than that obtained from the M-O method.

In the study proposed by Scoot (1973), the wall and the backfill of semi-infinite length, shown in Figure 3.19, have been considered as a one-dimensional elastic shear beam connected to the wall using systems of Winkler springs.

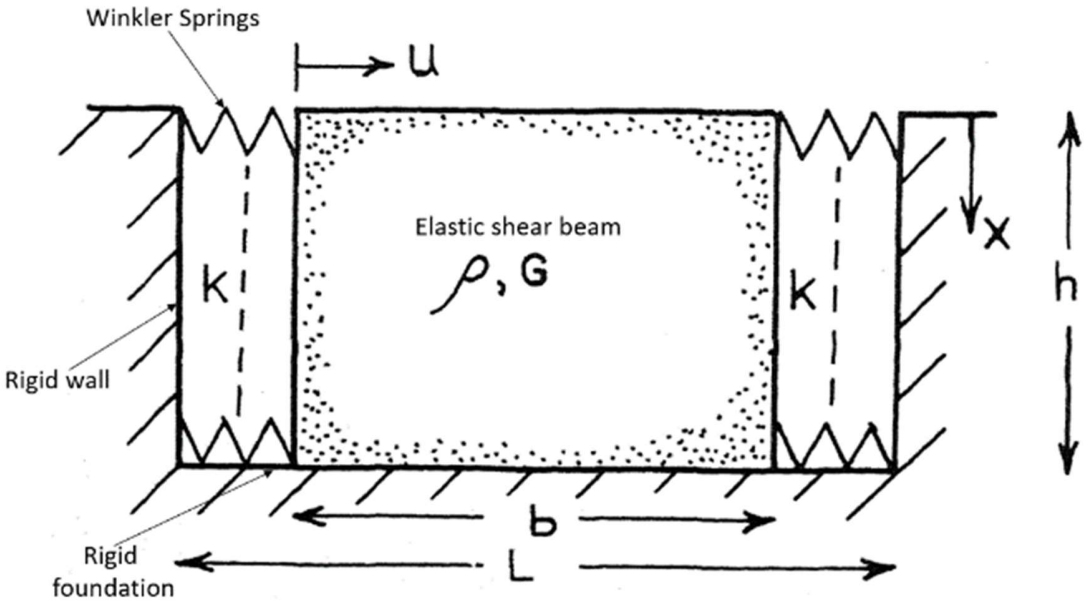

Figure 3.19. The soil-wall system evaluated by Scoot (1973).

The springs were used to represent the interaction between the retained soil and the rigid wall. The density, ρ, and the shearing stiffness, G, of the beam and the spring constant, k, change over depth due to the properties of backfill soil such as density, shear modulus, G, Young's modulus, E, vary with depth. The total maximum force (P_{m1}) can be calculated as

$$P_{m1} = \frac{2}{\pi} P_0 h, \tag{3.20}$$

where P_0 is the maximum pressure acting on the wall, h is the height of the wall.

The maximum pressure is determined as

$$P_0 = \frac{32GS_{V1}(1-\nu)}{\pi\omega_1 L(1-2\nu)}. \quad (3.21)$$

In this expression, ν is the Poisson's ratio, L is the distance between vertical boundaries, S_{V1} is the relative velocity response at the frequency, ω_1, and ω_1 is the fundamental frequency of the system which calculated as $\frac{\pi V_s}{2h}\left[1+\frac{64}{\pi^2}\frac{(1-\upsilon)}{(1-2\upsilon)}\left(\frac{h}{L}\right)^2\right]^{1/2}$. The point at the total force acted was found as $\frac{2h}{\pi}(=0.64h)$ above the base of the wall.

Another analytical method to determine the earth pressure acting on the rigid wall with a rigid foundation under seismic loading was developed by Veletsos and Younan (1994a, 1994b). The investigated model was established with visco-elastic material, which is uniform, semi-infinite, and free at the surface. This material was supported by vertical boundaries, one of which is a rigid wall founded on a rigid base. The model can be seen in Figure 3.20.

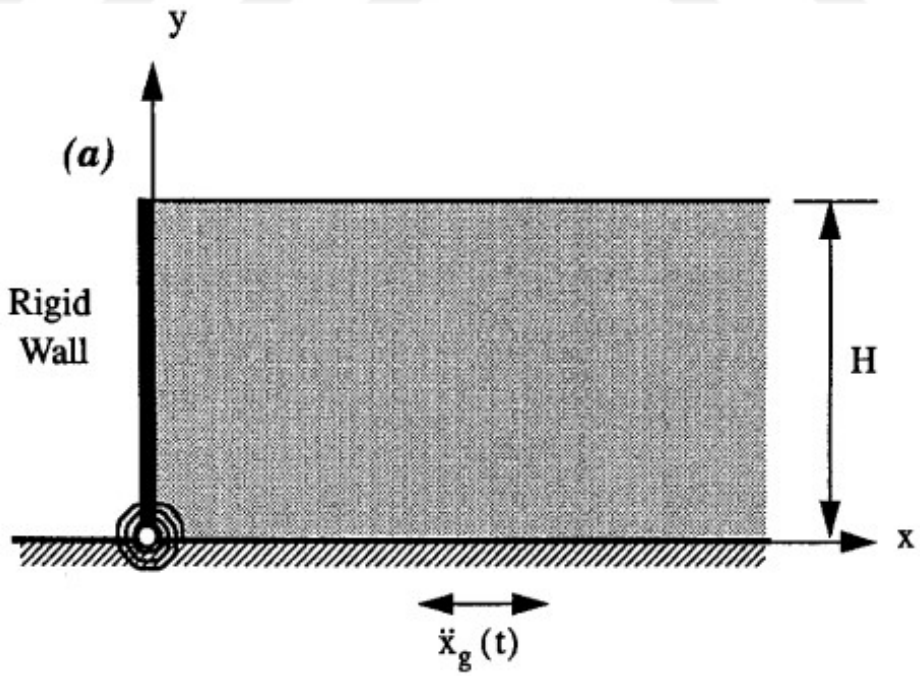

Figure 3.20. The model evaluated by Veletsos and Younan (1994b).

Their method took into account amplification and wave propagation of the ground motion within the backfill soil, which was not included in Wood's method. However, this method was complex and not easily applicable due to the absence of simple steps [30,34].

In the study of Ostadan (2005) (also Ostadan and White, 1998), the proposed method for the estimation of the dynamic earth pressure acting on a building wall was simple and easily applicable, unlike the method of Veletsos and Younan (1994b). This simplified method was developed on the basis of the concept of a single degree of freedom (SDOF) system. The model wall used in the development of this method was assumed to be rigid, non-yielding, and rested on firm soil or rock. Additionally, several dynamic soil properties, such as the shear wave velocity, damping, Poisson's ratio, soil density, and nonlinearity of the soil, were taken into consideration. Furthermore, the frequency content of the input motion, the soil-wall interaction, and wave propagation effects were incorporated into the solution. However, the impacts of the superstructure and its inertia on dynamic earth pressure were not considered. Ostadan (2005) investigated the accuracy of his five-step method by using the finite element method and by comparing it with the M-O method and Wood's Solution.

3.3.2. Displacement-based Methods

Force-based methods determine the performance of the wall by calculating dynamic forces acting on it. However, the wall performance is mainly connected with the displacement of the wall occurring after the earthquake. As a result, an alternative method has been developed to design retaining walls under seismic conditions by determining post-earthquake wall displacement based on the selection of permissible permanent displacement. This method is called the displacement-based or performance-based method.

3.3.2.1. Richard and Elms Method. The conventional methods to design retaining walls under seismic loading have taken the inertial forces of the soil wedge into consideration while neglecting those of the wall. Elms and Richard (1979) suggested that as opposed to this conservative and unreasonable approach, the wall inertia forces should be considered because

most of the resistance to wall movement is provided by the weight of the wall. However, the inclusion of the inertia forces due to the wall weight results in uneconomical wall designs. Moreover, these walls are impossible to construct in some cases. As a result, Elms and Richard (1979) developed a new design by using an acceleration with less-than-expected peak ground acceleration. The wall was allowed to move up to a predetermined displacement value during the earthquake. The wall was considered to perform satisfactorily during ground shaking when the post-earthquake displacement was below the permissible slip value [36,37]. In this method, the earthquake-induced displacement of the retaining wall supporting dry and cohesionless soil was predicted in a way that was an extended version of the sliding block method proposed by Newmark (1965) used for the estimation of post-earthquake slip occurring in dams and embankments. Additionally, the following assumptions were made for evaluating the method:

1. The gravity retaining wall is rigid.
2. The soil wedge behind the wall behaves as a rigid body.
3. Only the sliding mode of failure is considered.
4. The acceleration propagates uniformly within the backfill; that is, the amplification factor of the acceleration in the field is not considered.
5. The wall starts to slip away retained soil then the horizontal acceleration (a_{max}) exceeds the limiting ground acceleration (yield acceleration. a_y).

Elms and Richard (1979) evaluated the model and forces shown in Figure 3.21 in order to develop the performance-based method.

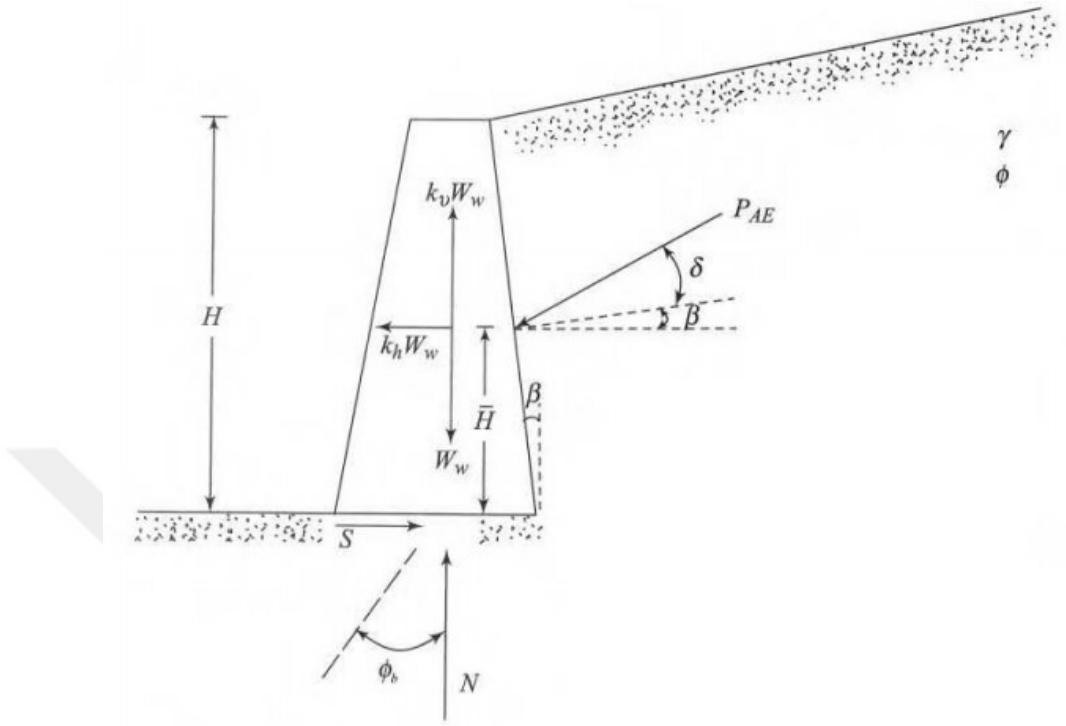

Figure 3.21. The model and forces evaluated by Elms and Richard (1979) [10].

According to the free body diagram illustrated in Figure 3.21, forces in the horizontal and vertical directions are derived as

$$S = P_{AE}\cos(\delta + \beta) + k_h W_w \tag{3.22}$$

$$N = W_w - k_v W_w + P_{AE}\sin(\delta + \beta)\,, \tag{3.23}$$

in which S and N are the horizontal and vertical components of the reaction of the wall base, respectively, W_w is the weight of the wall, P_{AE} is the dynamic active earth pressure calculated by the M-O method, δ is the angle of the wall friction, β is the slope angle of the back face of the wall relative to the vertical, k_h and k_v are the horizontal and vertical acceleration coefficients of the ground motion, respectively. In sliding mode, the relationship between vertical and horizontal forces is expressed as

$$S = N\tan\phi_b\,, \tag{3.24}$$

where ϕ_b is the friction angle at the wall base. Therefore, if the S and N are substituted in the equation, the expression can be written as

$$P_{AE}[\cos(\delta + \beta) - \sin(\delta + \beta)\tan\phi_b] = W_w[(1 - k_v)\tan\phi_b - k_h]\,. \tag{3.25}$$

Hence, the weight of the wall can be calculated as

$$W_w = C_{1E} P_{AE} \,. \tag{3.26}$$

Substituting P_{AE} and θ, mentioned in the Mononobe-Okabe method, into the above equation, the weight of the wall can also be written as

$$W_w = C_{1E} \left[\frac{1}{2}\gamma H^2 (1 - k_v) K_{AE}\right]. \tag{3.27}$$

where

$$C_{1E} = \frac{\cos(\delta+\beta) - \text{si}\ \ (\delta+\beta)\tan\phi_b}{(1-k_v)(\tan\phi_b - \tan\theta)} \tag{3.28}$$

Regarding these mentioned equations, the analysis can be performed to calculate the weight of the wall by following steps [18]:

1. Select a value of allowable displacement "d" of the wall (in mm)
2. Determine a design value of k_h using the following equation.

   $$k_h = \left[0.087 \frac{v_{max}^2}{a_{max}} \frac{1}{d}\right]^{1/4} A \,,$$

   where v_{max} is the maximum ground velocity, and A is the coefficient of maximum ground acceleration (a_{max}=A.g). The equation of k_h has been established on the basis of Newmark (1965) and the results of the study conducted by Franklin and Chang (1977).
3. Using calculated k_h and the assumption of "k_v=0", determine the value of P_{AE}
4. Determine the weight of the wall using the relationship between P_{AE} and W_w
5. Apply the safety factor on the wall weight.

Zarrabi-Kashani (1979) has established a more realistic solution than the Richard-Elms method. Similar to Elms and Richard (1979), he assumed that the failure occurred on the wall by only sliding and that the ground acceleration propagated uniformly within the backfill. That is to say, the tilting mode of failure and the amplification factor were neglected (Nadim and Whitman, 1983; Nadim and Whitman, 1985). Additionally, the vertical acceleration of ground motion was assumed as zero [17]. Zarrabi-Kashani (1979) has taken into account the inertia forces of the soil wedge as well as those of the wall and developed a two-block model, which is depicted in Figure 3.22.

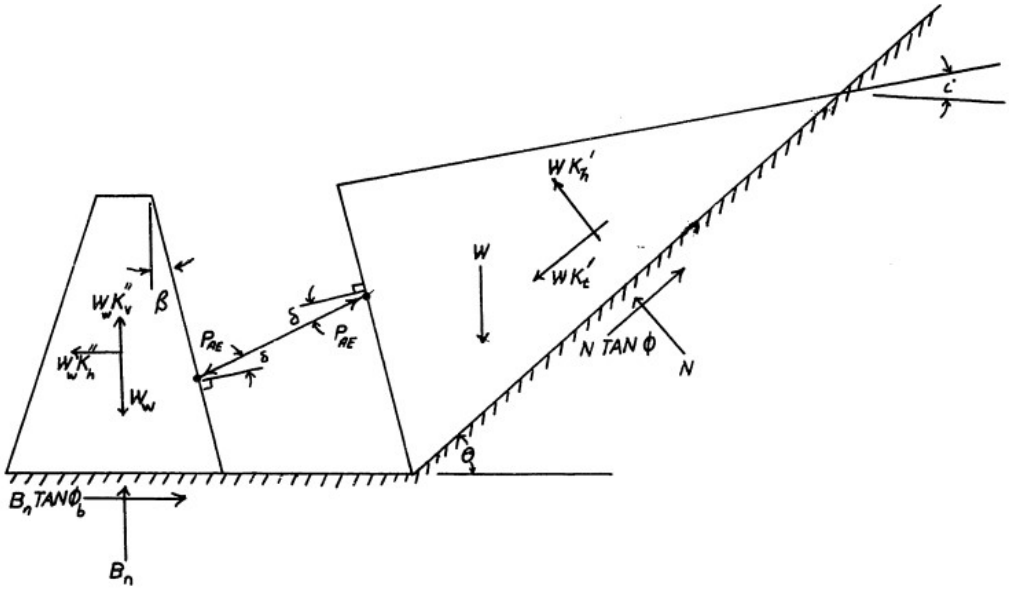

Figure 3.22. The model and forces evaluated by Zarrabi-Kashani(1979).

In this model, the equilibrium of the wall and soil wedge were considered separately with changing horizontal acceleration coefficient and the inclination angle of the failure surface. As a result, the two-block method proposed by Zarrabi-Kashani (1979) gave slightly lower displacement results than the method of Richard and Elms [36].

Dissimilar to Elms and Richard (1979) and Zarrabi-Kashani (1979), Nadim and Whitman (1983) have claimed that the amplification factor has a profound impact on permanent wall displacement. In addition, he used the constant inclination angle of the failure surface, in contrast to the model of Zarrabi-Kashani (1979). He modified the method proposed by Elms and Richard (1979) by suggesting a relationship between the ratio of the estimated dominant frequency of input motion to the fundamental frequency of backfill soil (f/f_1) and the required increment in peak acceleration and peak velocity of input motion before the calculation of permanent wall displacement. According to this study,

1. When the value of f/f_1 is less than 0.25, the amplification factor should be neglected.
2. When the value of f/f_1 is approximately 0.5, the peak acceleration and peak velocity of input motion should be increased by 25-30%.

3. When the value of f/f_1 is between 0.7 and 1, the rate of increase should be 50%.

Different from Elms and Richard (1979) and Zarrabi-Kashani (1979), Nadim and Whitman (1985) have considered the rotation mode of failure in their study by modifying the method proposed by Elms and Richard (1979). With the purpose of determination of earthquake-induced tilting and sliding movements, they have developed a model of a rigid gravity wall with a vertical back face and with dry, cohesionless sand for simplicity, shown in Figure 3.23, and they have ignored elastic deformations.

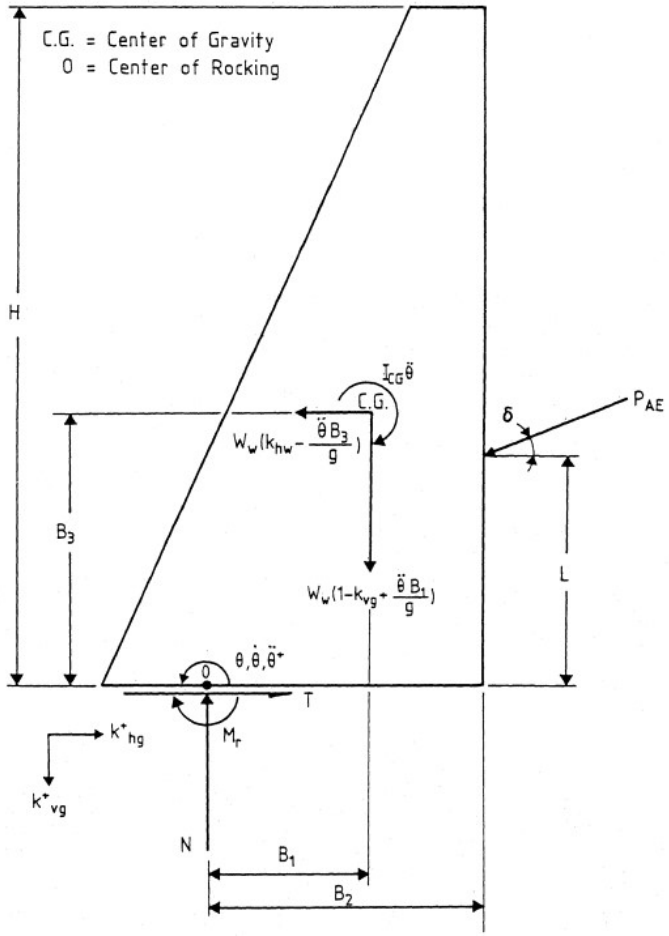

Figure 3.23. The model and forces evaluated by Nadim and Whitman (1985).

Additionally, the following conditions were assumed:

1. The model is examined by the condition of plane strain.
2. The foundation soil has a constant moment capacity. There is no tilting under this moment value. However, when the value is reached, plastic rotation occurs in the foundation soil.
3. The rocking center is at a fixed point at the base of the wall.
4. During the active condition, there are an infinite number of parallel planes within the failure zone, which satisfy the continuity assumption when the tilting occurs in the wall.

Nadim and Whitman (1985) have evaluated the equations of the horizontal ground acceleration coefficient that results in plastic tilting (N_{tilt}) and causes sliding (N_{slid}) in which the vertical ground acceleration equals zero. However, if vertical acceleration exists, the coefficients of N_{tilt} and N_{slid} should be multiplied with ($1-k_v$). Using the minimum value of N_{tilt} and N_{slid}, the permanent displacement (tilting and sliding) was calculated as (developed by Wong, 1982)

$$D = \frac{37 v_{max}^2}{a_{max}} e^{-9.4\left(\frac{a_y}{a_{max}}\right)}, \tag{3.29}$$

where a_{max} is the peak ground acceleration, v_{max} is the peak ground velocity, a_y is the yielding acceleration (N is equal to the minimum value of N_{tilt} and N_{slid}).

Whitman and Liao (1985) published a study that pointed out the deficiencies and required developments of the Richard and Elms method without changing its simplicity. The deficiencies of Richard and Elms method were the consequences of simplifying the dynamic features of the soil-wall system, such as ignoring the amplification factor, not including the tilting mode of failure, and neglecting vertical acceleration of ground motion. In order to compensate for these problems, the factor of safety was used. Whitman and Liao (1985) brought together the effects which were the main causes of modeling error by considering studies on the amplification factor [36], tilting mechanism [37], and the inertia forces of the backfill material and soil separately [17]. Additionally, the statistical variability of earthquake characteristics and

uncertainty of soil properties (especially friction angle of backfill soil, φ, and the angle of wall friction, δ) were considered to evaluate the equations of the permanent displacement expressed as a lognormally distributed random variable with mean value ($\bar{d}$) and variance ($\sigma_{\ln}$), respectively. They can be expressed as (Kramer,1996; Whitman and Liao, 1985)

$$\bar{d} = \frac{37\ \bar{a}_{max}^{2}}{a_{max}} exp\left(\frac{-9.4\bar{a}_y}{a_{max}}\right) \bar{Q}\bar{M} \tag{3.30}$$

$$\sigma^2_{\ln d} = \left(\frac{9.4g}{a_{max}}\right)^2 \sigma^2_{a_y} + \sigma^2_{\ln Q} + \sigma^2_{\ln M}\ , \tag{3.31}$$

in which $\bar{a}_y$ is the mean value of yield acceleration defined as a random variable (calculated with the mean value of φ and δ), σ_{a_y} is the standard deviation of yield acceleration, $\bar{Q}$ is the mean value of the uncertainty of statistical variability of ground motion expressed as a lognormally distributed random variable, $\sigma_{\ln Q}$ is the standard deviation of the uncertainty of statistical variability of ground motion, $\bar{M}$ is the mean value of modeling error expressed as a lognormally distributed random variable, $\sigma_{\ln M}$ is the standard deviation of modeling error.

Suggested values of the above variables are given in Table 3.2.

Table 3.2. Mean and standard deviation values for gravity wall displacement analysis [9].

Factor	Mean	Standard Deviation
Model error	$\bar{\mathrm{M}} = 3.5$	$\sigma_{\ln \mathrm{M}} = 0.84$
Soil resistance	$\bar{\mathrm{a}}_{\mathrm{y}} = \mathrm{a}_{\mathrm{y}}(\bar{\phi}, \bar{\delta})$	$\sigma_{\mathrm{a_y}} = 0.004$ to 0.065
Ground motion	$\bar{\mathrm{Q}} = 1$	$\sigma_{\ln \mathrm{Q}} = 0.58$ to 1.05

Wu and Prakash (2001) developed a realistic model in order to evaluate the post-earthquake displacement of a rigid wall, as illustrated in Figure 3.24.

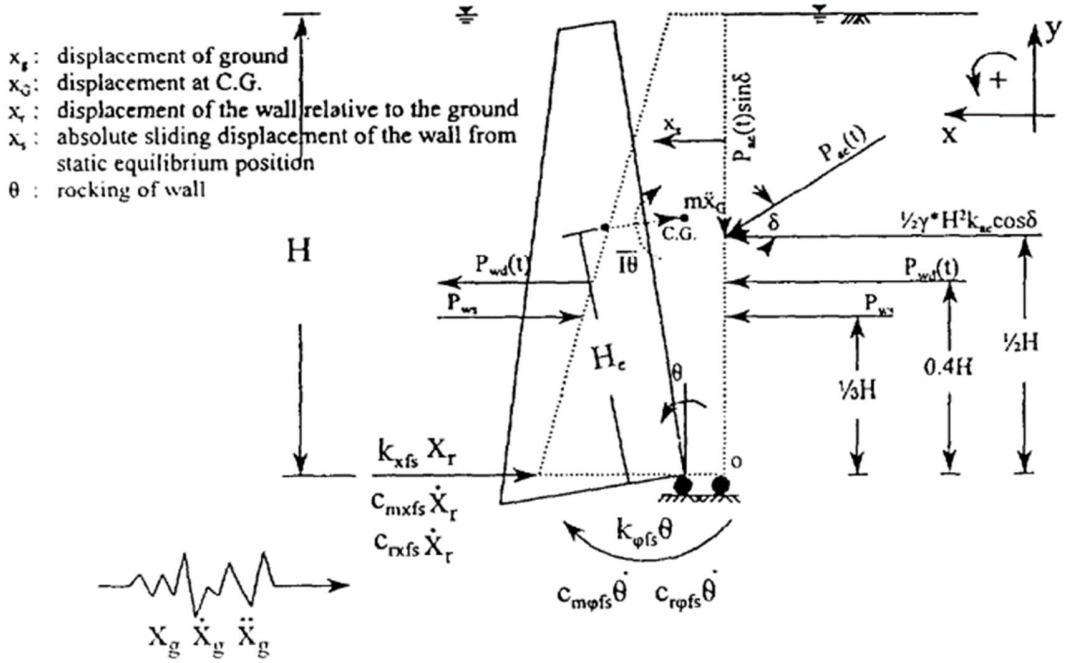

Figure 3.24. The model and forces evaluated by Wu and Prakash (2001).

In this model, the sliding and rocking displacement of the wall, as well as the water effects behind the wall were taken into account under plain-strain conditions. The nonlinear properties of the foundation soil were also considered, such as soil stiffness (shear modulus-dependent) in sliding and rocking, geometrical damping (shear modulus-dependent) in sliding and rocking, and material damping (strain-dependent) in sliding and rocking. The proposed model illustrated the response of the retaining wall experiencing earthquake loading and gave quite reasonable results for the estimation of permanent displacement of the retaining wall. Moreover, this model can be implemented in the analysis of bridge abutments.

4. LIGHTWEIGHT MATERIALS AS A CUSHION

4.1. Introduction

The lightweight materials are utilized in order to reduce the lateral forces against the retaining walls. This improvement method makes the wall design cost-effective because of diminishing the material amount used for wall construction and the cost of lightweight materials compared to conventional backfill. Additionally, these materials have advantageous characteristics, such as low unit weight, low bulk density, and high vibration absorption. Some materials can be used as lightweight materials, such as chipped bark, sawdust, dried peat, fly ash, slag, cinders, shredded and chipped tire waste, and expanded polystyrene (EPS geofoam) [39].

In this section, material properties of tire-derived materials and sand-tire waste mixtures, and EPS geofoam will be explained briefly. The literature review on material properties and the influence of the cushion layer consisting of EPS geofoam or waste tire-derived materials on static and dynamic forces acting on the retaining wall will be explained.

4.2. Previous Studies on Material Properties

4.2.1. Waste Tire-derived Materials

Waste tire-derived materials are obtained by cutting scrap tire/waste tires into small pieces using a mechanical process. According to ASTM D6270-98, the obtained materials can be defined as ground rubber, granulated rubber, powdered rubber, tire chips, and tire shreds based on their particle sizes. The range of particle size of these materials is given in Table 4.1.

Table 4.1. The particle size of tire-derived materials [40].

Material name	Particle size
Powdered rubber	≤ 0.425 mm
Ground rubber	0.425 – 2 mm
Granulated rubber	2 – 12 mm
Tire chips	12 – 50 mm
Tire shreds	50 – 305 mm

Some researchers have investigated the mechanical and chemical properties of tire shreds and tire chips. A few studies performed on these materials are briefly explained.

Humphrey and Standford (1993) and Humphrey et al. (1993) have aimed to determine the engineering properties of tire chips which were used as lightweight fill material. The tire chips used for tests have a size of 13-76 mm and were provided by four suppliers. As a result of conducted tests mentioned in the two studies:

- The specific gravity of tire chips varies from 1.14 to 1.27.
- The compacted dry density of tire chips changes between 0.614 Mg/m^3.
- The shear strength parameters f tire chips determined by large-scale direct shear tests vary from 19° to 25° for friction angle (φ) and from 8 to 11 kPa for cohesion (c).
- The compressibility of tire chips is high for initial loading; however, it becomes less during subsequent loading/reloading cycles.
- The permeability of tire chips changes between 1.5 and 15 cm/sec.

Wu et al. (1997) have carried out a study using five tire-chips specimens with different sources, particle shapes, and gradations, as shown in Table 4.2. According to Table 4.2, the specific gravity of the specimen ranges from 1.08 to 1.18, and the density of tire chips changes between 505 and 600 kg/m^3. The authors performed triaxial compression tests on these five

different specimens in order to determine the shear strength parameters of tire chips. The determined parameters are summarized in Table 4.3.

Table 4.2. The properties of tire chips samples [43].

Product	Source	Maximum size (mm)	Particle Shape	Density (kg/m³)	Specific gravity
1	Palmer Shredding, Inc., Ferrisburg, Vt.	38	Flat	600	1.11
2	Palmer Shredding, Inc., Ferrisburg, Vt.	19	Granular	574	1.08
3	Palmer Shredding, Inc., Ferrisburg, Vt.	9.5	Elongated	505	1.18
4	Recycling Concepts International, Ltd., Hicksville, N.Y.	9.5	Granular	600	1.18
5	The Baker Rubber Co., Chambersburg, Pa.	2	Powder	534	1.12

Table 4.3. The determined parameters of five different specimens consisting of tire chips [43].

Product	Shape	Maximum size (mm)	Volume strain at 55 kPa (%)	Young's modulus E (kPa)	Friction angle Φ (°)	Interparticle friction φ_f (°)
1	Flat	38	27.0	580-690	57	56
2	Granular	19	26.5	430-580	54	53
3	Elongated	9.5	31.6	350-480	60	53
4	Granular	9.5	25.4	450-600	47	47
5	Powder	2	27.0	450-820	45	44

Humphrey (1999) has studied the use of tire shreds in various civil engineering applications. In his study, he also investigated the properties of tire shreds which make them lightweight fill material, thermal insulation, and drainage layer. The mentioned properties of tire chips were:

- lower unit weight (7.07 – 9.11 kN/m^3) compared to the unit weight of soil (typically 19.64 kN/m^3),

- high permeability greater than 1 cm/sec,
- high temperature-isolation potential with a thermal conductivity equivalent to 0.14 Btu/hr·ft·°F (for particles smaller than 3 mm) which is seven times smaller than soil (1 Btu/hr·ft·°F).

Moo-Young et al. (2003) developed a study using physical and chemical testing methods to evaluate the changes in material properties of tire shreds depending on particle size. The change in specific gravity and water absorption capacity of tire shreds depending on particle size were determined by required physical tests, as shown in Table 4.4. Furthermore, the compaction, hydraulic conductivity, large-scale direct shear, and compression tests were performed on tire shreds. Additionally, chemical testing procedures have been performed to determine the effects of particle size on total organic carbon (TOC), pH, turbidity, and thermal stability of tire shreds, as well as the effects of tire shreds on water quality. As a result, the following conclusions have been drawn:

- The increase in the particle size of tire shreds resulted in an increase in hydraulic conductivity, compressibility, and shear strength of tire shreds. Furthermore, TOC and turbidity decreased, and pH increased slightly as the particle size increased.
- The tire shreds have resistance to temperatures up to 200 ºC.
- Whereas the tire shreds placed above the groundwater table have a slight or no effect on their surroundings, the one placed below the groundwater table might affect water quality adversely.

Table 4.4. The results of specific gravity and water absorption [45].

Tire size (mm)	**Specific gravity**	**Water absorption (%)**
<50	1.10	6.70
50-100	1.10	6.95
100-200	1.06	7.10
200-300	1.10	7.00

Yang et al. (2002) performed two confined compression tests with an oedometer, two isotropic compression tests with triaxial cells, and a direct shear test with varying normal stress from 0 to 82,7 kPa on dry tire chips having a particle size between 2 and 10 mm. The aim of their study is to evaluate the mechanical properties of tire-derived materials by analyzing the test results and previous studies. Tire chips showed lower compressibility compared to tire shreds due to a greater void ratio of tire shreds than tire chips and greater compressibility capacity of tire shred particles than tire chip particles. This means that compressibility increases as the particle size increases. The direct shear test results showed that the shear strength of materials does not rely on the particle size but rather on normal stress changes. Additionally, the authors listed the shear strength parameters determined using direct shear tests and triaxial tests by the previous studies and their studies in Tables 4.5 and 4.6.

Table 4.5. Shear strength parameters of tire chips and shreds determined using direct shear testing [46].

Author	Maximum Size, mm	Unit Weight, kN/m^3	Normal Stress, kPa	Cohesion Intercept, kPa	Friction Angle, °	The criterion of Failure Stress
Humprey et al. (1993)	51	6,30	17-68	7,7	21	Peak or at 10% disp. [a]
	76	6,08	17-63	11,5	19	
	38	6,06	17-62	8,6	25	
Foose et al. (1996)	50, 100, 150	NA	1-76	3	30	Peak or at 9% disp. [a]
Gebhardt (1997)	1400	NA	5,5-28	0	38	10% disp.
Yang et al. (2002)	10	5,73	0-83	0	32	10% disp.

[a] The failure was considered to be the peak shear stress or, if no peak was reached, the shear stress at a horizontal displacement equal to 10% (or 9%) of the length of the shear box was taken.

Table 4.6. Shear strength parameters of tire chips and shreds determined using triaxial testing [46].

Author	Maximum size (mm)	Unit weight (kN/m2)	Confining pressure (kPa)	Failure criterion and shear strength							
				10% strain		20% strain		Maximum		NA	
				c (kPa)	φ (°)	c (kPa)	φ (°)	c (kPa)	φ (°)	c (kPa)	φ (°)
Benda (1995)	38	5.89	35-55	0	21.1	0	35.5				
	19	5.62	35-55	0	21.4	0	34.1				
	9.5	4.95	35-55	0	17.2	0	31.2				
	9.5	5.88	35-55	0	20.6	0	32.1				
	2	5.23	35-55	0	25.8	0	36				
Ahmed (1993)	13	6.19	36-199	22.7	11.2	35.8	20.5				
	25	6.32	31-199	25.4	12.6	37.3	22.7				
	25	6.42	32-307	22.1	14.6	33.2	25.3				
	25	6.75	32-199	24.6	14.3	39.2	24.7				
Masad et al. (1996)	4.75	6.24	150-350	70	6	82	15				
Wu et al. (1997)	38	5.89	35-55					0	57		
	19	5.62	35-55					0	54		
	9.5	4.95	35-55					0	60		
	9.5	5.88	35-55					0	47		
	2	5.23	35-55					0	45		
Bressene (1984)	51	5.98	NA							25.9	21
Lee et al. (1999)	51	5.96	NA							31.6	14
	30	6.3	28- 193							7.6	21
Yang et al. (2002)	10	5.73	23.4-84.1	21.6	11.0	37.7	18.8				

Additionally, some researchers have conducted tests on the mixture of sand and waste tire-derived materials. A few of these studies are briefly examined as follows.

Edil and Bosscher (1994) have presented a study in order to determine the material properties of tire chips and soil-tire chips mixture, which were planned to use as lightweight fill or drainage material in construction. The conducted tests and their results are listed below briefly:

- Due to their vibration absorbent feature, the tire chips samples could not be compacted by vibration. The standard and modified proctor tests were performed on the samples consisting of tire chips and soil (sand or clay) with different mixture ratios. The soil type and the ratio of the soil-tire chips were found to be significant parameters. Furthermore, the unit weight decreased as the content of tire chips increased.
- Compression tests were performed on the samples consisting of tire chips and tire chips-soil mixtures. The tire chips showed a greater vertical compression under the first loading than that under subsequent loading cycles. Additionally, the static and dynamic strain of the samples decreased as the volumetric percentage of soil in the mixture increased.
- Large direct shear tests were performed on the samples with different mixture ratios. The shear strength parameters of the tire-chips soil mixture were higher than the dense sand.
- The hydraulic conductivity of the samples was determined under changing pressures. The tire chips have high permeability, which was difficult to measure. Mixing tire chips with sand of 30%-50% by volume resulted in a considerable decrease in the permeability of tire chips. This situation was valid for the compressibility of tire chips.

Foose et al. (1996) performed a series of direct shear tests on the sample consisting of sand and tire shreds in order to interpret the impact of various factors on shear strength. According to the test results, the normal stress, sand matrix, unit weight, and shred content showed a significant influence on shear strength, while shred length and shred orientation were not determined as important as the other factors. The authors found that the initial friction angle increased with an increase in shred content and unit weight. Furthermore, the shear strength of

the mixture of sand and tire shreds was determined to be greater than the specimen consisting of only sand.

Ghazavi (2004) determined the shear strength parameters of the mixture of sand and waste garden hose grains with varying mixture ratios in order to understand the use of tire chips-soil mixture as a lightweight material. A series of small direct shear tests were performed on the specimens with various rubber content. The unit weight of the mixture decreased with the increasing content of tire chips. According to the test results, an apparent cohesion was obtained from the samples with tire chips, and the maximum value of initial friction angle was obtained from the samples consisting of 10-20% rubber. Although the shear strength parameters did not vary considerably depending on tire chips content, the rubber content could provide a reduction in lateral earth pressure.

Hyodo et al. (2008) have performed undrained cyclic triaxial tests on the sample containing tire chips and sand with various mixture ratios in order to examine the effects of the change in mix ratio on the undrained shear behavior and strength characteristics of the tire chip-sand mixture. Sand content of total mixture by volume (sand fraction-sf), density (ρ_s), minimum and maximum dry densities (ρ_{min} and ρ_{max}), maximum and minimum void ratios (e_{min} and e_{max}), mean diameter (D_{50}), and coefficient of curvature (U_c) belonging to the mixture were listed in Table 4.7. The specimens were prepared with an initial water content of 10%. The experimental results showed that when the sand fraction was greater than 0.5, the characteristics of the mixture were governed predominately by tire chips. Additionally, the specimens with sand fraction higher than 0.5 showed the inclination to liquefy, whereas those with sf<0.5 were believed not to display liquefaction. For the specimen consisting entirely of tire chips that have very low stiffness, during cyclic shear loading, the excess pore pressure was not generated, the liquefaction did not occur, and displacement was easily produced. Additionally, during shearing, the increase in pore water pressure was controlled by tire chips.

Table 4.7. The physical properties of tire chip-sand mixture [50].

Sand Fraction	ρ_s (g/cm^3)	ρ_{dmin} (g/cm^3)	ρ_{dmax} (g/cm^3)	e_{max}	e_{min}	D_{50} (mm)	C_c
sf=1 (Soma sand)	2.645	1.273	1.574	1.077	0.680	0.395	1.65
sf=0,9	2.576	-	-	-	-	0.399	1.67
sf=0,8	2.498	-	-	-	-	0.403	1.67
sf=0,7	2.41	0.939	1.234	1.565	0.953	0.407	1.69
sf=0,6	2.309	-	-	-	-	0.414	1.72
sf=0,5	2.192	0.744	0.988	1.948	1.218	0.423	1.15
sf=0,3	1.892	0.563	0.735	2.361	1.576	0.453	1.91
sf=0 (Tire chips)	1.15	0.347	0.442	2.318	1.600	0.655	2.72

Edinçliler (2008) aimed to obtain shear strength parameters and deformation behavior of the samples consisting of tire buffings and sand with various mixture ratios while performing a direct shear test using large-scale test apparatus. The samples were prepared in dry condition by mixing sand with a unit weight of 15.3 kN/m^3 and tire buffings with a unit weight of 5.1 kN/m^3. With the experiments, the shear stress vs. displacement of the mixture with 5%, 10%, 20%, and 30% tire buffings by weight, only sand, and only tire buffings were determined at the normal stress of 20, 40, and 80 kPa. As a result of the tests, an increase in friction angle (from 22° to 29°) and cohesion (from 3.1 kPa to 15.45 kPa) have been observed. Additionally, the inclusion of tire buffings caused a change in the deformation behavior of sand. When the aforementioned results were considered, tire buffing can be utilized as a fiber reinforcement agent by mixing sand.

Edinçliler et al. (2010) used the same experimental method mentioned in Edinçliler (2008) in order to determine shear strength parameters and deformation behavior of tire crumbs having a unit weight of 5.4 kN/m^3 and dry sand having a unit weight of 13.8 kN/m^3. The samples were prepared by mixing sand and tire crumbs with various ratios (tire crumb-sand having 5%, 10%, 20%, and 30% tire crumb by weight, 100% sand, and 100% tire crumbs). Based on test results, the improvement in shear strength parameters of sand has been observed as a result of mixing with tire crumb. Additionally, the mechanical properties of sand could be enhanced with other waste tire-derived materials (i.e., tire shreds, tire crumbs, tire buffings). The authors

proposed a literature summary table with an addition of their results, which is given in Table 4.8.

Table 4.8. The summary of the literature review proposed by Edinçliler et al. (2010).

Reference	Material	Unit weight (kN/m^3)	Shear strength parameters
Humphrey et al. (1993)	Product 1 (<76 mm tire chips-1)	7.01	c = 8.6 kPa; ϕ = 25°
	Product 2 (<76 mm tire chips-1)	6.82	c = 11.5 kPa; ϕ = 19°
	Product 3 (<76 mm tire chips-1)	7.24	c = 7.7 kPa; ϕ = 21°
	Product 3 (<76 mm tire chips-2)	-	c = 4.3 kPa; ϕ = 26°
Ahmed and Lovell (1993)	Tire shreds (Size1.3 cm) – Stand. Comp.	4.67	c = 35.8 kPa; ϕ = 20.5°
	Tire shreds (size. 2.5 cm) – Mod. Comp.	6.71	c = 39.2 kPa; ϕ = 24.6°
	Tire shreds (size. 2.5 cm) – Stand. Comp.	6.29	c = 33.2 kPa; ϕ = 25.3°
	Tire shreds (size. 2.5 cm) – Stand. Comp.	6.45	c = 37.3 kPa; ϕ = 22.6°
Wu et al. (1997)	Tire chips–product 1 (max. 38 mm-flat)	5.89	c = 0 kPa; ϕ = 57°
	Tire chips–product 2 (max. 19 mm-gran.)	5.69	c = 0 kPa; ϕ = 54°
	Tire chips–product 3 (max 9.5 mm-elong.)	4.95	c = 0 kPa; ϕ = 54°
	Tire chips–product 4 (max.9.5 mm-gran.)	5.89	c = 0 kPa; ϕ = 47°
	Tire chips–product 5 (max.2 mm-powder)	5.69	c = 0 kPa; ϕ = 45°
Tatlisoz et al. (1998)	100% tire chips	5.90	c = 0 kPa; ϕ = 30°
	100% sand	16.8	c = 2 kPa; ϕ = 34°
	90% sand + 10% tire chips	15.6	c = 2 kPa; ϕ = 46°
	80% sand + 20% tire chips	14.5	c = 2 kPa; ϕ = 50°
	70% sand + 30% tire chips	13.3	c = 2 kPa; ϕ = 52°
	100% sandy silt	18.3	c = 21 kPa; ϕ = 30°
	90% sandy silt + 10% tire chips	17.6	c = 8 kPa; ϕ = 53°
	80% sandy silt + 20% tire chips	17	c = 38 kPa; ϕ = 54°
	70% sandy silt + 30% tire chip	18.9	c = 39 kPa; ϕ = 53°
Foose et al. (1996)	90% sand + 10% tire shred (15 cm-random)	16.8	τ = 37.9 kPa (σ = 25.5 Pa)
	90% sand + 10% tire shred (15 cm-vertical)	16.8	τ = 18.6 kPa (σ = 25.5 kPa)
	90% sand + 10% tire shred (15 cm-random)	14.7	τ = 8.30 kPa (σ = 25.5 kPa)
	70% sand + 30% tire shred (5 cm-vertical)	14.7	τ = 37.2 kPa (σ = 25.5 kPa)
	70% sand + 30% tire shred (5 cm-random)	17.4	τ = 11.0 kPa (σ = 25.5 kPa)
	70% sand + 30% tire shred (5 cm-vertical)	16.8	τ = 20.7 kPa (σ = 25.5 kPa)
	70% sand + 30% tire shred (5 cm-random)	16.8	τ = 55.2 kPa (σ = 25.5 kPa)
	70% sand + 30% tire shred (5 cm-vertical)	14.7	τ = 32.4 kPa (σ = 25.5 kPa)
	90% sand + 10% tire shred (15 cm-vertical)	14.7	τ = 32.4 kPa (σ = 25.5 kPa)
	90% sand + 10% tire shred (5 cm-random)	16.8	τ = 32.4 kPa (σ = 25.5 kPa)
	90% sand + 10% tire shred (5 cm-vertical)	14.7	τ = 13.8 kPa (σ = 25.5 kPa)
	70% sand + 30% tire shred (15 cm-vertical)	16.8	τ = 78.6 k Pa (σ = 25.5 kPa)
	70% sand + 30% tire shred (15 cm-vertical)	16.8	τ = 22.8 kPa (σ = 25.5 kPa)
	90% sand + 10% tire shred (5 cm-vertical)	16.8	τ = 29.0 kPa (σ = 25.5 kPa)
	70% sand + 30% tire shred (15 cm-random)	14.7	τ = 42.1 kPa (σ = 25.5 kPa)
	90% sand + 10% tire shred (5 cm-random)	14.7	τ = 19.3 kPa (σ = 25.5 kPa)
Attom (2006)	100% sand A	15.5	ϕ = 25
	10% shredded tire + 90% sand A	14	ϕ = 30
	20% shredded tire + 80% sand A	15	ϕ = 37
	30% shredded tire + 70% sand A	15.5	ϕ = 41
	40% shredded tire + 60% sand A	16	ϕ = 45
	100% sand B	15.9	ϕ = 28
	10% shredded tire + 90% sand B	14	ϕ = 35
	20% shredded tire + 80% sand B	15	ϕ = 42
	30% shredded tire + 70% sand B	15.9	ϕ = 47
	40% shredded tire + 60% sand B	16	ϕ = 49
	100% sand C	16.6	ϕ = 36
	10% shredded tire + 90% sand C	15	ϕ = 42
	20% shredded tire + 80% sand C	16	ϕ = 45
	30% shredded tire + 70% sand C	16.5	ϕ = 48
	40% shredded tire + 60% sand C	16.6	ϕ = 50

Table 4.8. The summary of the literature review proposed by Edinçliler et al. (2010). (cont.)

Edinçliler et al. (2004)	100% tire buffings	5.1	c = 3.1 kPa; ϕ = 22°
	100% sand	15.3	c = 6.9 kPa; ϕ = 33°
	90% sand + 10% tire buffings	13.0	c = 8.7 kPa; ϕ = 29°
Edinçliler (2008)	100% tire buffings	5.1	c = 3.1 kPa; ϕ = 22°
	100% sand	15.3	c = 6.9 kPa; ϕ = 33°
	95% sand + 5% tire buffings	15.2	c = 10.4 kPa; ϕ = 28.2°
	90% sand + 10% tire buffings	14.9	c = 8.7 kPa; ϕ = 29°
	80% sand + 20% tire buffings	14.2	c = 15.5 kPa; ϕ = 5°
	70% sand + 30% tire buffings	13.5	c = 10.7 kPa; ϕ = 8.3°
Ghazavi (2004)	100% sand	$\gamma_{L/D}$= 14/14.5	$\phi_{L/D}$= 31.2°/37°
	90% sand + 10% granular rubber	$\gamma_{L/D}$ = 13/13.5	$\phi_{L/D}$ = 31°/37°
	85% sand + 15% granular rubber	$\gamma_{L/D}$= 12.3/13	$\phi_{L/D}$= 35.3°/37.6°
	80% sand + 20% granular rubber	$\gamma_{L/D}$= 11/12.4	$\phi_{L/D}$= 34.5°/33.5°
	50% sand + 50% granular rubber	$\gamma_{L/D}$= 7.7/8	$\phi_{L/D}$= 33°/35°
	30% sand + 70% granular rubber	$\gamma_{L/D}$= 6.4/6.7	$\phi_{L/D}$= 33°/33°
	100% granular rubber	$\gamma_{L/D}$= 4.7/5.1	$\phi_{L/D}$= 31°/31°
Edinçliler et al. (2010)	100% tire crumb	5.4	c = 4.6 kPa; ϕ = 31.0°
	100% sand	13.78	c = 0 kPa; ϕ = 38.7°
	95% sand + 5% tire crumb	13.38	c = 1.3 kPa; ϕ = 41.2°
	90% sand + 10% tire crumb	13.02	c = 0.2 kPa; ϕ = 41.4°
	80% sand + 20% tire crumb	12.38	c = 1.1 kPa; ϕ = 42.6°
	70% sand + 30% tire crumb	11.85	c = 1.2 kPa; ϕ = 40.0°

4.2.2. EPS Geofoam

Geofoam is a rigid cellular foam polymetric material, and it is produced in the shape of a block or plane. EPS (Expanded Polystyrene) and XPS (Extruded Polystyrene) are manufactured from geofoam. Although EPS and XPS consist of polystyrene, they are named differently due to their manufacturing processes. EPS and XPS materials are produced by a molding process and an extrusion process, respectively. In this study, the properties of EPS and the studies carried out on EPS will be examined since EPS will be used in the experiments of this study.

According to ASTM D6817,

- The dimensions commonly used for EPS production are given in Table 4.9.
- The density of EPS varies from 11.2 kg/m^3 to 45.7 kg/m^3, which is equivalent to 0.6-2.5% of the sand (approximately 1940 kg/m^3) [54]. The densities of different EPS types are given in Table 4.10.

- The compressive resistance of a 1%, 5%, and 10% strain and the flexural strength of EPS material with varying densities were calculated as given in Table 4.10.
- The oxygen index of EPS is equivalent to 24% by volume regardless of the change in density, as given in Table 4.10. This value, which expresses the minimum oxygen content that will support a flaming burn in a polymer specimen, is significant as the EPS material has a flammable nature [54].
- The values of flexure, tension, shear, and compression strength belonging to EPS depending on a density change were evaluated, as given in Figure 4.1.

Table 4.9. The dimension of EPS that is commonly used during the manufacturing process [53].

Dimension, mm [in.]	**All EPS Types**
Width	305 to 1219 [12 to 48]
Length	1219 to 4877 [48 to 192]
Thickness	25 to 1219 [1 to 48]

Table 4.10. The properties of EPS geofoams with different densities [53].

Type	**EPS12**	**EPS15**	**EPS19**	**EPS22**	**EPS29**	**EPS39**	**EPS46**
Density, min. (kg/m3)	11,2	14,4	18,4	21,6	28,8	38,4	45,7
Compressive Resistance, min (kPa at 1% strain)	15	25	40	50	75	103	128
Flexural Strength, min. (kPa)	69	172	207	240	345	414	517
Oxygen Index, min. (volume %)	24,0	24,0	24,0	24,0	24,0	24,0	24,0

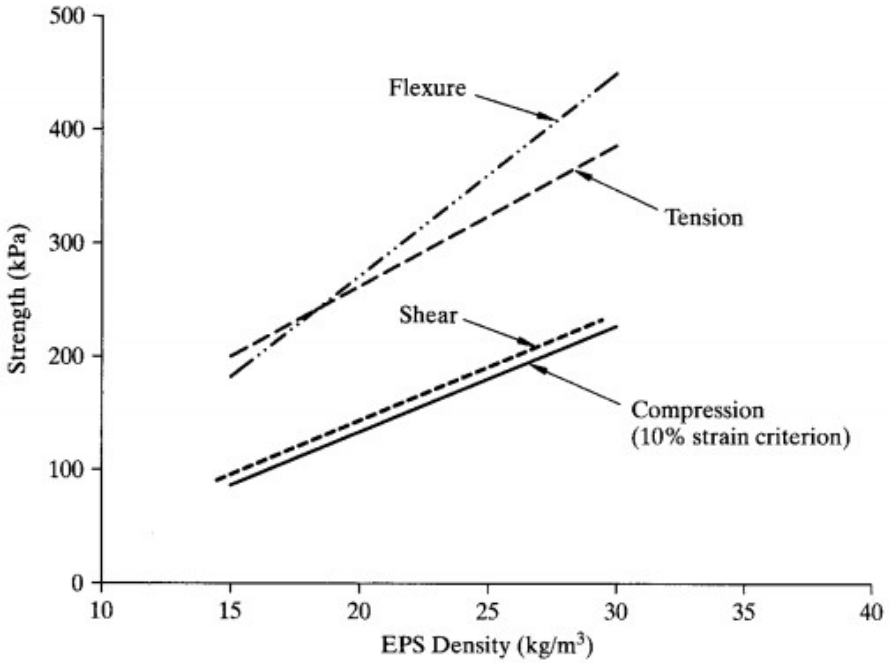

Figure 4.1. Different strength values of EPS based on density change [54].

Some researchers conducted studies to evaluate the material properties of EPS. A few studies performed on EPS are given below briefly:

Elragi et al. (2001) investigated how the change in sample size influences the determination of elastic parameters by conducting unconfined compression tests on EPS samples. The samples have various densities (15 and 29 kg/m^3) and various shapes (cubic samples with a height of 0.05 m and 0.6 m and cylindrical samples with a diameter of 0.08 m and with changing heights). Additionally, a stack of four 0.6 m cubic specimens was tested. Young's modulus and Poisson's ratio were determined by the examination of axial and lateral deformations of samples. According to test results, Young's modulus of large specimens is shown in Figure 4.2. Furthermore, Poisson's ratio determined from the middle section of 0.6 m cubic samples was greater than that evaluated in the lower and upper sections. Young's modulus and Poisson's ratio were underestimated due to crushing and damage in the geofoam located adjacent to the loading platens.

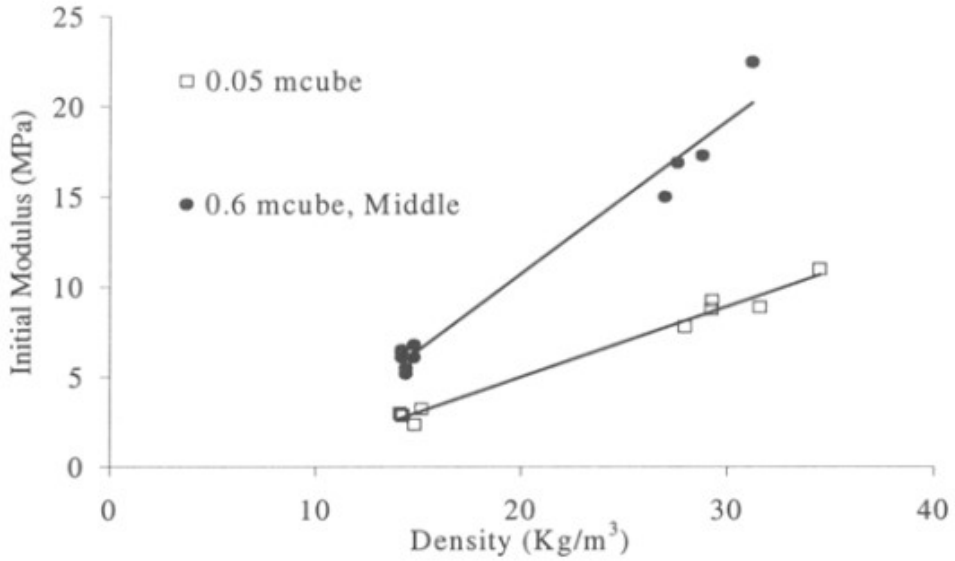

Figure 4.2. Young modules as a function of EPS density [55].

Athanasopoulos et al. (1999) have performed resonant column and cyclic triaxial tests on EPS geofoam having two different densities (12.4 and 17.1 kg/m3) by aiming to evaluate the dynamic properties belonging to EPS and the effects of strain amplitude (varying between 0.0005 and 0.08), frequency of loading (ranging from 0.01 to 2.00 Hz) and change in sample density. No confining pressure is applied on specimens that have a cylindrical shape with a diameter of 36 mm and a height of 80 mm. The damping ratio, the dynamic shear modulus, and the secant modulus of elasticity depending on cyclic shear strain amplitudes were determined for two different EPS geofoam samples using the test results. Consequently, the following conclusions have been drawn:

- The low amplitude shear modulus (G_o) and the initial modulus of elasticity (E_o) of EPS geofoam samples were determined as given in Table 4.11. As seen in the table below, the density of EPS has a significant effect on the dynamic modulus of specimens.
- The damping ratio was not significantly affected by the change in density.
- The change in loading frequency did not change the elastic modulus of EPS, whereas an increase in frequency resulted in a decrease in the damping ratio.

- The Poisson's ratios of EPS samples were calculated by using a computer program on the basis of the test results. The determined values are given in Table 4.12.
- An increase in the cyclic strain amplitude brought about a decrease in the elastic modulus and an increase in the damping ratio of EPS samples.

Table 4.11. Shear modulus and initial modulus of elasticity of EPS geofoam samples[56].

Density of EPS (kg/m^3)	Shear Modulus (G_o) (MPa)	Initial Modulus of Elasticity (E_o) (MPa)
12.1	2.1	1.2
17.4	4.9	4.88

Table 4.12. Poisson's ratio of EPS samples[56].

Density of EPS (kg/m3)	12.1	17.4
Poisson's Ratio (ν)	-0.50	-0.75

The mechanical properties of EPS blocks were evaluated by performing various laboratory tests in the study proposed by Preber et al. (1994). According to test results, an increase in the unit weight of EPS brought about an increase in the initial and elastic modulus, the material strength, and the punching shear strength. Additionally, while a decrease in confining pressure results in a decrease in elastic modulus, it contributed to an increase in initial modulus and Poisson's ratio (up to below zero for higher confining pressures). The authors concluded that the performance of EPS under repeated loading was satisfying, and EPS materials were insensitive to creep due to a very low creep strain rate for a year.

Horvath (1994) has given information about the properties of EPS in this study. The mentioned features of EPS are listed below briefly:

- The density of the EPS block varies between 10 kg/m^3 and 40 kg/m^3. The type of EPS commonly used in geotechnical applications as a lightweight material has a density of 20 kg/m^3.

- EPS has no ability to decompose in nature, and it does not produce a chemical reaction with soil or water. Additionally, additives having no effect on the EPS properties can be used to prevent the EPS from infesting.
- Despite a closed-cell form of EPS preventing water absorption, water (in a state of gas or liquid) might go into the tiny pores in the EPS. The mechanical properties of EPS are not affected by this situation.
- The EPS should not be exposed to ultraviolet (UV) radiation for a long-lasting period since the exposure to UV makes the surface of the EPS yellow and brittle.
- The protection of EPS using geomembrane or other materials may be needed due to its nature of dissolving in a few liquids such as gasoline and diesel fuel.
- The EPS beads having additives preventing materials from quickly burning are commonly used due to their nature of flammability and melting at a temperature above 150℃.
- The relationship between the initial tangent Young's modulus and the density of EPS was linear, as depicted in Figure 4.3.
- The elastic limit and the compressive strength decrease as the density of EPS reduces.
- The increase in creep effect results from the decrease in EPS or an increase in temperature at a specified EPS density.
- The mean strength values vs. EPS density were evaluated in Figure 4.4.

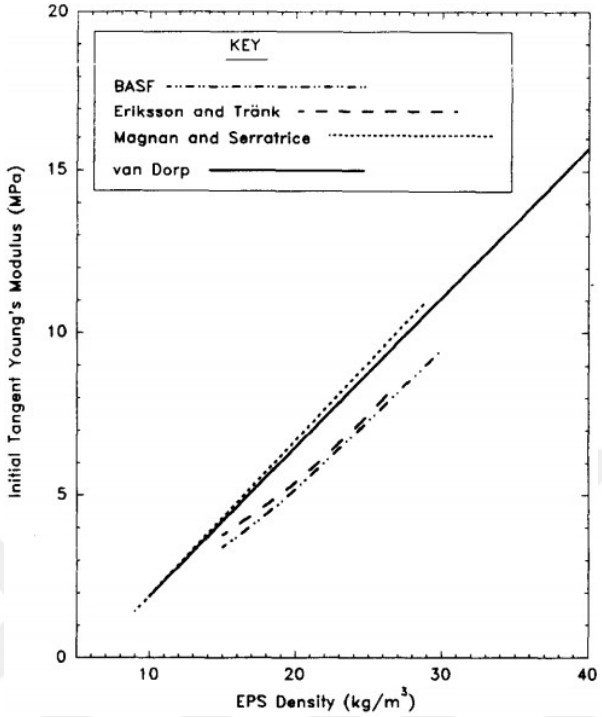

Figure 4.3. The correlation between the initial Young's modulus and density of EPS [58].

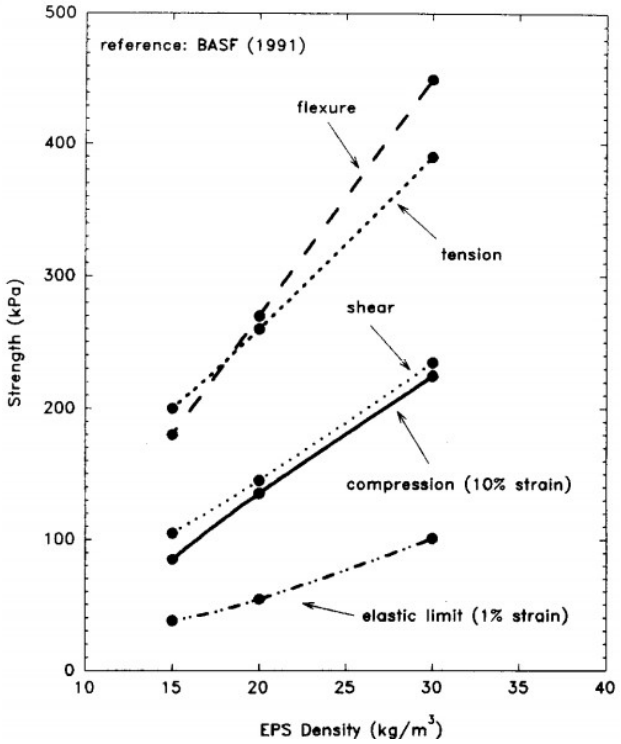

Figure 4.4. The correlation between the strength and density of EPS [58].

Hazarika (2006) has developed a constitutive model for large-strain applications of EPS geofoam. The properties of EPS were determined by the unconfined compression tests for specimens having varying sizes, shapes, and densities. The author has measured the compressive strength at a strain of 10% for different densities, sizes, and shapes, as illustrated in Figure 4.5.

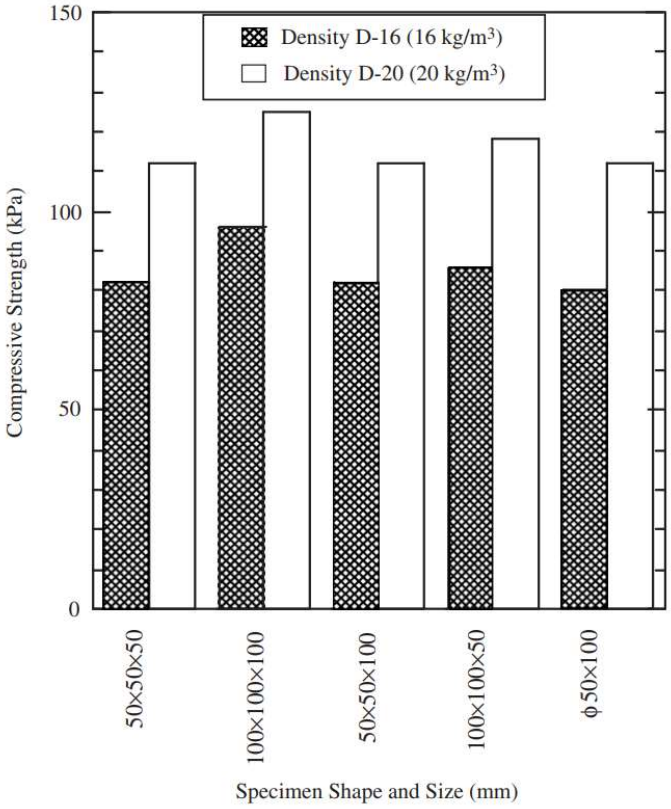

Figure 4.5. The compressive strength values corresponding to density, size, and shape [59].

As it can be inferred that the 50 mm cubic sample gave the least value of compressive strength, while the highest one was obtained from a 100 mm cubic specimen. In addition to specimen size and shape, the other reason for higher strength is the larger contacting surface on which the compression stress acted. Additionally, the correlation between the elastic modulus and the density of EPS was evaluated in this study and was compared to the others proposed in the literature previously in Figure 4.6.

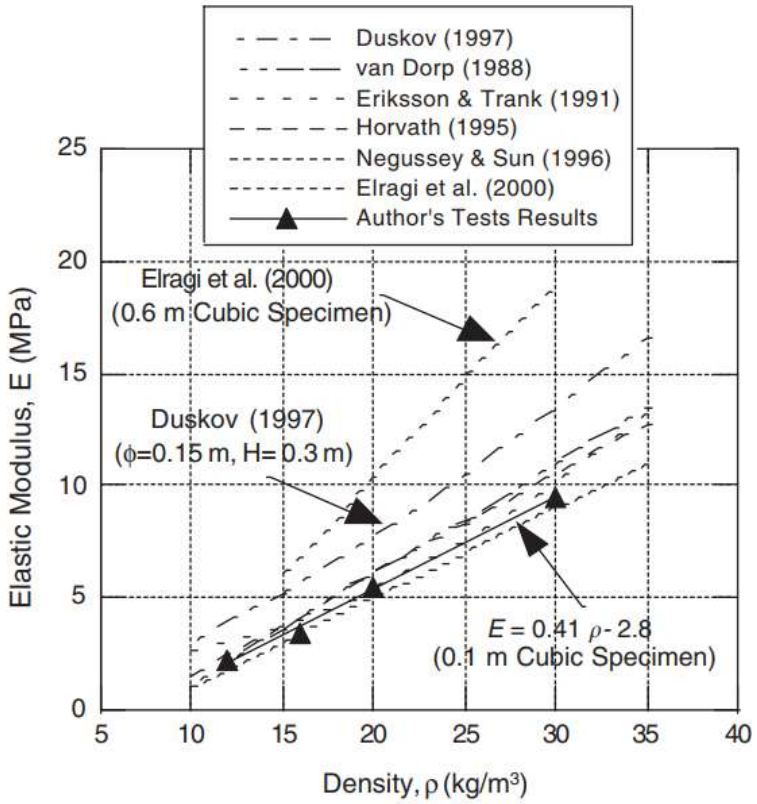

Figure 4.6. The relationship between Elastic modulus and EPS density [59].

4.3. Previous Studies on the Use of Lightweight Materials as a Cushion

4.3.1. Numerical and Experimental Studies on the Effects of Cushion Layer on Static Conditions

Karpurapu and Bathurst (1992) have implemented a numerical study in order to evaluate preliminary design charts used for the selection of inclusion materials placed adjacent to the rigid wall. Using the GEOFEM program, which performs a non-linear finite element method, the effects of inclusion layer with various thicknesses (1%, 2.5%, 5%, and 10% of the wall height) and stiffness values and backfill soil with different compaction densities on static lateral earth pressure were investigated. Additionally, the analyses were conducted for three different

wall heights (3, 5, and 10 meters). As a result of a numerical parametric study, the following inferences have been made:

- The increase in thickness of the inclusion layer led to a reduction in lateral earth pressure. The decrease in the elastic modulus of the compressible layer also brought about the same effect on lateral earth pressure while the inclusion thickness remained constant.
- The lateral movement of the backfill becomes lower as the friction angle and stiffness of the backfill increase while the inclusion thickness keeps constant.
- The inclusion layer with lower compression modulus and higher thickness had to be utilized for denser soils which have a greater friction angle compared with loose soils.

Based on investigated parameters, preliminary design charts have been proposed in order to select an appropriate inclusion thickness to reduce lateral earth pressure to a minimum, as shown in Figure 4.7.

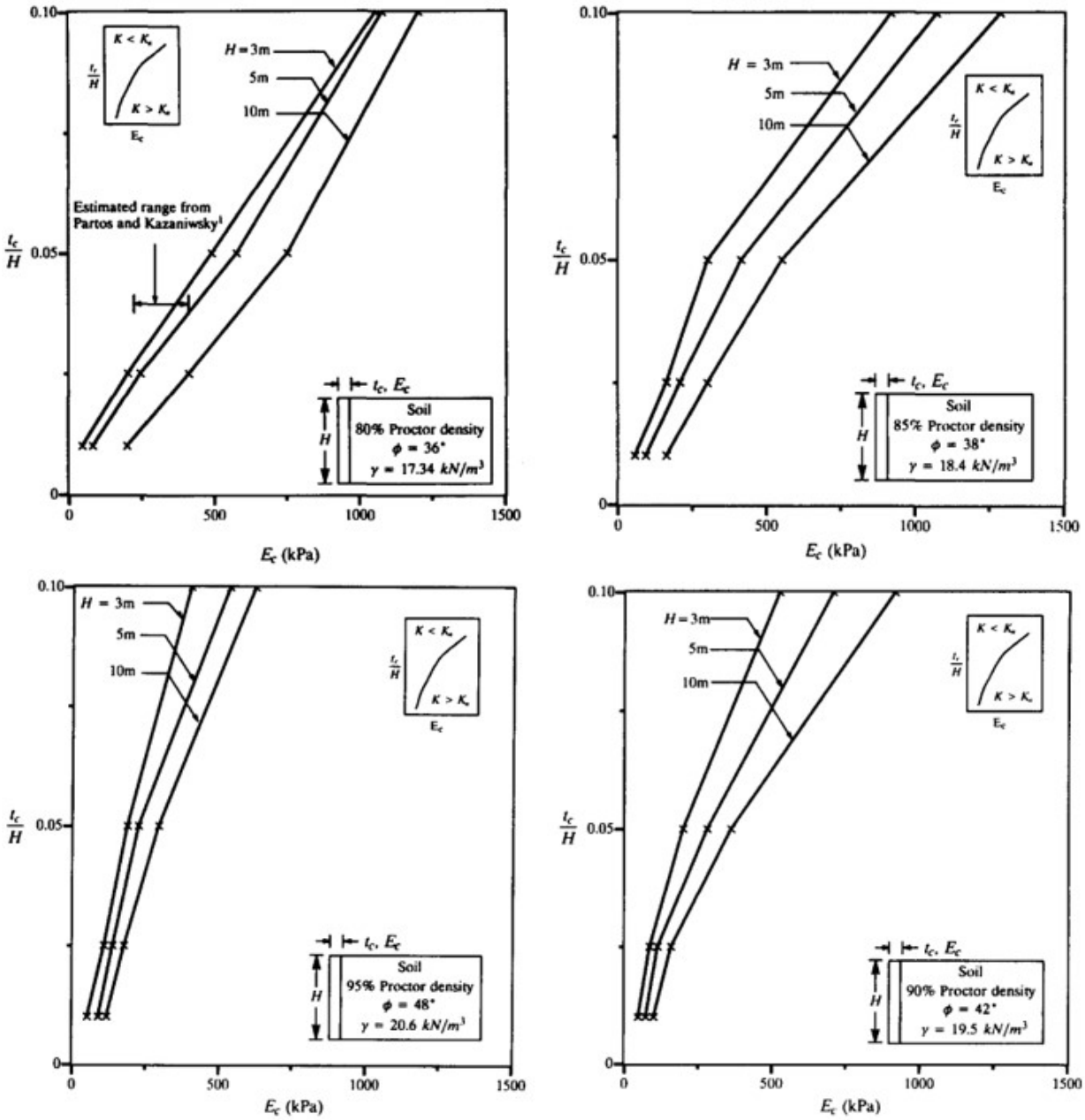

Figure 4.7. The inclusion layer thickness depending on elastic modulus to obtain an active state for soils having different friction angles [60].

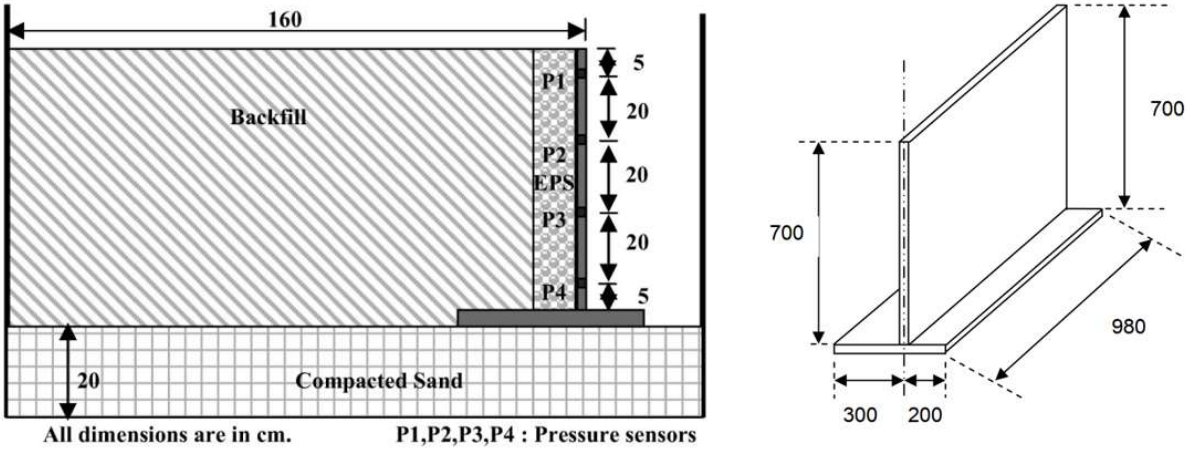

Figure 4.8. (a) The cross section of test setup [61] and (b) the dimensions of the steel wall model [62].

Ertuğrul and Trandafir (2011) have investigated the effects of geofoam inclusion installed adjacent to the rigid retaining wall on static lateral earth pressure by establishing a small-scale experimental model (Figure 4.8 (a)) and a numerical model. Concerning the 1-g physical wall model, the steel wall model was manufactured by welding the stem with the dimension of 700x980x8 mm on the base with the dimensions of 980x500x8 mm rigidly, as shown in Figure 4.8 (b) and the soil placed under, and back of the wall was dry and cohesionless. The numerical model was generated by using the experimental wall using UWLC software, and a plane-strain finite element analysis was performed. In their study, EPS geofoam utilized as an inclusion material has a density of 15 kg/m^3. The parameters whose effects were investigated on static earth pressure against the rigid non-yielding wall were the ratio of the thickness of EPS to wall height (t/H=0.07, 0.14, and 0.28), the characteristics of geofoam (stiffness varying from 2 to 10), the strength parameters of retained soil (various friction angle; 30°, 35°, 40°, and 45°), and the wall height (2.8, 3.5, and 4.2 meters). The test results showed that the change in wall height did not have a significant effect on the efficiency of the inclusion layer. However, the thickness and stiffness parameters had a significant effect on the reduction potential of the compressible layer. As the relative stiffness and thickness of the inclusion layer, the internal

friction angle of backfill soil increased, and the isolation efficiency of the geofoam layer increased.

Ertuğrul et al. (2012) conducted an experimental setup using the model depicted in Figure 4.8 with the same aim explained in the study by Ertuğrul and Trandafir (2011). The only difference in the wall model was the thickness of the stem which was selected as 5 mm. The EPS inclusion having a density of 16 kg/m^3 was installed behind the wall at 7%, 14%, and 28% of the wall height. During the experiments, both the rigid wall and the flexible wall were used in order to investigate the effect of wall type on the static earth pressure, accompanied by the geofoam thickness. According to the result of experiments, the inclusion layer results in lateral earth thrust acting on both flexible and rigid wall models. However, the reduction amount was greater in forces against rigid walls compared to those against the flexible wall. Figure 4.9 illustrates the reduction amount in static lateral earth thrust for rigid and flexible walls depending on the inclusion thickness.

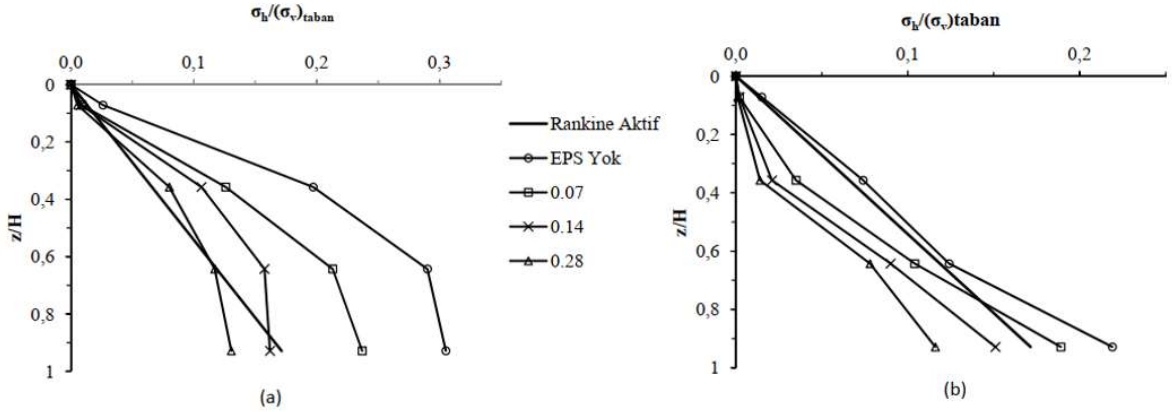

Figure 4.9. The static earth pressure acting along the wall depending on the thickness of EPS inclusion (a) for the rigid wall, (b) for the flexible wall [61].

Ertuğrul and Özkan (2012) have extended the study proposed by Ertuğrul et al. (2012) by performing physical tests on the model shown in Figure 4.8. Different from Ertuğrul et al. (2012), the authors used EPS geofoam with a density of 15 kg/m^3 as an inclusion, they changed the thickness of the wall stem (2, 4, 5, and 8 mm), and they selected two different inclusion

thicknesses (7% and 14% of the wall height). Thus, the effect of the wall flexibility was also investigated, in addition to the thickness of inclusion and wall type. The tests have indicated that the existence of the inclusion layer caused a decrease in static lateral earth forces; however, this reduction depended on the flexibility of the wall and the properties of the inclusion material. Additionally, the lateral forces acting on the rigid wall decreased more than those on the flexible wall, which was because the increase in flexibility of the wall stem brought about a decrease in lateral thrust. It can be inferred that the increase in flexibility of the wall led to a decrease in the load reduction efficiency of the inclusion. Moreover, the thickness of the EPS geofoam also significantly influenced the lateral force reduction. The increase in inclusion thickness resulted in a more attenuating effect on lateral forces.

Ertuğrul and Trandafir (2013) have broadened the parameters investigated by Ertuğrul and Özkan (2012) by conducting an experimental study on the small-scale experimental setup illustrated in Figure 4.8. As an inclusion material, EPS15 (ρ_s=15 kg/m^3) and XPS22 (ρ_s=22 kg/m^3) were placed behind the wall model. Additionally, a numerical study has been carried out in order to evaluate the effects of strength parameters and elastic modulus of backfill, stiffness of inclusion material, and wall flexibility by using FLAC 2D software. In the numerical model, two different wall heights (2 and 4 m) were used, and the wall thickness to wall height ratio was selected as 0.05, 0.1, 0.15, and 0.2. The inclusion material used in numerical analysis was EPS18 (ρ_s=18 kg/m^3) and EPS26 (ρ_s=26 kg/m^3). The following conclusions have been drawn by taking into account the results of both experimental and numerical analyses:

- The change in wall height did not significantly affect the reduction efficiency of the inclusion layer on the condition that the lateral forces acting on the geofoam were not greater than the yield stress of the inclusion.
- The increase in wall flexibility resulted in a decrease in lateral forces since the stem of the wall could move away from the retained soil.
- The reduction in lateral thrust and earth pressure coefficient took place in various amounts depending on the change in inclusion thickness and stiffness, wall flexibility, and strength parameters of the retained soil.

- The reduction potential of the geofoam layer decreased with the increase in wall flexibility.

Hasanpouri Notash and Dabiri (2018) have carried out a numerical analysis of yielding and non-yielding walls with heights of 3, 6, and 9 meters using the FLAC program. The aim of the study was to investigate the effects of the geofoam layer placed behind the wall on the behavior of the cantilever wall under static conditions. The geofoam cushions used in this study were three different densities (15, 20, and 25 kg/m^3), and they were installed adjacent to the wall with various thicknesses (the ratio of the geofoam thickness to wall height was equal to 0.05, 0.2, and 0.4). Additionally, the change in the shape of the geofoam layer was also investigated by using an EPS buffer in the shape of a rectangle and trapezoid. Moreover, the authors installed two geofoam layers behind the yielding and non-yielding wall, and the distance between panels was selected as 50, 100, 150, and 200 cm. The authors have come to the following conclusions:

- The increase in geofoam thickness resulted in a decrease in the static lateral thrust against the wall. However, the decrease in forces acting on yielding walls was lower than those on non-yielding walls.
- The decrease in the density of EPS caused a decrease in lateral forces and an increase in lateral displacement.
- The static forces acting on both yielding and non-yielding walls were not affected significantly by the placement of two geofoam layers placed at intervals behind the wall. However, the geofoam buffer with a trapezoidal shape had more effect on the reduction of static forces and the increase in displacement in comparison to using a rectangular layer and two panels behind the wall.
- Whereas the geofoam layer with a thickness of 0.05H resulted in an improvement in the overturning stability, the stability of the wall might be disturbed by the EPS buffer having a thickness greater than 0.2H. Additionally, the safety factor against overturning of yielding wall was reduced by using geofoam with a thickness of 0.4H.

Adelsalam and Azzam (2016) have proposed a study with the purpose of generation of design charts and correlation to determine the reduction of lateral forces and lateral earth pressure coefficient under active and at-rest conditions when the EPS cushion was placed behind the wall. Firstly, the authors conducted laboratory tests on geofoam samples to examine their strength and interface properties with concrete and retained soil. Then, they established a numerical model using a concrete wall with a 1-m height and EPS cushion with various thicknesses (changing from 2 to 50 cm). The behavior of flexible and rigid walls under static conditions was evaluated using the finite-element method implemented by PLAXIS 2D. Based on the results of the analyses, the following inferences have been made:

- For both flexible and rigid walls, the lateral pressure decreased with an increasing thickness of EPS inclusion. However, the amount of reduction in lateral forces against flexible walls was 8% lower than that on rigid walls.
- For flexible walls, the inclusion thickness, interface, and flexure properties had a significant influence on the lateral forces compared to the geofoam density.
- The design charts and correlations for the assessment of the reduction amount in lateral earth pressure were established, as shown in Figure 4.10.

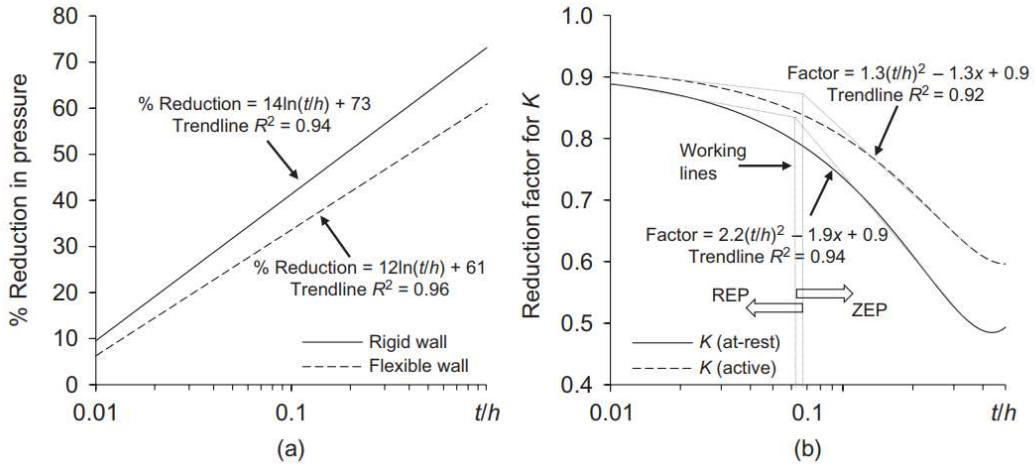

Figure 4.10. The reduction in lateral earth pressure (a) and lateral earth pressure coefficient (b) corresponding to the ratio of inclusion thickness to wall height on a logarithmic scale [66].

4.3.2. Numerical and Experimental Studies on the Effects of Cushion Layer on Dynamic Conditions

Ertuğrul and Trandafir (2014) have carried out 1-g shake table tests using the small-scale wall model given in Figure 4.8 in order to evaluate the effects of inclusion properties and wall flexibility on dynamic earth pressure acting on flexible cantilever walls. The frequency (4 to 10 Hz) and peak acceleration (0.1 to 0.7g) of input motion were investigated in addition to the parameters examined by Ertuğrul and Trandafir (2013). According to the results of experiments by taking into account various parameters, the following inferences have been made:

- The increase in amplitude and frequency of input motion caused an increase in the horizontal displacement and vertical settlement within retained soil.
- The deformation of the inclusion material due to its compressibility resulted in an additional surface settlement at the end of the test. This is because the surface settlement of the model without a geofoam layer was obtained remarkably less than those determined from the wall model with inclusion. Moreover, this additional settlement increased with the increase in the thickness of the geofoam layer.
- The compressible layer reduced not only lateral forces against the wall but the amount of flexural movement of the wall stem as well.
- The load reduction potential of XPS was observed to be slightly lower than those of EPS.
- The increase in wall flexibility led to a reduction in the load and displacement reduction potential of the deformable layer.
- The compressible inclusion resulted in a reduction in residual wall stresses occurring under seismic shaking due to the backfill soil densification.
- Inclusion material, wall flexibility, and input motion parameter affected the application point of maximum seismic pressure, which changes from 0.4H to 0.6H. Additionally, the loading point obtained from experimental test results was greater than that calculated from the Steedman-Zeng method.

- Similar to lateral forces, deformable layer properties and wall flexibility also resulted in a reduction in a lateral earth pressure coefficient (K_{AE}). Additionally, K_{AE} considerably increased with an increase in frequency ratio (f/f_n*= the ratio of frequencies belonging to input motion and the soil-backfill system).
- The lateral earth pressure determined by the Steedman-Zeng method and those obtained from the experimental test were in good agreement with the model with low flexibility.

Zarnani et al. (2005) and Zarnani and Bathurst (2005) were companion studies, both of which investigated the reduction effect of geofoam inclusion behind the rigid wall on the lateral earth thrust by shaking table tests. The former study was about experimental tests conducted using EPS geofoam with six different properties, whereas the numerical study was carried out using EPS with two different densities in the latter study. The numerical model was verified by the data collected from the results of shaking table tests. The experimental setup contained a rigid wall model, the inclusion material, and a dry and cohesionless backfill soil, as depicted in Figure 4.11(a). The scaling factor was selected as 1/6 for the establishment of a small-scale test model. The wall model was made of aluminum, and it was installed on a shaking table. The numerical analysis has been carried out with the model shown in Figure 4.11(b), which was similar to the experimental setup. A sinusoidal acceleration time history with a frequency of 5 Hz and with amplitude increasing gradually up to 0.8g was applied to both models, as given in Figure 4.12. As a result of an experimental study, Zarnani et al. (2005) have observed that a reduction in density or modulus of EPS geofoam brought about a decrease in lateral forces occurring under seismic shaking, similar to Karpurapu and Bathurst (1992), who observed the same trend in static forces. The load reduction amount of seismic buffer reached 60% of the forces acting on the rigid wall without a geofoam panel. Moreover, the compressibility of EPS decreased as the density or modulus increased. After the end of the experiments, the elastic rebound of the inclusion layer was observed.

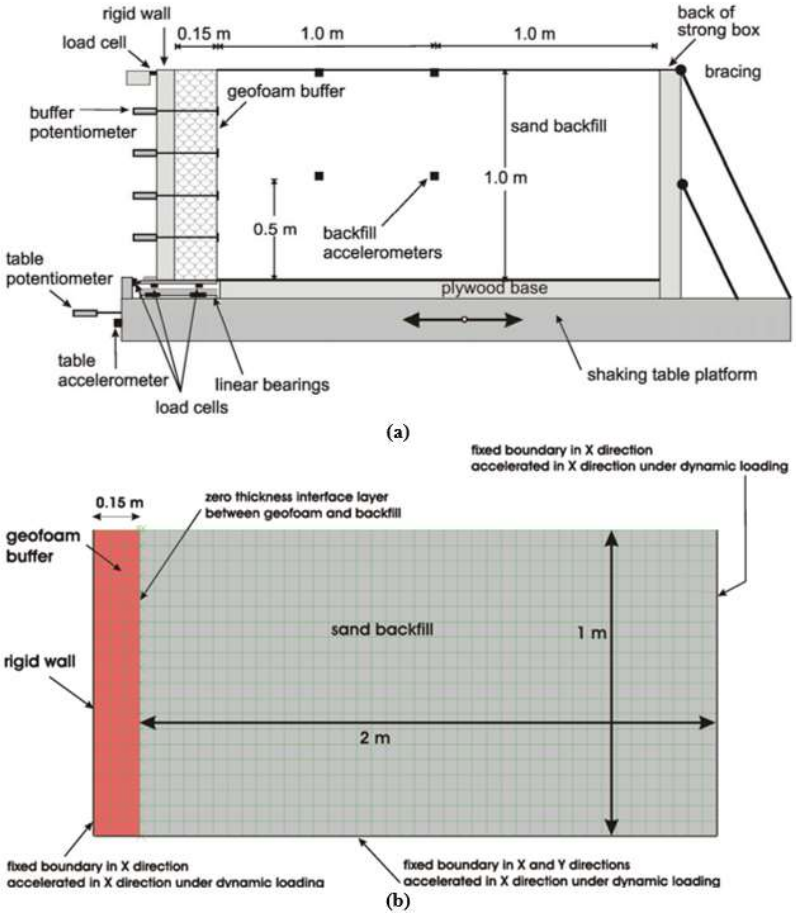

Figure 4.11. (a) The experimental setup and instrumentation [67], (b) The numerical model established using FLAC software [68].

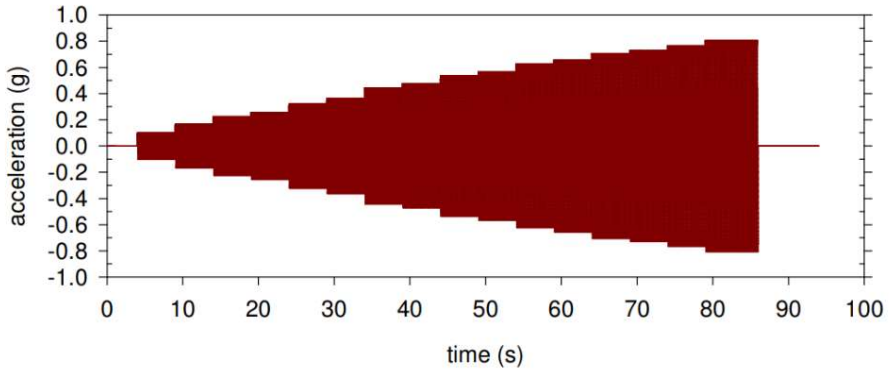

Figure 4.12. A sinusoidal input motion with stepped amplitudes up to 0.8 g and with a frequency of 5 Hz [68].

Zarnani and Bathurst (2005) have simulated the changes in wall force due to the geofoam buffer application using FLAC software. A comparison of the results showed good agreement between the predictions made by numerical analysis and the experimental data, as given in Figures 4.13(a), (b), and (c). Additionally, the reduction in lateral earth thrust has been observed because of geofoam inclusion, as shown in Figure 4.13(d).

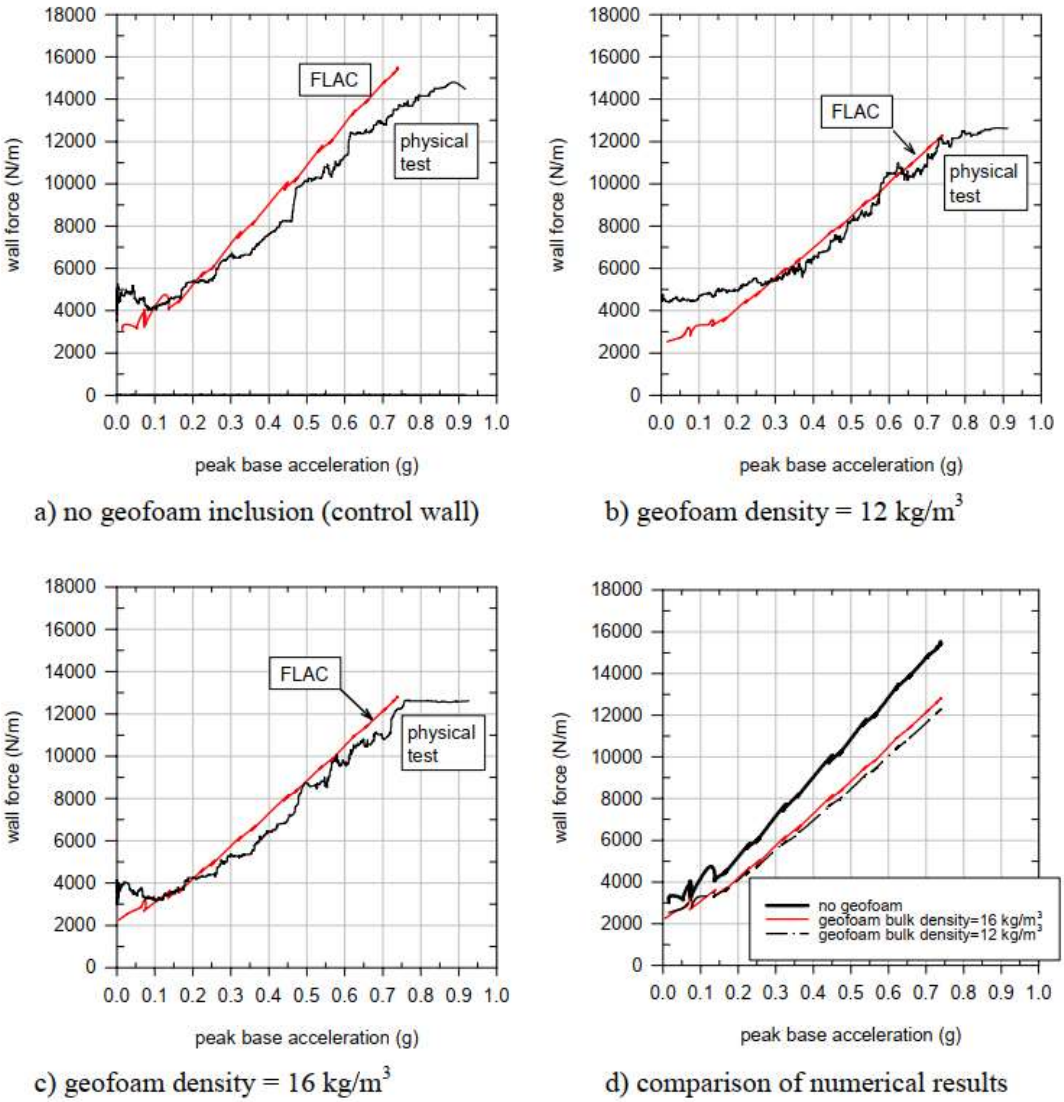

Figure 4.13. The change in wall forces depending on peak acceleration from numerical and experimental analyses [68].

Zarnani and Bathurst (2006) have conducted a study in order to comprehend the effect of inclusion consisting of EPS geofoam on dynamic lateral earth thrust due to earthquake. The authors gave brief information about the experimental setup and carried out a numerical study using FLAC software to simulate the shaking table test results. The physical and numerical models are illustrated in Figures 4.11(a) and (b). In this study, the density values of the inclusion material were chosen as 16, 14, and 12 kg/m^{3,} and the elastic modulus was calculated as 5.4, 2.8, and 4 MPa, respectively. Shaking table tests and numerical analyses indicated that the application of geofoam behind the wall provided a lateral earth pressure attenuation. Additionally, the decrease in elastic modulus of inclusion resulted in higher load reduction. Furthermore, the load reduction amount could exceed 36% of the force acting on the wall without inclusion, according to the results of the numerical study.

Bathurst et al. (2007) have implemented an experimental study with the aim of comprehending whether the buffer application provided a reduction in dynamic lateral forces acting on a rigid wall. The shaking table tests were performed on the setup given in Figure 4.11(a). The properties of the inclusion material were similar to those used in Zarnani and Bathurst (2006). As a result of the tests, the observation of lateral thrust attenuation has been made. The decrease in density and stiffness of buffer material caused an increase in load reduction amount. The greatest reduction in lateral loads was observed as 31% at a peak acceleration of 0.7g.

Zarnani and Bathurst (2007) have performed six shaking table tests on the small-scale experimental setup depicted in Figure 4.11(a). The six different inclusion material was used with varying elastic modulus and density. The authors investigated the load reduction potential of EPS geofoam adjacent to rigid walls, similar to the aforementioned studies. Different from them, buffer compression, dynamic elastic modulus of inclusion material, dynamic friction angle between retained soil and EPS geofoam, amplification of excitation, stress relaxation, and creep after shaking have been examined in this study. Based on the results, the following conclusions have been made:

- As the density and stiffness of the geofoam increased, the load reduction of the buffer decreased, as given in Figure 4.14.
- The seismic buffer with the lowest stiffness reduced the lateral forces by 40%, whereas the one with the highest stiffness led to a 15% reduction in forces against the rigid wall.
- EPS materials compressed exceed their elastic limit provided the greatest reduction in lateral forces.
- The stiffness of the non-elasticized geofoam material diminished as the density decreased.
- The cohesive (or adhesive) interface shear strength parameters between retained soil and buffer panel increased with decreasing density and stiffness of EPS.
- The stress-relax and creep could be observed in the EPS-soil system after base excitation ceased.

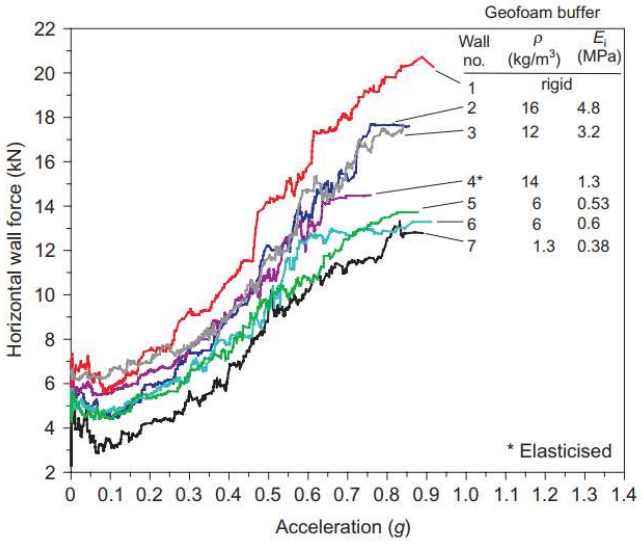

Figure 4.14. The change in horizontal forces against the wall depending on the density or elastic modulus of EPS geofoam [72].

A numerical study has been carried out by Zarnani and Bathurst (2009). In order to examine the effects of wall height, EPS inclusion parameters, and input motion parameters on

the seismic performance of inclusion placed behind the rigid wall, the numerical simulations were performed using FLAC software. The investigated parameters are tabulated in Table 4.13.

Table 4.13. The investigated parameters in numerical analysis [73].

Parameter	**Type or Value**
Wall height (H)	1, 3, 6, and 9 meters
Thickness of EPS buffer (t)	2.5%, 5%, 10%, 20%, and 40% of wall height
Types of EPS	EPS19 (ρ=18.4 kg/m^3) EPS22 (ρ=21.6 kg/m^3) EPS29 (ρ=28.9 kg/m^3)
Buffer stiffness (K=E/t, the ratio of elastic modulus to thickness of EPS)	from 1.58 to 113.8 for EPS19 from 1.92 to 138 for EPS22 from 2.70 to 195 for EPS 29
Ratios of motion frequency to the fundamental frequency of the soil-wall system (f/f_{11})	0.3, 0.5, 0.85, 1.2, and 1.4
Frequency of excitation	from 0.7 Hz to 21 Hz*

*Maximum amplitude and duration remained constant for all inputs, as 0.7g and 17 sec, respectively.

According to the test results, the following interpretations have been made:

- The EPS geofoam layer provided a decrease in lateral forces with an increasing thickness.
- The increase in buffer thickness and the decrease in EPS density resulted in an increase in the isolation efficiency of EPS.
- The total force acting on the wall increased as the frequency of input motion increased. However, this pattern was valid for frequencies lower than the natural frequency of the soil wall system. Beyond this frequency, the wall forces reduced as the frequency excitation increased.
- While the frequency of input motion was reaching the natural frequency of the rigid wall (the resonance threshold, f/f_{11} =1), the isolation efficiency of the buffer material decreased. This trend was least noticeable for the buffer having greater thicknesses.

- In general, the isolation efficiency decreased as the wall height decreased.
- The isolation efficiency decreased nonlinearly as the EPS stiffness increased. The tests show that the practical range of stiffness was K equal to or smaller than 50 MN/m^3 for the design of systems which was aimed to reduce seismic loads.
- Strains occurring on EPS buffer increased with a decrease in the buffer modulus, an increase in wall height, and a reduction in the buffer thickness, with an excitation frequency approaching the fundamental frequency of the wall.

Zarnani and Bathurst (2011) conducted a parametric study on the model shown in Figure 4.11(b) using FLAC software. The investigated parameters were the same as those given in Table 4.13. In this study, the results of the numerical analysis were demonstrated as design charts for the determination of buffer, as given in Figure 4.15. Considering all results and design charts, the practical range of K was equal to or smaller than 50 MN/m^3 for the design of systems using load reduction with EPS installation.

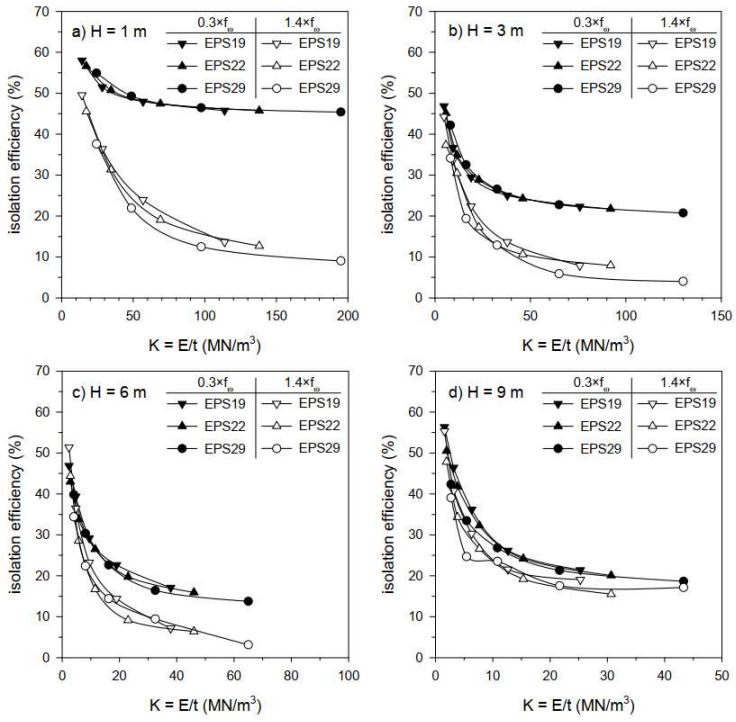

Figure 4.15. The design charts proposed by Zarnani and Bathurst (2011).

Wang and Bathurst (2012) have investigated the effects of EPS geofoam cushion placed behind rigid walls on dynamic earth pressure by conducting a numerical study which was established based on the results of three shaking table tests performed on a small-scale model illustrated in Figure 4.11(a). ABAQUS software, which performed Finite Element Method (FEM), utilized numerical simulations. The wall model was similar to the model depicted in Figure 4.11(b). The cushion layer consisted of EPS with a thickness of 0.15 m. EPS geofoam used in this study had two different densities which were 12 and 16 kg/m^3. According to a numerical study, the compression of EPS increased as time increased. Moreover, the decrease in density (also elastic modulus) caused an increase in the compressibility of EPS buffer. Based on the comparison between experimental and numerical results, ABAQUS software can be a successful program for analyzing geofoam buffers.

Hazarika et al. (2001) investigated the influence of a lightweight material placed behind the wall instead of conventional backfill by conducting numerical analyses using the finite element method. The replacement of backfill with EPS geofoam with a density of 20 kg/m^3 soil only took place for the predicted failure zone. The rigid wall retaining a dry cohesionless soil was modeled with a height of 10 meters, and two input motions (a sinusoidal recording having a 3.5 Hz frequency and a 0.2g amplitude (200 gals) – North-South component of Hyogo-Ken Nanbu earthquake) were used for analyses. Additionally, the movements of the soil-wall system were simulated for non-yielding and yielding (for active and passive state) conditions. Therefore, the EPS geofoam placed in lieu of retained soil resulted in approximately a 50% - 60% reduction in lateral pressure acting on the wall before the replacement of the lightweight material. The use of lightweight material instead of soil behind the wall can be an economical way to reduce the earthquake-induced forces causing excessive deformations in earthquake-prone areas.

Hazarika (2001) has performed numerical analyses with the aim of assessing the effects of the use of EPS geofoam as a compressible buffer behind the retaining wall. The model wall had a height of 10 meters, and it was embedded 3 meters in soil, as established in Figure 4.16.The investigated conditions and the excitation used to shake the soil-wall system were

similar to the study of Hazarika et al. (2001). Additionally, the geofoam panel with a density of 20 kg/m^3 was installed behind the wall at a thickness of 1 m. The result of the numerical analyses showed that the reduction in lateral forces has occurred for both non-yielding and yielding conditions. The compressible inclusion gave rise to a decrease exceeding 40% in lateral pressure, as depicted in Figure 4.17.

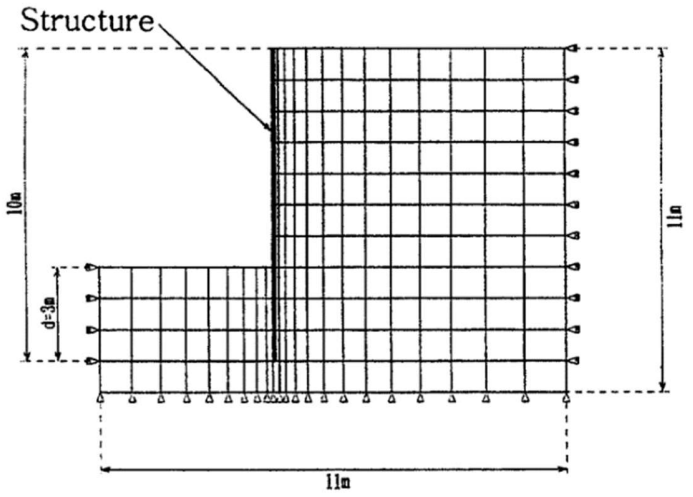

Figure 4.16. The model wall used in numerical analyses [77].

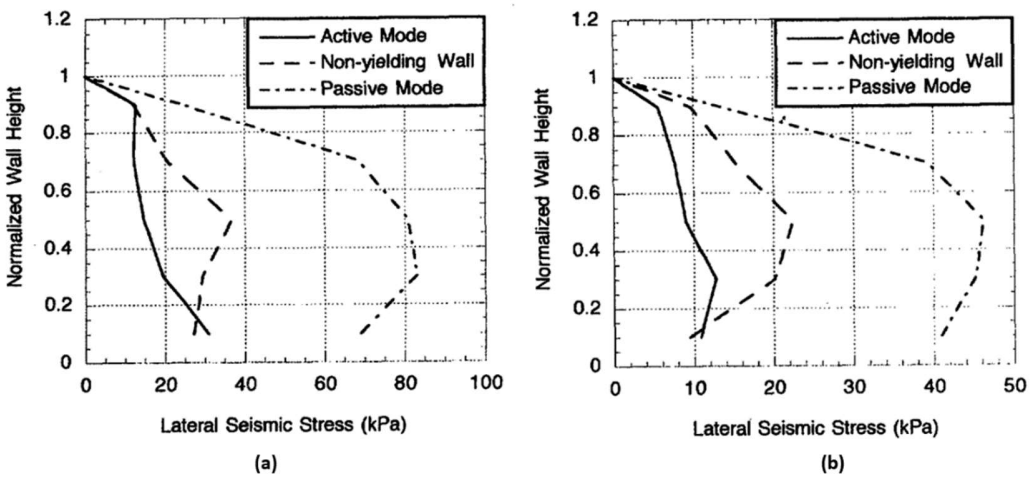

Figure 4.17. The lateral earth pressure acting along the wall; (a) before the application of inclusion, (b) after the application of inclusion [77].

Hazarika et al. (2008a) have conducted a series of shaking table tests to determine the enhancement of seismic response of geotechnical structures after the placement of a cushion layer between the backfill soil and the structure. A caisson quay wall scaled by 1/10 has been investigated in experimental testing, as illustrated in Figure 4.18. The cushion layer with a thickness of 0.3 m was made of tire chips, and the ratio of cushion thickness to wall height was selected as 0.4. Moreover, the drains containing tire chips were installed within the retained soil. As an input motion, the North-South component of the Hyogo-Ken Nanbu earthquake was used during the testing procedure. In accordance with the test results, the buffer layer caused a reduction in both lateral forces and permanent displacement occurring due to excitation. Furthermore, liquefaction was prevented since the tire chips led to the dissipation of pore water pressure quickly.

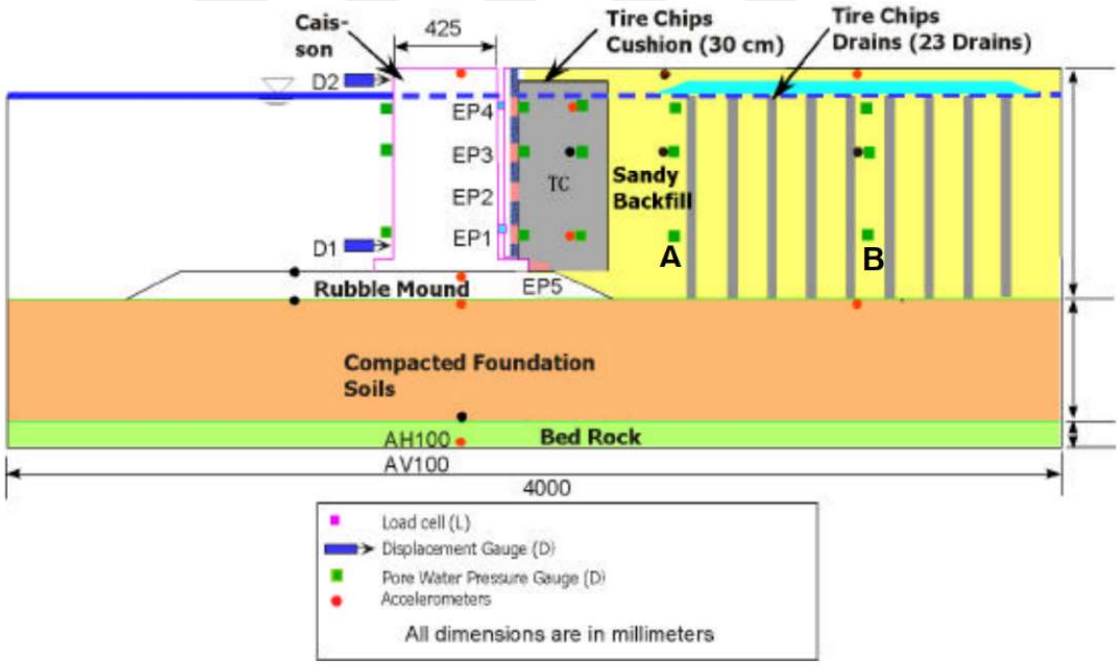

Figure 4.18. The experimental setup [78].

Hazarika et al. (2008b) have performed shaking table tests on the model of gravity-type caisson quay wall scaling by 1/10. The aim of the study was to investigate whether the reduction in seismic loads was provided by the cushion layer installed between the caisson and the

cohesionless backfill. The compressible buffer was prepared with tire chips with a grain size of 20 mm and filled in a geotextile bag to prevent tire chips from mixing with sand. Three different earthquake recordings (two actual earthquake time histories and a synthetic acceleration time history) were applied to the experimental setup. According to test results, the buffer layer resulted in a reduction in seismic forces, which means that it caused the improvement of the seismic performance of the quay wall. Additionally, the decrease in loads brought about a decrease in the dimensions of the wall, which lowered the material cost. Moreover, the permanent displacement is reduced due to the use of a cushion layer. Also, tire chips cushion helped the porewater pressure to dissipate relatively faster compared to sand backfill without a cushion.

Hazarika (2008) investigated the effectiveness of the technique called SAFETY (**S**tability **A**nd **F**lexibility of structures during **E**arthquake using **TY**res) which provides a cost-effective improvement on the dynamic response of the geotechnical structures. In line with this objective, the 1G shaking table tests were performed on both small-scale and large-scale models under underwater conditions, as depicted in Figure 4.19. The tire chips filled into a bag made of geotextile were utilized as a cushion layer behind the quay wall. The tire chips with a particle size of 2 mm and 20 mm were used in small-scale and large-scale models, respectively. As an input motion, a sinusoidal record was used for the small-scale model, whereas two actual earthquake time histories and one synthetic earthquake motion were applied to the large-scale model. As a result, SAFETY techniques:

- reduced lateral loads and permanent displacement due to seismic loading.
- reduced wall dimensions by virtue of the decrease in loads.
- reduced project cost by virtue of the decrease in wall dimension.
- were environmental-friendly due to the use of recycled waste tires.
- could be applied not only during construction but also after the construction.

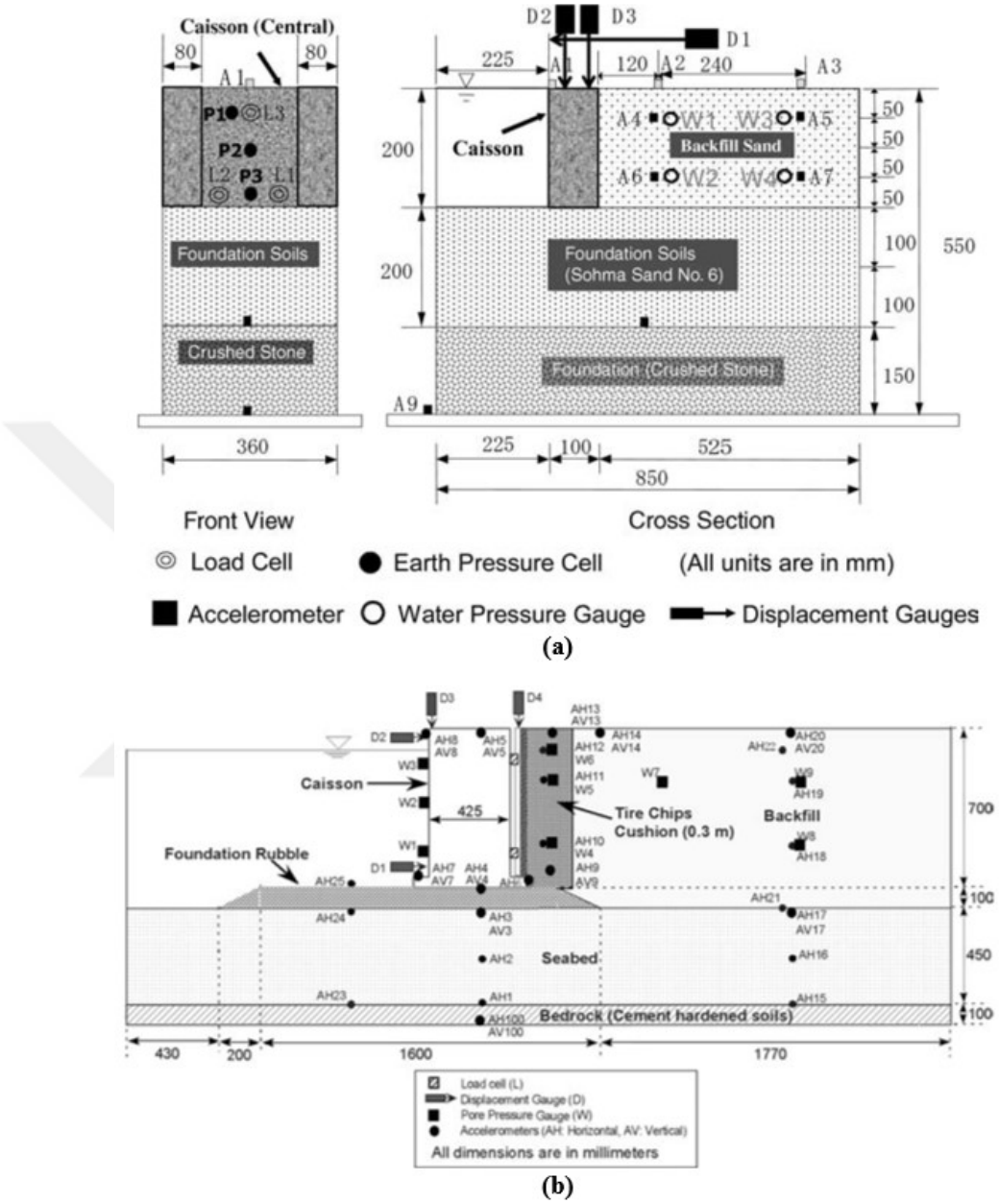

Figure 4.19. (a) The small-scale experimental model with a scale factor of 1/35, (b) The large-scale experimental model with a scale factor of 1/10 [80].

Hazarika et al. (2010) have explained the use of scrapped tire-derived materials (specifically tire chips and tire shreds) in three categories which were tire shreds utilized as a drainage layer under an embankment, tire chips and sand mixture used as a seismic buffer behind retaining wall, and tire chips utilized as a ductility and roughness improver by mixing with

cement-treated clay. The authors have established a caisson-type quay wall model with a scale of 1/35 to investigate the effects of a compressible cushion installed behind the quay wall on lateral forces. The wall model is shown in Figure 4.19 (a). Three types of the seismic cushion have been prepared by using tire chips with a grain size of 35 mm and sand; (1) Fully tire chips with a density of 0.611 g/cm^3, (2) 75% tire chips and 25% sand mixture by volume, and (3) 50% tire chips and 50% sand mixture by volume. As an input motion, the sinusoidal acceleration time history with a period of 1 sec (a frequency of 20 Hz) was used. The model was subjected to the motion in stages, in which the acceleration increased from 0.1g up to 0.6g with an increment of 0.1g. As a result of the test, the cushion layer resulted in not only the residual displacement but also the lateral forces acting on the wall due to the excitation. Moreover, the seismic cushion with three different mixture percentages approximately resulted in a similar amount of decrease in terms of wall displacement under excitation with increasing amplitude. Consequently, as far as the project cost and wall performance were concerned, the mixture of %50 tire chips and 50% sand could be appropriate.

In the numerical study proposed by Dabiri and Hasanpouri Notash (2020), the effects of the geofoam layer installed behind the cantilever wall on static and dynamic earth pressure have been investigated while considering various parameters such as wall height (6 and 9 meters), wall type (yielding and non-yielding), and geofoam characteristics (unit weight= 0.15 and 0.2 kN/m^3 and thickness=10% and 20% of the wall height). The analyses have been carried out using FLAC software, and for the dynamic analysis, two earthquake recordings (Loma Prieta Earthquake (far-field) and Kocaeli Earthquake (near-field)) and the acceleration-scaled version of these two motions were used as an input motion. According to the tests, as the thickness of inclusion increased, the relative stiffness decreased. The reduction in stiffness resulted in an increase in the compressibility of geofoam, which decreased lateral forces against the wall and increased the lateral displacement of soil. The geofoam inclusion showed a significant impact on lateral forces under static and dynamic loadings. However, the performance of inclusion under static conditions was better than that under dynamic conditions. Additionally, the amount of load reduction was greater for non-yielding walls compared to yielding walls. Moreover, the inclusion layer under near-field earthquake recording showed better performance than under

far-field seismic motion. The potential of displacement reduction due to inclusion might exceed 40% for yielding walls, depending on an input motion characteristic (peak acceleration, frequency, and relative frequency), inclusion thickness, and wall height. Lastly, the height of the application point of dynamic lateral forces above the wall base increased due to the application of inclusion behind the wall.

Edinçliler and Toksoy (2017a) have performed a finite element analysis using PLAXIS 2D with the aim of the examination of the effectiveness of the cushion layer under excitation with different characteristics. The inclusion material was tire crumb with a unit weight of 6.5 $kN/m^{3,}$ and the analysis was carried out with a wall with a height of 7 m. Additionally, the numerical model was subjected to two actual earthquake recordings, which were Kobe and El-Centro Earthquakes. Kobe earthquake has a 0.68g peak amplitude and a 2.1 Hz predominant frequency, whereas the maximum amplitude and predominant frequency of the El-Centro earthquake are 0.36g and 4 Hz, respectively. During the dynamic analysis, the reduction in peak acceleration transmitted to the wall due to input motions and the decrease in the acceleration distribution along the wall have been observed successfully. Additionally, the compressible cushion resulted in a decrease in not only axial stress but also shear stress under both earthquake recordings. As seen in the results, the wall performance under static and seismic loadings has been enhanced due to using the installation of a tire crumb as a seismic buffer behind the wall.

Edinçliler and Toksoy (2018) have performed a finite element analysis using PLAXIS 2D in order to investigate the optimum cushion thickness installed behind the cantilever wall to improve the seismic performance of the structure. The wall with heights of 5 and 7 meters and the cushion layer prepared by mixing 30% tire crumbs and 70% sand by weight were used in the analysis. The ratio of compressible layer thickness (t) to wall height (H) was selected as 0.4 and 0.3. The numerical model was subjected to Kobe Earthquake. The results indicated that the cushion has enhanced the seismic performance of the wall, as expected. Moreover, the t/H ratio should be selected as 0.3 in lieu of 0.4 to increase stability.

Athanosopoulos-Zekkos and Athanosopoulos (2012) have proposed a parametric study using PLAXIS 2D software. The load, displacement, and rotation reduction efficiency of the inclusion layer was examined under the influence of various parameters. These parameters were: (1) the frequency of input motion (0.3 Hz to 3 Hz), (2) the amplitude of input motion (0.1g to 0.7g), (3) wall height (4 m and 7.5 m), and (4) the thickness of compressible inclusion. The wall model was selected as a yielding gravity wall, and as a seismic buffer, the EPS (a unit weight of 0.20 kN/m^3) was utilized. Based on the results of the numerical parametric study, the following conclusions have been drawn:

- The presence of a cushion resulted in a decrease in not only static and dynamic earth pressure but also displacement due to earthquake shaking.
- Whereas for non-yielding walls, the load reduction efficiency of inclusion could exceed 90%, the isolation efficiency for yielding walls reached a limit value (approximately 30% or 40%).
- Based on numerical results, the relationship between the intensity of input motion and the load, displacement, and rotation reduction potential of the inclusion layer could not be inferred clearly.
- The isolation potential (for load, displacement, and rotation) of the cushion increased almost linearly for lower thicknesses (t/H=5% - 15%). Further increase in the buffer thicknesses resulted in a non-linear increasing pattern until a limit threshold.
- The isolation potential of the seismic buffer relied on the frequency of the input motion. Moreover, it is also affected by the ratio of the frequencies of shaking and the wall (f/f_1, where $f_1=V_s/4H$).

5. EXPERIMENTAL SETUP

5.1. General

The experimental study determines the effects of the cushion type on the seismic behavior of the retaining wall by implementing a series of shake table tests on the 1/25 scaled test model. EPS geofoam and the mixture of sand and tire crumb are considered as cushion materials. Additionally, the effects of the thickness of the cushion layer, the density of EPS geofoam, the mixture ratio of the sand-tire crumb mixture, and the characteristics of input motions on the seismic behavior of the wall model are investigated. This section includes materials, design of test setup, instrumentation, and selection of input motions.

5.2. Experimental Equipment and Facilities

5.2.1. Shake Table

The experimental study was carried out using the large shaking table located in Prof. Dr. Mustafa Erdik Shake Table Laboratory, Kandilli Observatory, and Earthquake Research Institute of Boğaziçi University. The used shake table can apply a motion on a specimen with a weight of up to 10 tons and with a height of up to 6.5 m. The table provides a uni-axial horizontal movement by a servo-hydraulic actuator. It is capable of simulating real or synthetic motions with up to an amplitude of 2g and a lateral movement of ±12 cm (20cm in total).

5.2.2. Measurement Instruments

In this study, the accelerometer with a capacity of ±3g was placed on the shake table, whereas the capacity of other accelerometers was ±20g. Additionally, displacement sensors

were used in experiments to measure displacement by laser sensors. The sensors were Leuze ODSL 96B M/V6.XL-1200-S12 optical distance sensors with a measurement range of 150 - 1200 mm and an absolute measurement accuracy of ±2 %.

5.3. Materials

The experimental setup was established in a rigid-sided soil box by using a small-scale wall model, cohesionless backfill, and inclusion material consisting of EPS geofoam and tire waste-sand mixture. The preparation of the experimental setup started with the design of the scaled retaining wall and the selection of material. The wall model was established using a scale factor of 1/25 depending on the dimensions of the rigid soil box, and the backfill soil and materials used as cushions were prepared. This section covers the shaking table, rigid-sided soil box used in shaking table tests, design and preparation of the wall model, and the properties of sand and cushion material.

5.3.1. Soil Box

The rigid-sided soil box that was used for shake table tests with dimensions of 900x400x500 mm is depicted in Figure 5.1. It is made of transparent plexiglass having 15 mm thickness. The bottom of the box is made of steel. Additionally, the sides of the box were assembled using screws. The flexibility of plexiglass is prevented with metal strips. The plexiglass soil box was firstly used in the M.Sc. thesis by Toksoy, 2014, and the studies by Edinçliler and Toksoy, 2017b and 2017c.

Figure 5.1. The rigid-sided plexiglass soil box.

5.3.2. Retaining Wall Model

The proportioning of the cantilever retaining wall was studied in order to implement a preliminary dimensioning according to different codes and researchers that are shown in Figure 5.2.

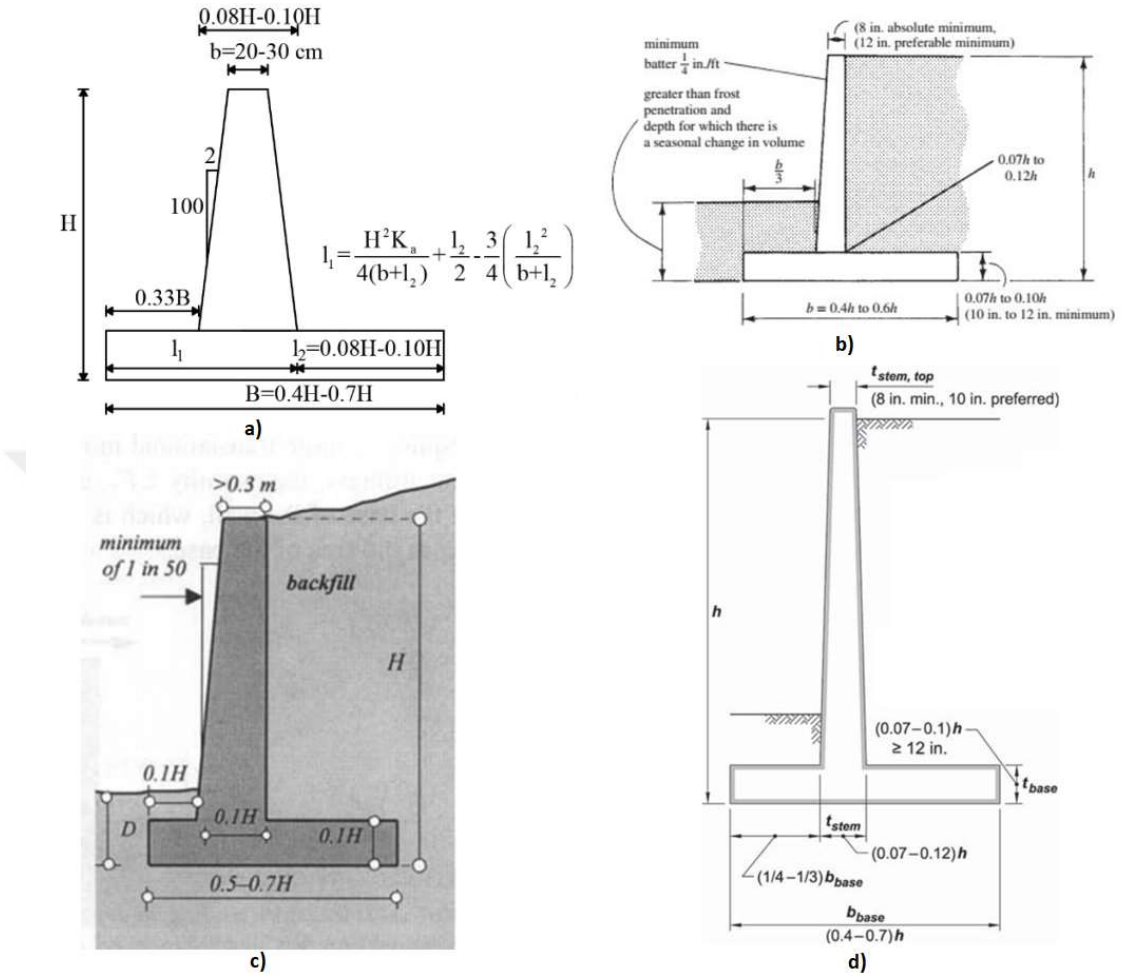

Figure 5.2. The preliminary dimensions for the cantilever retaining wall; a) TS7994 [89], b) McCormac and Brown (2015), c) Azizi (1999), d) ACI 318-14.

Regarding the preliminary dimensions in Figure 5.1, the wall dimensions were selected for this study, as given in Table 5.1 and Figure 5.3. The height of the prototype wall was considered 6 meters.

Table 5.1. Preliminary dimensions of the prototype wall (H_s: height of the stem, B: width of the base, t_s: the thickness of the stem, t_b: the thickness of the base, B_{front}: the length of the base in front of the wall stem).

H_s (m)	B (m)	t_s (m)	t_b (m)	B_{front} (m)
6	3.9	0.35	0.35	0.6

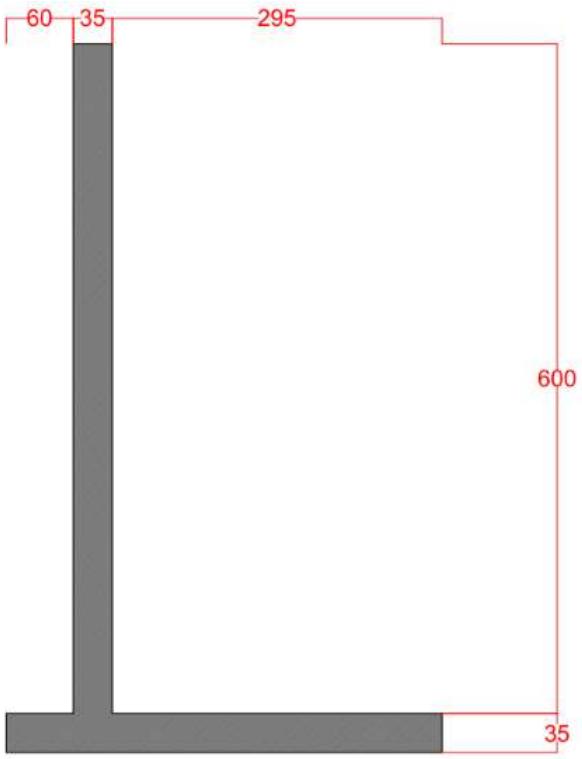

Figure 5.3. The determined dimensions of the prototype wall.

The designed wall dimensions were controlled for whether they were sufficient to remain stable under static and dynamic conditions (for a_{max}=0.3g) by hand calculations. The methods of Coulomb, Rankine, and Mononobe-Okabe were used. The safety factors against overturning and sliding for each method were calculated as given in Table 5.2.

Table 5.2. The safety factor of the prototype wall for the methods of Coulomb, Rankine, and Mononobe-Okabe (M-O).

METHOD	**$FS_{(overturning)}$**		**$FS_{(sliding)}$**	
Coulomb	4.36	≥ 1.5	1.72	≥ 1.5
Rankine	3.91	≥ 1.5	1.55	≥ 1.5
M-O (a_{max}=0.3g)	3.71	> 1.3	1.11	> 1.1

According to Coulomb and Rankine methods, the calculated safety factors should be equal to or greater than 1.5 for stability against both overturning and sliding. However, based on the M-O method, the factor of safety against overturning should be higher than 1.3, while the safety factor for sliding should be greater than 1.1. As seen in Table 5.2, the wall dimensions were satisfying according to the aforementioned conditions [3].

The wall stability was also controlled by GEO5 software version 2021. According to the software, when the factor of safety against overturning and sliding should be greater than 1.5, the wall is satisfactory for slipping and overturning under static conditions. However, under seismic conditions, the factor of safety against overturning and sliding should be higher than 1.0 for the wall to be satisfactory. The values of safety factors under static and seismic conditions were determined. For seismic conditions, the coefficient of horizontal acceleration of ground motion was selected as 0.3g, 0.4g, and 0.5g, while the factor of vertical acceleration was selected as 0g. The determined safety factors are given in Table 5.3. As seen in Table 5.3, the wall is safe for overturning and sliding.

Table 5.3. The safety factor of the prototype wall determined using GEO5.

Loading Condition	**FS(overturning)**		**FS(sliding)**	
Static-Active	4.00	> 1.5	2.56	> 1.5
Seismic-Active (0.3g)	1.52	> 1.0	1.35	> 1.0
Seismic-Active (0.4g)	1.25	> 1.0	1.22	> 1.0
Seismic-Active (0.5g)	1.05	> 1.0	1.16	> 1.0

The scaled model was established with a scale factor of 1/25. The scaling factor was selected depending on the dimensions of the rigid-sided soil box. The scaled model dimensions were determined using scaling relations proposed by Iai (1989) and developed by Muir Wood et al. (2002) and Muir Wood (2004).

5.3.2.1. Scaling Relations. In this study, the prototype wall was scaled to 1/25, which is expressed by 'n'. Many variables of the prototype wall were scaled. These relations were obtained from the similitude method proposed by Iai (1989). The scaling factors are given in Table 5.4.

Table 5.4. The scale factor for the 1g shaking table test [93].

Variable	For 1g Model	Scale Factor
Length	n	25
Density	1	1
Stiffness	$n^{0.5}$	5
Acceleration	1	1
Velocity	$n^{0.5}$	5
Displacement	n	25
Stress	n	25
Strain	1	1
Dynamic Time	$n^{0.5}$	5
Frequency	$1/n^{0.5}$	1/5

5.3.2.2. Determination of The Dimensions of Retaining Wall Model. The following step was scaling the prototype wall dimensions in order to conduct a shake table test on a small-scale model. The model wall was established by scaling the prototype wall using a scale factor of 1/25. While the material of the prototype wall was selected as concrete, the model wall was established using aluminum because it cannot be constructed using concrete in smaller dimensions. According to Muir Wood (2004), the thickness of the aluminum model wall can be

calculated from the correlation depending on the prototype wall dimensions and Young's modulus for 1-g modeling. These scaling correlations are expressed as

$$t_m = t_p \left(\frac{E_p}{E_m}\frac{1}{n^{3+\alpha}}\right)^{\frac{1}{3}}, \quad (5.1)$$

where t_m is the thickness of the model wall, t_p is the thickness of the prototype wall, E_m is Young's modulus of the model wall, E_p is Young's modulus of the prototype wall.

In this study, α was selected as 0.5 since the backfill consists of sandy materials. E_p is Young's modulus of concrete which is equal to 20 GPa, and E_m is Young's modulus of aluminum which is equal to 70 GPa (Muir Wood, 2004). Additionally, the value of t_p was selected as 0.35, which was illustrated in Figure 5.2. When the equation was solved, t_m was determined as 5 mm. The thickness and other scaled dimensions were controlled by hand calculations based on the methods of Coulomb, Rankine, and Mononobe-Okabe. The calculated factor of safety values for overturning and sliding is shown in Table 5.5.

Table 5.5. The safety factors of the scaled wall model for the methods of Coulomb, Rankine, and Mononobe-Okabe (M-O).

Method	**$FS_{(overturning)}$**		**$FS_{(sliding)}$**	
Coulomb	4.58	≥ 1.5	1.72	≥ 1.5
Rankine	4.11	≥ 1.5	1.54	≥ 1.5
M-O (a_{max}=0.3g)	4.08	> 1.3	1.11	> 1.1

The dimensions of the model wall which were used in the experimental test setup are depicted in Figure 5.4.

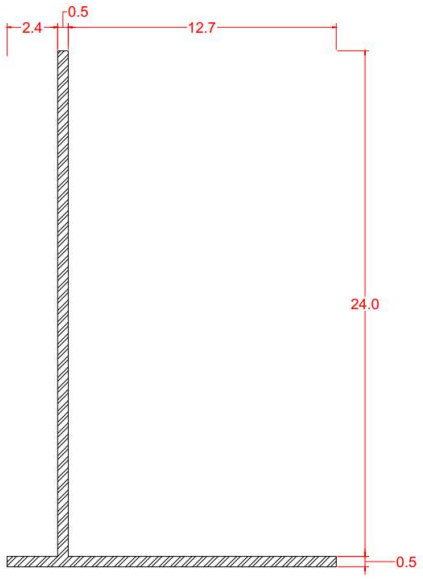

Figure 5.4. The determined dimensions of the scaled wall model.

The test setup of the retaining wall was established in the rigid-sided soil box. The experimental setup is illustrated in Figure 5.5, and the picture of experimental setup is given in Figure 5.6. The cushion consisting of EPS geofoam and tire crumb and sand mixture were placed behind the wall with different thicknesses and densities in order to study the effect of inclusion layer properties on the seismic behavior of the cantilever retaining wall with cohesionless and dry backfill.

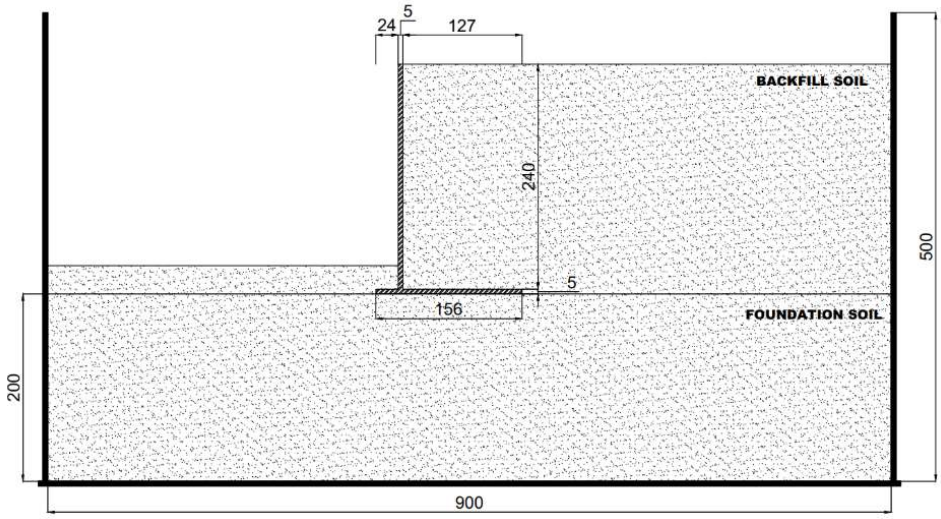

Figure 5.5. The 1/25 scaled retaining wall test setup.

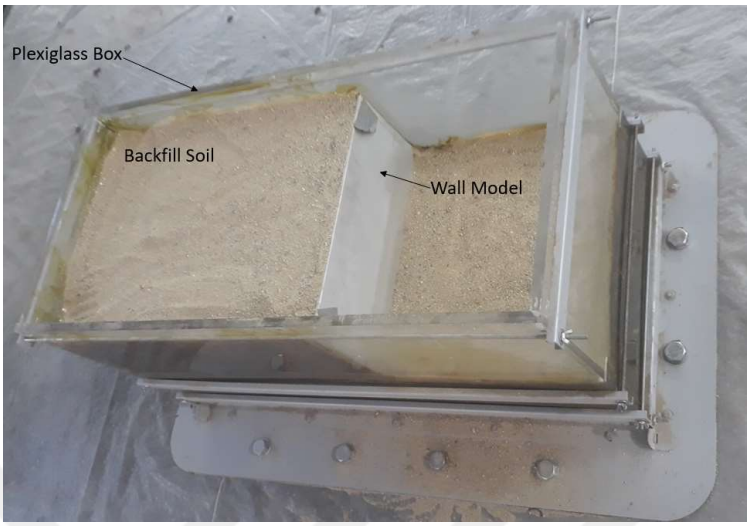

Figure 5.6. The picture of the experimental setup.

5.3.2.3. Fundamental Frequency of Retaining Wall. The equations proposed by Matsuo and Ohara (1960), Scott (1973), Richardson and Lee (1975), Richardson (1978), and Wu (1994) were used to determine the fundamental frequency of the wall system [96].

Matsuo and Ohara (1960) have suggested a solution to evaluate the fundamental frequency of soil-wall systems for two different presumptions (no vertical displacement, v=0, and no vertical stress, σ_v=0). The fundamental frequency (f_{11}) was expressed as

$$f_{11} = f_1 . GF \tag{5.2}$$

where f_1 is the frequency of infinitely long and uniform soil (1D approach) and GF is a geometric factor for the expression of the two-dimensional effect of soil with restricted width. The frequency of soil in the one-dimensional approach was determined as

$$f_1 = \frac{1}{4H}\sqrt{\frac{G}{\rho}}\,. \tag{5.3}$$

In this expression, H is the height of the wall, G is the shear modulus of the backfill soil, and ρ is the density of the backfill soil. The geometric factor for cases i and ii was defined, respectively, as

$$GF_{v=0} = \sqrt{1 + \frac{8(1-v)}{1-2v}\left(\frac{H}{B}\right)^2} \tag{5.4}$$

$$GF_{\sigma_v=0} = \sqrt{1 + \frac{2-v}{1-v}\left(\frac{H}{B}\right)^2} \tag{5.5}$$

where v is Poisson's ratio of the backfill soil and B is the width of the backfill soil. The fundamental frequency equation belonging to Scott (1973) was similar to Equation 5.2. However, the geometric factor was different from the equation of Matsuo and Ohara (1960). The geometric factor of Scott (1973) can be written as

$$GF_S = \sqrt{1 + \frac{64}{\pi^2}\left(\frac{1-v}{1-2v}\right)\left(\frac{H}{B}\right)^2}\,. \tag{5.6}$$

Additionally, Equation 5.2 was also used by Wu (1994). The geometric factor was written by Wu (1994) as

$$GF_W = \sqrt{1 + \left(\frac{2}{1-v}\right)\left(\frac{H}{B}\right)^2}\,. \tag{5.7}$$

Richardson and Lee (1975) have suggested the equation to determine the fundamental period (T_1) of the retaining wall supporting reinforced backfill soil. The fundamental period can be written as

$$T_1 = 0.020H \; to \; 0.033H. \tag{5.8}$$

Richardson (1978) has proposed the equation for the evaluation of the fundamental frequency of the retaining wall supporting reinforced backfill soil. The fundamental frequency can be expressed as

$$f_{11} = \frac{38.1}{H}\,. \tag{5.9}$$

The aforementioned equations were used in order to determine the fundamental frequency of the retaining wall system established for this study. The calculated fundamental frequencies of the full-scale wall for different equations are given in Table 5.6. The fundamental frequency of the scaled wall was determined using the scaling relations of Iai (1989), as shown in Table 5.7.

Table 5.6. The fundamental frequencies of the prototype wall based on different researchers.

The Method	Frequency (Hz)
Matsuo and Ohara, 1960 - case (i)	10.38
Matsuo and Ohara, 1960 - case (ii)	5.59
Scott, 1973	9.50
Wu, 1994	5.84
Richardson and Lee (1975)	6.32
Richardson (1978)	6
Average	**7.27**

Table 5.7. The fundamental frequencies of the scaled wall based on different researchers.

The Method	Frequency (Hz)
Matsuo and Ohara, 1960 - case (i)	51.91
Matsuo and Ohara, 1960 - case (ii)	27.95
Scott, 1973	47.52
Wu, 1994	29.19
Richardson and Lee (1975)	31.62
Richardson (1978)	30
Average	**36.37**

5.3.3. Sand

The experiments were performed using dry, cohesionless sand, which is called “Silivri Sand.” This sand is regionally located in Istanbul. The grain size distribution of Silivri sand was determined based on ASTM Standards of D422 and D6913, as given in Figure 5.7. The uniformity coefficient (C_u) and the curvature coefficient (C_c) were calculated as 2.68 and 1.06, respectively. According to United Soil Classification System (USCS), Silivri sand is classified as poorly graded sand (SP). Additionally, the bulk unit weight of sand is 16.5 kN/m^3.

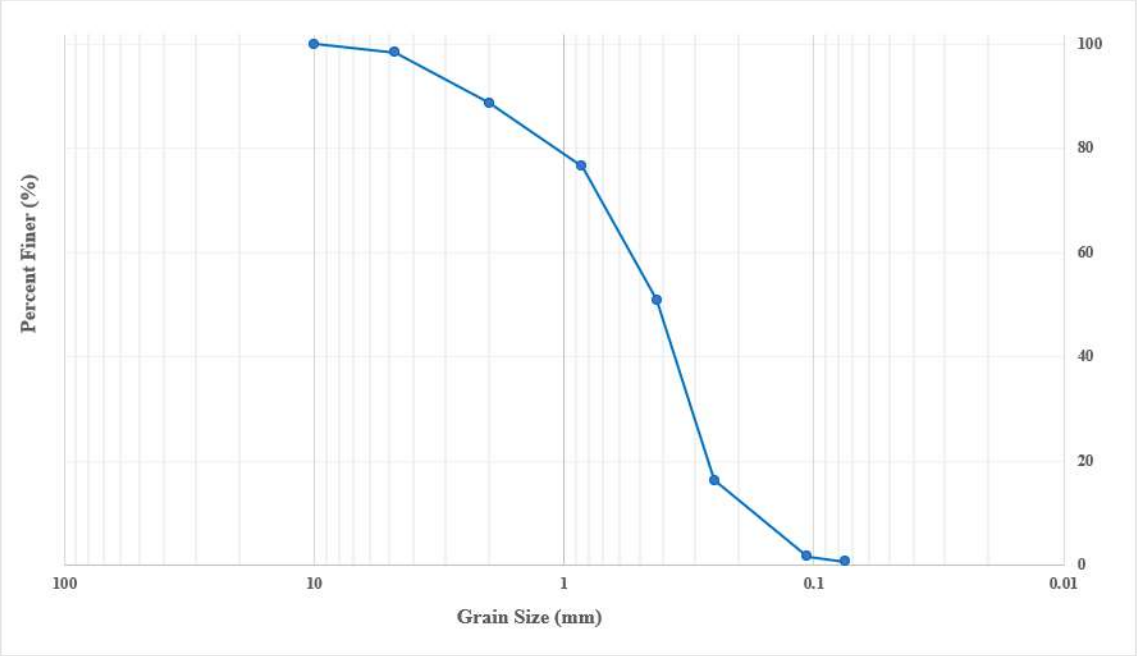

Figure 5.7. The grain size distribution of Silivri Sand.

5.3.4. EPS Geofoam

In this study, EPS geofoam with densities of 10 and 20 kg/m^3 were used, and they were named EPS10 and EPS20, respectively. The properties of EPS geofoam are usually determined with correlations based on their densities. Elastic moduli of EPS geofoam were calculated by calculating the arithmetic mean of the valued determined as [64,71]

$$E_g = 0.45\rho_{EPS} - 3.0 \quad (5.10)$$

$$E_g = 16.431 - 1.645\rho_{EPS} + 0.061{\rho_{EPS}}^2 \quad (5.11)$$

$$E_g = 0.1284{\rho_{EPS}}^{1.368} \quad (5.12)$$

$$E_g = 0.82\rho_{EPS} - 49 \quad (5.13)$$

$$E_g = 0.41\rho_{EPS} - 2.8 \quad (5.14)$$

where E_g is elastic modulus of EPS, ρ_{EPS} is density of EPS.

The correlations were proposed by Hovarth (1995), Duskov (1997a), Duskov (1997b), Negussey and Anasthas (2001), and Hazarika (2006), respectively. The calculated elastic modulus values and determined elastic moduli of each EPS type are given in Table 5.8.

Table 5.8. The calculated elastic modulus of EPS10, EPS20, and EPS30.

EPS Type	EPS10	EPS20	EPS30
Density of EPS (kg/m^3)	10	20	30
Horvath, 1995	1.5	6	10.5
Duskov, 1997a	6.1	7.9	22.0
Duskov, 1997b	3.0	7.7	13.5
Negussey and Anasthas, 2001	3.3	11.5	19.7
Hazarika, 2006	1.3	5.4	9.5
Average	3.04	7.7	15.04
Selected Elastic modulus (MPa)	3	7.7	15

The EPS geofoam was prepared by cutting with the same dimensions of the wall stem (0.24*0.40 m), and the thicknesses of the EPS geofoam were selected as 2 and 4 cm for the experiments, which corresponds to 50 and 100 cm at the full-scale model. The utilized cushion layers in tests, as shown in Figure 5.8.

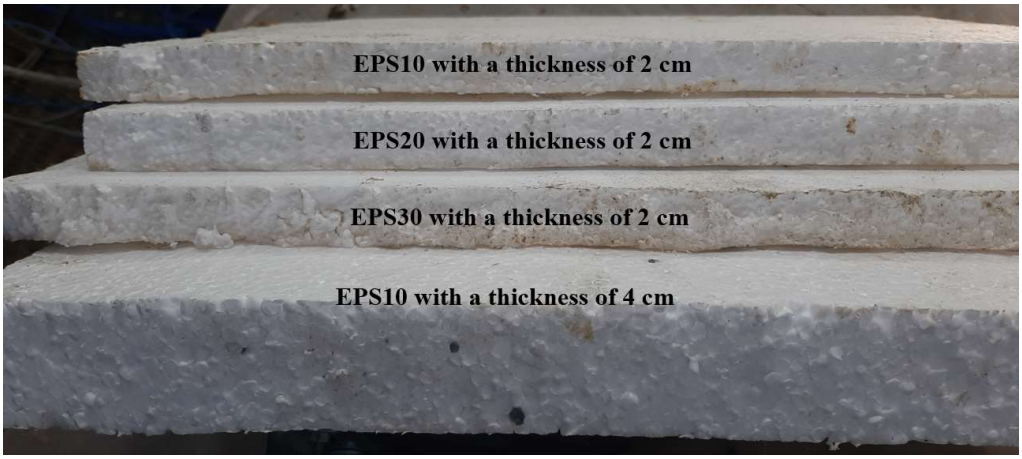

Figure 5.8. The EPS geofoam cushion used in experiments.

5.3.5. Tire Crumbs

The grain size distribution of tire crumb, determined based on ASTM Standards of D422 and D6913, is given in Figure 5.9. The tire waste material is illustrated in Figure 5.10. In this thesis, as a cushion material, the tire crumb and sand were mixed with different ratios. The tire contents of mixtures were selected as 10%, 20%, and 30% by weight. Additionally, the mixtures were named TC10, TC20, and TC30, according to their tire contents. The unit weights of TC10, TC20, and TC30 were determined as 14.5 kN/m^3, 13.3 kN/m^3, and 12.5 kN/m^3 by Çağatay (2008), respectively. The shear strength parameters of sand-tire crumb mixtures given in Table 4.8 were evaluated by Edinçliler et al. (2010). The tire waste-sand mixture was placed behind the 1/25 scaled wall at a thickness of 2 and 4 cm. These thicknesses correspond to 50 and 100 cm at the prototype wall.

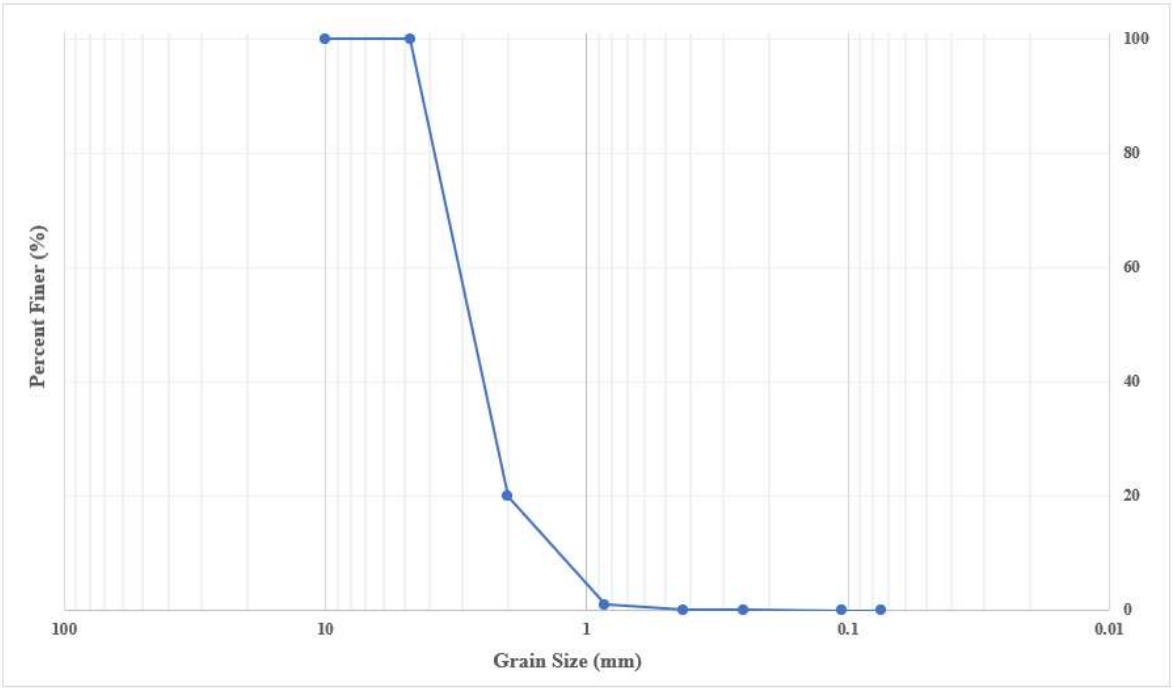

Figure 5.9. The grain size distribution of tire crumb.

Figure 5.10. Tire crumb used in mixtures.

The cushion layer consisting of tire waste-sand mixture was placed behind the wall using a 1.5 mm thick solid polycarbonate plate. The polycarbonate plate was placed 2 or 4 cm behind the wall, and the mixture was filled between the polycarbonate plate and the aluminum model wall. After the tire crumb-sand mixture and the backfill soil were completely filled, the solid polycarbonate plate was slowly pulled.

5.4. Input motions

The selected input motions can be divided into two groups, such as real earthquake recordings and harmonic motions. The properties of sinusoidal motions and actual earthquake records are tabulated in Table 5.9.

Table 5.9. The properties of base excitations applied to a scaled model.

Name of Input	PGA (g)	Frequency (Hz)	Duration (sec)
İzmit-F	0.124	-	6
İzmit-N	0.22	-	6
İzmir-F	0.183	-	12.5
El-Centro	0.318	-	6.24
Kobe	0.823	-	9.6
Sinusoidal	0.4	5	30
Sinusoidal	0.4	10	30
Sinusoidal	0.4	15	30
Sinusoidal	0.3	10	30
Sinusoidal	0.5	10	30

The motions in the first group include varying amplitudes (0.3g - 0.5g) and varying frequencies (5 Hz – 15 Hz). In accordance with the scaling laws of Iai (1989) mentioned in Section 5.2.1.1., the acceleration of motion does not need to be scaled, while the frequency of harmonic excitation does. Therefore, the frequency values of harmonic base excitations (5, 10, and 15 Hz) correspond to 1, 2, and 3 Hz, respectively, at the full-scale model, and the acceleration values remain unchanged. It must be noted that the frequencies were selected as 1, 2, and 3 Hz for the prototype wall since the motions with frequency content between 2 and 3 Hz represent actual earthquakes with medium and high-frequency content [104].

In the second group, there are actual earthquake recordings, such as Kocaeli Earthquake (August 17, 1999, M_w=7.4), El-Centro Earthquake (May 14, 1940, M_w=6.9), Kobe Earthquake (January 17, 1995, M_w=6.9), and İzmir Earthquake (October 30, 2020, M_w=6.9). They are time-scaled based on the similitude laws by Iai (1989). Of these acceleration-time histories, two of them are far-field earthquakes, and the others are near-field earthquakes. The motions are expressed using some abbreviations in Table 5.9. They can be explained as follows:

- İzmit-F= The far-field recording of Kocaeli Earthquake measured from the station located in İznik,

- İzmit-N= The near-field recording of Kocaeli Earthquake measured from the station located in İzmit,
- İzmir-F= The far-field recording of İzmir Earthquake taken measured the station located in Kuşadası,

The acceleration-time histories of time-scaled actual earthquakes and scaled sinusoidal motions are given between Figures 5.11 and 5.20.

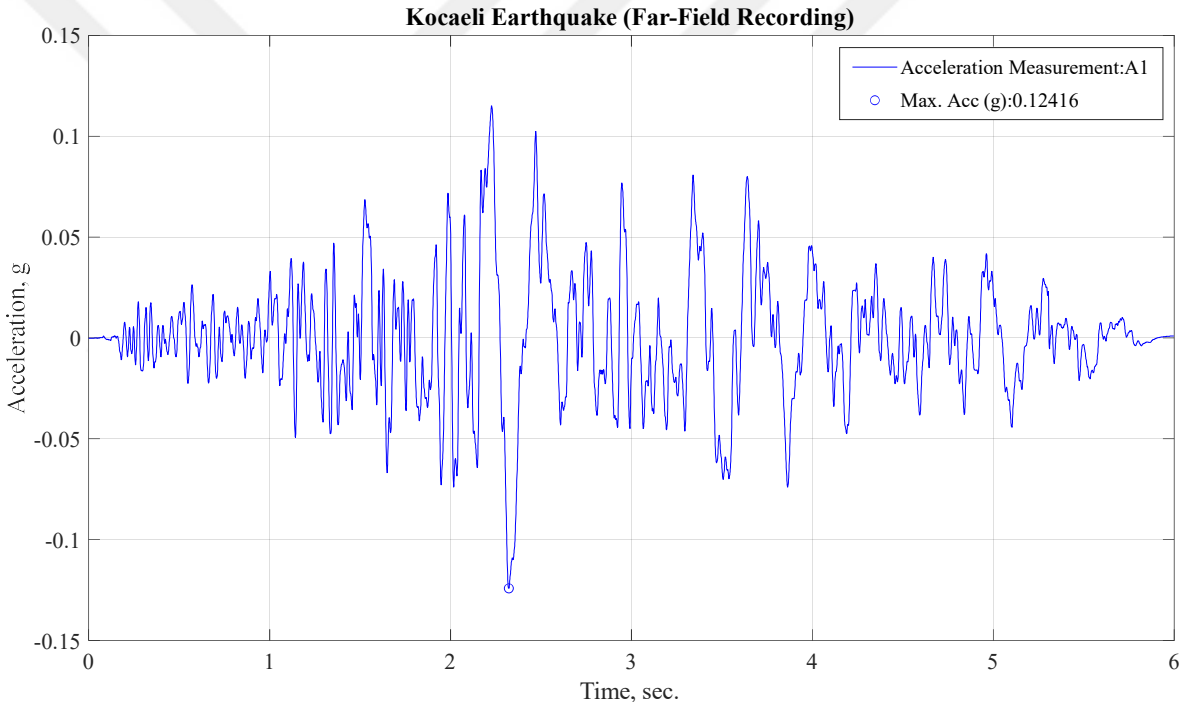

Figure 5.11. The acceleration-time history of Kocaeli Earthquake (far-field).

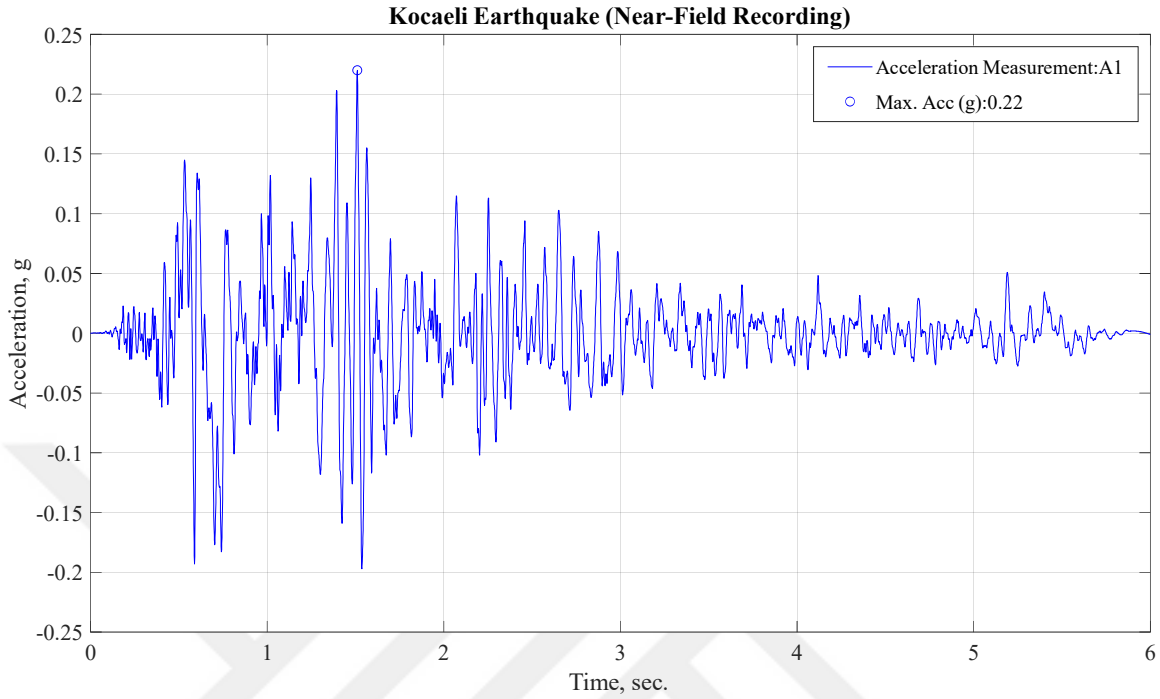

Figure 5.12. The acceleration-time history of Kocaeli Earthquake(near- field).

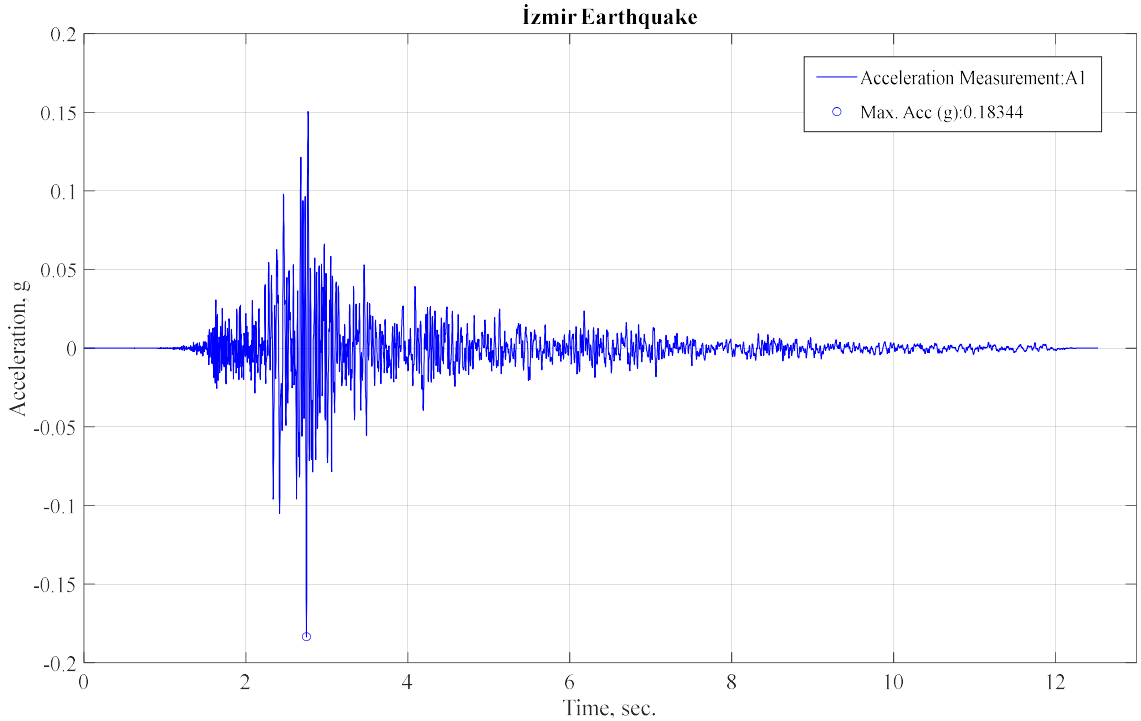

Figure 5.13. The acceleration-time history of İzmir Earthquake (far-field).

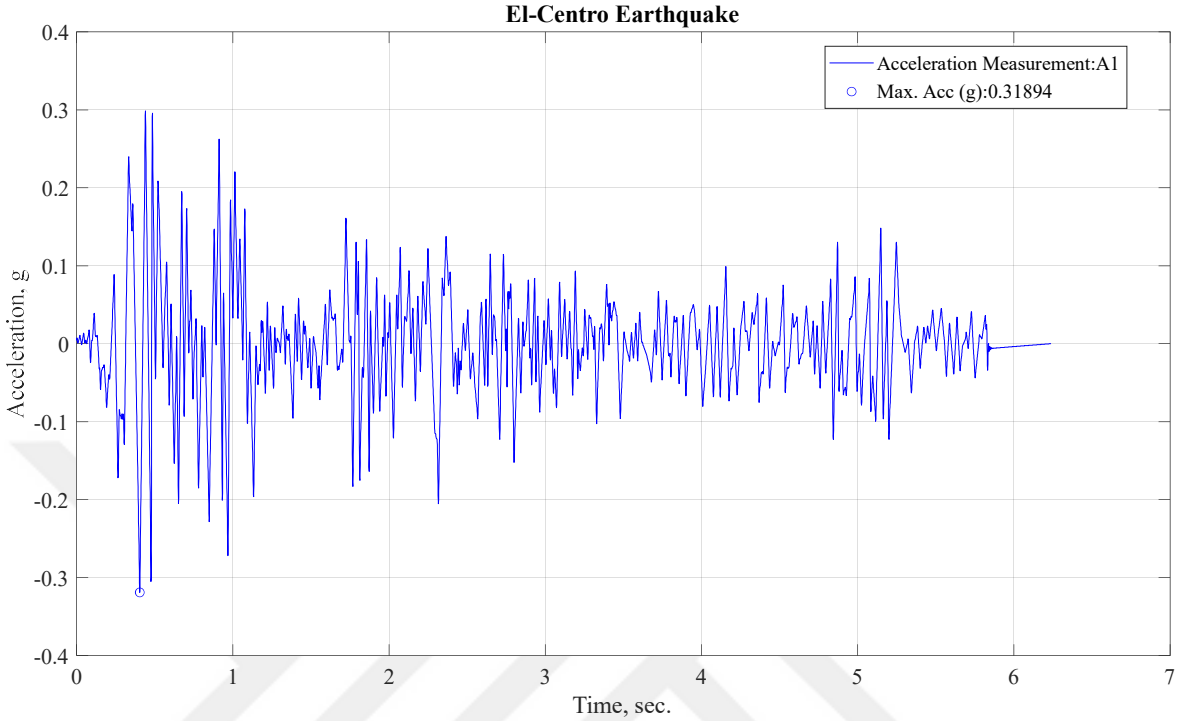

Figure 5.14. The acceleration-time history of El-Centro Earthquake (near-field).

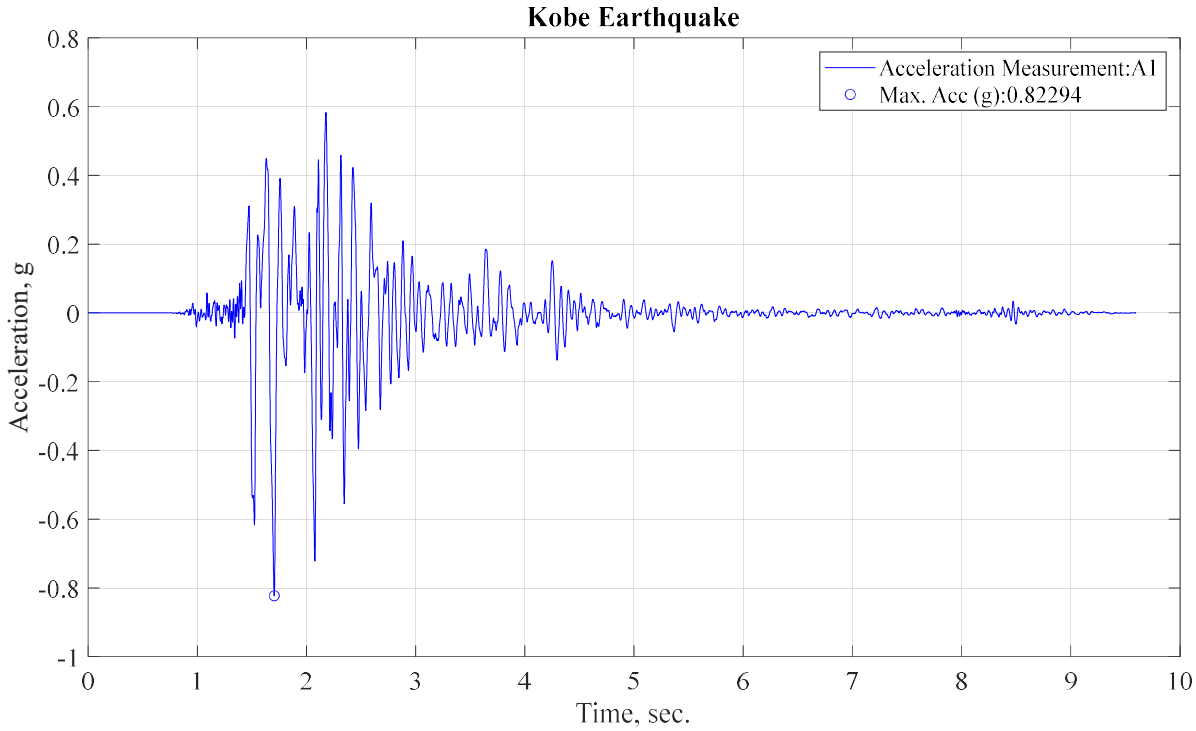

Figure 5.15. The acceleration-time history of Kobe Earthquake (near-field).

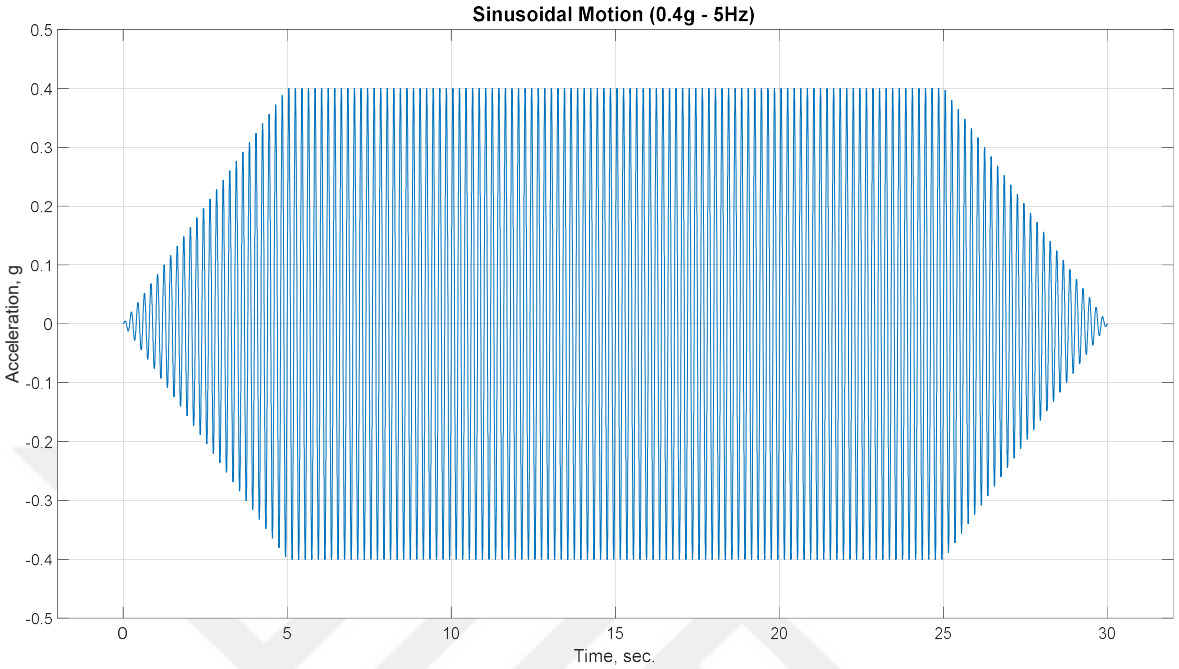

Figure 5.16. The sinusoidal motion (0.4g - 5 Hz).

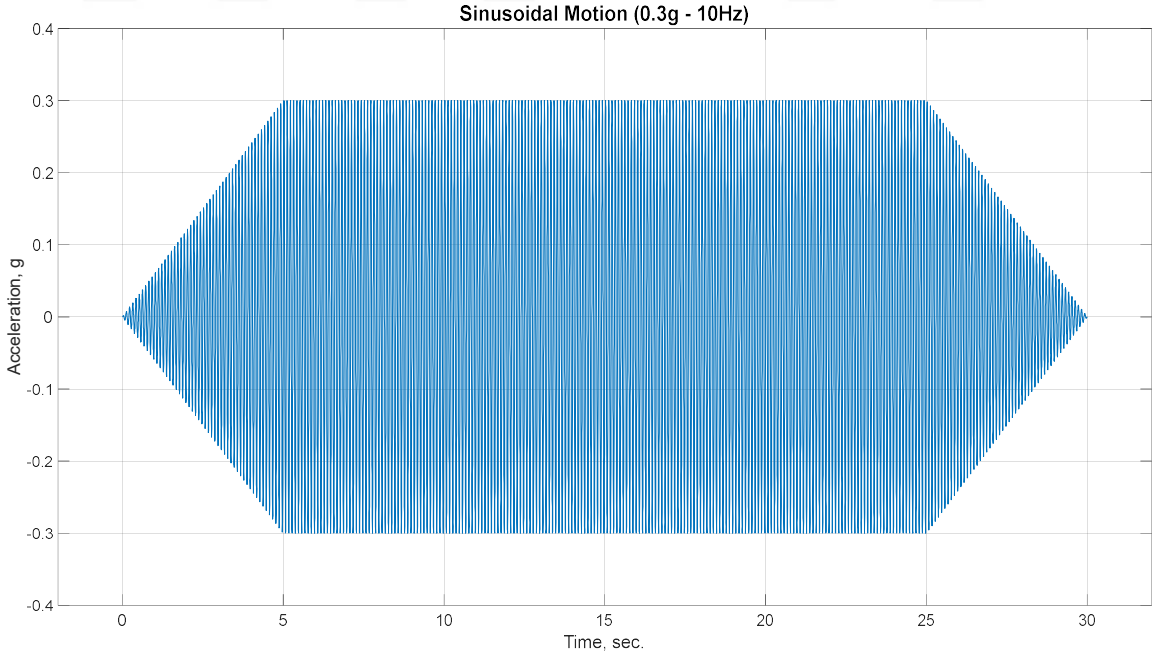

Figure 5.17. The sinusoidal motion (0.3g - 10 Hz).

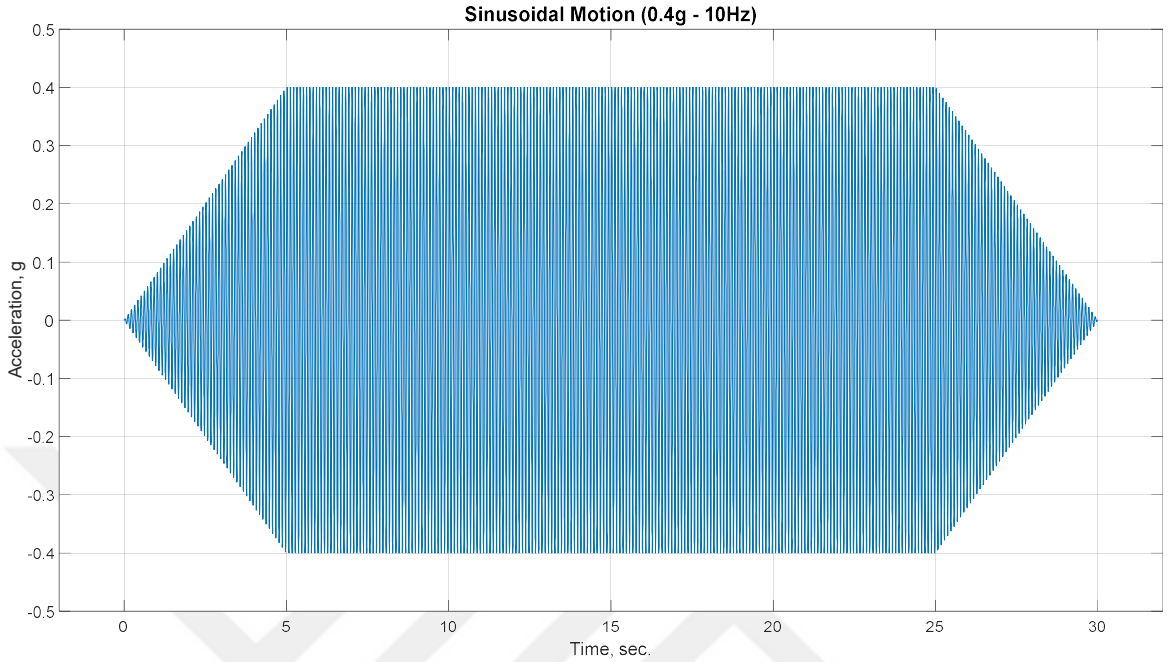

Figure 5.18. The sinusoidal motion (0.4g - 10 Hz).

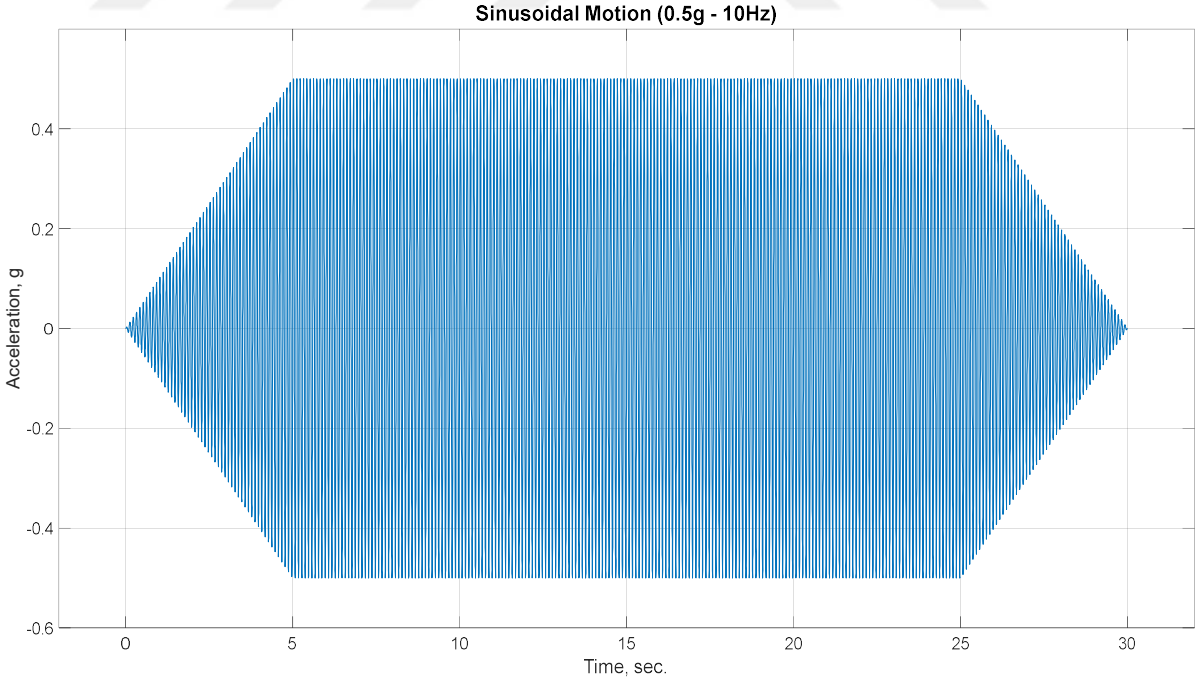

Figure 5.19. The sinusoidal motion (0.5g - 10 Hz).

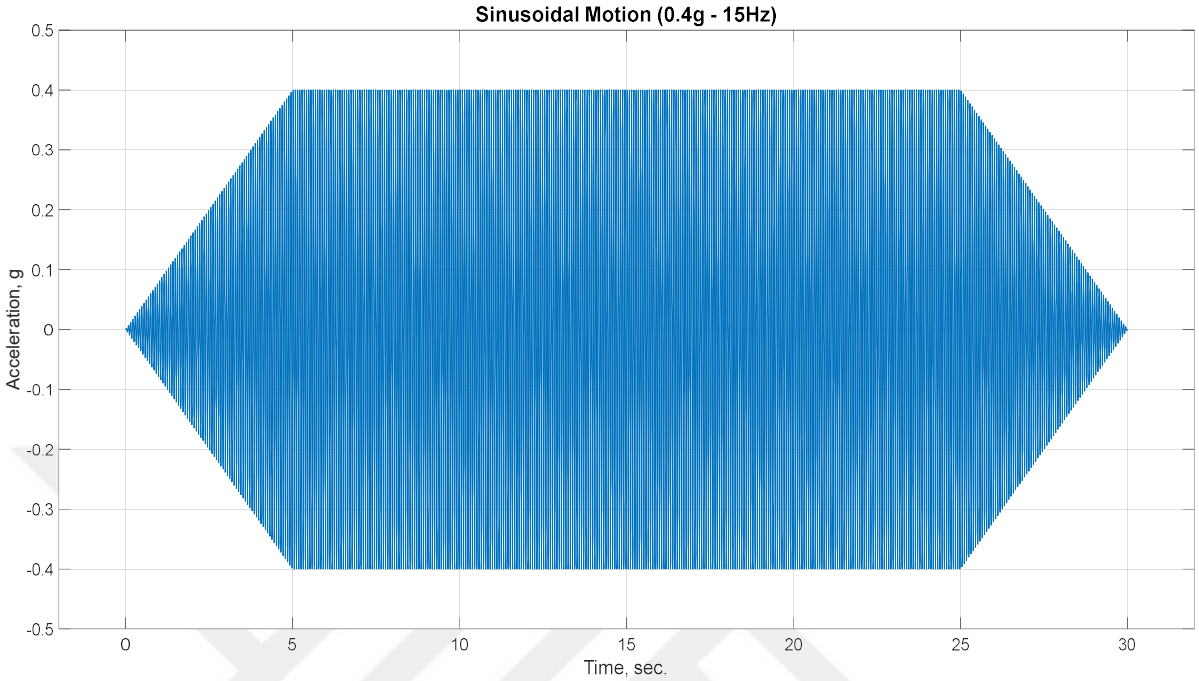

Figure 5.20. The sinusoidal motion (0.4g - 15 Hz).

5.5. Shaking Table Experimental Setup and Instrumentation

This section consists of the instrumentation used, the preparation of the experimental setup.

5.5.1. Preparation of Retaining Wall Model

In the first step, the plexiglass box was mounted on the shake table, and it was fixed using screws and nuts. Then, the inner surfaces of the plexiglass box were covered with grease oil in order to imitate actual field conditions adequately, eliminate the reflection of motion waves on the box surfaces, and prevent the boundary conditions, as shown in Figure 5.21.

Figure 5.21. The application of grease oil on the inner surface of a rigid box.

After the application of grease oil, the retaining wall system was established with or without a cushion layer consisting of EPS geofoam and sand-tire crumb mixture on a scale of 1/25. The sand backfill was compacted to obtain a unit weight of 16.5 kN/m^3. In Figure 5.22, the experimental setup with the cushion layers was illustrated. The eleven different cases were investigated by physical testing methods. Of the models used in experiments, one of them was unimproved case with the sand backfill, while the others were improved cases where the EPS geofoam and tire waste-sand mixtures were included behind the model wall as a cushion layer.

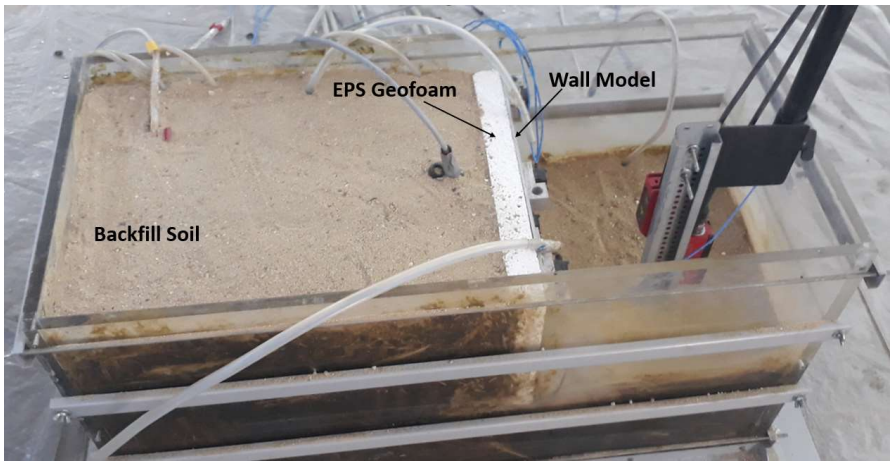

Figure 5.22. The 1/25 scaled wall model with the application of EPS geofoam cushion.

5.5.2. Instrumentation of Test Setup

Sixteen accelerometers (A) and three displacement sensors (D) were used for the instrumentation of the model, as demonstrated in Figures 5.23 and 5.24. The instrumented retaining wall model is illustrated in Figure 5.25.

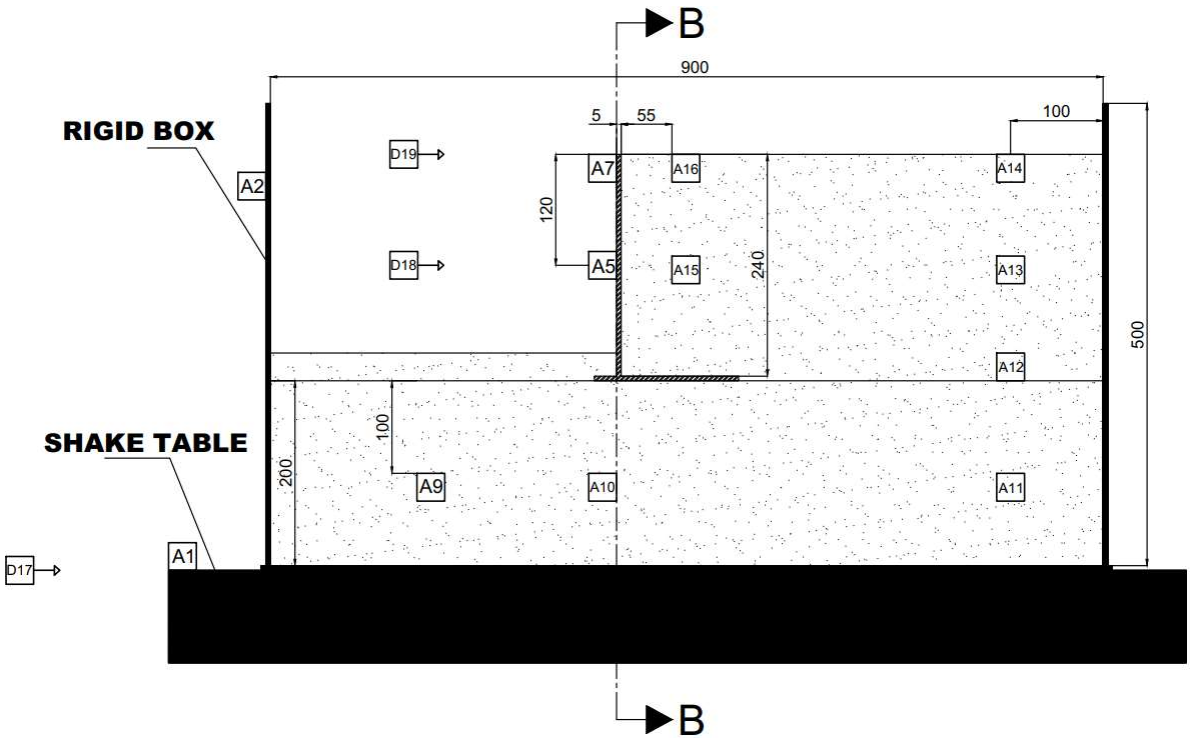

Figure 5.23. The side view of the instrumented experimental setup.

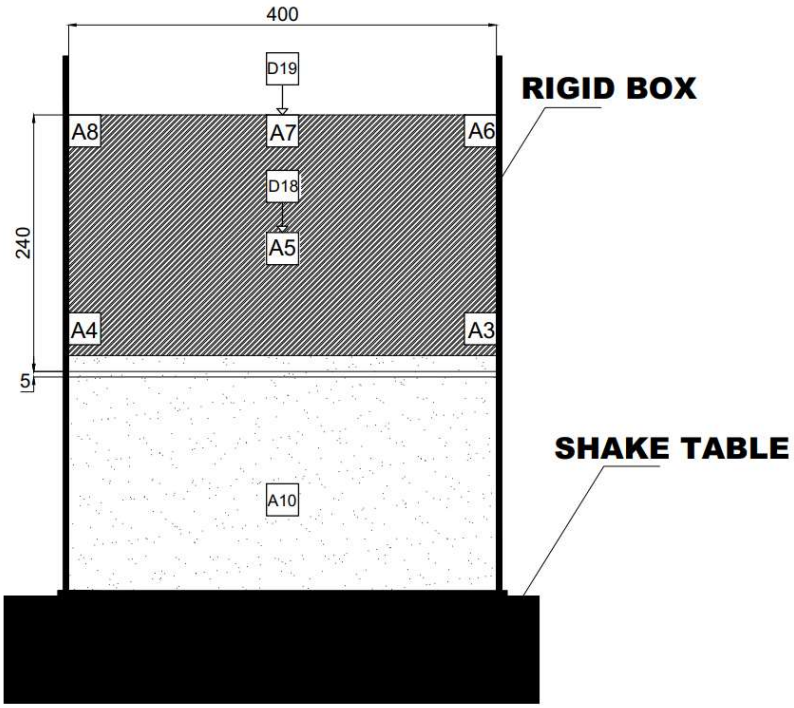

Figure 5.24. The cross-section (B-B) of the experimental setup.

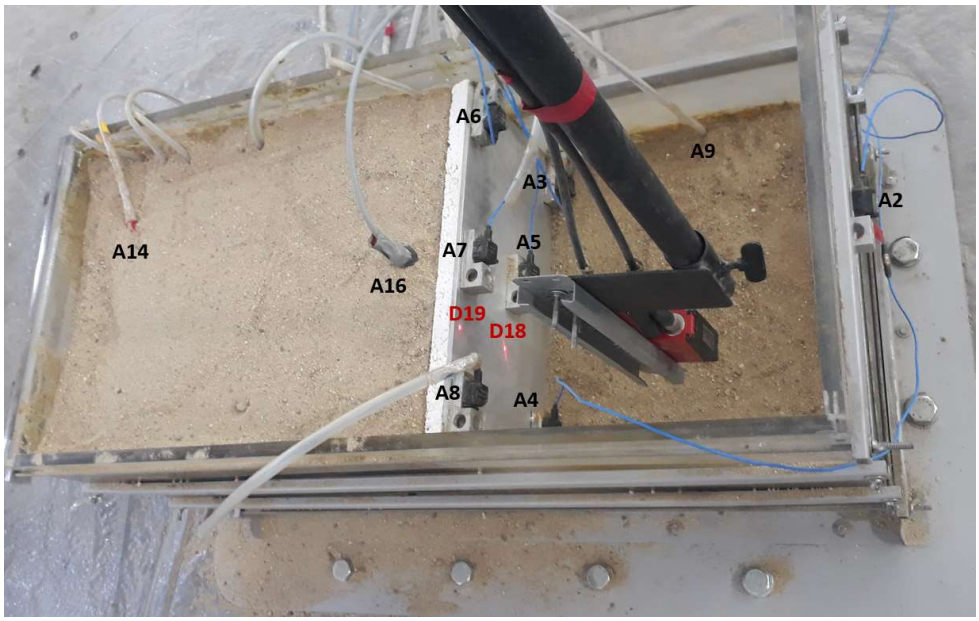

Figure 5.25. The picture of instrumented experimental setup.

As given in Figures 5.23 and 5.24, A1 was located on the shake table which records input motion applied to the models, and A2 was placed outside of the plexiglass box. While eight of the accelerometers were located within the foundation and backfill soil, six of them were installed on the front of the wall. A9, A10, and A11 were placed within the foundation soil and at approximately the same level. A12 was placed at the same level as the base of the model wall. A5 was positioned at nearly the same level as A15 and A13; however, A5 was placed on the wall, while others were placed within the backfill soil. A7 was positioned near the top of the model wall, whereas A16 and A14 were placed close to the surface of the backfill. The displacement sensor, D17, was placed to measure the displacement of the shake table. Two displacement sensors were placed to measure the movements occurring at the top and half height of the wall. Additionally, the sensors, D19 and D18, were positioned close to A7 and A5, respectively.

After the shaking table test setup was completed, the experimental setup was vibro-compacted by applying the sinusoidal motion with a 9 Hz frequency and a 0.2g amplitude for 90 seconds, shown in Figure 5.26, before the test setup was shaken with the input motions.

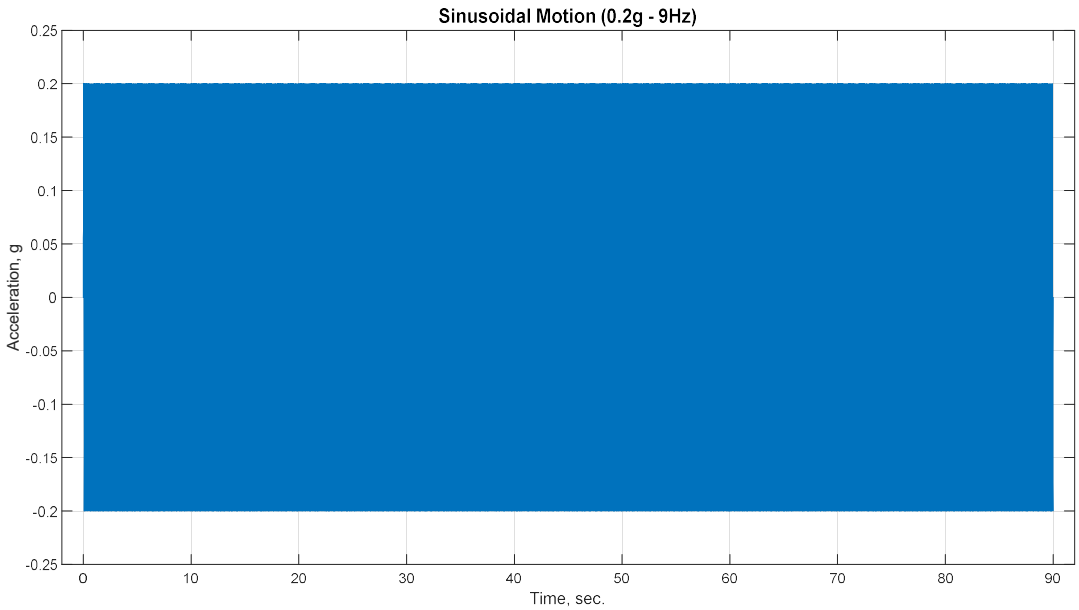

Figure 5.26. The sinusoidal motion used for vibro-compaction.

6. EXPERIMENTAL RESULTS

6.1. Shake Table Tests

This study investigates the effects of cushion type on the seismic performance of the retaining wall. Eleven cases were studied in this thesis. In the first case (Case 1), the backfill consisted of only sand, which is an unimproved case. The cushion layer was not applied in this case, while the others were built with a cushion layer behind the wall. Therefore, the cushions were established using EPS geofoam with different densities and thicknesses and sand-tire crumb mixture with different thicknesses and mixture ratios. The unimproved case and the cases established with different cushion inclusion are illustrated in Table 6.1.

Table 6.1. The classification and illustration of experimental setups.

Case No	Cushion Type	The Picture of Cases
Case 1	-	
Case 2	EPS10 (t=2 cm)	

Table 6.1. The classification and illustration of experimental setups. (cont.)

Case 3	EPS10 (t=4 cm)	
Case 4	EPS20 (t=2 cm)	
Case 5	EPS30 (t=2 cm)	
Case 6	TC10 (t=2 cm)	
Case 7	TC10 (t=4 cm)	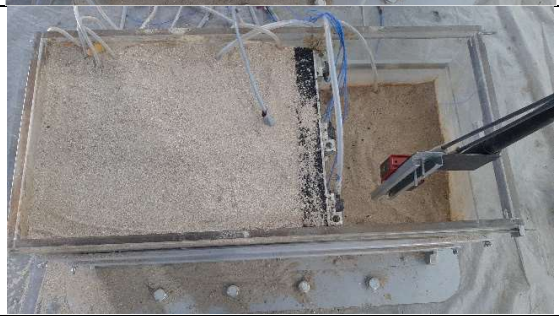

Table 6.1. The classification and illustration of experimental setups. (cont.)

Case 8	TC20 (t=2 cm)	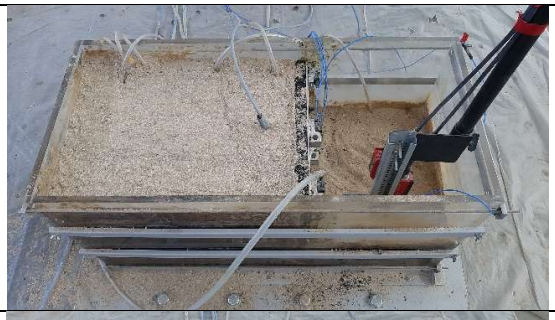
Case 9	TC20 (t=4 cm)	
Case 10	TC30 (t=2 cm)	
Case 11	TC30 (t=4 cm)	

The eleven different test setup was subjected to input motions with different characteristics. The investigated parameters are given in Table 6.2. Additionally, the details of the experimental program conducted using EPS geofoam and sand-tire crumb mixture were given in Tables 6.3 and 6.4, respectively.

Table 6.2. The investigated parameters in this study.

Parameters	**Values of Types**
Cushion Type	EPS geofoam and Sand-Tire crumb mixture
Thickness of Cushion (t_c)	2 cm and 4 cm
Density of EPS Geofoam	10, 20, and 30 kg/m^3 (EPS10, EPS20, EPS30)
Mixture Ratio of Tire Crumb	10%, 20%, and 30% (TC10, TC20, TC30)
Input Motion Characteristics	İzmit-F, İzmir-F, İzmit-N, El-Centro, and Kobe Earthquakes
Amplitude of Sinusoidal Motions	0.3g, 0.4g, and 0.5g
Frequency of Sinusoidal Motions	5, 10, and 15 Hz

Table 6.3. The experiment program used EPS geofoam.

Case No	**Test No**	**Input Motion**	**PGA (g)**	**Frequency (Hz)**	**Inclusion Type**	**Thickness of Cushion**
Case 1	1	Sinusoidal	0.3	5	None	-
	2	Sinusoidal	0.3	10	None	-
	3	Sinusoidal	0.3	15	None	-
	4	Sinusoidal	0.4	10	None	-
	5	Sinusoidal	0.5	10	None	-
	6	İzmit-F	0.124	-	None	-
	7	İzmir-F	0.183	-	None	-
	8	İzmit-N	0.22	-	None	-
	9	El-Centro	0.318	-	None	-
	10	Kobe	0.823	-	None	-
Case 2	11	Sinusoidal	0.3	5	EPS10	2 cm
	12	Sinusoidal	0.3	10	EPS10	2 cm
	13	Sinusoidal	0.3	15	EPS10	2 cm
	14	Sinusoidal	0.4	10	EPS10	2 cm
	15	Sinusoidal	0.5	10	EPS10	2 cm
	16	İzmit-F	0.124	-	EPS10	2 cm
	17	İzmir-F	0.183	-	EPS10	2 cm
	18	İzmit-N	0.22	-	EPS10	2 cm
	19	El-Centro	0.318	-	EPS10	2 cm
	20	Kobe	0.823	-	EPS10	2 cm
Case 3	21	Sinusoidal	0.3	5	EPS10	4 cm
	22	Sinusoidal	0.3	10	EPS10	4 cm
	23	Sinusoidal	0.3	15	EPS10	4 cm
	24	Sinusoidal	0.4	10	EPS10	4 cm
	25	Sinusoidal	0.5	10	EPS10	4 cm

Table 6.3. The experiment program used EPS geofoam. (cont.)

Case 3	26	İzmit-F	0.124	-	EPS10	4 cm
	27	İzmir-F	0.183	-	EPS10	4 cm
	28	İzmit-N	0.22	-	EPS10	4 cm
	29	El-Centro	0.318	-	EPS10	4 cm
	30	Kobe	0.823	-	EPS10	4 cm
Case 4	31	Sinusoidal	0.3	5	EPS20	2 cm
	32	Sinusoidal	0.3	10	EPS20	2 cm
	33	Sinusoidal	0.3	15	EPS20	2 cm
	34	Sinusoidal	0.4	10	EPS20	2 cm
	35	Sinusoidal	0.5	10	EPS20	2 cm
	36	İzmit-F	0.124	-	EPS20	2 cm
	37	İzmir-F	0.183	-	EPS20	2 cm
	38	İzmit-N	0.22	-	EPS20	2 cm
	39	El-Centro	0.318	-	EPS20	2 cm
	40	Kobe	0.823	-	EPS20	2 cm
Case 5	41	Sinusoidal	0.3	5	EPS30	2 cm
	42	Sinusoidal	0.3	10	EPS30	2 cm
	43	Sinusoidal	0.3	15	EPS30	2 cm
	44	Sinusoidal	0.4	10	EPS30	2 cm
	45	Sinusoidal	0.5	10	EPS30	2 cm
	46	İzmit-F	0.124	-	EPS30	2 cm
	47	İzmir-F	0.183	-	EPS30	2 cm
	48	İzmit-N	0.22	-	EPS30	2 cm
	49	El-Centro	0.318	-	EPS30	2 cm
	50	Kobe	0.823	-	EPS30	2 cm

Table 6.4. The experiment program used tire crumb and sand mixture.

Case No	Test No	Input Motion	PGA (g)	Frequency (Hz)	Inclusion Type	Thickness of Cushion
Case 1	1	Sinusoidal	0.3	5	None	-
	2	Sinusoidal	0.3	10	None	-
	3	Sinusoidal	0.3	15	None	-
	4	Sinusoidal	0.4	10	None	-
	5	Sinusoidal	0.5	10	None	-
	6	İzmit-F	0.124	-	None	-
	7	İzmir-F	0.183	-	None	-
	8	İzmit-N	0.22	-	None	-
	9	El-Centro	0.318	-	None	-
	10	Kobe	0.823	-	None	-
Case 6	11	Sinusoidal	0.3	5	TC10	2 cm
	12	Sinusoidal	0.3	10	TC10	2 cm
	13	Sinusoidal	0.3	15	TC10	2 cm
	14	Sinusoidal	0.4	10	TC10	2 cm
	15	Sinusoidal	0.5	10	TC10	2 cm
	16	İzmit-F	0.124	-	TC10	2 cm
	17	İzmir-F	0.183	-	TC10	2 cm
	18	İzmit-N	0.22	-	TC10	2 cm
	19	El-Centro	0.318	-	TC10	2 cm
	20	Kobe	0.823	-	TC10	2 cm
Case 7	21	Sinusoidal	0.3	5	TC10	4 cm
	22	Sinusoidal	0.3	10	TC10	4 cm
	23	Sinusoidal	0.3	15	TC10	4 cm
	24	Sinusoidal	0.4	10	TC10	4 cm
	25	Sinusoidal	0.5	10	TC10	4 cm
	26	İzmit-F	0.124	-	TC10	4 cm
	27	İzmir-F	0.183	-	TC10	4 cm
	28	İzmit-N	0.22	-	TC10	4 cm
	29	El-Centro	0.318	-	TC10	4 cm
	30	Kobe	0.823	-	TC10	4 cm
Case 8	31	Sinusoidal	0.3	5	TC20	2 cm
	32	Sinusoidal	0.3	10	TC20	2 cm
	33	Sinusoidal	0.3	15	TC20	2 cm
	34	Sinusoidal	0.4	10	TC20	2 cm
	35	Sinusoidal	0.5	10	TC20	2 cm
	36	İzmit-F	0.124	-	TC20	2 cm
	37	İzmir-F	0.183	-	TC20	2 cm
	38	İzmit-N	0.22	-	TC20	2 cm
	39	El-Centro	0.318	-	TC20	2 cm
	40	Kobe	0.823	-	TC20	2 cm

Table 6.4. The experiment program used tire crumb and sand mixture. (cont.)

Case 9	41	Sinusoidal	0.3	5	TC20	4 cm
	42	Sinusoidal	0.3	10	TC20	4 cm
	43	Sinusoidal	0.3	15	TC20	4 cm
	44	Sinusoidal	0.4	10	TC20	4 cm
	45	Sinusoidal	0.5	10	TC20	4 cm
	46	İzmit-F	0.124	-	TC20	4 cm
	47	İzmir-F	0.183	-	TC20	4 cm
	48	İzmit-N	0.22	-	TC20	4 cm
	49	El-Centro	0.318	-	TC20	4 cm
	50	Kobe	0.823	-	TC20	4 cm
Case 10	51	Sinusoidal	0.3	5	TC30	2 cm
	52	Sinusoidal	0.3	10	TC30	2 cm
	53	Sinusoidal	0.3	15	TC30	2 cm
	54	Sinusoidal	0.4	10	TC30	2 cm
	55	Sinusoidal	0.5	10	TC30	2 cm
	56	İzmit-F	0.124	-	TC30	2 cm
	57	İzmir-F	0.183	-	TC30	2 cm
	58	İzmit-N	0.22	-	TC30	2 cm
	59	El-Centro	0.318	-	TC30	2 cm
	60	Kobe	0.823	-	TC30	2 cm
Case 11	61	Sinusoidal	0.3	5	TC30	4 cm
	62	Sinusoidal	0.3	10	TC30	4 cm
	63	Sinusoidal	0.3	15	TC30	4 cm
	64	Sinusoidal	0.4	10	TC30	4 cm
	65	Sinusoidal	0.5	10	TC30	4 cm
	66	İzmit-F	0.124	-	TC30	4 cm
	67	İzmir-F	0.183	-	TC30	4 cm
	68	İzmit-N	0.22	-	TC30	4 cm
	69	El-Centro	0.318	-	TC30	4 cm
	70	Kobe	0.823	-	TC30	4 cm

The shake table tests were performed under the input motions given in Section 5.3. The acceleration- and displacement-time histories were measured using accelerometers from A1 to A16 and displacement sensors from D17 to D19. Therefore, the acceleration-time histories (ATH), the Fourier Amplitude Spectra (FAS), Spectral Acceleration (SA) in the period domain, and the displacement-time histories (DTH) are presented for each input motion. Representative graphical results are given due to a large number of graphical outputs. As a result, among the instruments, one accelerometer (A7) and one displacement sensor (D19) were selected. A7 and

D19 measured the transmitted acceleration and the displacement near the top of the wall, respectively. Additionally, one of the input motions, the near-field Kocaeli Earthquake, was chosen as the representative results of the tests to reduce the number of test results. Furthermore, the reason for the selection of the near-field Kocaeli Earthquake is its importance in near Turkish Earthquake History. Apart from test results, the peak values of acceleration, spectral acceleration, and displacement values for each instrument are tabulated.

6.2. Test Results under Kocaeli Earthquake Motion

The results of the retaining wall model with sand backfill with/without the cushion layer are given in this section. Because of the great number of graphical outputs, in order to give representative graphical results, the recordings of two instruments (A7 and D19) were selected under the 1999 Kocaeli Earthquake (near-field) motion recorded in İzmit Station. The input motion was time scaled based on the similitude laws proposed by Iai (1989). The peak acceleration, maximum spectral acceleration, and maximum displacement will be tabulated for each input motion in the following section.

6.2.1. Case 1 under Kocaeli Earthquake (near-field) motion

The experimental setup without a cushion layer was subjected to Kocaeli Earthquake recorded in İzmit Station. The results are given in Figures 6.1 and 6.2. The PGA, SA, and displacement for Case 1 were determined as 0.314g, 1.422g, and 1.63 cm, respectively.

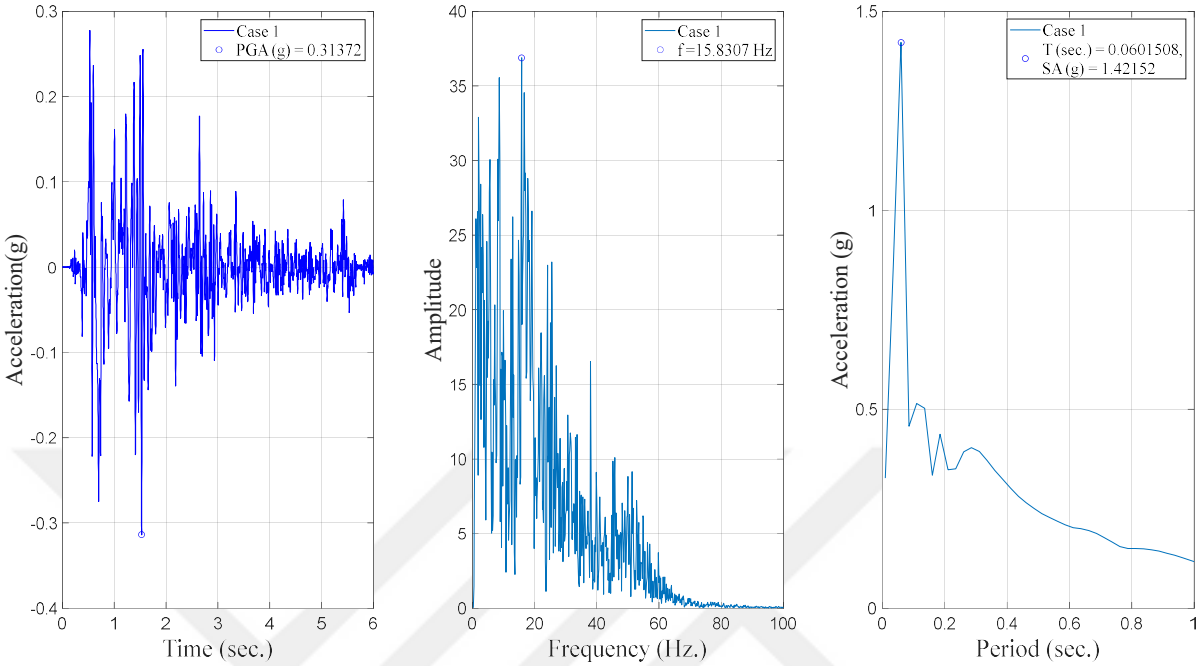

Figure 6.1. The ATH, the FAS, and the SA of A7 under Kocaeli Earthquake (Case 1).

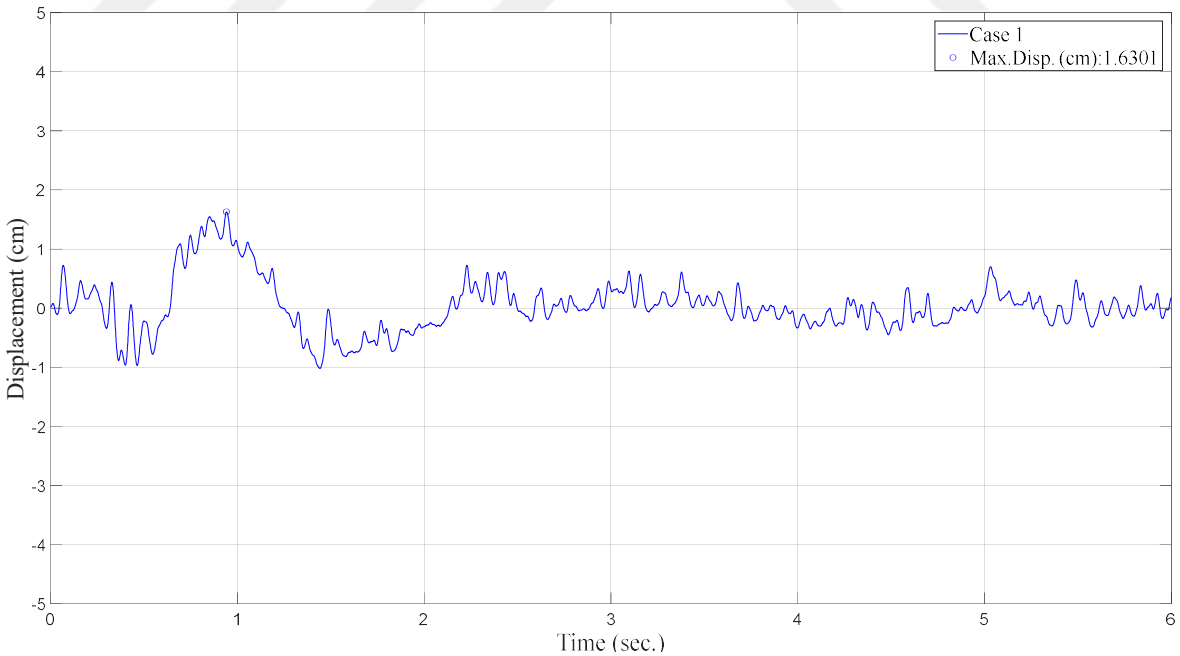

Figure 6.2. The displacement-time history of D19 under Kocaeli Earthquake (Case 1).

6.2.2. Case 2 under Kocaeli Earthquake (near-field) motion

The experimental setup with a cushion layer consisting of EPS10 having a thickness of 2 cm was subjected to Kocaeli Earthquake recorded in İzmit Station. The results are given in Figures 6.3 and 6.4. The PGA, SA, and displacement for Case 2 were determined as 0.283g, 1.203g, and 1.54 cm, respectively.

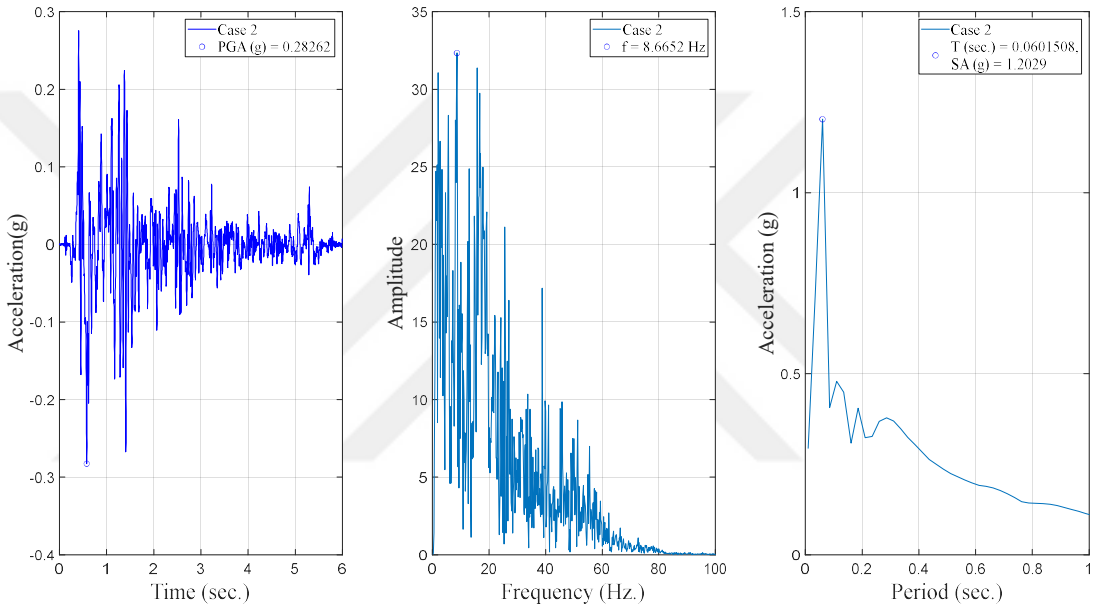

Figure 6.3. The ATH, the FAS, and the SA of A7 under Kocaeli Earthquake (Case 2).

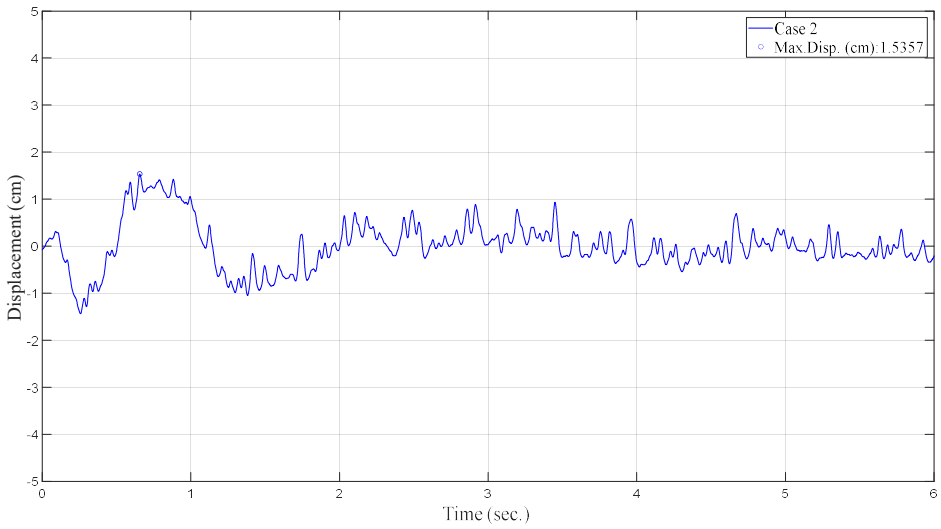

Figure 6.4. The displacement-time history of D19 under Kocaeli Earthquake (Case 2).

6.2.3. Case 3 under Kocaeli Earthquake (near-field) motion

The experimental setup with a cushion layer consisting of EPS10 having a thickness of 4 cm was subjected to Kocaeli Earthquake recorded in İzmit Station. The results are given in Figures 6.5 and 6.6. The PGA, SA, and displacement for Case 3 were determined as 0.248g, 1.006g, and 1.26 cm, respectively.

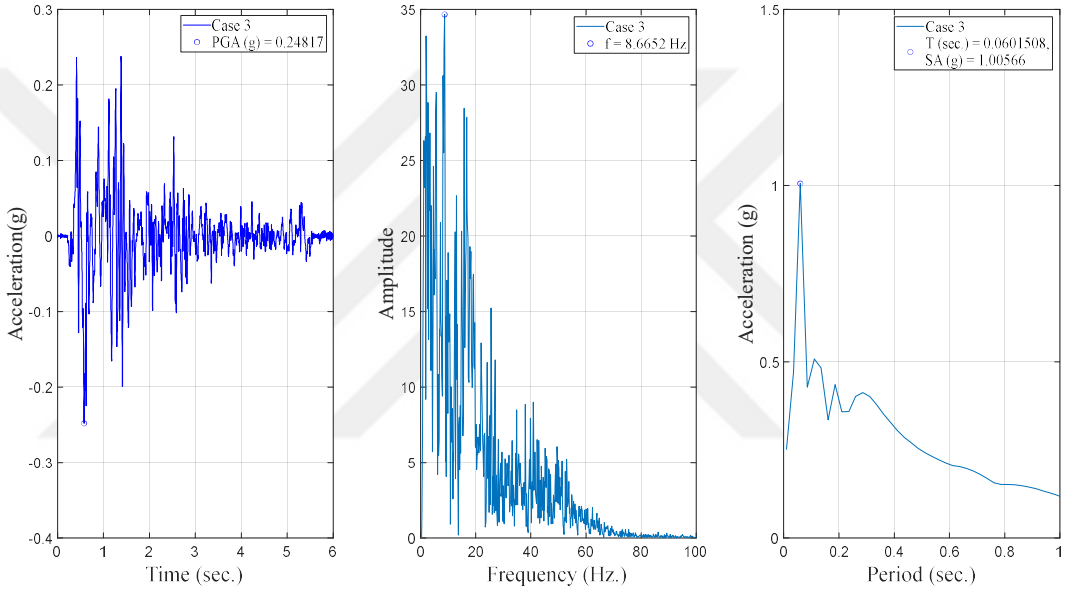

Figure 6.5. The ATH, the FAS, and the SA of A7 under Kocaeli Earthquake (Case 3).

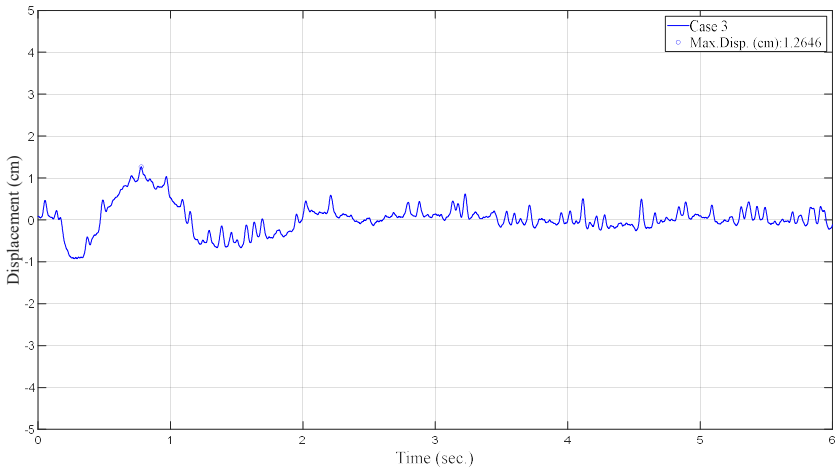

Figure 6.6. The displacement-time history of D19 under Kocaeli Earthquake (Case 3).

6.2.4. Case 4 under Kocaeli Earthquake (near-field) motion

The experimental setup with a cushion layer consisting of EPS20 having a thickness of 2 cm was subjected to Kocaeli Earthquake recorded in İzmit Station. The results are given in Figures 6.7 and 6.8. The PGA, SA, and displacement for Case 4 were determined as 0.262g, 0.938g, and 1.49 cm, respectively.

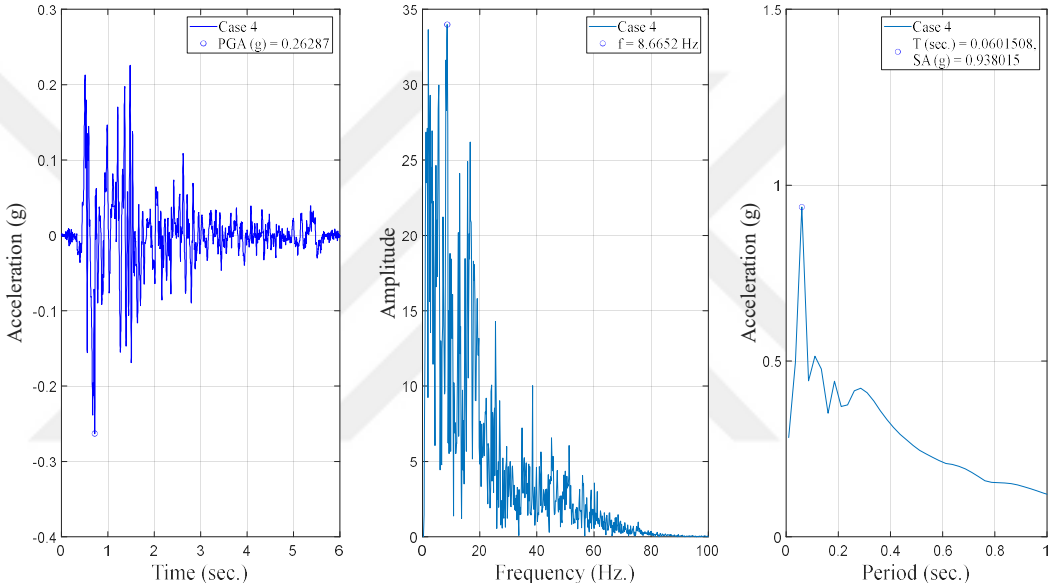

Figure 6.7. The ATH, the FAS, and the SA of A7 under Kocaeli Earthquake (Case 4).

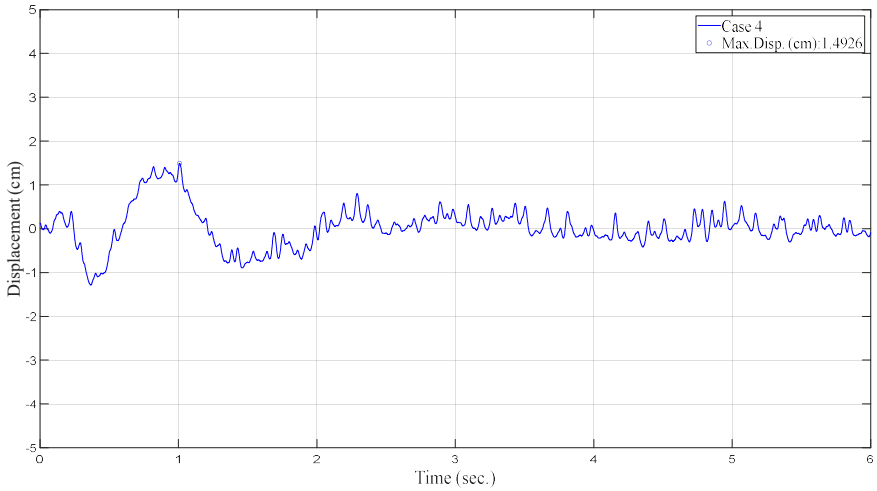

Figure 6.8. The displacement-time history of D19 under Kocaeli Earthquake (Case 4).

6.2.5. Case 5 under Kocaeli Earthquake (near-field) motion

The experimental setup with a cushion layer consisting of EPS30 having a thickness of 2 cm was subjected to Kocaeli Earthquake recorded in İzmit Station. The results are given in Figures 6.9 and 6.10. The PGA, SA, and displacement for Case 5 were determined as 0.286g, 1.191g, and 1.42 cm, respectively.

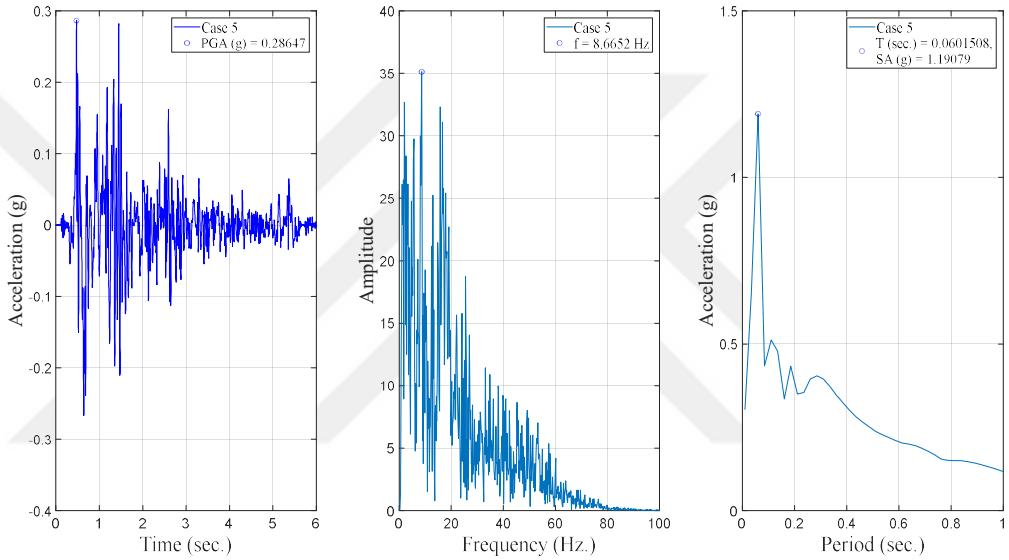

Figure 6.9. The ATH, the FAS, and the SA of A7 under Kocaeli Earthquake (Case 5).

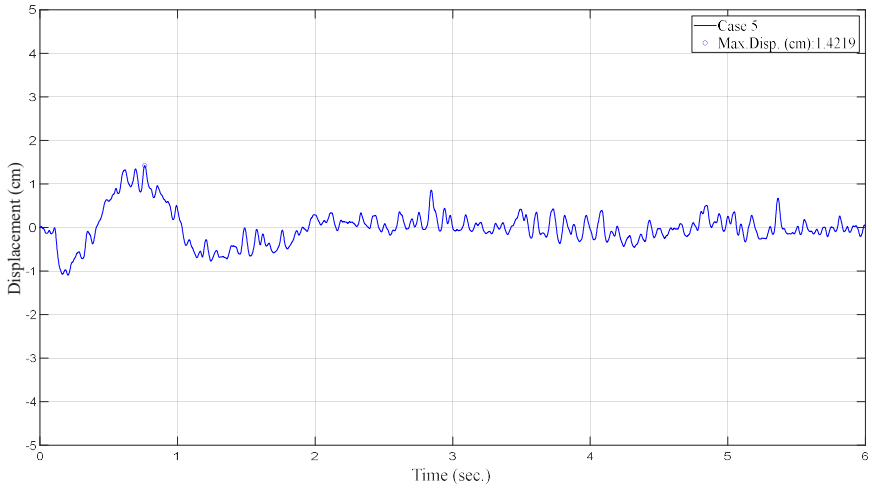

Figure 6.10. The displacement-time history of D19 under Kocaeli Earthquake (Case 5).

6.2.6. Case 6 under Kocaeli Earthquake (near-field) motion

The experimental setup with a cushion layer consisting of TC10 having a thickness of 2 cm was subjected to Kocaeli Earthquake recorded in İzmit Station. The results are given in Figures 6.11 and 6.12. The PGA, SA, and displacement for Case 6 were determined as 0.268g, 1.089g, and 1.59 cm, respectively.

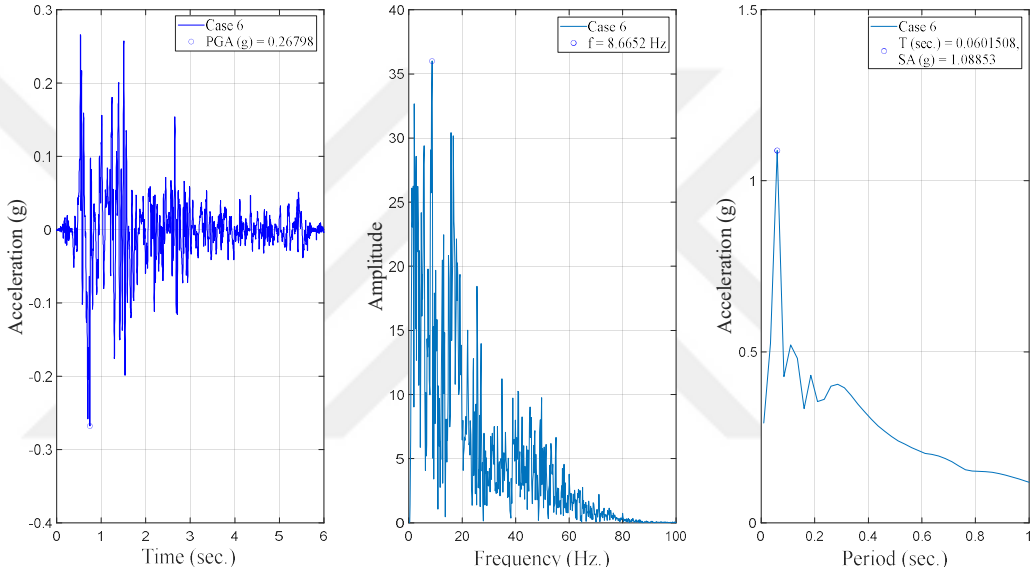

Figure 6.11. The ATH, the FAS, and the SA of A7 under Kocaeli Earthquake (Case 6).

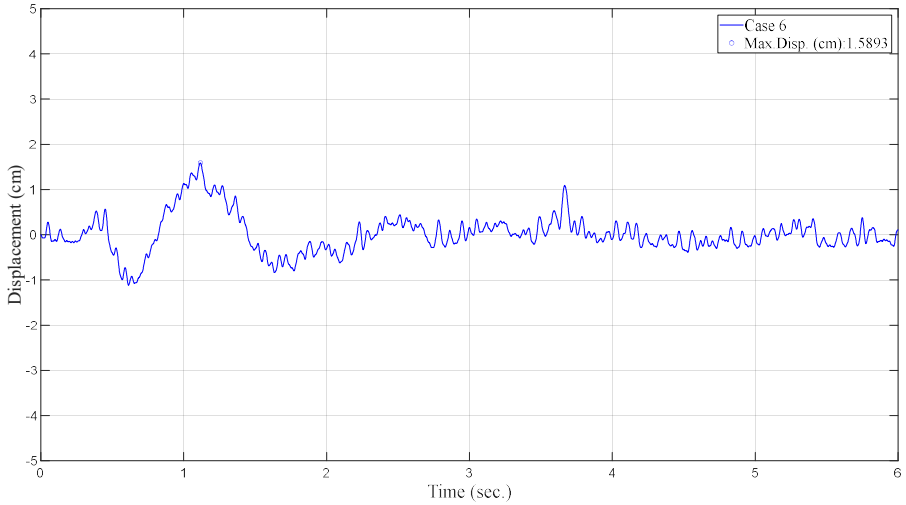

Figure 6.12. The displacement-time history of D19 under Kocaeli Earthquake (Case 6).

6.2.7. Case 7 under Kocaeli Earthquake (near-field) motion

The experimental setup with a cushion layer consisting of TC10 having a thickness of 4 cm was subjected to Kocaeli Earthquake recorded in İzmit Station. The results are given in Figures 6.13 and 6.14. The PGA, SA, and displacement for Case 7 were determined as 0.283g, 1.259g, and 1.59 cm, respectively.

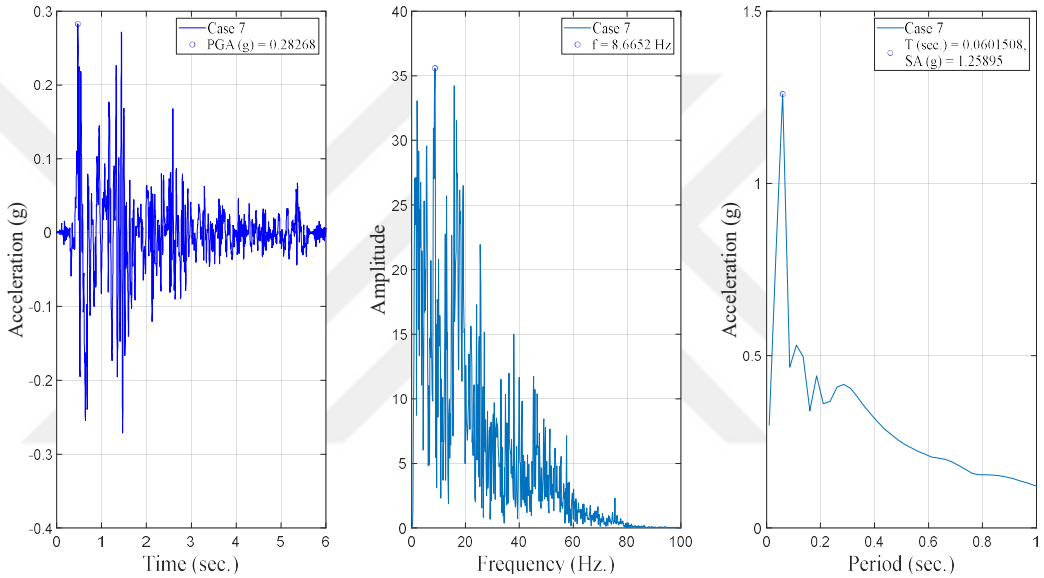

Figure 6.13. The ATH, the FAS, and the SA of A7 under Kocaeli Earthquake (Case 7).

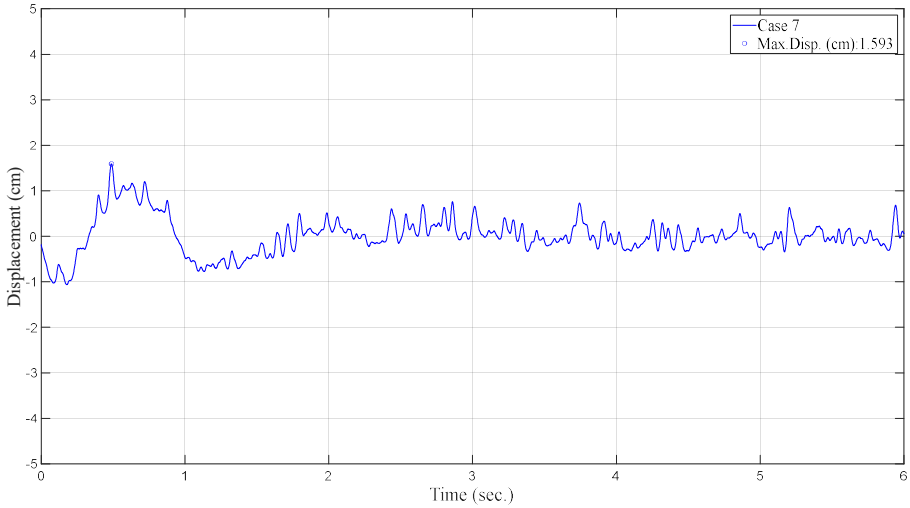

Figure 6.14. The displacement-time history of D19 under Kocaeli Earthquake (Case 7).

6.2.8. Case 8 under Kocaeli Earthquake (near-field) motion

The experimental setup with a cushion layer consisting of TC20 having a thickness of 2 cm was subjected to Kocaeli Earthquake recorded in İzmit Station. The results are given in Figures 6.15 and 6.16. The PGA, SA, and displacement for Case 8 were determined as 0.291g, 1.234g, and 1.54 cm, respectively.

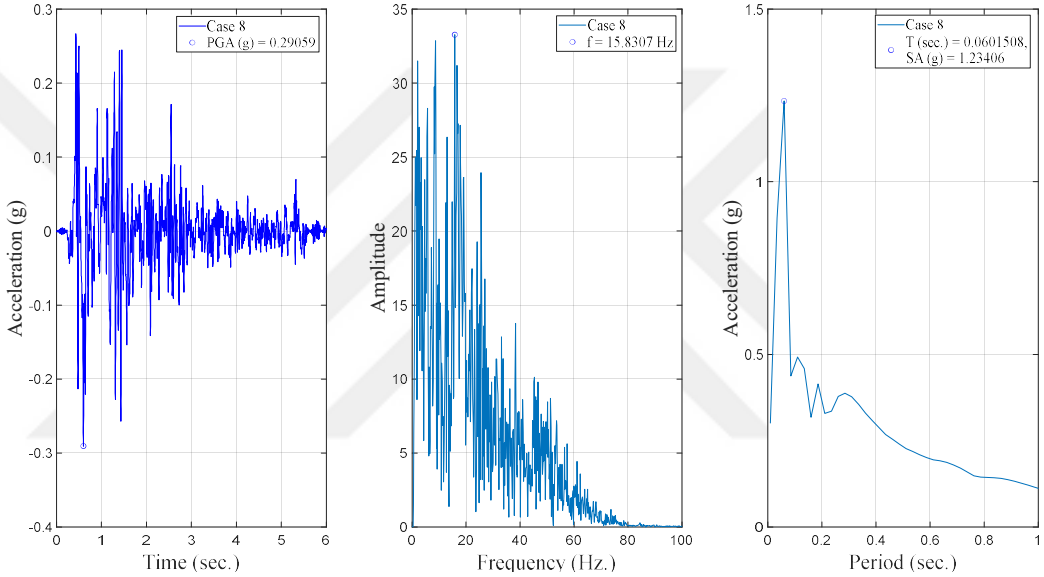

Figure 6.15. The ATH, the FAS, and the SA of A7 under Kocaeli Earthquake (Case 8).

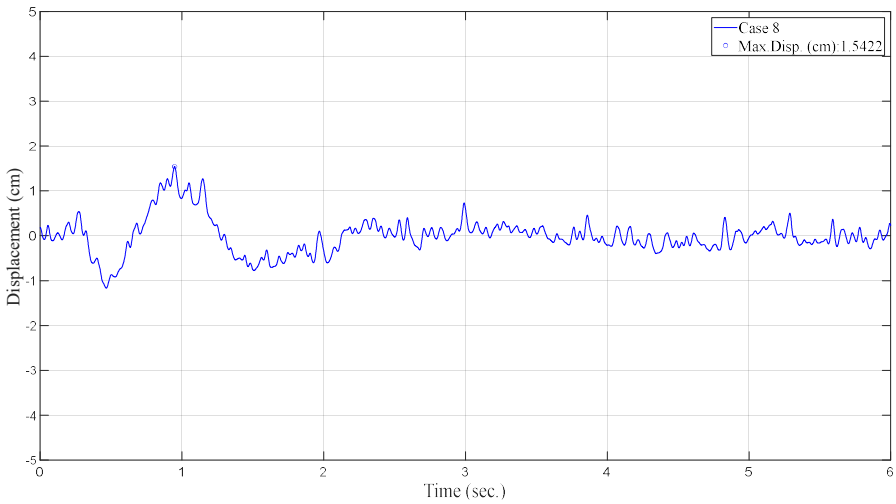

Figure 6.16. The displacement-time history of D19 under Kocaeli Earthquake (Case 8).

6.2.9. Case 9 under Kocaeli Earthquake (near-field) motion

The experimental setup with a cushion layer consisting of TC20 having a thickness of 4 cm was subjected to Kocaeli Earthquake recorded in İzmit Station. The results are given in Figures 6.17 and 6.18. The PGA, SA, and displacement for Case 9 were determined as 0.299g, 1.223g, and 1.57 cm, respectively.

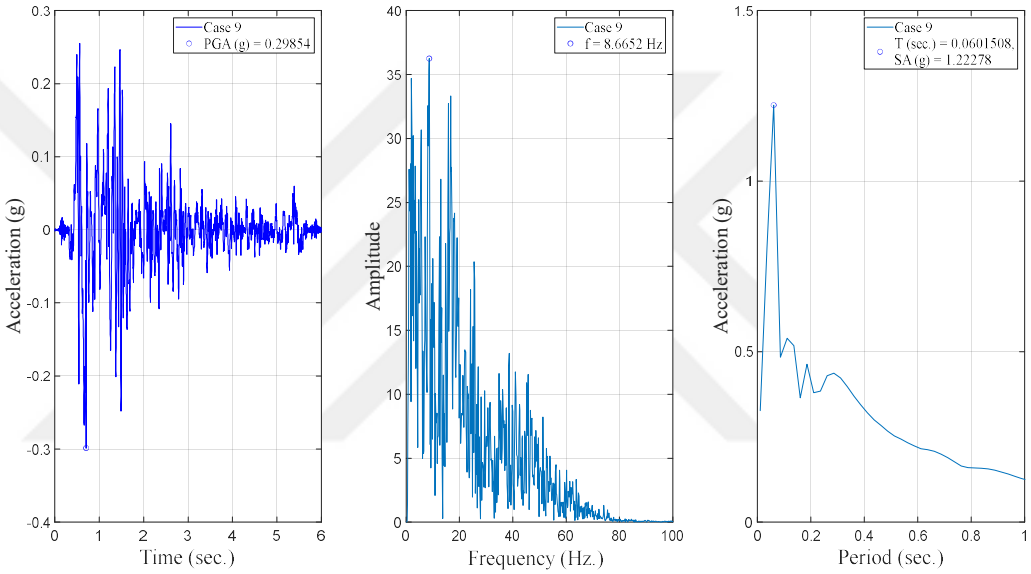

Figure 6.17. The ATH, the FAS, and the SA of A7 under Kocaeli Earthquake (Case 9).

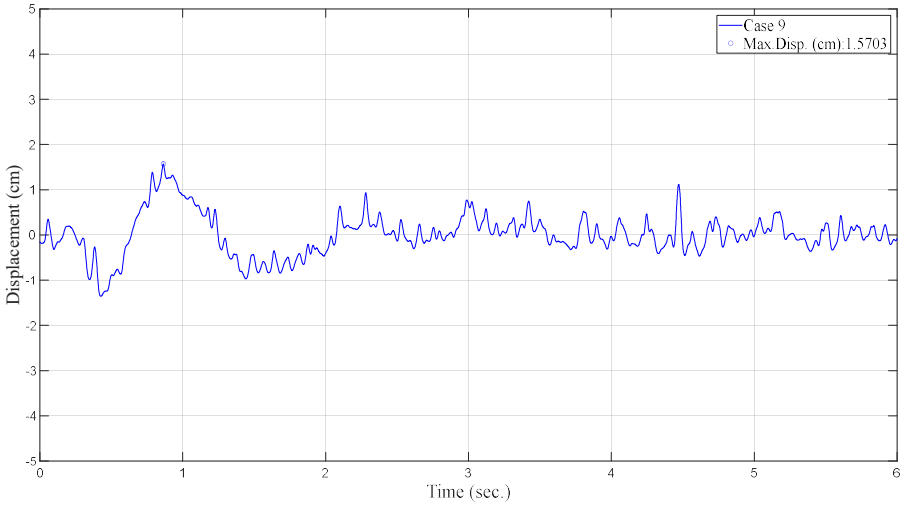

Figure 6.18. The displacement-time history of D19 under Kocaeli Earthquake (Case 9).

6.2.10. Case 10 under Kocaeli Earthquake (near-field) motion

The experimental setup with a cushion layer consisting of TC30 having a thickness of 2 cm was subjected to Kocaeli Earthquake recorded in İzmit Station. The results are given in Figures 6.19 and 6.20. The PGA, SA, and displacement for Case 10 were determined as 0.292g, 1.272g, and 1.51 cm, respectively.

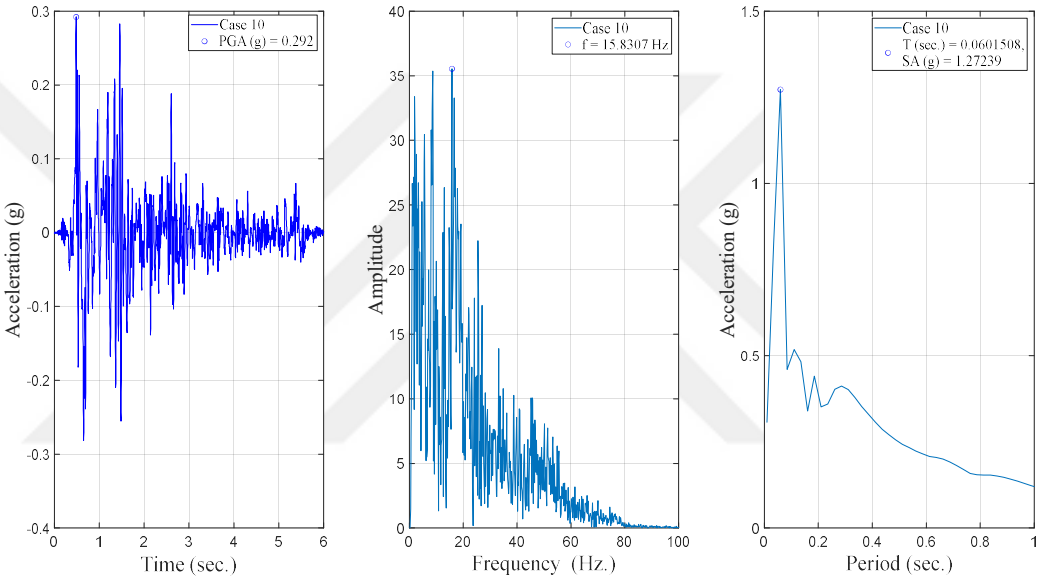

Figure 6.19. The ATH, the FAS, and the SA of A7 under Kocaeli Earthquake (Case 10).

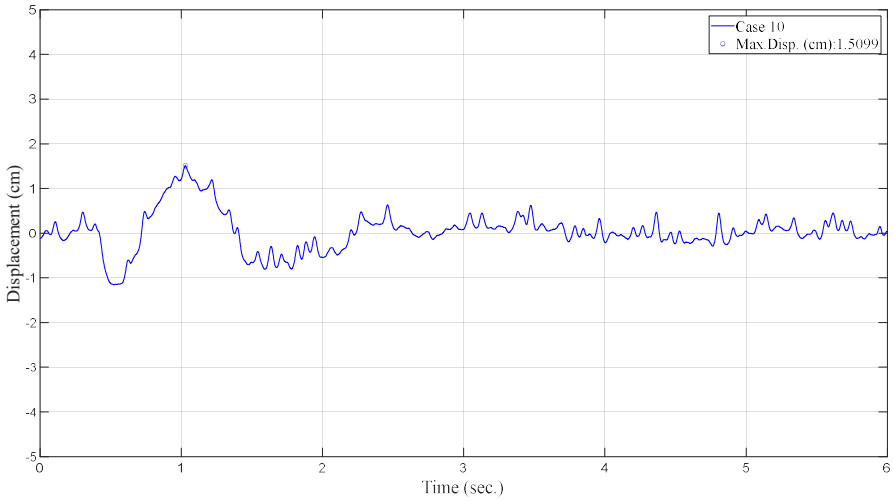

Figure 6.20. The displacement-time history of D19 under Kocaeli Earthquake (Case 10).

6.2.11. Case 11 under Kocaeli Earthquake (near-field) motion

The experimental setup with a cushion layer consisting of TC30 having a thickness of 4 cm was subjected to Kocaeli Earthquake recorded in İzmit Station. The results are given in Figures 6.21 and 6.22. The PGA, SA, and displacement for Case 11 were determined as 0.283g, 1.267g, and 1.52 cm, respectively.

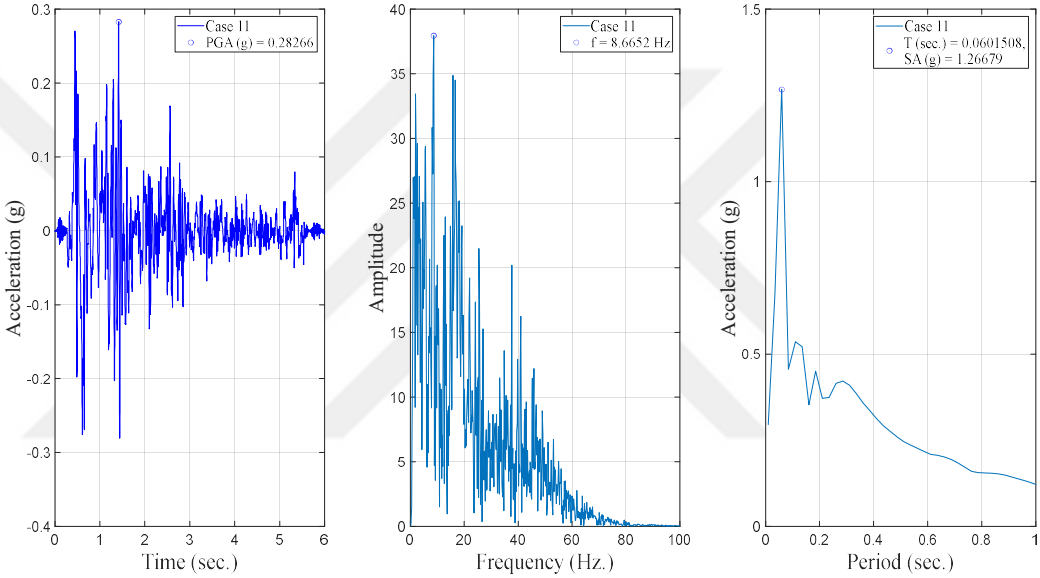

Figure 6.21. The ATH, the FAS, and the SA of A7 under Kocaeli Earthquake (Case 11).

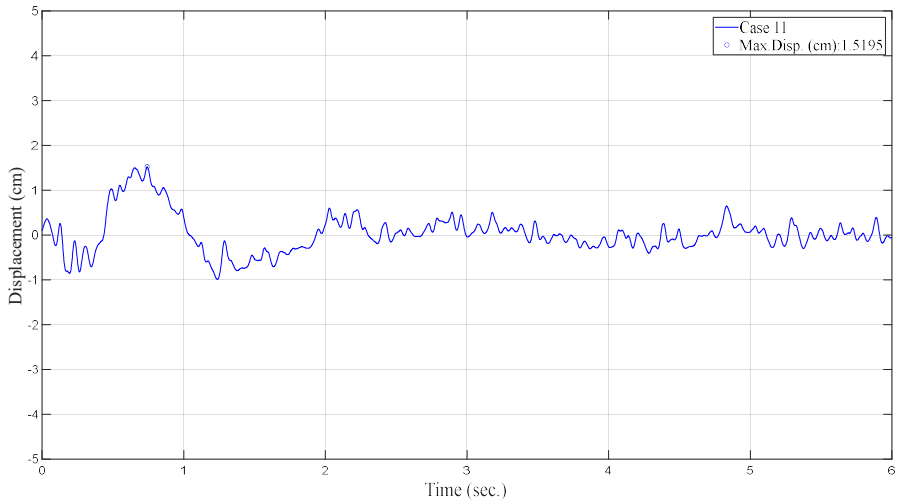

Figure 6.22. The displacement-time history of D19 under Kocaeli Earthquake (Case 11).

6.3. The Results of The Shake Table Tests for All Cases

In this section, all cases are presented under tested input motions. The peak acceleration, peak spectral acceleration, and maximum displacement recorded from all instruments are tabulated between Tables 6.5 and 6.37.

6.3.1. Case 1 under all considered motions

In Case 1, the experimental setup was prepared with only sand backfill without the cushion layer. This case was named an unimproved case. Additionally, it is a control case because Case 1 showed the seismic behavior of the scaled model without a cushion layer. The accelerometers and displacement sensors were placed as shown in Figures 5.23 and 5.24. The same instrumental layout was used for each case. The recorded maximum accelerations and the maximum displacements are tabulated in Tables 6.5 and 6.7. The maximum values of spectral acceleration are also listed in Table 6.6. The results under five different earthquake motions with different characteristics and five different sinusoidal motions with various amplitudes (0.3g, 0.4g, and 0.5g) and frequency contents (5, 10, and 15 Hz) were presented in Tables 6.5, 6.6, and 6.7. The performance of the cushion layer is evaluated by comparing the cases having cushion layers with the control case.

As seen in Table 6.5, the acceleration at the top (A7) of the scaled model was recorded as highest under the sinusoidal motion with 0.5g amplitude and 10 Hz frequency. Additionally, the acceleration change within Case 1 could not be observed clearly under the far-field Kocaeli Earthquake motion. The increase in the frequency and amplitude of sinusoidal motion resulted in an increase in the recorded acceleration at the top of the wall. Moreover, the percentage change between A1 and A7 diminishes with the reducing amplitude and frequency of sinusoidal motion. Among the earthquake recordings, the highest acceleration recorded from A7 was under Kobe Earthquake. However, the amplification from A1 to A7 was greatest under the far-field İzmir Earthquake, which was 138.3% increase. When comparing the earthquake recordings and

the sinusoidal motions, the sinusoidal motions cause more acceleration amplification throughout the experimental setup than the real earthquake motions.

The input acceleration (A1) applied to the shake table and the acceleration recorded outside the rigid box (A2) were very close to one another, which means that the acceleration reached the box surface with less distortion. Additionally, the accelerometers placed at the same level within the foundation soil (A9, A10, and A11) recorded almost identical accelerations. That is to say; there is not much difference in the acceleration within the foundation soil at the same level. Moreover, the change between accelerometers placed near the bottom of the wall (A3 and A4) was not considerable. The accelerometers installed near the top of the wall (A6, A7, and A8) recorded peak accelerations that were in close proximity to each other. The highest acceleration values were measured at the top of the wall. Below the ground surface, the recorded maximum acceleration decreased as the depth increased.

Table 6.5. The peak acceleration measurements under all input motions for Case 1.

Case 1	İzmit-F	İzmir-F	İzmit-N	El-Centro	Kobe	0.4g-5 Hz	0.3g-10 Hz	0.4g-10 Hz	0.5g-10 Hz	0.4g-15 Hz
	PGA (g)	PGA (g)	PGA (g)	PGA (g)	PGA (g)	PGA (g)	PGA (g)	PGA (g)	PGA (g)	PGA (g)
A1	0.124	0.183	0.220	0.318	0.823	0.400	0.300	0.400	0.500	0.400
A2	0.124	0.184	0.209	0.316	0.824	0.384	0.301	0.408	0.518	0.427
A3	0.134	0.216	0.230	0.340	0.644	0.439	0.353	0.476	0.665	0.556
A4	0.135	0.230	0.231	0.358	0.650	0.436	0.355	0.474	0.677	0.546
A5	0.146	0.301	0.247	0.428	0.741	0.476	0.400	0.563	0.778	0.665
A6	0.156	0.419	0.309	0.535	0.897	0.540	0.495	0.733	1.003	0.900
A7	0.162	0.436	0.314	0.547	0.871	0.535	0.490	0.734	0.999	0.899
A8	0.149	0.414	0.298	0.519	0.842	0.511	0.464	0.704	0.965	0.844
A9	0.128	0.194	0.223	0.330	0.858	0.409	0.315	0.426	0.542	0.434
A10	0.128	0.193	0.222	0.329	0.857	0.408	0.314	0.423	0.536	0.430
A11	0.127	0.192	0.221	0.329	0.857	0.406	0.312	0.419	0.530	0.427
A12	0.135	0.208	0.228	0.348	0.860	0.423	0.334	0.450	0.569	0.476
A13	0.143	0.234	0.234	0.355	0.807	0.455	0.370	0.487	0.656	0.600
A14	0.147	0.279	0.240	0.407	0.771	0.515	0.422	0.689	1.043	0.954
A15	0.143	0.285	0.239	0.412	0.729	0.464	0.386	0.558	0.776	0.634
A16	0.158	0.359	0.295	0.472	0.882	0.524	0.451	0.748	1.113	0.964

Table 6.6 showed that the spectral acceleration values for Case 1 did not change considerably. The greatest spectral acceleration at the top of the wall was calculated under the

sinusoidal motion with 0.4g amplitude and 15 Hz frequency. Nevertheless, the change in spectral acceleration from A1 to A7 was the highest under the far-field İzmir Earthquake, which was determined as 119.5%. As the amplitude of sinusoidal base excitation increases, the spectral acceleration at the top of the wall increases. However, the frequency of sinusoidal motion change did not cause the same effect. The lowest spectral acceleration was calculated for the sinusoidal motion with 0.4g amplitude and 10 Hz frequency.

Table 6.6. The peak spectral acceleration under all input motions for Case 1.

Case 1	İzmit-F	İzmir-F	İzmit-N	El-Centro	Kobe	0.4g-5 Hz	0.3g-10 Hz	0.4g-10 Hz	0.5g-10 Hz	0.4g-15 Hz
	SA (g)	SA (g)	SA (g)	SA (g)	SA (g)	SA (g)	SA (g)	SA (g)	SA (g)	SA (g)
A1	0.393	0.527	0.925	0.976	2.153	2.465	1.157	1.609	2.054	1.949
A2	0.364	0.532	0.918	0.920	2.053	2.292	1.099	1.533	1.965	1.971
A3	0.392	0.635	1.077	1.041	2.238	2.531	1.261	1.848	2.545	2.614
A4	0.387	0.663	1.100	1.048	2.253	2.501	1.255	1.858	2.525	2.554
A5	0.392	0.811	1.237	1.210	2.472	2.572	1.345	2.094	2.950	3.110
A6	0.393	1.108	1.407	1.569	2.761	2.641	1.457	2.419	3.555	3.992
A7	0.388	1.157	1.422	1.593	2.753	2.604	1.442	2.417	3.544	3.951
A8	0.371	1.089	1.350	1.523	2.656	2.493	1.376	2.325	3.409	3.721
A9	0.390	0.545	0.968	0.983	2.192	2.464	1.178	1.647	2.118	2.079
A10	0.389	0.545	0.965	1.479	2.184	2.454	1.173	1.640	2.109	2.072
A11	0.387	0.545	0.962	1.975	2.175	2.444	1.168	1.633	2.100	2.064
A12	0.389	0.610	1.029	0.997	2.163	2.473	1.208	1.702	2.206	2.251
A13	0.387	0.685	1.099	1.030	2.199	2.502	1.263	1.850	2.500	2.706
A14	0.374	0.733	1.165	1.121	2.511	2.496	1.342	2.364	3.105	3.415
A15	0.343	0.771	1.194	1.152	2.362	2.496	1.298	2.059	2.859	2.812
A16	0.395	1.048	1.384	1.584	2.762	2.661	1.463	2.667	3.780	3.666

When Table 6.7 is analyzed, it is observed that the maximum displacement recorded at the top of the wall was close to the peak movement of the shaking table. The increase in the amplitude of the sinusoidal motion causes an increase in the maximum displacement at the top of the wall. However, as the frequency of sinusoidal recordings increases, the amount of wall movement decreases. Additionally, the movement at the wall was recorded as the highest under El-Centro Earthquake motion. The highest change in displacement from D17 to D19 was determined as 18.8% under the sinusoidal motion with 0.3g amplitude and 10 Hz frequency.

Table 6.7. The peak displacement under all input motions for Case 1.

Case 1	İzmit-F	İzmir-F	İzmit-N	El-Centro	Kobe	0.4g-5 Hz	0.3g-10 Hz	0.4g-10 Hz	0.5g-10 Hz	0.4g-15 Hz
	Disp. (cm)	Disp. (cm)	Disp. (cm)	Disp. (cm)	Disp. (cm)	Disp. (cm)	Disp. (cm)	Disp. (cm)	Disp. (cm)	Disp. (cm)
D17	1.21	0.90	1.69	1.79	1.43	1.20	0.85	1.00	1.11	0.90
D18	1.16	0.85	1.60	1.74	1.37	1.08	0.65	0.88	1.00	0.73
D19	1.19	0.89	1.63	1.76	1.41	1.10	0.69	0.92	1.02	0.75

6.3.2. Case 2 under all considered motions

In Case 2, the cushion consisted of EPS10 with a thickness of 2 cm. The results under five different earthquake motions and five different sinusoidal motions were given in Tables 6.8, 6.9, and 6.10.

In Table 6.8, the peak accelerations recorded from A7 were greater than A1, which means that the acceleration amplified while reaching the top of the wall. The percentage change in the acceleration from A1 to A7 was greatest under İzmir Earthquake, while the lowest change in acceleration was under Kobe Earthquake. The highest change was calculated as a 137.7% increase, and the lowest one was a 5.2% increase.

Table 6.8. The peak acceleration measurements under considered input motions for Case 2.

Case 2	İzmit-F	İzmir-F	İzmit-N	El-Centro	Kobe	0.4g-5 Hz	0.3g-10 Hz	0.4g-10 Hz	0.5g-10 Hz	0.4g-15 Hz
	PGA (g)	PGA (g)	PGA (g)	PGA (g)	PGA (g)	PGA (g)	PGA (g)	PGA (g)	PGA (g)	PGA (g)
A1	0.124	0.183	0.220	0.318	0.823	0.400	0.300	0.400	0.500	0.400
A2	0.124	0.194	0.212	0.314	0.790	0.383	0.302	0.406	0.510	0.426
A3	0.134	0.236	0.229	0.314	0.588	0.408	0.334	0.426	0.554	0.490
A4	0.134	0.238	0.228	0.312	0.574	0.404	0.332	0.425	0.559	0.485
A5	0.146	0.314	0.247	0.385	0.645	0.442	0.373	0.494	0.643	0.601
A6	0.163	0.436	0.283	0.496	0.857	0.492	0.455	0.608	0.781	0.772
A7	0.163	0.435	0.283	0.496	0.865	0.496	0.452	0.611	0.781	0.768
A8	0.153	0.401	0.266	0.466	0.833	0.471	0.420	0.571	0.744	0.725
A9	0.127	0.193	0.223	0.327	0.837	0.405	0.313	0.419	0.530	0.433
A10	0.127	0.195	0.222	0.326	0.835	0.404	0.312	0.418	0.528	0.433
A11	0.127	0.197	0.222	0.326	0.834	0.403	0.312	0.417	0.525	0.433
A12	0.134	0.226	0.231	0.344	0.846	0.417	0.333	0.447	0.562	0.484
A13	0.135	0.243	0.230	0.344	0.770	0.415	0.337	0.452	0.565	0.506
A14	0.137	0.270	0.235	0.353	0.694	0.473	0.374	0.538	0.844	0.836
A15	0.145	0.311	0.244	0.385	0.636	0.448	0.379	0.511	0.641	0.583
A16	0.159	0.412	0.275	0.467	0.669	0.526	0.468	0.714	0.848	0.880

In Table 6.9, whereas the maximum spectral acceleration increased at a rate of 156% from A1 to A7 under İzmir Earthquake, the spectral acceleration change under the far-field Kocaeli earthquake was a 0.5% decrease. The spectral accelerations at the top of the wall were greater than the peak spectral accelerations of input motions, except for the far-field Kocaeli Earthquake.

Table 6.9. The peak spectral acceleration under considered input motions for Case 2.

Case 2	İzmit-F	İzmir-F	İzmit-N	El-Centro	Kobe	0.4g-5 Hz	0.3g-10 Hz	0.4g-10 Hz	0.5g-10 Hz	0.4g-15 Hz
	SA (g)	SA (g)	SA (g)	SA (g)	SA (g)	SA (g)	SA (g)	SA (g)	SA (g)	SA (g)
A1	0.389	0.544	0.904	0.996	2.167	2.467	1.156	1.601	2.030	1.963
A2	0.360	0.519	0.890	0.937	2.043	2.264	1.095	1.523	1.936	1.970
A3	0.388	0.619	0.988	1.017	2.163	2.547	1.255	1.773	2.272	2.387
A4	0.382	0.628	0.985	1.008	2.149	2.532	1.238	1.762	2.269	2.345
A5	0.389	0.911	1.081	1.118	2.351	2.646	1.350	1.970	2.568	2.800
A6	0.389	1.382	1.206	1.423	2.608	2.759	1.498	2.259	2.960	3.475
A7	0.387	1.392	1.203	1.431	2.608	2.755	1.484	2.252	2.964	3.447
A8	0.368	1.129	1.135	1.353	2.475	2.621	1.392	2.123	2.800	3.193
A9	0.387	0.549	0.928	0.999	2.171	2.462	1.170	1.626	2.070	2.078
A10	0.385	0.547	0.928	0.996	2.165	2.453	1.167	1.621	2.065	2.073
A11	0.383	0.546	0.927	0.993	2.159	2.444	1.163	1.617	2.060	2.069
A12	0.385	0.588	0.978	1.013	2.195	2.474	1.199	1.676	2.145	2.246
A13	0.373	0.643	0.983	0.994	2.069	2.417	1.186	1.671	2.197	2.395
A14	0.362	0.746	1.005	1.025	2.248	2.523	1.261	2.050	2.835	3.069
A15	0.383	0.885	1.070	1.110	2.310	2.664	1.362	2.014	2.587	2.667
A16	0.390	1.364	1.183	1.461	2.646	2.921	1.650	2.710	3.154	3.442

In Table 6.10, the amount of wall movement at the wall top was lower than the maximum displacement of the shake table. The highest reduction in displacement was obtained under İzmir earthquake. However, the lowest reduction was under the near-field Kocaeli Earthquake. The greatest and the lowest change in displacement were 38.9% and 8.9%, respectively.

Table 6.10. The peak displacement under considered input motions for Case 2.

Case 2	İzmit-F	İzmir-F	İzmit-N	El-Centro	Kobe	0.4g-5 Hz	0.3g-10 Hz	0.4g-10 Hz	0.5g-10 Hz	0.4g-15 Hz
	Disp. (cm)	Disp. (cm)	Disp. (cm)	Disp. (cm)	Disp. (cm)	Disp. (cm)	Disp. (cm)	Disp. (cm)	Disp. (cm)	Disp. (cm)
D17	1.21	0.90	1.69	1.79	1.43	1.20	0.85	1.00	1.11	0.90
D18	0.84	0.52	1.50	1.35	1.09	0.93	0.64	0.86	0.95	0.71
D19	0.87	0.55	1.54	1.38	1.17	0.95	0.68	0.88	0.98	0.74

6.3.3. Case 3 under all considered motions

In Case 3, the cushion was composed of EP10 with a thickness of 4 cm. The results under five different earthquake recordings and five different sinusoidal motions were tabulated in Tables 6.11, 6.12, and 6.13.

In Table 6.11, the percentage change in the acceleration from A1 to A7 was greatest under the sinusoidal motion with 0.4g amplitude and 15 Hz frequency, while the lowest change in acceleration was under Kobe Earthquake. The former was calculated as a 75.2% increase, and the latter was a 12.8% decrease. The peak accelerations recorded from A7 were greater than A1, which means that the acceleration amplified while reaching the top of the wall, except for the Kobe Earthquake.

Table 6.11. The peak acceleration measurements under considered input motions for Case 3.

Case 3	İzmit-F	İzmir-F	İzmit-N	El-Centro	Kobe	0.4g-5 Hz	0.3g-10 Hz	0.4g-10 Hz	0.5g-10 Hz	0.4g-15 Hz
	PGA (g)	PGA (g)	PGA (g)	PGA (g)	PGA (g)	PGA (g)	PGA (g)	PGA (g)	PGA (g)	PGA (g)
A1	0.124	0.183	0.220	0.318	0.823	0.400	0.300	0.400	0.500	0.400
A2	0.123	0.178	0.208	0.317	0.792	0.387	0.302	0.404	0.499	0.412
A3	0.130	0.203	0.227	0.322	0.582	0.415	0.331	0.434	0.572	0.477
A4	0.129	0.203	0.225	0.319	0.567	0.411	0.328	0.434	0.573	0.473
A5	0.137	0.244	0.236	0.328	0.620	0.436	0.355	0.463	0.653	0.570
A6	0.155	0.317	0.253	0.364	0.732	0.486	0.415	0.569	0.788	0.715
A7	0.156	0.318	0.248	0.361	0.718	0.475	0.407	0.554	0.774	0.701
A8	0.154	0.311	0.239	0.351	0.695	0.454	0.395	0.530	0.745	0.670
A9	0.127	0.187	0.221	0.328	0.840	0.408	0.313	0.416	0.518	0.420
A10	0.127	0.187	0.221	0.327	0.837	0.407	0.312	0.414	0.516	0.421
A11	0.127	0.187	0.220	0.326	0.835	0.406	0.311	0.413	0.514	0.421
A12	0.133	0.200	0.226	0.343	0.850	0.422	0.333	0.441	0.549	0.469
A13	0.137	0.227	0.231	0.348	0.771	0.437	0.353	0.463	0.590	0.531
A14	0.137	0.263	0.233	0.341	0.662	0.497	0.403	0.602	0.979	0.868
A15	0.150	0.293	0.243	0.354	0.645	0.480	0.398	0.578	0.768	0.672
A16	0.167	0.339	0.257	0.395	0.691	0.537	0.453	0.709	1.011	0.897

In Table 6.12, whereas the maximum spectral acceleration increased at a rate of 61.9% from A1 to A7 under İzmir Earthquake, the spectral acceleration change under the far-field Kocaeli earthquake was 1.7% decrease. The spectral accelerations at the top of the wall were

greater than the peak spectral accelerations of input motions, except for the far-field Kocaeli Earthquake.

Table 6.12. The peak spectral acceleration under considered input motions for Case 3.

Case 3	İzmit-F	İzmir-F	İzmit-N	El-Centro	Kobe	0.4g-5 Hz	0.3g-10 Hz	0.4g-10 Hz	0.5g-10 Hz	0.4g-15 Hz
	SA (g)	SA (g)	SA (g)	SA (g)	SA (g)	SA (g)	SA (g)	SA (g)	SA (g)	SA (g)
A1	0.425	0.596	0.828	0.989	2.216	2.446	1.194	1.630	2.052	1.955
A2	0.393	0.568	0.816	0.932	2.101	2.275	1.137	1.555	1.963	1.961
A3	0.424	0.619	0.887	1.005	2.152	2.522	1.260	1.770	2.302	2.304
A4	0.418	0.614	0.882	0.991	2.130	2.496	1.252	1.762	2.299	2.293
A5	0.423	0.717	0.936	1.031	2.295	2.594	1.319	1.931	2.605	2.635
A6	0.425	0.970	1.019	1.078	2.540	2.712	1.416	2.198	3.082	3.205
A7	0.418	0.965	1.006	1.060	2.489	2.663	1.391	2.158	3.027	3.142
A8	0.401	0.950	0.973	1.021	2.392	2.561	1.342	2.080	2.917	3.037
A9	0.422	0.601	0.850	0.992	2.231	2.441	1.210	1.657	2.095	2.062
A10	0.420	0.600	0.849	0.989	2.225	2.432	1.207	1.653	2.091	2.060
A11	0.419	0.598	0.849	0.987	2.220	2.424	1.204	1.650	2.087	2.058
A12	0.421	0.616	0.894	1.006	2.268	2.454	1.242	1.711	2.179	2.228
A13	0.418	0.661	0.927	1.014	2.160	2.485	1.271	1.777	2.335	2.512
A14	0.404	0.795	0.944	1.022	2.372	2.646	1.349	2.279	3.146	3.204
A15	0.419	0.868	0.980	1.056	2.424	2.699	1.390	2.188	3.083	3.076
A16	0.426	1.050	1.038	1.101	2.664	2.885	1.493	2.639	3.767	3.696

In Table 6.13, the amount of wall movement at the top was lower than the maximum displacement of the shake table. The highest reduction in displacement was obtained under the sinusoidal motion with 0.3g amplitude and 10 Hz frequency; however, the lowest reduction was under the sinusoidal motion with 0.5g amplitude and 10 Hz frequency. The greatest and the lowest change in displacement were 52.9% and 15%, respectively.

Table 6.13. The peak displacement under considered input motions for Case 3.

Case 3	İzmit-F	İzmir-F	İzmit-N	El-Centro	Kobe	0.4g-5 Hz	0.3g-10 Hz	0.4g-10 Hz	0.5g-10 Hz	0.4g-15 Hz
	Disp. (cm)	Disp. (cm)	Disp. (cm)	Disp. (cm)	Disp. (cm)	Disp. (cm)	Disp. (cm)	Disp. (cm)	Disp. (cm)	Disp. (cm)
D17	1.21	0.90	1.69	1.79	1.43	1.20	0.85	1.00	1.11	0.90
D18	0.81	0.46	1.22	1.32	1.08	0.88	0.38	0.83	0.86	0.64
D19	0.84	0.48	1.26	1.35	1.13	0.91	0.40	0.85	0.89	0.67

6.3.4. Case 4 under all considered motions

In Case 4, the cushion was composed of EPS 20 with a thickness of 2 cm. The results under five different earthquake recordings and five different sinusoidal motions were given in Tables 6.14, 6.15, and 6.16.

In Table 6.14, the peak accelerations recorded from A7 were greater than A1, which means that the acceleration amplified while reaching the top of the wall, except for the Kobe Earthquake. The percentage change in the acceleration from A1 to A7 was greatest under the sinusoidal motion with 0.4g amplitude and 15 Hz frequency, while the lowest change in acceleration was under Kobe Earthquake. The former was calculated as an 82.3% increase, and the latter was a 2.8% decrease.

Table 6.14. The peak acceleration measurements under considered input motions for Case 4.

Case 4	İzmit-F	İzmir-F	İzmit-N	El-Centro	Kobe	0.4g-5 Hz	0.3g-10 Hz	0.4g-10 Hz	0.5g-10 Hz	0.4g-15 Hz
	PGA (g)	PGA (g)	PGA (g)	PGA (g)	PGA (g)	PGA (g)	PGA (g)	PGA (g)	PGA (g)	PGA (g)
A1	0.124	0.183	0.220	0.318	0.823	0.400	0.300	0.400	0.500	0.400
A2	0.122	0.176	0.205	0.314	0.793	0.387	0.295	0.391	0.494	0.403
A3	0.133	0.203	0.225	0.315	0.678	0.420	0.329	0.439	0.595	0.486
A4	0.133	0.207	0.223	0.312	0.578	0.411	0.323	0.431	0.573	0.479
A5	0.143	0.250	0.232	0.326	0.639	0.451	0.365	0.482	0.688	0.585
A6	0.153	0.296	0.251	0.349	0.843	0.494	0.413	0.580	0.862	0.716
A7	0.156	0.313	0.263	0.359	0.800	0.502	0.427	0.594	0.846	0.729
A8	0.151	0.305	0.256	0.349	0.736	0.482	0.413	0.565	0.809	0.705
A9	0.127	0.186	0.220	0.327	0.843	0.408	0.308	0.412	0.515	0.421
A10	0.127	0.186	0.219	0.327	0.841	0.407	0.307	0.411	0.513	0.419
A11	0.127	0.185	0.219	0.326	0.839	0.406	0.305	0.409	0.510	0.418
A12	0.132	0.193	0.222	0.337	0.858	0.416	0.320	0.421	0.534	0.441
A13	0.134	0.211	0.220	0.338	0.754	0.422	0.331	0.430	0.557	0.491
A14	0.137	0.252	0.223	0.334	0.662	0.482	0.381	0.638	0.990	0.909
A15	0.139	0.241	0.225	0.318	0.623	0.447	0.360	0.494	0.631	0.545
A16	0.154	0.307	0.255	0.355	0.647	0.511	0.421	0.668	0.959	0.857

In Table 6.15, The spectral accelerations at the top of the wall were greater than the peak spectral accelerations of input motions, except for the far-field Kocaeli Earthquake. Whereas the maximum spectral acceleration increased at a rate of 67.4% from A1 to A7 under the

sinusoidal motion with 0.4g amplitude and 15 Hz frequency, the spectral acceleration change under the far-field Kocaeli earthquake was a 1.9% decrease.

Table 6.15. The peak spectral acceleration under considered input motions for Case 4.

Case 4	İzmit-F	İzmir-F	İzmit-N	El-Centro	Kobe	0.4g-5 Hz	0.3g-10 Hz	0.4g-10 Hz	0.5g-10 Hz	0.4g-15 Hz
	SA (g)	SA (g)	SA (g)	SA (g)	SA (g)	SA (g)	SA (g)	SA (g)	SA (g)	SA (g)
A1	0.399	0.614	0.776	0.993	2.181	2.455	1.188	1.608	2.062	1.932
A2	0.369	0.584	0.765	0.935	2.068	2.285	1.131	1.535	1.972	1.940
A3	0.398	0.637	0.834	1.007	2.168	2.540	1.260	1.753	2.318	2.315
A4	0.393	0.631	0.829	0.999	2.115	2.489	1.246	1.736	2.304	2.284
A5	0.397	0.703	0.883	1.035	2.307	2.596	1.326	1.942	2.663	2.677
A6	0.398	0.828	0.931	1.068	2.549	2.708	1.402	2.200	3.106	3.184
A7	0.391	0.869	0.938	1.062	2.507	2.660	1.404	2.211	3.121	3.235
A8	0.375	0.844	0.905	1.024	2.386	2.543	1.354	2.127	2.998	3.105
A9	0.396	0.620	0.798	0.997	2.196	2.452	1.204	1.636	2.105	2.042
A10	0.395	0.618	0.797	0.994	2.189	2.443	1.201	1.631	2.100	2.037
A11	0.393	0.616	0.795	0.990	2.182	2.434	1.198	1.627	2.094	2.033
A12	0.394	0.627	0.823	1.001	2.219	2.449	1.222	1.665	2.150	2.142
A13	0.383	0.623	0.833	0.985	2.069	2.415	1.221	1.682	2.215	2.328
A14	0.367	0.715	0.848	0.991	2.363	2.578	1.314	2.224	3.234	3.283
A15	0.387	0.677	0.860	1.008	2.233	2.551	1.296	1.936	2.723	2.457
A16	0.398	0.847	0.936	1.078	2.498	2.775	1.439	2.394	3.652	3.332

In Table 6.16, the amount of wall movement at the top was lower than the maximum displacement of the shake table. The highest reduction in displacement was obtained under İzmir Earthquake; however, the lowest reduction was under the sinusoidal motion with 0.4g amplitude and 10 Hz frequency. The greatest and the lowest change in displacement were 33.3% and 9%, respectively.

Table 6.16. The peak displacement under considered input motions for Case 4.

Case 4	İzmit-F	İzmir-F	İzmit-N	El-Centro	Kobe	0.4g-5 Hz	0.3g-10 Hz	0.4g-10 Hz	0.5g-10 Hz	0.4g-15 Hz
	Disp. (cm)	Disp. (cm)	Disp. (cm)	Disp. (cm)	Disp. (cm)	Disp. (cm)	Disp. (cm)	Disp. (cm)	Disp. (cm)	Disp. (cm)
D17	1.21	0.90	1.69	1.79	1.43	1.20	0.85	1.00	1.11	0.90
D18	0.88	0.57	1.45	1.37	1.11	1.03	0.63	0.87	0.95	0.72
D19	0.90	0.60	1.49	1.41	1.15	1.06	0.65	0.91	0.99	0.74

6.3.5. Case 5 under all considered motions

In Case 5, the cushion was composed of EPS30 with a thickness of 2 cm. The results under five different earthquake recordings and five different sinusoidal motions were given in Tables 6.17, 6.18, and 6.19.

In Table 6.17, the percentage change in the acceleration from A1 to A7 was greatest under the sinusoidal motion with 0.4g amplitude and 15 Hz frequency, while the lowest change in acceleration was under Kobe Earthquake. The former was calculated as a 102.7% increase, and the latter was a 6.8% decrease. The peak accelerations recorded from A7 were greater than A1, which means that the acceleration amplified while reaching the top of the wall, except for the Kobe Earthquake.

Table 6.17. The peak acceleration measurements under considered input motions for Case 5.

Case 5	İzmit-F	İzmir-F	İzmit-N	El-Centro	Kobe	0.4g-5 Hz	0.3g-10 Hz	0.4g-10 Hz	0.5g-10 Hz	0.4g-15 Hz
	PGA (g)	PGA (g)	PGA (g)	PGA (g)	PGA (g)	PGA (g)	PGA (g)	PGA (g)	PGA (g)	PGA (g)
A1	0.124	0.183	0.220	0.318	0.823	0.400	0.300	0.400	0.500	0.400
A2	0.123	0.181	0.209	0.313	0.800	0.384	0.299	0.400	0.507	0.420
A3	0.133	0.208	0.232	0.322	0.575	0.430	0.346	0.461	0.585	0.500
A4	0.131	0.206	0.229	0.318	0.637	0.422	0.339	0.453	0.567	0.487
A5	0.140	0.231	0.247	0.376	0.658	0.458	0.382	0.524	0.681	0.612
A6	0.165	0.276	0.287	0.457	0.784	0.523	0.462	0.697	0.886	0.845
A7	0.167	0.278	0.286	0.458	0.767	0.520	0.449	0.668	0.845	0.811
A8	0.153	0.253	0.262	0.422	0.738	0.480	0.396	0.593	0.760	0.708
A9	0.127	0.189	0.222	0.327	0.843	0.407	0.314	0.415	0.528	0.431
A10	0.127	0.189	0.221	0.326	0.842	0.406	0.312	0.413	0.524	0.429
A11	0.126	0.189	0.221	0.325	0.841	0.404	0.311	0.411	0.520	0.428
A12	0.130	0.197	0.225	0.336	0.849	0.416	0.327	0.433	0.546	0.461
A13	0.137	0.226	0.241	0.368	0.643	0.465	0.388	0.544	0.721	0.652
A14	0.135	0.218	0.236	0.351	0.650	0.486	0.391	0.643	0.987	0.882
A15	0.133	0.207	0.228	0.341	0.713	0.436	0.351	0.458	0.585	0.536
A16	0.155	0.255	0.268	0.420	0.724	0.529	0.449	0.717	1.011	0.934

In Table 6.18, whereas the maximum spectral acceleration increased at a rate of 73.8% from A1 to A7 under the sinusoidal motion with 0.4g amplitude and 15 Hz frequency, the spectral acceleration change under the far-field Kocaeli earthquake was 0.4% decrease. The

spectral accelerations at the top of the wall were greater than the peak spectral accelerations of input motions, except for the far-field Kocaeli Earthquake.

Table 6.18. The peak spectral acceleration under considered input motions for Case 5.

Case 5	İzmit-F	İzmir-F	İzmit-N	El-Centro	Kobe	0.4g-5 Hz	0.3g-10 Hz	0.4g-10 Hz	0.5g-10 Hz	0.4g-15 Hz
	SA (g)	SA (g)	SA (g)	SA (g)	SA (g)	SA (g)	SA (g)	SA (g)	SA (g)	SA (g)
A1	0.407	0.561	0.905	1.006	2.148	2.456	1.171	2.018	2.047	1.966
A2	0.377	0.534	0.892	0.947	2.033	2.283	1.111	1.917	1.953	1.963
A3	0.407	0.588	1.004	1.036	2.154	2.550	1.249	2.220	2.342	2.374
A4	0.401	0.581	0.996	1.023	2.160	2.528	1.234	2.188	2.308	2.330
A5	0.406	0.653	1.083	1.084	2.357	2.640	1.316	2.418	2.651	2.772
A6	0.408	0.769	1.197	1.311	2.651	2.768	1.425	2.737	3.138	3.477
A7	0.405	0.764	1.191	1.300	2.643	2.752	1.409	2.708	3.098	3.417
A8	0.385	0.701	1.109	1.192	2.493	2.602	1.306	2.504	2.844	3.072
A9	0.404	0.566	0.932	1.010	2.164	2.452	1.187	2.051	2.090	2.075
A10	0.403	0.564	0.931	1.006	2.153	2.443	1.182	2.044	2.084	2.067
A11	0.401	0.562	0.929	1.003	2.143	2.433	1.178	2.037	2.077	2.060
A12	0.402	0.573	0.965	1.015	2.166	2.450	1.203	2.085	2.136	2.171
A13	0.397	0.633	1.055	1.060	2.315	2.637	1.313	2.501	2.871	2.867
A14	0.387	0.616	1.027	1.032	2.288	2.642	1.295	2.663	3.102	3.306
A15	0.394	0.589	1.000	1.014	2.066	2.469	1.228	2.213	2.353	2.535
A16	0.409	0.715	1.151	1.263	2.587	2.876	1.460	2.984	3.616	3.599

In Table 6.19, the amount of wall movement at the wall top was lower than the maximum displacement of the shake table. The highest reduction in displacement was obtained under İzmir Earthquake. However, the lowest reduction was under the sinusoidal motion with 0.4g amplitude and 5 Hz frequency. The greatest and the lowest change in displacement were 28.2% and 10%, respectively.

Table 6.19. The peak displacement under considered input motions for Case 5.

Case 5	İzmit-F	İzmir-F	İzmit-N	El-Centro	Kobe	0.4g-5 Hz	0.3g-10 Hz	0.4g-10 Hz	0.5g-10 Hz	0.4g-15 Hz
	Disp. (cm)	Disp. (cm)	Disp. (cm)	Disp. (cm)	Disp. (cm)	Disp. (cm)	Disp. (cm)	Disp. (cm)	Disp. (cm)	Disp. (cm)
D17	1.21	0.90	1.69	1.79	1.43	1.20	0.85	1.00	1.11	0.90
D18	0.90	0.61	1.40	1.45	1.18	1.05	0.58	0.85	0.96	0.68
D19	0.95	0.63	1.42	1.51	1.24	1.08	0.61	0.88	0.99	0.73

6.3.6. Case 6 under all considered motions

In Case 6, the cushion consisted of TC10 with a thickness of 2 cm. The cushion was placed behind the wall using the method explained in Section 5.2.6. The results under five different earthquake recordings and five different sinusoidal motions were given in Tables 6.20, 6.21, and 6.22.

In Table 6.20, the percentage change in the acceleration from A1 to A7 was greatest under the sinusoidal motion with 0.4g amplitude and 15 Hz frequency, while the lowest change in acceleration was under Kobe Earthquake. The former was calculated as a 143.1% increase, and the latter was a 5.4% decrease. The peak accelerations recorded from A7 were greater than A1, which means that the acceleration amplified while reaching the top of the wall, except for the Kobe Earthquake.

Table 6.20. The peak acceleration measurements under considered input motions for Case 6.

Case 6	İzmit-F	İzmir-F	İzmit-N	El-Centro	Kobe	0.4g-5 Hz	0.3g-10 Hz	0.4g-10 Hz	0.5g-10 Hz	0.4g-15 Hz
	PGA (g)	PGA (g)	PGA (g)	PGA (g)	PGA (g)	PGA (g)	PGA (g)	PGA (g)	PGA (g)	PGA (g)
A1	0.124	0.183	0.220	0.318	0.823	0.400	0.300	0.400	0.500	0.400
A2	0.118	0.186	0.207	0.312	0.794	0.382	0.297	0.401	0.503	0.417
A3	0.126	0.212	0.228	0.332	0.596	0.427	0.339	0.443	0.585	0.514
A4	0.124	0.213	0.226	0.324	0.592	0.421	0.339	0.437	0.596	0.516
A5	0.133	0.266	0.240	0.345	0.632	0.458	0.387	0.507	0.698	0.668
A6	0.152	0.343	0.258	0.396	0.792	0.523	0.461	0.645	0.897	0.964
A7	0.161	0.364	0.268	0.410	0.778	0.526	0.469	0.661	0.885	0.972
A8	0.153	0.347	0.255	0.387	0.728	0.495	0.446	0.624	0.833	0.909
A9	0.125	0.192	0.221	0.327	0.840	0.407	0.313	0.419	0.528	0.435
A10	0.124	0.193	0.221	0.326	0.838	0.405	0.312	0.417	0.524	0.434
A11	0.124	0.193	0.220	0.325	0.835	0.404	0.311	0.415	0.519	0.433
A12	0.125	0.206	0.224	0.335	0.834	0.415	0.326	0.436	0.546	0.476
A13	0.128	0.224	0.229	0.346	0.751	0.437	0.350	0.467	0.596	0.609
A14	0.126	0.246	0.230	0.346	0.669	0.486	0.398	0.588	0.953	0.941
A15	0.128	0.255	0.234	0.339	0.628	0.458	0.380	0.521	0.713	0.611
A16	0.154	0.351	0.258	0.400	0.757	0.561	0.463	0.825	1.248	0.860

In Table 6.21, the spectral accelerations at the top of the wall were greater than the peak spectral accelerations of input motions, except for the far-field Kocaeli Earthquake. Whereas the maximum spectral acceleration increased at a rate of 100.4% from A1 to A7 under the

sinusoidal motion with 0.4g amplitude and 15 Hz frequency, the spectral acceleration change under the far-field Kocaeli Earthquake was a 0.3% decrease.

Table 6.21. The peak spectral acceleration under considered input motions for Case 6.

Case 6	İzmit-F	İzmir-F	İzmit-N	El-Centro	Kobe	0.4g-5 Hz	0.3g-10 Hz	0.4g-10 Hz	0.5g-10 Hz	0.4g-15 Hz
	SA (g)	SA (g)	SA (g)	SA (g)	SA (g)	SA (g)	SA (g)	SA (g)	SA (g)	SA (g)
A1	0.404	0.541	0.849	1.008	2.156	2.461	1.185	1.634	2.060	1.960
A2	0.374	0.540	0.834	0.949	2.036	2.285	1.122	1.547	1.955	1.965
A3	0.404	0.596	0.923	1.035	2.161	2.547	1.258	1.790	2.356	2.454
A4	0.398	0.596	0.917	1.023	2.122	2.514	1.249	1.781	2.373	2.471
A5	0.404	0.758	0.994	1.075	2.354	2.631	1.346	2.004	2.792	3.037
A6	0.405	0.992	1.074	1.138	2.663	2.755	1.459	2.325	3.382	3.896
A7	0.403	1.045	1.089	1.157	2.652	2.744	1.467	2.340	3.419	3.927
A8	0.383	0.997	1.030	1.100	2.506	2.604	1.394	2.218	3.250	3.679
A9	0.402	0.552	0.875	1.013	2.170	2.457	1.201	1.661	2.105	2.094
A10	0.400	0.552	0.874	1.009	2.163	2.447	1.197	1.655	2.098	2.083
A11	0.398	0.552	0.872	1.006	2.156	2.438	1.193	1.650	2.090	2.072
A12	0.399	0.589	0.904	1.018	2.172	2.453	1.218	1.690	2.153	2.229
A13	0.401	0.632	0.943	1.036	2.098	2.511	1.258	1.771	2.354	2.678
A14	0.386	0.696	0.951	1.028	2.292	2.616	1.324	2.208	3.188	3.556
A15	0.396	0.721	0.970	1.053	2.266	2.614	1.318	2.002	2.896	2.818
A16	0.407	1.000	1.070	1.142	2.789	2.899	1.507	2.922	4.317	3.574

In Table 6.22, the amount of wall movement at the top was lower than the maximum displacement of the shake table. The highest reduction in displacement was obtained under the sinusoidal motion with 0.3g amplitude and 10 Hz frequency. However, the lowest reduction was under İzmir Earthquake. The greatest and the lowest change in displacement were 24.7% and 4.4%, respectively.

Table 6.22. The peak displacement under considered input motions for Case 6.

Case 6	İzmit-F	İzmir-F	İzmit-N	El-Centro	Kobe	0.4g-5 Hz	0.3g-10 Hz	0.4g-10 Hz	0.5g-10 Hz	0.4g-15 Hz
	Disp. (cm)	Disp. (cm)	Disp. (cm)	Disp. (cm)	Disp. (cm)	Disp. (cm)	Disp. (cm)	Disp. (cm)	Disp. (cm)	Disp. (cm)
D17	1.21	0.90	1.69	1.79	1.43	1.20	0.85	1.00	1.11	0.90
D18	1.13	0.84	1.54	1.61	1.29	1.02	0.61	0.87	0.98	0.66
D19	1.10	0.86	1.59	1.63	1.32	1.05	0.64	0.90	1.00	0.69

6.3.7. Case 7 under all considered motions

In Case 7, the cushion was composed of TC10 with a thickness of 4 cm. The results under five different earthquake recordings and five different sinusoidal motions were given in Tables 6.23, 6.24, and 6.25.

In Table 6.23, the percentage change in the acceleration from A1 to A7 was greatest under İzmir Earthquake, while the lowest change in acceleration was under Kobe Earthquake. The former was calculated as a 174.1% increase, and the latter was a 2.8% decrease. The peak accelerations recorded from A7 were greater than A1, which means that the acceleration amplified while reaching the top of the wall, except for the Kobe Earthquake.

Table 6.23. The peak acceleration measurements under considered input motions for Case 7.

Case 7	İzmit-F	İzmir-F	İzmit-N	El-Centro	Kobe	0.4g-5 Hz	0.3g-10 Hz	0.4g-10 Hz	0.5g-10 Hz	0.4g-15 Hz
	PGA (g)	PGA (g)	PGA (g)	PGA (g)	PGA (g)	PGA (g)	PGA (g)	PGA (g)	PGA (g)	PGA (g)
A1	0.124	0.183	0.220	0.318	0.823	0.400	0.300	0.400	0.500	0.400
A2	0.122	0.191	0.207	0.313	0.794	0.382	0.299	0.399	0.500	0.418
A3	0.130	0.222	0.224	0.334	0.659	0.427	0.334	0.440	0.580	0.494
A4	0.130	0.229	0.222	0.329	0.675	0.423	0.336	0.444	0.580	0.499
A5	0.143	0.327	0.237	0.386	0.686	0.468	0.395	0.517	0.708	0.628
A6	0.171	0.480	0.276	0.492	0.798	0.545	0.505	0.673	0.894	0.862
A7	0.178	0.502	0.283	0.503	0.800	0.553	0.520	0.684	0.880	0.881
A8	0.169	0.480	0.267	0.477	0.778	0.523	0.495	0.648	0.836	0.838
A9	0.126	0.191	0.220	0.327	0.838	0.406	0.312	0.417	0.524	0.429
A10	0.126	0.192	0.220	0.326	0.836	0.405	0.311	0.415	0.521	0.428
A11	0.126	0.193	0.219	0.326	0.834	0.403	0.310	0.414	0.519	0.426
A12	0.129	0.212	0.222	0.338	0.834	0.414	0.325	0.433	0.544	0.458
A13	0.132	0.234	0.223	0.346	0.765	0.422	0.336	0.447	0.562	0.490
A14	0.133	0.276	0.223	0.350	0.686	0.455	0.364	0.503	0.747	0.676
A15	0.140	0.329	0.237	0.394	0.694	0.484	0.399	0.566	0.742	0.640
A16	0.154	0.413	0.252	0.448	0.729	0.547	0.480	0.758	1.039	0.990

In Table 6.24, the spectral accelerations at the top of the wall were greater than the peak spectral accelerations of input motions. However, the maximum spectral acceleration recorded by A1 and A7 were the same under the far-field Kocaeli Earthquake. The maximum spectral acceleration increased at a rate of 161.2% from A1 to A7 under İzmir Earthquake.

Table 6.24. The peak spectral acceleration under considered input motions for Case 7.

Case 7	İzmit-F	İzmir-F	İzmit-N	El-Centro	Kobe	0.4g-5 Hz	0.3g-10 Hz	0.4g-10 Hz	0.5g-10 Hz	0.4g-15 Hz
	SA (g)	SA (g)	SA (g)	SA (g)	SA (g)	SA (g)	SA (g)	SA (g)	SA (g)	SA (g)
A1	0.420	0.587	0.879	1.006	2.163	2.453	1.176	1.645	2.052	1.966
A2	0.389	0.575	0.865	0.947	2.043	2.278	1.114	1.559	1.950	1.950
A3	0.419	0.657	0.967	1.043	2.157	2.542	1.254	1.814	2.357	2.379
A4	0.414	0.671	0.971	1.037	2.155	2.523	1.254	1.818	2.381	2.380
A5	0.420	0.884	1.091	1.128	2.416	2.668	1.376	2.105	2.873	2.988
A6	0.422	1.419	1.241	1.462	2.775	2.830	1.527	2.510	3.573	3.940
A7	0.420	1.534	1.239	1.506	2.790	2.824	1.538	2.532	3.607	3.975
A8	0.399	1.493	1.197	1.442	2.661	2.685	1.467	2.402	3.425	3.741
A9	0.417	0.593	0.904	1.010	2.171	2.448	1.190	1.669	2.092	2.068
A10	0.416	0.592	0.905	1.007	2.164	2.437	1.187	1.663	2.084	2.063
A11	0.414	0.592	0.905	1.003	2.156	2.426	1.184	1.658	2.075	2.059
A12	0.415	0.641	0.941	1.017	2.181	2.445	1.208	1.699	2.140	2.172
A13	0.410	0.696	0.970	1.019	2.093	2.446	1.221	1.727	2.210	2.296
A14	0.401	0.733	1.002	1.042	2.200	2.527	1.271	1.944	2.693	2.791
A15	0.415	0.860	1.081	1.128	2.423	2.692	1.370	2.172	3.113	2.919
A16	0.413	1.193	1.155	1.346	2.695	2.825	1.498	2.711	3.990	3.846

In Table 6.25, the highest reduction in displacement was obtained under the sinusoidal motion with 0.3g amplitude and 10 Hz frequency. However, the lowest reduction was under Kobe Earthquake. The greatest and the lowest change in displacement were 27.1% and 2.8%, respectively. The amount of wall movement at the wall top was lower than the maximum displacement of the shake table.

Table 6.25. The peak displacement under considered input motions for Case 7.

Case 7	İzmit-F	İzmir-F	İzmit-N	El-Centro	Kobe	0.4g-5 Hz	0.3g-10 Hz	0.4g-10 Hz	0.5g-10 Hz	0.4g-15 Hz
	Disp. (cm)	Disp. (cm)	Disp. (cm)	Disp. (cm)	Disp. (cm)	Disp. (cm)	Disp. (cm)	Disp. (cm)	Disp. (cm)	Disp. (cm)
D17	1.21	0.90	1.69	1.79	1.43	1.20	0.85	1.00	1.11	0.90
D18	1.14	0.84	1.57	1.65	1.37	1.04	0.59	0.86	0.97	0.67
D19	1.16	0.86	1.59	1.68	1.39	1.06	0.62	0.89	1.00	0.71

6.3.8. Case 8 under all considered motions

In Case 8, the cushion was composed of TC20 with a thickness of 2 cm. The results under five different earthquake recordings and five different sinusoidal motions were given in Tables 6.26, 6.27, and 6.28.

In Table 6.26, the percentage change in the acceleration from A1 to A7 was greatest under İzmir Earthquake, while the lowest change in acceleration was under Kobe Earthquake. The former was calculated as a 133% increase, and the latter was a 1.8% decrease. The peak accelerations recorded from A7 were greater than A1, which means that the acceleration amplified while reaching the top of the wall, except for the Kobe Earthquake.

Table 6.26. The peak acceleration measurements under considered input motions for Case 8.

Case 8	İzmit-F	İzmir-F	İzmit-N	El-Centro	Kobe	0.4g-5 Hz	0.3g-10 Hz	0.4g-10 Hz	0.5g-10 Hz	0.4g-15 Hz
	PGA (g)	PGA (g)	PGA (g)	PGA (g)	PGA (g)	PGA (g)	PGA (g)	PGA (g)	PGA (g)	PGA (g)
A1	0.124	0.183	0.220	0.318	0.823	0.400	0.300	0.400	0.500	0.400
A2	0.124	0.181	0.210	0.310	0.797	0.382	0.297	0.399	0.500	0.407
A3	0.133	0.216	0.233	0.327	0.625	0.432	0.348	0.440	0.592	0.499
A4	0.132	0.213	0.229	0.318	0.580	0.426	0.345	0.438	0.582	0.519
A5	0.147	0.290	0.252	0.394	0.628	0.463	0.397	0.513	0.695	0.652
A6	0.177	0.412	0.288	0.496	0.823	0.530	0.495	0.663	0.882	0.904
A7	0.184	0.426	0.291	0.507	0.809	0.535	0.496	0.666	0.861	0.920
A8	0.173	0.402	0.273	0.480	0.756	0.508	0.466	0.628	0.807	0.864
A9	0.128	0.190	0.223	0.326	0.841	0.407	0.314	0.418	0.525	0.429
A10	0.127	0.190	0.222	0.326	0.840	0.406	0.313	0.416	0.522	0.426
A11	0.127	0.189	0.221	0.325	0.839	0.404	0.311	0.414	0.518	0.423
A12	0.131	0.199	0.227	0.338	0.847	0.416	0.327	0.435	0.543	0.455
A13	0.133	0.220	0.229	0.342	0.722	0.429	0.347	0.451	0.573	0.562
A14	0.135	0.249	0.233	0.352	0.662	0.456	0.371	0.509	0.771	0.829
A15	0.146	0.307	0.253	0.416	0.639	0.477	0.406	0.585	0.813	0.753
A16	0.160	0.355	0.270	0.452	0.662	0.534	0.459	0.735	1.038	0.936

In Table 6.27, whereas the maximum spectral acceleration increased at a rate of 165% from A1 to A7 under İzmir Earthquake, the spectral acceleration change under the far-field Kocaeli Earthquake was a 0.3% decrease. The spectral accelerations at the top of the wall were greater than the peak spectral accelerations of input motions, except for the far-field Kocaeli Earthquake

Table 6.27. The peak spectral acceleration under considered input motions for Case 8.

Case 8	İzmit-F	İzmir-F	İzmit-N	El-Centro	Kobe	0.4g-5 Hz	0.3g-10 Hz	0.4g-10 Hz	0.5g-10 Hz	0.4g-15 Hz
	SA (g)	SA (g)	SA (g)	SA (g)	SA (g)	SA (g)	SA (g)	SA (g)	SA (g)	SA (g)
A1	0.408	0.520	0.878	1.027	2.155	2.467	1.169	1.615	2.047	1.957
A2	0.377	0.508	0.861	0.966	2.033	2.290	1.106	1.530	1.942	1.949
A3	0.407	0.592	0.980	1.063	2.163	2.556	1.253	1.809	2.389	2.391
A4	0.402	0.590	0.968	1.047	2.128	2.529	1.244	1.793	2.385	2.476
A5	0.407	0.835	1.082	1.149	2.350	2.645	1.345	2.048	2.826	3.016
A6	0.409	1.303	1.222	1.448	2.650	2.770	1.474	2.405	3.446	3.866
A7	0.406	1.378	1.234	1.481	2.639	2.760	1.474	2.406	3.454	3.939
A8	0.386	1.304	1.164	1.403	2.495	2.621	1.398	2.277	3.273	3.731
A9	0.405	0.526	0.906	1.032	2.168	2.462	1.186	1.643	2.088	2.080
A10	0.403	0.525	0.905	1.028	2.160	2.452	1.181	1.636	2.080	2.070
A11	0.402	0.524	0.903	1.025	2.152	2.443	1.176	1.630	2.071	2.060
A12	0.402	0.563	0.940	1.037	2.175	2.458	1.201	1.670	2.134	2.187
A13	0.392	0.599	0.964	1.027	2.051	2.453	1.212	1.732	2.316	2.583
A14	0.387	0.662	0.993	1.052	2.168	2.523	1.249	1.934	2.737	3.242
A15	0.400	0.881	1.085	1.192	2.381	2.681	1.351	2.206	3.276	3.204
A16	0.406	1.113	1.153	1.367	2.602	2.823	1.444	2.670	3.931	3.697

In Table 6.28, the highest reduction in displacement was obtained under the sinusoidal motion with 0.3g amplitude and 10 Hz frequency. However, the lowest reduction was under El-Centro Earthquake. The greatest and the lowest change in displacement were 28.2% and 3.9%, respectively. The amount of wall movement at the wall top was lower than the maximum displacement of the shake table.

Table 6.28. The peak displacement under considered input motions for Case 8.

Case 8	İzmit-F	İzmir-F	İzmit-N	El-Centro	Kobe	0.4g-5 Hz	0.3g-10 Hz	0.4g-10 Hz	0.5g-10 Hz	0.4g-15 Hz
	Disp. (cm)	Disp. (cm)	Disp. (cm)	Disp. (cm)	Disp. (cm)	Disp. (cm)	Disp. (cm)	Disp. (cm)	Disp. (cm)	Disp. (cm)
D17	1.21	0.90	1.69	1.79	1.43	1.20	0.85	1.00	1.11	0.90
D18	1.12	0.77	1.50	1.70	1.28	1.02	0.60	0.87	0.95	0.67
D19	1.14	0.79	1.54	1.72	1.33	1.06	0.61	0.90	0.98	0.70

6.3.9. Case 9 under all considered motions

In Case 9, the cushion was composed of TC20 with a thickness of 4 cm. The results under five different earthquake recordings and five different sinusoidal motions were given in Tables 6.29, 6.30, and 6.31.

In Table 6.29, the percentage change in the acceleration from A1 to A7 was greatest under İzmir Earthquake, while the lowest change in acceleration was under Kobe Earthquake. The former was calculated as a 140.5% increase, and the latter was a 1.5% decrease. The peak accelerations recorded from A7 were greater than A1, which means that the acceleration amplified while reaching the top of the wall, except for the Kobe Earthquake.

Table 6.29. The peak acceleration measurements under considered input motions for Case 9.

Case 9	İzmit-F	İzmir-F	İzmit-N	El-Centro	Kobe	0.4g-5 Hz	0.3g-10 Hz	0.4g-10 Hz	0.5g-10 Hz	0.4g-15 Hz
	PGA (g)	PGA (g)	PGA (g)	PGA (g)	PGA (g)	PGA (g)	PGA (g)	PGA (g)	PGA (g)	PGA (g)
A1	0.124	0.183	0.220	0.318	0.823	0.400	0.300	0.400	0.500	0.400
A2	0.120	0.178	0.207	0.314	0.796	0.385	0.297	0.400	0.499	0.403
A3	0.129	0.209	0.228	0.313	0.640	0.427	0.339	0.442	0.595	0.497
A4	0.128	0.206	0.225	0.312	0.621	0.418	0.332	0.436	0.579	0.495
A5	0.137	0.288	0.242	0.370	0.655	0.461	0.392	0.500	0.726	0.624
A6	0.156	0.435	0.294	0.498	0.842	0.537	0.514	0.653	0.970	0.856
A7	0.157	0.440	0.299	0.496	0.811	0.531	0.505	0.643	0.943	0.864
A8	0.148	0.410	0.280	0.460	0.743	0.490	0.459	0.589	0.867	0.802
A9	0.126	0.188	0.221	0.328	0.843	0.408	0.312	0.417	0.524	0.421
A10	0.126	0.187	0.220	0.328	0.841	0.407	0.311	0.415	0.521	0.420
A11	0.126	0.187	0.219	0.327	0.838	0.405	0.310	0.414	0.518	0.419
A12	0.129	0.194	0.222	0.341	0.848	0.417	0.326	0.434	0.543	0.446
A13	0.133	0.218	0.227	0.349	0.731	0.439	0.352	0.472	0.617	0.558
A14	0.130	0.255	0.223	0.355	0.675	0.487	0.401	0.624	1.023	0.877
A15	0.134	0.305	0.238	0.398	0.669	0.491	0.422	0.624	0.853	0.758
A16	0.140	0.352	0.248	0.432	0.698	0.533	0.464	0.747	1.065	0.951

In Table 6.30, the maximum spectral acceleration increased at a rate of 136.4% from A1 to A7 under İzmir Earthquake. The peak spectral acceleration of A1 and A7 were identical under the far-field Kocaeli Earthquake. The spectral accelerations at the top of the wall were greater than the peak spectral accelerations of input motions, except for the far-field Kocaeli Earthquake

Table 6.30. The peak spectral acceleration under considered input motions for Case 9.

Case 9	İzmit-F	İzmir-F	İzmit-N	El-Centro	Kobe	0.4g-5 Hz	0.3g-10 Hz	0.4g-10 Hz	0.5g-10 Hz	0.4g-15 Hz
	SA (g)	SA (g)	SA (g)	SA (g)	SA (g)	SA (g)	SA (g)	SA (g)	SA (g)	SA (g)
A1	0.399	0.575	0.857	0.985	2.187	2.455	1.192	1.653	2.075	1.942
A2	0.369	0.560	0.842	0.927	2.070	2.280	1.129	1.571	1.974	1.934
A3	0.398	0.648	0.946	1.023	2.188	2.547	1.282	1.849	2.414	2.389
A4	0.392	0.638	0.932	1.007	2.134	2.510	1.260	1.805	2.363	2.354
A5	0.399	0.810	1.054	1.093	2.386	2.647	1.386	2.095	2.841	2.938
A6	0.401	1.321	1.221	1.368	2.729	2.795	1.555	2.500	3.519	3.858
A7	0.399	1.360	1.223	1.368	2.696	2.776	1.541	2.471	3.482	3.844
A8	0.379	1.270	1.151	1.272	2.522	2.625	1.445	2.300	3.236	3.530
A9	0.396	0.581	0.883	0.990	2.206	2.451	1.209	1.682	2.118	2.055
A10	0.394	0.579	0.881	0.987	2.197	2.441	1.205	1.676	2.110	2.047
A11	0.393	0.578	0.880	0.984	2.187	2.432	1.200	1.670	2.103	2.039
A12	0.393	0.622	0.913	0.996	2.215	2.448	1.226	1.712	2.163	2.155
A13	0.395	0.686	0.960	1.014	2.140	2.510	1.243	1.825	2.448	2.572
A14	0.374	0.716	0.972	1.032	2.350	2.623	1.336	2.277	3.311	3.397
A15	0.388	0.844	1.043	1.095	2.473	2.706	1.419	2.358	3.474	3.247
A16	0.393	1.027	1.103	1.231	2.660	2.817	1.491	2.714	4.011	3.813

In Table 6.31, the highest reduction in displacement was obtained under the sinusoidal motion with 0.3g amplitude and 10 Hz frequency; however, the lowest reduction was under El-Centro Earthquake. The greatest and the lowest change in displacement were 30.6% and 5%, respectively. The amount of wall movement at the wall top was lower than the maximum displacement of the shake table.

Table 6.31. The peak displacement under considered input motions for Case 9.

Case 9	İzmit-F	İzmir-F	İzmit-N	El-Centro	Kobe	0.4g-5 Hz	0.3g-10 Hz	0.4g-10 Hz	0.5g-10 Hz	0.4g-15 Hz
	Disp. (cm)	Disp. (cm)	Disp. (cm)	Disp. (cm)	Disp. (cm)	Disp. (cm)	Disp. (cm)	Disp. (cm)	Disp. (cm)	Disp. (cm)
D17	1.21	0.90	1.69	1.79	1.43	1.20	0.85	1.00	1.11	0.90
D18	1.11	0.82	1.54	1.62	1.24	1.03	0.57	0.85	0.95	0.68
D19	1.13	0.85	1.57	1.70	1.29	1.05	0.59	0.88	0.97	0.72

6.3.10. Case 10 under all considered motions

In Case 10, the cushion was composed of TC30 with a thickness of 2 cm. The results under five different earthquake recordings and five different sinusoidal motions were given in Tables 6.32, 6.33, and 6.34.

In Table 6.32, the percentage change in the acceleration from A1 to A7 was greatest under İzmir Earthquake, while the lowest change in acceleration was under Kobe Earthquake. The former was calculated as a 126.7% increase, and the latter was a 4.3% decrease. The peak accelerations recorded from A7 were greater than A1, which means that the acceleration amplified while reaching the top of the wall, except for the Kobe Earthquake.

Table 6.32. The peak acceleration measurements under considered input motions for Case 10.

Case 10	İzmit-F	İzmir-F	İzmit-N	El-Centro	Kobe	0.4g-5 Hz	0.3g-10 Hz	0.4g-10 Hz	0.5g-10 Hz	0.4g-15 Hz
	PGA (g)	PGA (g)	PGA (g)	PGA (g)	PGA (g)	PGA (g)	PGA (g)	PGA (g)	PGA (g)	PGA (g)
A1	0.124	0.183	0.220	0.318	0.823	0.400	0.300	0.400	0.500	0.400
A2	0.122	0.182	0.211	0.314	0.803	0.380	0.297	0.398	0.502	0.418
A3	0.131	0.219	0.232	0.334	0.605	0.424	0.336	0.433	0.586	0.503
A4	0.130	0.223	0.231	0.331	0.592	0.422	0.337	0.431	0.593	0.494
A5	0.136	0.292	0.251	0.367	0.622	0.452	0.375	0.495	0.732	0.622
A6	0.159	0.405	0.288	0.450	0.785	0.508	0.435	0.638	0.959	0.830
A7	0.162	0.415	0.292	0.455	0.788	0.512	0.439	0.651	0.961	0.819
A8	0.154	0.389	0.276	0.427	0.747	0.484	0.416	0.615	0.921	0.772
A9	0.127	0.191	0.221	0.329	0.847	0.406	0.314	0.417	0.527	0.432
A10	0.126	0.191	0.220	0.327	0.843	0.404	0.312	0.415	0.522	0.429
A11	0.126	0.190	0.219	0.325	0.838	0.402	0.310	0.412	0.518	0.426
A12	0.130	0.204	0.227	0.337	0.853	0.412	0.325	0.431	0.543	0.457
A13	0.131	0.224	0.232	0.342	0.767	0.420	0.337	0.442	0.553	0.485
A14	0.131	0.248	0.234	0.344	0.680	0.448	0.374	0.531	0.868	0.739
A15	0.132	0.290	0.245	0.371	0.615	0.445	0.368	0.533	0.714	0.637
A16	0.138	0.336	0.255	0.399	0.638	0.468	0.390	0.625	0.918	0.864

In Table 6.33, the spectral accelerations at the top of the wall were greater than the peak spectral accelerations of input motions, except for the far-field Kocaeli Earthquake. The maximum spectral acceleration increased at a rate of 138% from A1 to A7 under İzmir Earthquake. The peak spectral acceleration of A1 and A7 were virtually identical under the far-field Kocaeli Earthquake.

Table 6.33. The peak spectral acceleration under considered input motions for Case 10.

Case 10	İzmit-F	İzmir-F	İzmit-N	El-Centro	Kobe	0.4g-5 Hz	0.3g-10 Hz	0.4g-10 Hz	0.5g-10 Hz	0.4g-15 Hz
	SA (g)	SA (g)	SA (g)	SA (g)	SA (g)	SA (g)	SA (g)	SA (g)	SA (g)	SA (g)
A1	0.406	0.537	0.945	0.990	2.109	2.467	1.170	1.609	2.030	1.961
A2	0.375	0.526	0.928	0.932	1.990	2.291	1.108	1.523	1.928	1.940
A3	0.405	0.591	1.036	1.015	2.093	2.506	1.234	1.753	2.333	2.398
A4	0.399	0.593	1.032	1.004	2.093	2.481	1.228	1.756	2.345	2.380
A5	0.405	0.827	1.134	1.078	2.268	2.551	1.302	1.943	2.757	2.949
A6	0.406	1.233	1.266	1.306	2.503	2.615	1.393	2.237	3.352	3.884
A7	0.404	1.279	1.272	1.318	2.507	2.603	1.392	2.247	3.368	3.855
A8	0.383	1.200	1.202	1.240	2.381	2.474	1.322	2.133	3.191	3.593
A9	0.403	0.544	0.976	0.995	2.123	2.462	1.186	1.637	2.075	2.069
A10	0.401	0.542	0.973	0.991	2.113	2.451	1.181	1.629	2.064	2.056
A11	0.399	0.540	0.969	0.987	2.103	2.440	1.175	1.620	2.053	2.043
A12	0.400	0.574	1.007	1.000	2.132	2.456	1.198	1.658	2.111	2.150
A13	0.393	0.605	1.033	0.996	2.035	2.432	1.204	1.682	2.181	2.269
A14	0.381	0.662	1.052	0.988	2.201	2.427	1.244	2.137	2.941	2.890
A15	0.390	0.802	1.103	1.066	2.249	2.472	1.263	1.977	2.995	2.898
A16	0.390	0.995	1.152	1.173	2.396	2.518	1.313	2.239	3.579	3.460

In Table 6.34, the greatest and the lowest change in displacement were 23.5% and 3.3%, respectively. The highest reduction in displacement was obtained under the sinusoidal motion with 0.3g amplitude and 10 Hz frequency. However, the lowest reduction was under İzmir Earthquake. The amount of wall movement at the wall top was lower than the maximum displacement of the shake table.

Table 6.34. The peak displacement under considered input motions for Case 10.

Case 10	İzmit-F	İzmir-F	İzmit-N	El-Centro	Kobe	0.4g-5 Hz	0.3g-10 Hz	0.4g-10 Hz	0.5g-10 Hz	0.4g-15 Hz
	Disp. (cm)	Disp. (cm)	Disp. (cm)	Disp. (cm)	Disp. (cm)	Disp. (cm)	Disp. (cm)	Disp. (cm)	Disp. (cm)	Disp. (cm)
D17	1.21	0.90	1.69	1.79	1.43	1.20	0.85	1.00	1.11	0.90
D18	1.05	0.83	1.45	1.60	1.21	1.01	0.61	0.86	0.92	0.69
D19	1.11	0.87	1.51	1.64	1.27	1.04	0.65	0.89	0.95	0.72

6.3.11. Case 11 under all considered motions

In Case 11, the cushion was composed of TC30 with a thickness of 4 cm.. The results under five different earthquake recordings and five different sinusoidal motions were given in Tables 6.35, 6.36, and 6.37.

In Table 6.35, the percentage change in the acceleration from A1 to A7 was greatest under İzmir Earthquake, while the lowest change in acceleration was under Kobe Earthquake. The former was calculated as a 144% increase, and the latter was a 0.3% decrease. The peak accelerations recorded from A7 were greater than A1, which means that the acceleration amplified while reaching the top of the wall, except for the Kobe Earthquake.

Table 6.35. The peak acceleration measurements under considered input motions for Case 11.

Case 11	İzmit-F	İzmir-F	İzmit-N	El-Centro	Kobe	0.4g-5 Hz	0.3g-10 Hz	0.4g-10 Hz	0.5g-10 Hz	0.4g-15 Hz
	PGA (g)	PGA (g)	PGA (g)	PGA (g)	PGA (g)	PGA (g)	PGA (g)	PGA (g)	PGA (g)	PGA (g)
A1	0.124	0.183	0.220	0.318	0.823	0.400	0.300	0.400	0.500	0.400
A2	0.119	0.181	0.207	0.314	0.797	0.382	0.299	0.401	0.499	0.409
A3	0.128	0.212	0.228	0.308	0.569	0.417	0.338	0.434	0.594	0.503
A4	0.127	0.217	0.227	0.305	0.567	0.414	0.341	0.435	0.595	0.493
A5	0.132	0.295	0.246	0.370	0.619	0.456	0.388	0.520	0.752	0.613
A6	0.156	0.436	0.280	0.486	0.829	0.529	0.497	0.679	1.016	0.825
A7	0.161	0.447	0.283	0.489	0.820	0.531	0.503	0.680	1.007	0.813
A8	0.155	0.425	0.269	0.462	0.773	0.503	0.479	0.647	0.950	0.753
A9	0.126	0.187	0.221	0.330	0.846	0.407	0.314	0.421	0.525	0.424
A10	0.125	0.187	0.220	0.329	0.842	0.405	0.313	0.418	0.521	0.422
A11	0.125	0.187	0.220	0.328	0.838	0.404	0.311	0.416	0.517	0.420
A12	0.127	0.204	0.223	0.341	0.852	0.414	0.327	0.435	0.541	0.450
A13	0.125	0.222	0.224	0.341	0.718	0.422	0.337	0.443	0.559	0.490
A14	0.127	0.251	0.232	0.333	0.666	0.473	0.376	0.534	0.833	0.779
A15	0.131	0.312	0.246	0.396	0.620	0.491	0.410	0.587	0.773	0.656
A16	0.135	0.371	0.261	0.433	0.683	0.550	0.482	0.803	1.048	0.958

In Table 6.36, the spectral accelerations at the top of the wall were greater than the peak spectral accelerations of input motions, except for the far-field Kocaeli Earthquake. The maximum spectral acceleration increased at a rate of 107.3% from A1 to A7 under İzmir Earthquake. The peak spectral acceleration of A1 and A7 were in really close proximity under the far-field Kocaeli Earthquake.

Table 6.36. The peak spectral acceleration under considered input motions for Case 11.

Case 11	İzmit-F	İzmir-F	İzmit-N	El-Centro	Kobe	0.4g-5 Hz	0.3g-10 Hz	0.4g-10 Hz	0.5g-10 Hz	0.4g-15 Hz
	SA (g)	SA (g)	SA (g)	SA (g)	SA (g)	SA (g)	SA (g)	SA (g)	SA (g)	SA (g)
A1	0.396	0.598	0.879	0.993	2.143	2.464	1.207	1.649	2.056	1.957
A2	0.367	0.568	0.862	0.933	2.024	2.287	1.141	1.563	1.953	1.936
A3	0.396	0.640	0.964	1.013	2.123	2.552	1.297	1.827	2.280	2.392
A4	0.391	0.656	0.967	1.006	2.106	2.528	1.299	1.830	2.265	2.386
A5	0.396	0.826	1.086	1.082	2.295	2.642	1.415	2.087	2.648	2.886
A6	0.398	1.186	1.254	1.378	2.548	2.767	1.571	2.443	3.193	3.689
A7	0.396	1.240	1.267	1.397	2.541	2.757	1.575	2.451	3.184	3.668
A8	0.376	1.190	1.206	1.324	2.407	2.619	1.500	2.328	3.006	3.438
A9	0.394	0.605	0.907	0.998	2.161	2.460	1.226	1.680	2.098	2.068
A10	0.392	0.603	0.905	0.994	2.152	2.450	1.220	1.672	2.088	2.057
A11	0.391	0.601	0.903	0.990	2.144	2.440	1.215	1.665	2.079	2.045
A12	0.391	0.622	0.939	1.003	2.173	2.456	1.241	1.705	2.133	2.153
A13	0.379	0.667	0.954	0.985	2.020	2.423	1.238	1.717	2.216	2.322
A14	0.378	0.729	0.993	1.020	2.191	2.580	1.329	2.045	2.763	2.999
A15	0.388	0.834	1.085	1.117	2.369	2.729	1.456	2.306	3.226	2.940
A16	0.392	0.998	1.166	1.335	2.598	2.906	1.586	2.858	4.067	3.765

In Table 6.37, the greatest and the lowest change in displacement were 27.1% and 4.4%, respectively. The highest reduction in displacement was obtained under the sinusoidal motion with 0.3g amplitude and 10 Hz frequency; however, the lowest reduction was under İzmir Earthquake. The amount of wall movement at the wall top was lower than the maximum displacement of the shake table.

Table 6.37. The peak displacement under considered input motions for Case 11.

Case 11	İzmit-F	İzmir-F	İzmit-N	El-Centro	Kobe	0.4g-5 Hz	0.3g-10 Hz	0.4g-10 Hz	0.5g-10 Hz	0.4g-15 Hz
	Disp. (cm)	Disp. (cm)	Disp. (cm)	Disp. (cm)	Disp. (cm)	Disp. (cm)	Disp. (cm)	Disp. (cm)	Disp. (cm)	Disp. (cm)
D17	1.21	0.90	1.69	1.79	1.43	1.20	0.85	1.00	1.11	0.90
D18	1.08	0.84	1.48	1.62	1.18	1.00	0.58	0.83	0.91	0.66
D19	1.13	0.86	1.52	1.66	1.22	1.03	0.62	0.86	0.94	0.71

7. DISCUSSION

7.1. General

The experimental study was performed on the 1/25 scaled retaining wall model with sand backfill by using the shake table. The tests were carried out in order to investigate the effects of the cushion type. Two different cushion materials, EPS geofoam and tire crumb-sand mixture, were studied in this thesis. The cushion thickness, EPS geofoam density, the mixture ratio of sand and tire crumb, earthquake characteristics, and frequency and amplitude of sinusoidal motions were investigated. In this section, the change in the transmitted accelerations, spectral accelerations, and displacement values are evaluated depending on investigated parameters listed in Table 6.2. The accelerometer, A7, and the displacement sensor, D19, were selected to evaluate the results because they measured acceleration and displacement at the top of the retaining wall. The percentage change in accelerations and displacements is tabulated. Additionally, the cases where the effect of the cushion layer was observed as the most and the least effective on the seismic behavior of the wall are compared by giving the graphical results side by side.

In the tables, the negative values represent a percentage decrease, and the positive values express a percentage increase in maximum acceleration, maximum spectral acceleration, and maximum displacement. The percentage changes are calculated by comparing the improved cases with Case 1. For all cases, the percentage changes were determined as

$$Percentage\ (\%)\ change = 100 * \left(\frac{Response\ of\ Case\ n}{Response\ of\ Case\ 1} - 1\right). \quad (7.1)$$

In this expression, n expresses the case number which varies from 2 to 11.

7.2. The Effects of Cushion Type

Two different materials were used as a cushion layer behind the scaled wall model. The first material was EPS geofoam with various densities, and the other one was a sand-tire crumb mixture having various mixing ratios of sand and tire crumb. The cushion layers were designed with two different thicknesses, such as 2 and 4 cm. The effects of cushion type are investigated by comparing improved cases with the control case. The comparison is made for five different real earthquake recordings and five different sinusoidal motions with various amplitudes and frequencies.

7.2.1. The Cushion Layers with a Thickness of 2 cm

In this section, the cushions having a thickness of 2 cm were examined. The cushion of Cases 2, 4, and 5 were composed of EPS geofoam with 10, 20, and 30 kg/m^3 density, respectively, and Cases 6, 8, and 10 were established with the cushions consisting of sand-tire crumb mixture having 10%, 20%, and 30% tire crumb by weight. The improved cases (Cases 2, 4, 5, 6, 8, and 10) were compared with Case 1 in order to calculate the percentage change due to the inclusion of cushion layers with a thickness of 2 cm.

The percentage change in acceleration recorded by A7 is given in Table 7.1. The cushion with EPS geofoam performed better than the other type of cushion in general. Under İzmir and El-Centro Earthquakes, the EPS geofoam cushion decreased the acceleration at the top of the wall by 36.3% and 34.4%, respectively. However, under near-field Kocaeli Earthquake and El-Centro Earthquakes, TC10 cushion (Case 6) caused more reduction in acceleration than EPS30 cushion (Case 5). Consequently, it is indicated that the cushion consisting of EPS geofoam resulted in more enhancement in the seismic performance of the wall model than the tire waste-sand cushion, considering the percentage changes in acceleration.

Table 7.1. The percentage change in PGA of A7 (Case 1 to Cases 2, 4, 5, 6, 8, and 10).

Input motion	İzmit-F	İzmir-F	İzmit-N	El-Centro	Kobe	0.4g-5 Hz	0.3g-10 Hz	0.4g-10 Hz	0.5g-10 Hz	0.4g-15 Hz
Case1-2	+0.5	-0.2	-9.9	-9.4	-0.7	-7.3	-7.7	-16.7	-21.8	-14.5
Case1-4	-3.7	-28.3	-16.2	-34.4	-8.2	-6.2	-12.9	-19.1	-15.3	-18.9
Case1-5	+2.9	-36.3	-8.7	-16.3	-12.0	-2.9	-8.3	-9.0	-15.4	-9.8
Case1-6	-1.0	-16.5	-14.6	-25.1	-10.7	-1.7	-4.2	-10.0	-11.4	+8.2
Case1-8	+13.3	-2.2	-7.4	-7.4	-7.2	-0.1	+1.3	-9.2	-13.8	+2.4
Case1-10	0.0	-4.9	-6.9	-16.8	-9.6	-4.5	-10.4	-11.2	-3.8	-8.9

A comparison of the cases that caused the greatest and lowest reduction in acceleration at the top of the wall for each input motion is given between Figures 7.1 and 7.10. The improvement in seismic performance due to cushion layer was clear in Figure 7.2.

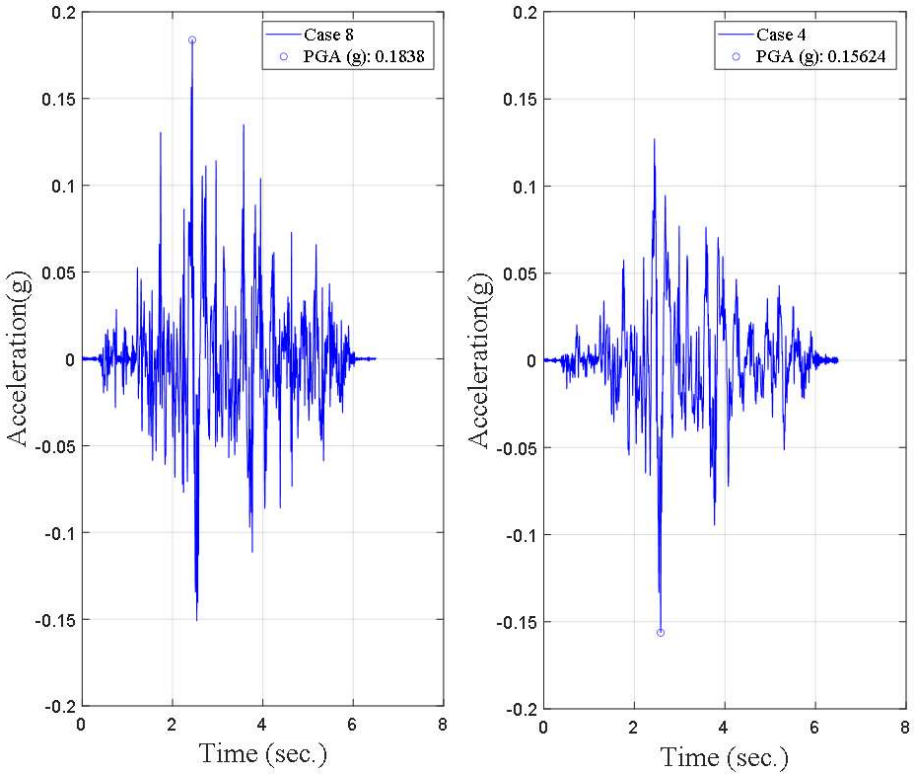

Figure 7.1. The ATH of Case 8 and Case 4 under the far- field Kocaeli Earthquake.

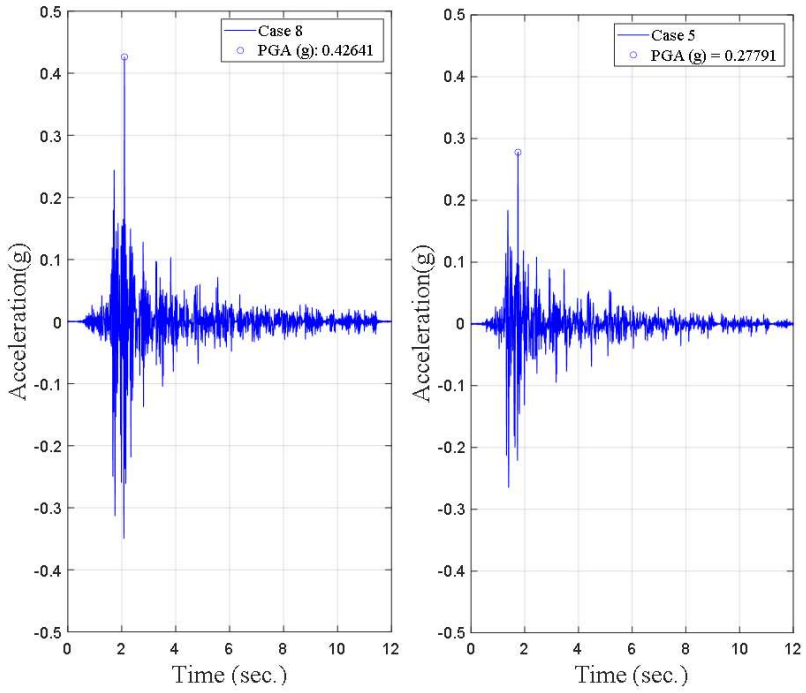

Figure 7.2. The ATH of Case 8 and Case 5 under the far- field İzmir Earthquake.

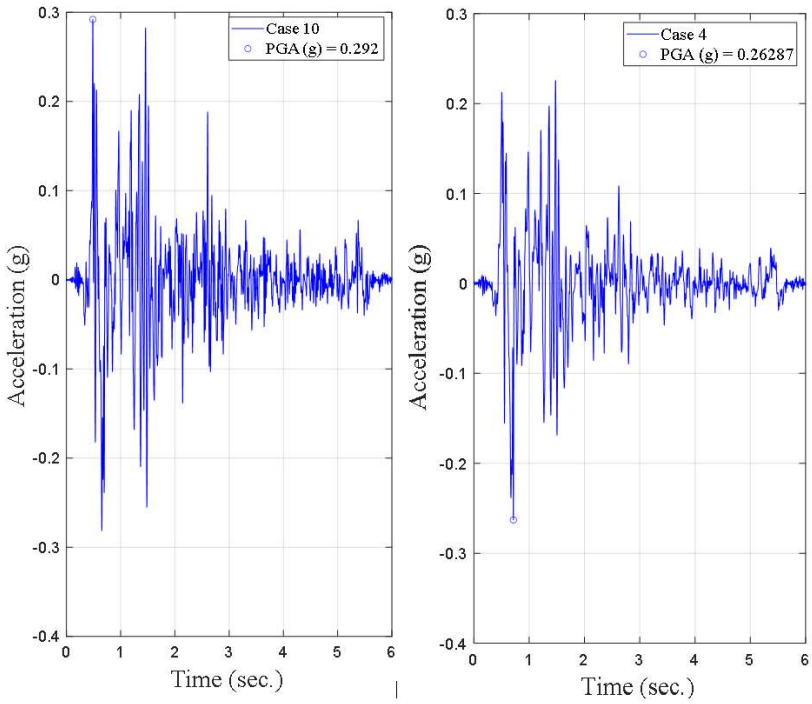

Figure 7.3. The ATH of Case 10 and Case 4 under the near- field Kocaeli Earthquake.

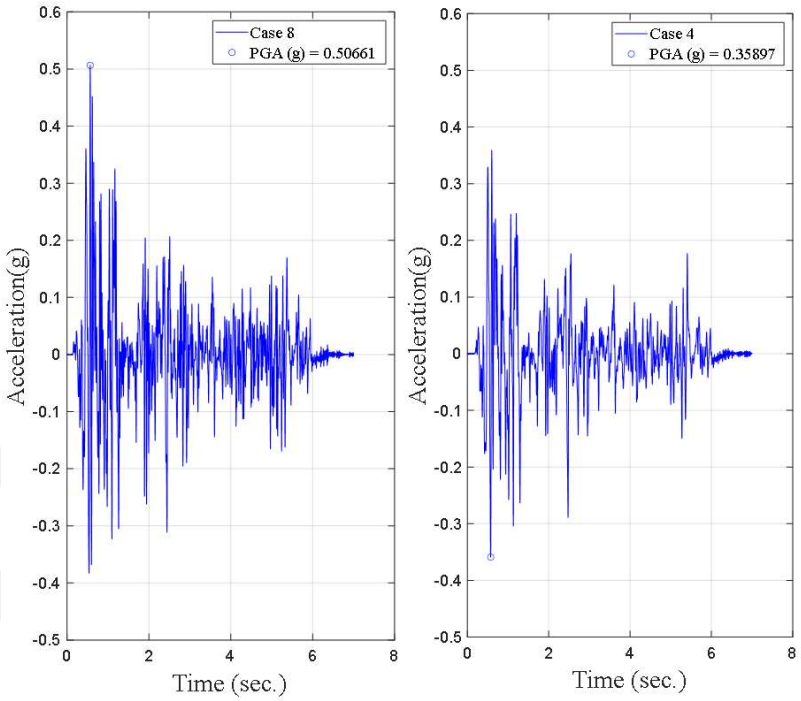

Figure 7.4. The ATH of Case 8 and Case 4 under El-Centro Earthquake.

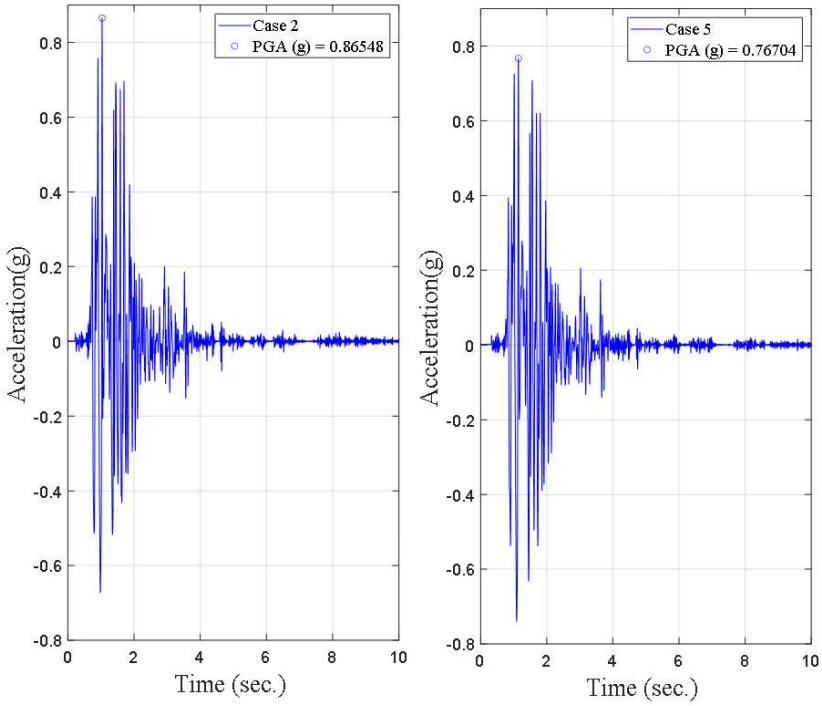

Figure 7.5. The ATH of Case 2 and Case 5 under Kobe Earthquake.

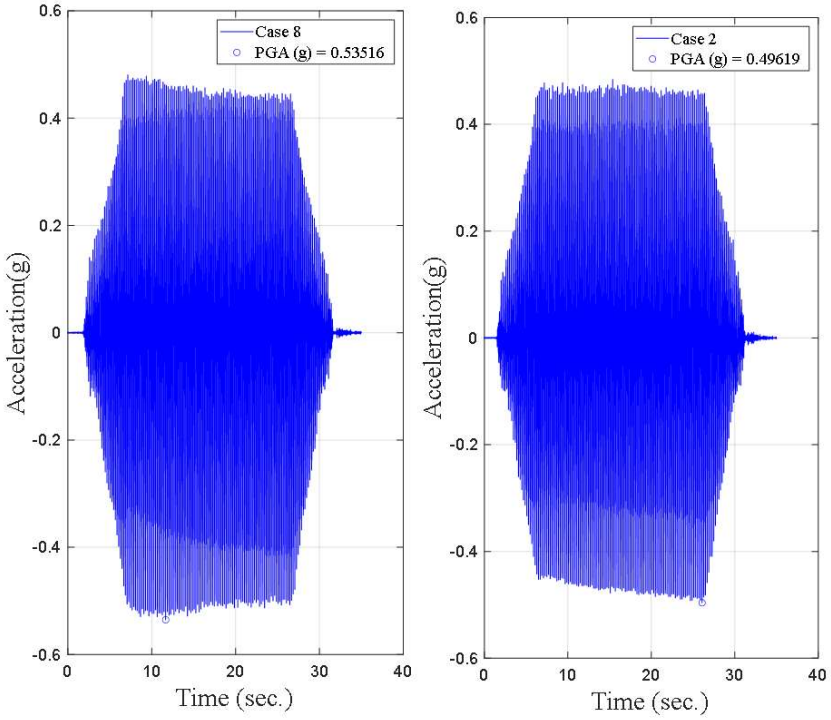

Figure 7.6. The ATH of Case 8 and Case 2 under the sinusoidal motion (0.4g - 5 Hz).

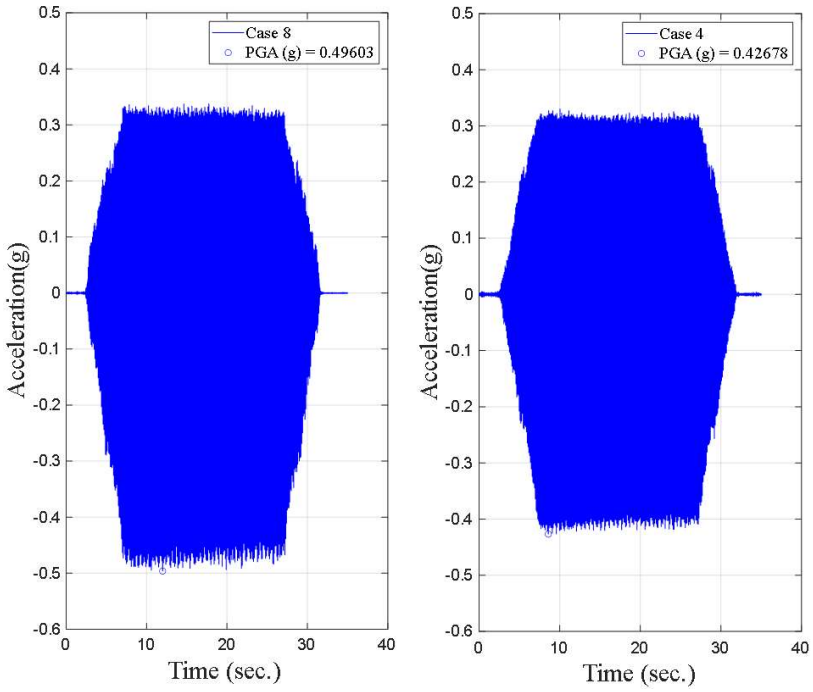

Figure 7.7. The ATH of Case 8 and Case 4 under the sinusoidal motion (0.3g - 10 Hz).

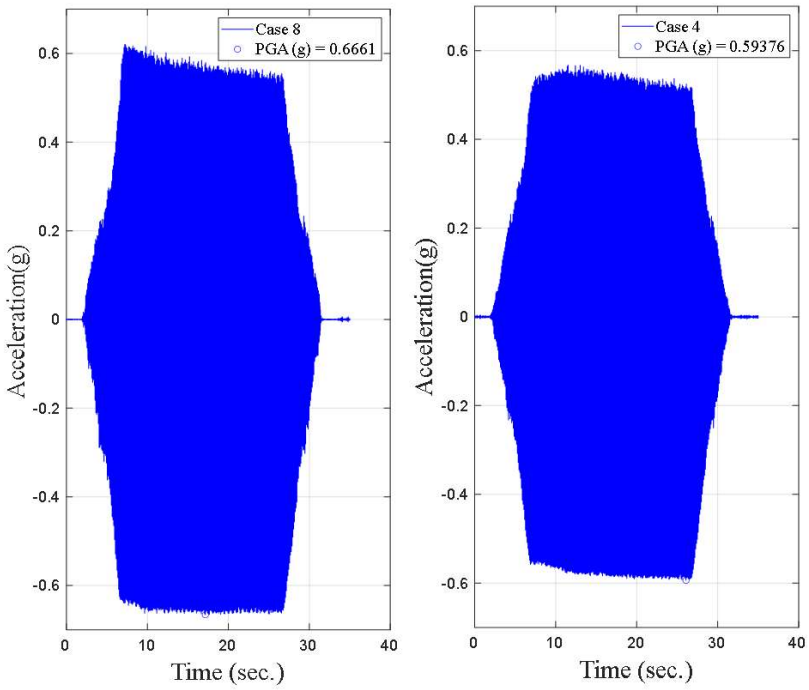

Figure 7.8. The ATH of Case 8 and Case 4 under the sinusoidal motion (0.4g - 10 Hz).

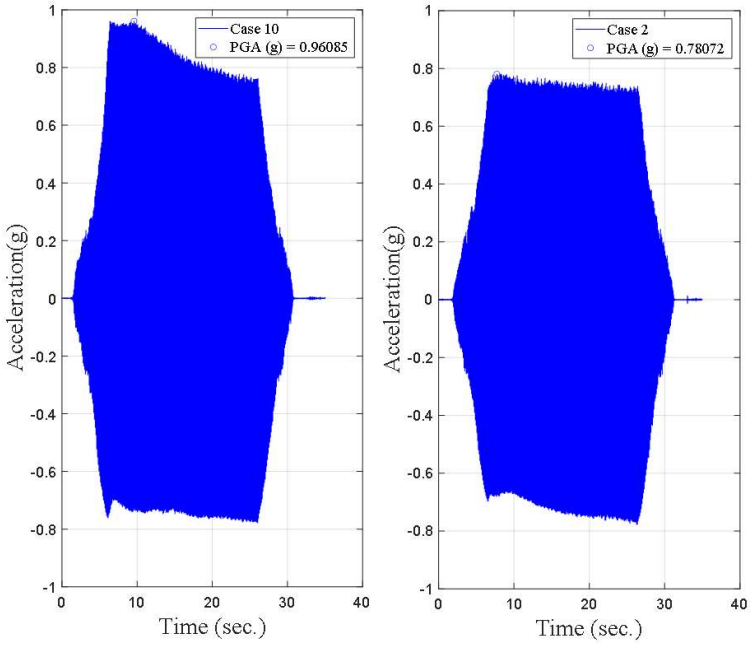

Figure 7.9. The ATH of Case 10 and Case 2 under the sinusoidal motion (0.5g - 10 Hz).

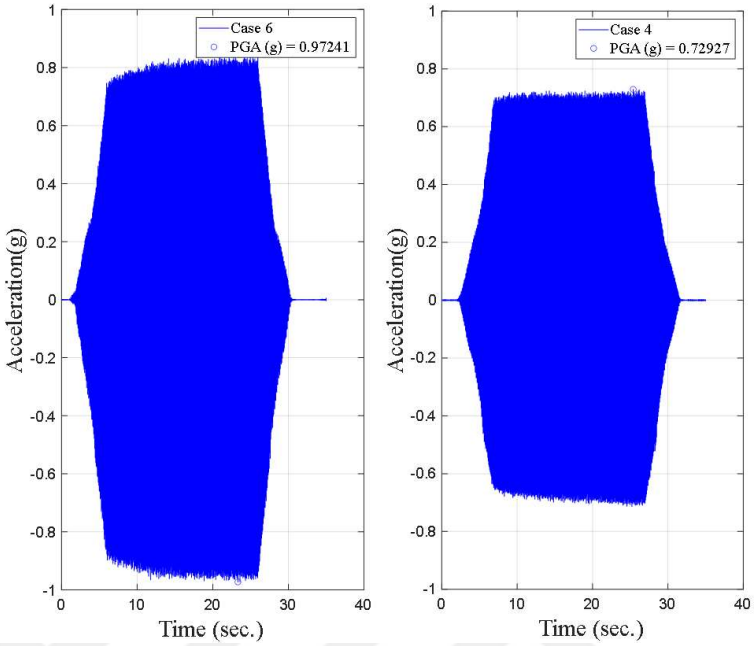

Figure 7.10. The ATH of Case 6 and Case 4 under the sinusoidal motion (0.4g - 15 Hz).

The percentage changes in spectral acceleration calculated from the acceleration recordings of A7 are given in Table 7.2. In general, EPS geofoam cushions caused a more significant reduction in spectral acceleration than cushions made of a sand-tire crumb mixture. Under the near-field Kocaeli, İzmir, and El-Centro Earthquakes, the EPS geofoam cushion brought about a reduction in spectral acceleration at the top of the wall by 34%, 33.9%, and 33.4%, respectively. Additionally, Case 6 resulted in more reduction in spectral acceleration than Case 5 under El-Centro and near-field Kocaeli Earthquakes. Under the far-field Kocaeli Earthquake, the effects of cushion on spectral acceleration could not be observed.

Table 7.2. The percentage change in SA of A7 (Case 1 to Cases 2, 4, 5, 6, 8, and 10).

Input motion	İzmit-F	İzmir-F	İzmit-N	El-Centro	Kobe	0.4g-5 Hz	0.3g-10 Hz	0.4g-10 Hz	0.5g-10 Hz	0.4g-15 Hz
Case1-2	-0.2	20.3	-15.4	-10.2	-5.3	+5.8	+2.9	-6.8	-16.4	-12.8
Case1-4	+0.9	-24.9	-34.0	-33.4	-8.9	+2.2	-2.6	-8.5	-11.9	-18.1
Case1-5	+4.4	-33.9	-16.2	-18.4	-4.0	+5.7	-2.3	+12.0	-12.6	-13.5
Case1-6	+3.9	-9.6	-23.4	-27.4	-3.7	+5.4	+1.7	-3.2	-3.5	-0.6
Case1-8	+4.7	+19.1	-13.2	-7.1	-4.1	+6.0	+2.2	-0.4	-2.5	-0.3
Case1-10	+4.0	+10.5	-10.5	-17.3	-8.9	0.0	-3.5	-7.0	-5.0	-2.4

For each input motion, the comparison of the cases in which the reduction in spectral acceleration at the top of the wall was the greatest and lowest is given between Figures 7.11 and 7.20. The improvement in seismic performance due to cushion layer was clear in Figure 7.12.

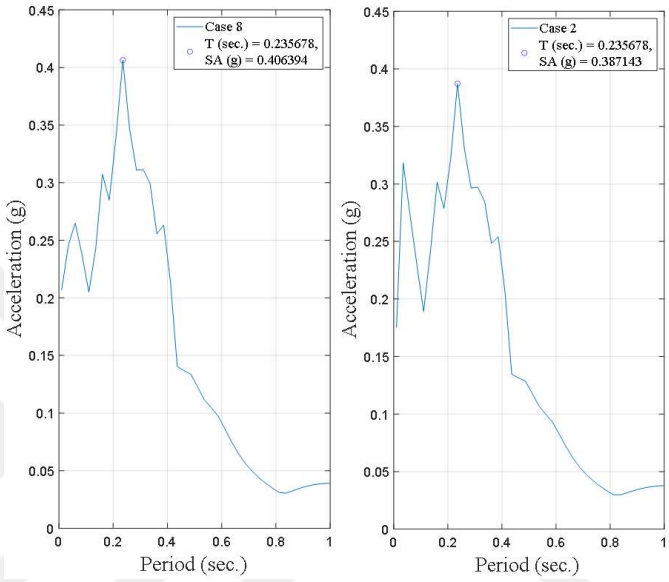

Figure 7.11. The SA of Case 8 and Case 2 under the far- field Kocaeli Earthquake.

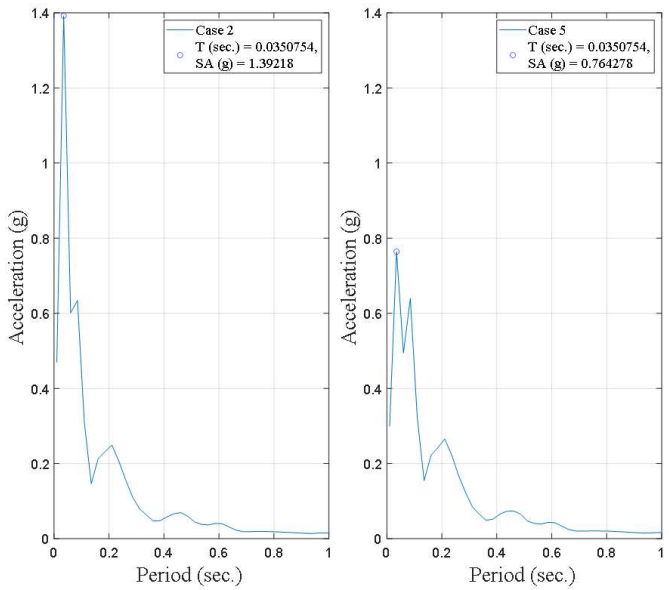

Figure 7.12. The SA of Case 2 and Case 5 under the far- field İzmir Earthquake.

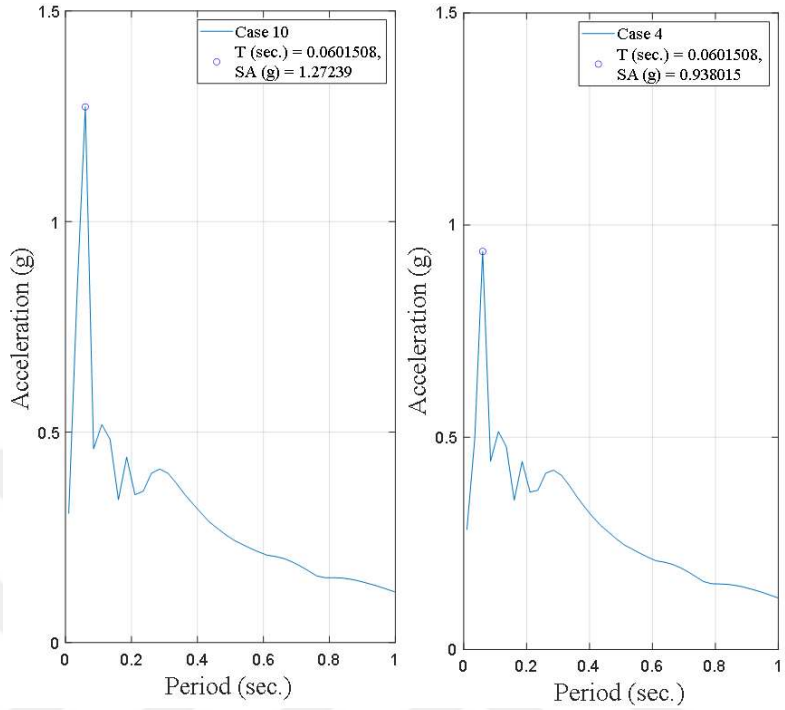

Figure 7.13. The SA of Case 10 and Case 4 under the near- field Kocaeli Earthquake.

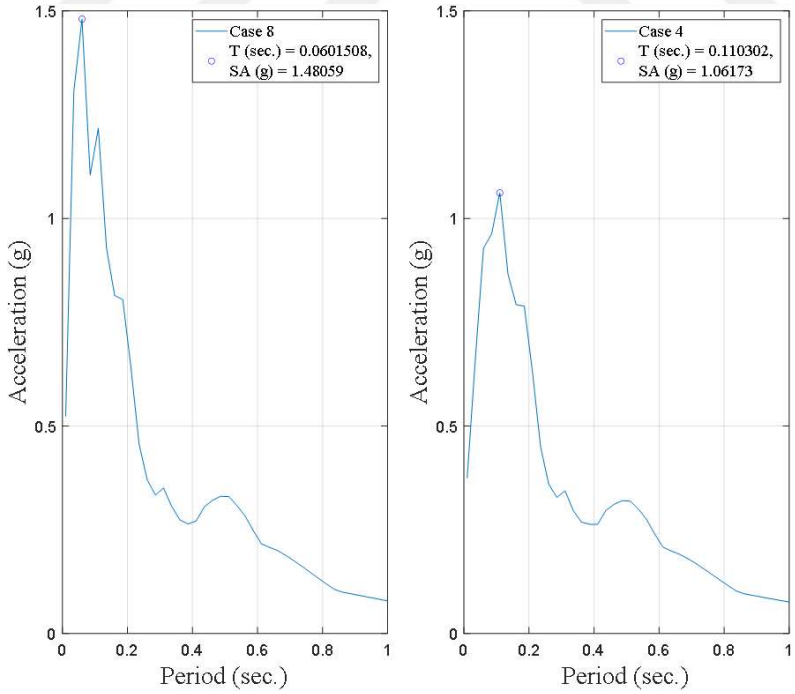

Figure 7.14. The SA of Case 8 and Case 4 under El-Centro Earthquake.

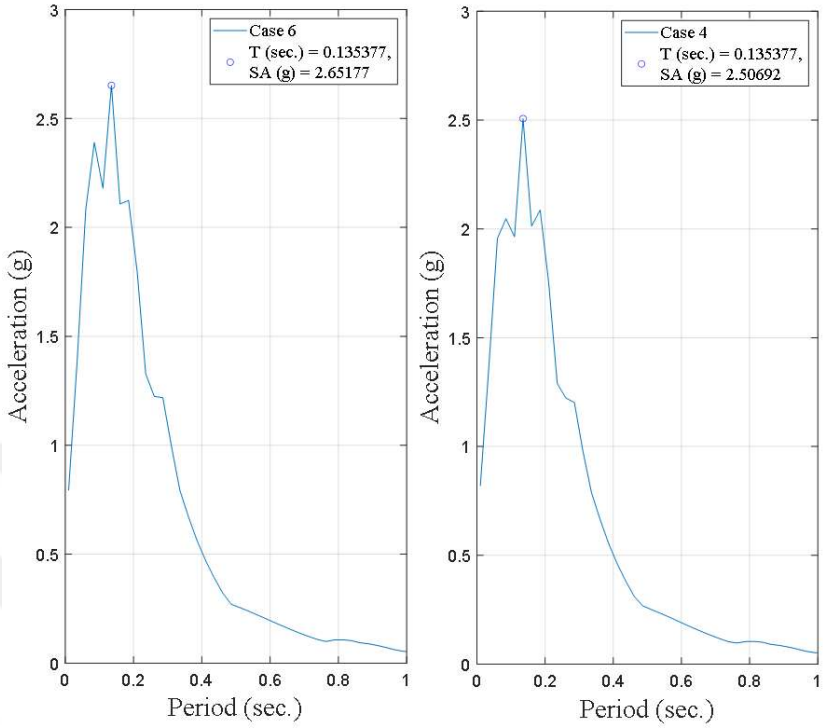

Figure 7.15. The SA of Case 6 and Case 4 under Kobe Earthquake.

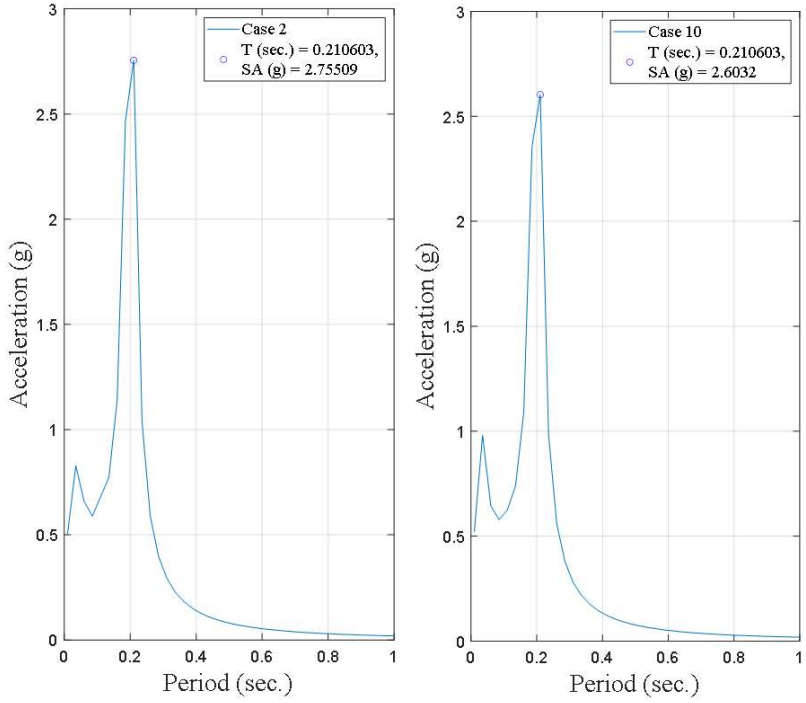

Figure 7.16. The SA of Case 2 and Case 10 under the sinusoidal motion (0.4g - 5 Hz).

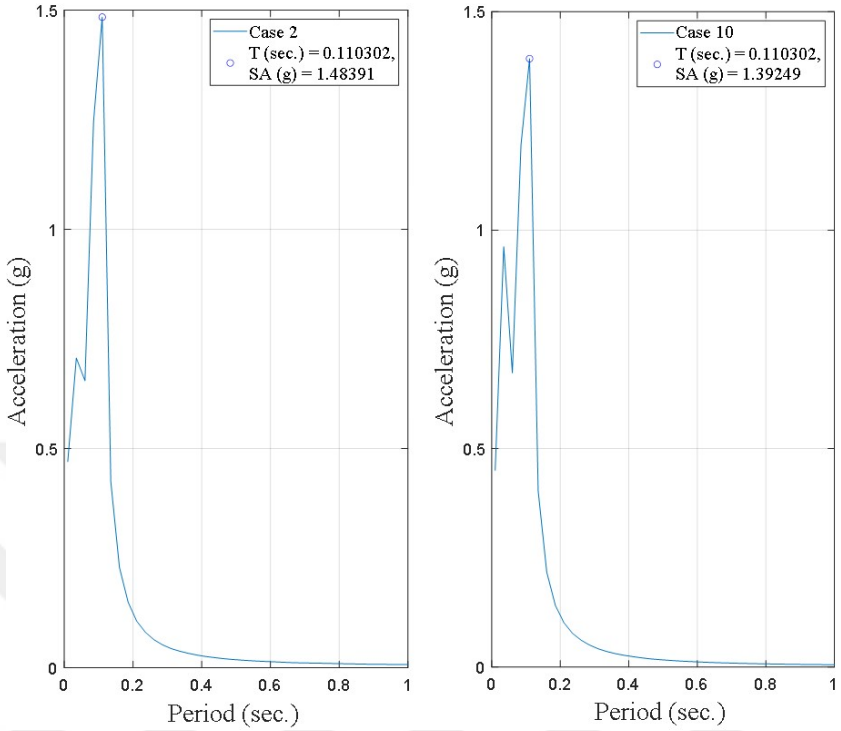

Figure 7.17. The SA of Case 2 and Case 10 under the sinusoidal motion (0.3g - 10 Hz).

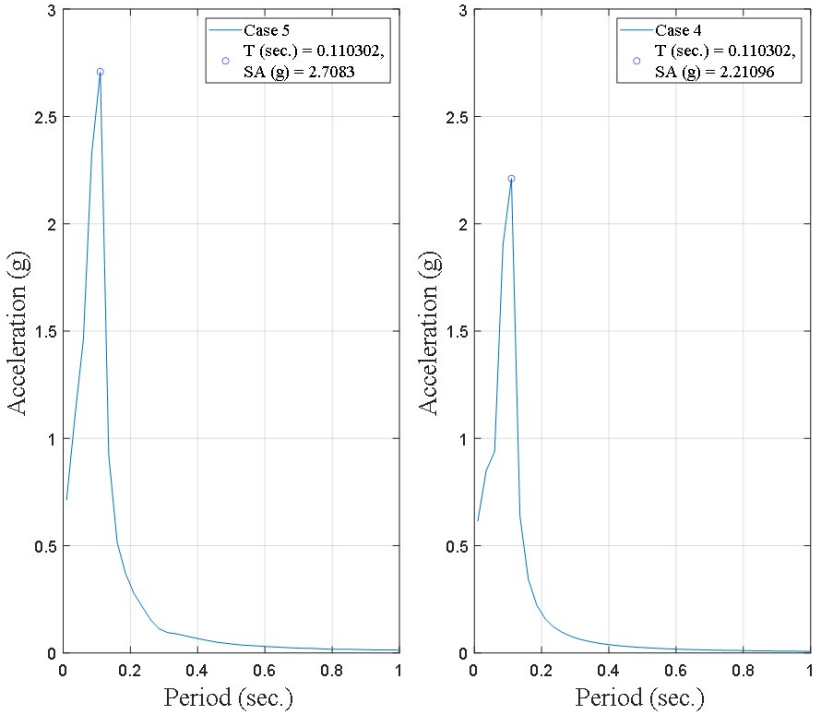

Figure 7.18. The SA of Case 5 and Case 4 under the sinusoidal motion (0.4g - 10 Hz).

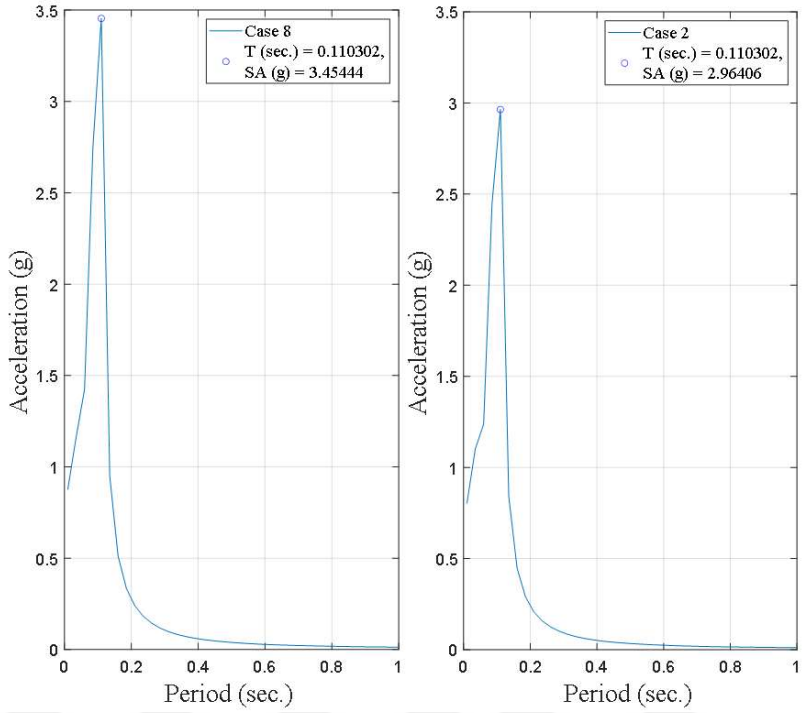

Figure 7.19. The SA of Case 8 and Case 2 under the sinusoidal motion (0.5g - 10 Hz).

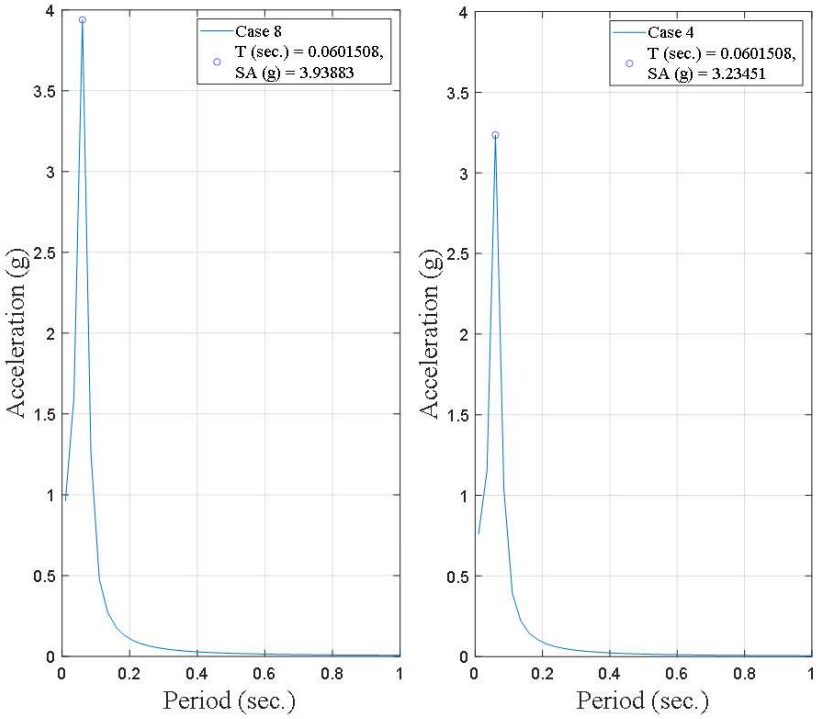

Figure 7.20. The SA of Case 8 and Case 4 under the sinusoidal motion (0.4g - 15 Hz).

The percentage change in displacement recorded by D19 is given in Table 7.3. The cushions composed of EPS geofoam resulted in more decrease in the displacement of the wall than the ones consisting of sand-tire crumb mixture. Under İzmir Earthquake, the reduction amount in displacement was determined 38.2% and 32.6% for Case 2 and Case 4, respectively. The EPS geofoam cushions showed better performance under İzmir Earthquake than other motions. The change in displacement was observed more clearly under real earthquake motions than sinusoidal motions.

Table 7.3. The percentage change in maximum displacement of D19 (Case 1 to Cases 2, 4, 5, 6, 8, and 10).

Input motion	İzmit-F	İzmir-F	İzmit-N	El-Centro	Kobe	0.4g-5 Hz	0.3g-10 Hz	0.4g-10 Hz	0.5g-10 Hz	0.4g-15 Hz
Case1-2	-26.9	-38.2	-5.5	-21.6	-17.0	-13.6	-1.4	-4.3	-3.9	-1.3
Case1-4	-24.4	-32.6	-8.6	-19.9	-18.4	-3.6	-5.8	-1.1	-2.9	-1.3
Case1-5	-20.2	-29.2	-12.9	-14.2	-12.1	-1.8	-11.6	-4.3	-2.9	-2.7
Case1-6	-7.6	-3.4	-2.5	-7.4	-6.4	-4.5	-7.2	-2.2	-2.0	-8.0
Case1-8	-4.2	-11.2	-5.5	-2.3	-5.7	-3.6	-11.6	-2.2	-3.9	-6.7
Case1-10	-6.7	-2.2	-7.4	-6.8	-9.9	-5.5	-5.8	-3.3	-6.9	-4.0

For each base excitation, the cases that resulted in the greatest and lowest decrease in wall movement at the top of the wall were compared between Figures 7.21 and 7.30. The improvement in seismic performance due to cushion layer was clear in Figure 7.22.

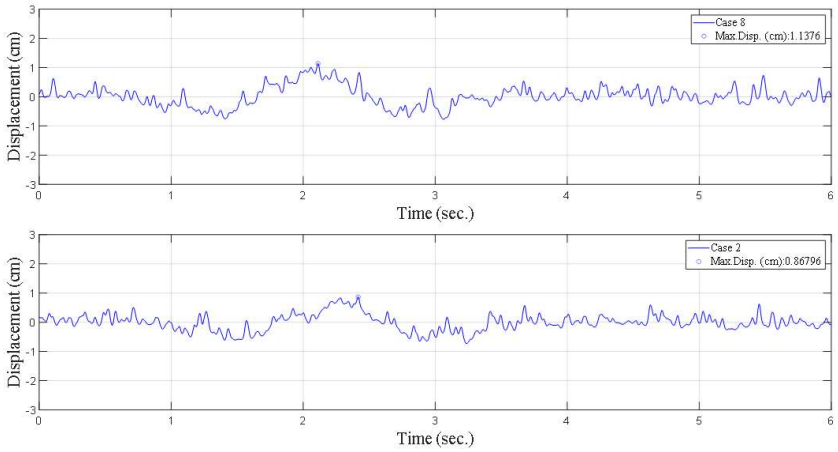

Figure 7.21. The DTH of Case 8 and Case 2 under the far- field Kocaeli Earthquake.

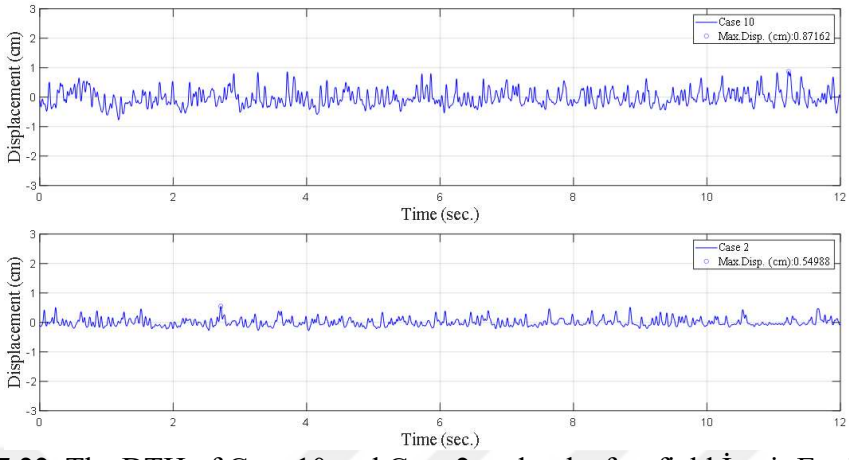

Figure 7.22. The DTH of Case 10 and Case 2 under the far- field İzmir Earthquake.

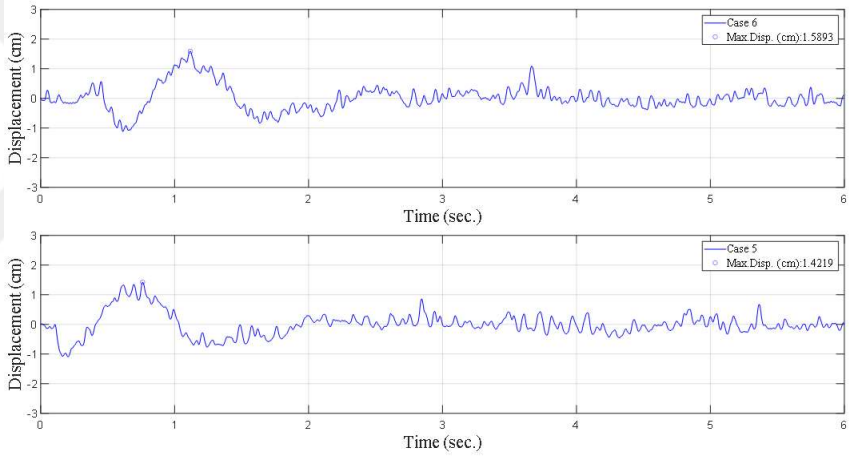

Figure 7.23. The DTH of Case 6 and Case 5 under the near- field Kocaeli Earthquake.

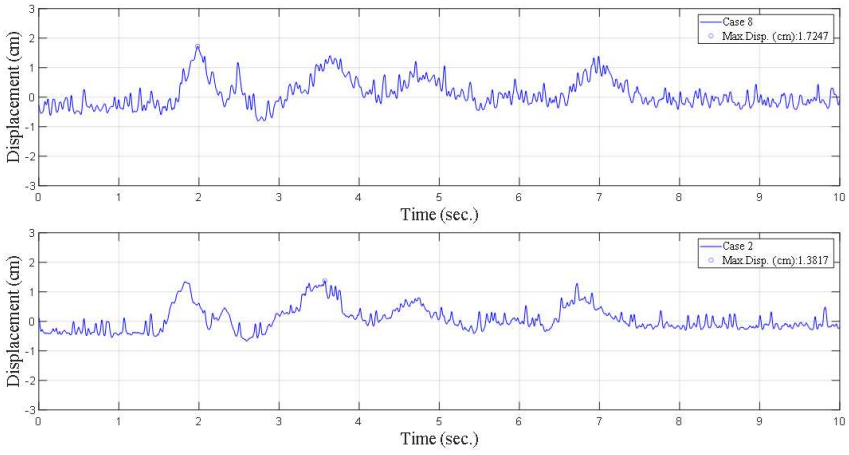

Figure 7.24. The DTH of Case 8 and Case 2 under El-Centro Earthquake.

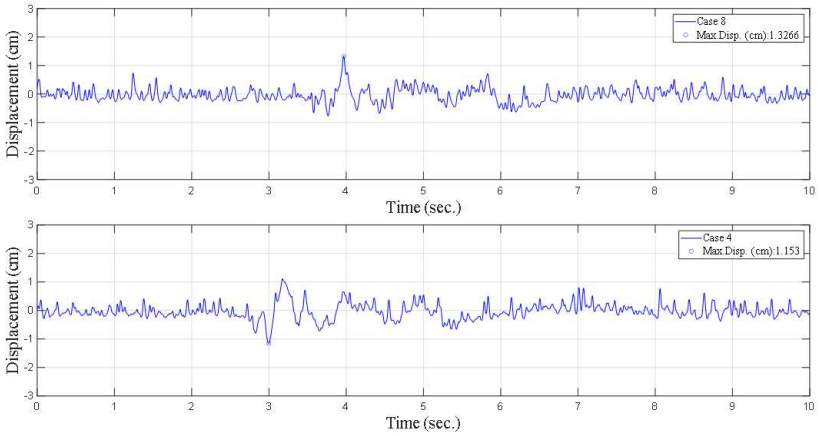

Figure 7.25. The DTH of Case 8 and Case 4 under Kobe Earthquake.

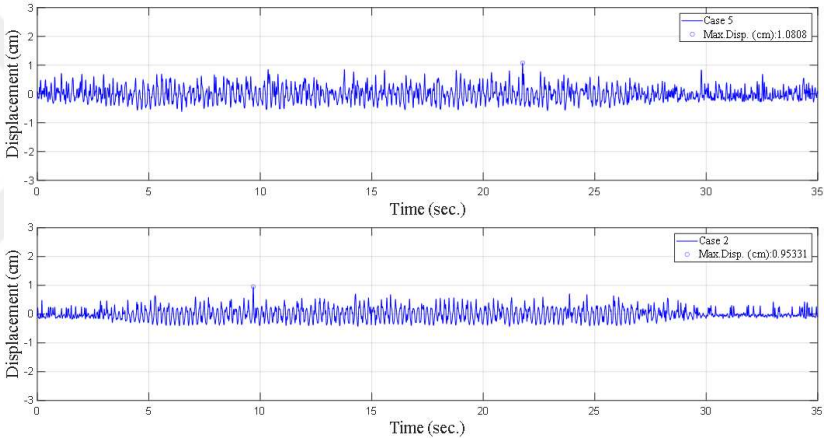

Figure 7.26. The DTH of Case 5 and Case 2 under the sinusoidal motion (0.4g - 5 Hz).

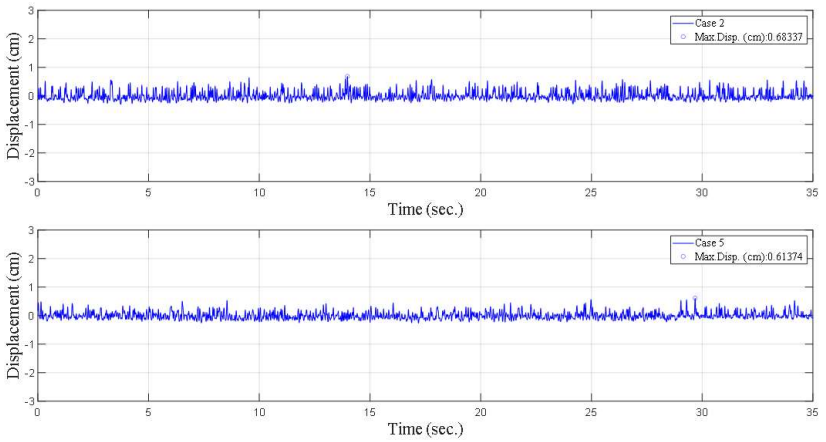

Figure 7.27. The DTH of Case 2 and Case 5 under the sinusoidal motion (0.3g - 10 Hz).

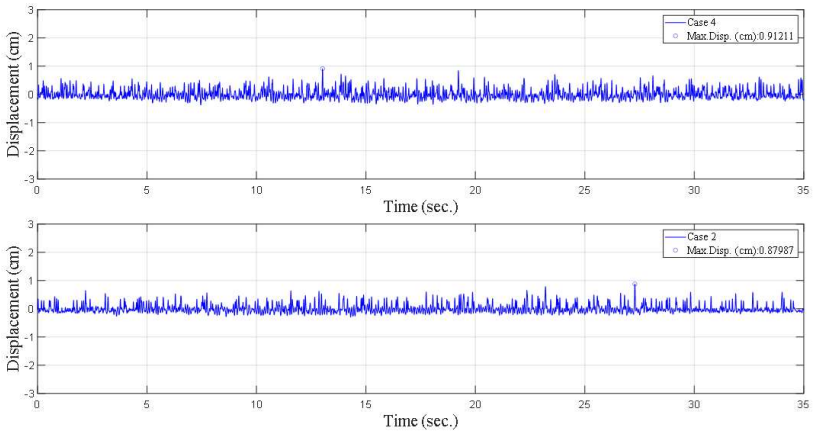

Figure 7.28. The DTH of Case 4 and Case 2 under the sinusoidal motion (0.4g - 10 Hz).

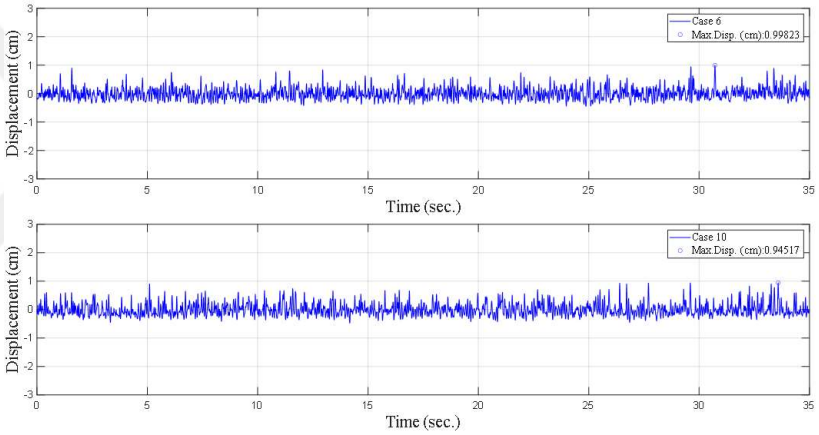

Figure 7.29. The DTH of Case 6 and Case 10 under the sinusoidal motion (0.5g - 10 Hz).

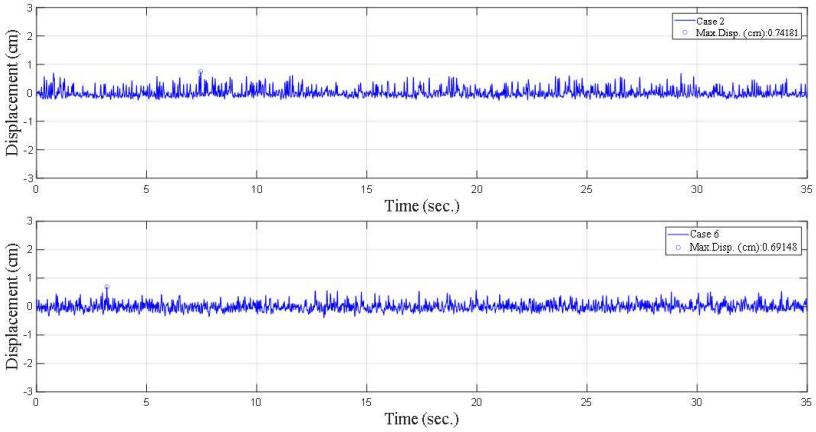

Figure 7.30. The DTH of Case 2 and Case 6 under the sinusoidal motion (0.4g - 15 Hz).

7.2.2. The Cushion Layers with a Thickness of 4 cm

In this section, the compressible layers having a thickness of 4 cm were examined. They were composed of EPS geofoam with 10 kg/m^3 density and tire waste-sand mixture with 10%, 20%, and 30% tire crumb by weight. The improved cases (Cases 3, 7, 9, and 11) were compared with Case 1 in order to calculate the percentage change due to the inclusion of cushion layers with a thickness of 4 cm.

The percentage change in acceleration recorded by A7 is given in Table 7.4. The EPS geofoam cushion caused a greater reduction in acceleration than the other type of cushion. Under El-Centro Earthquake, the EPS geofoam cushion (Case 3) resulted in a 34% reduction in peak acceleration at the top of the wall; that is, the EPS geofoam cushion improves the seismic performance of the model compared to the sand-tire crumb cushion. Under El-Centro Earthquake, the cushion of Case 2 resulted in the greatest reduction in peak acceleration at the top of the wall, comparing the other cases. On the other hand, under far-field Kocaeli Earthquake, the effects of cushion type on transmitted acceleration were not clear.

Table 7.4. The percentage change in PGA of A7 (Case 1 to Cases 3, 7, 9, and 11)..

Input motion	İzmit-F	İzmir-F	İzmit-N	El-Centro	Kobe	0.4g-5 Hz	0.3g-10 Hz	0.4g-10 Hz	0.5g-10 Hz	0.4g-15 Hz
Case1-3	-3.7	-27.1	-20.9	-34.0	-17.6	-11.4	-17.0	-24.5	-22.5	-22.0
Case1-7	+9.5	+15.0	-9.9	-8.0	-8.2	+3.3	+6.1	-6.7	-11.9	-2.0
Case1-9	-3.0	+0.9	-4.8	-9.3	-7.0	-0.9	+3.1	-12.3	-5.6	-3.9
Case1-11	-1.0	+2.4	-9.9	-10.6	-5.9	-0.8	2.6	-7.4	0.8	-9.5

The comparison of the cases that caused the greatest and lowest reduction in acceleration at the top of the wall for each input motion is given between Figures 7.31 and 7.40. The improvement in seismic performance due to cushion layer was clear in Figure 7.32.

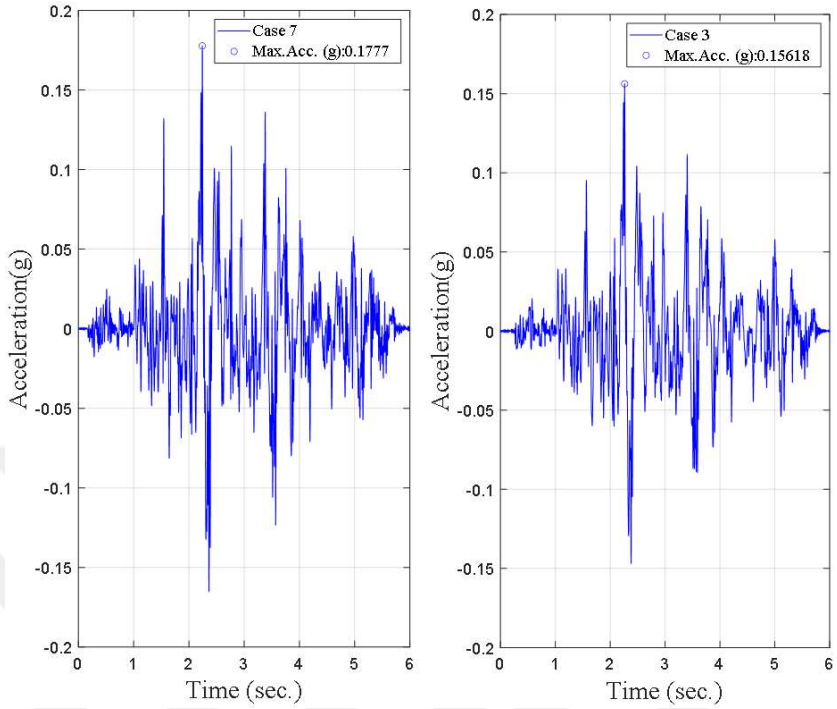

Figure 7.31. The ATH of Case 7 and Case 3 under the far- field Kocaeli Earthquake.

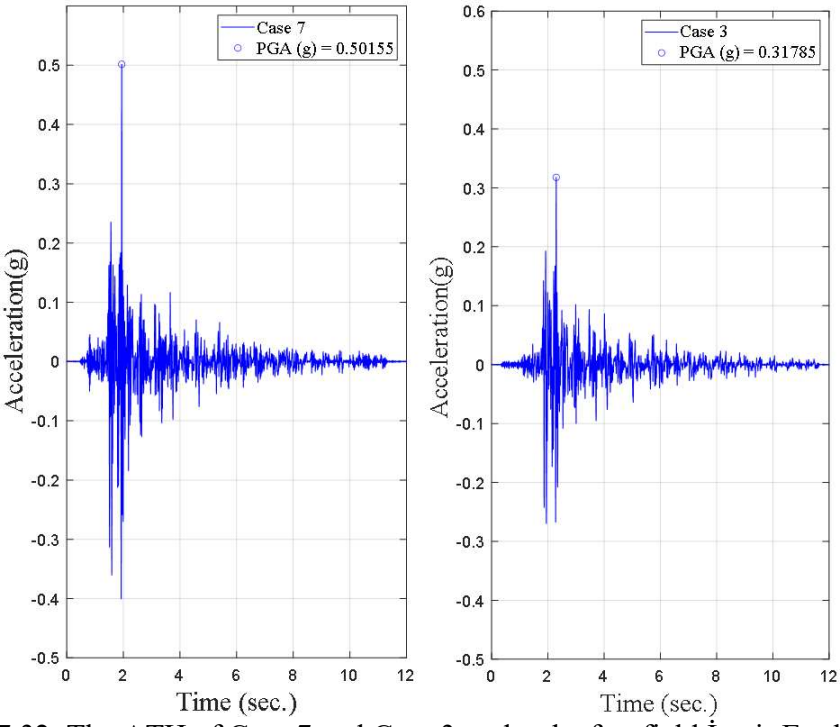

Figure 7.32. The ATH of Case 7 and Case 3 under the far- field İzmir Earthquake.

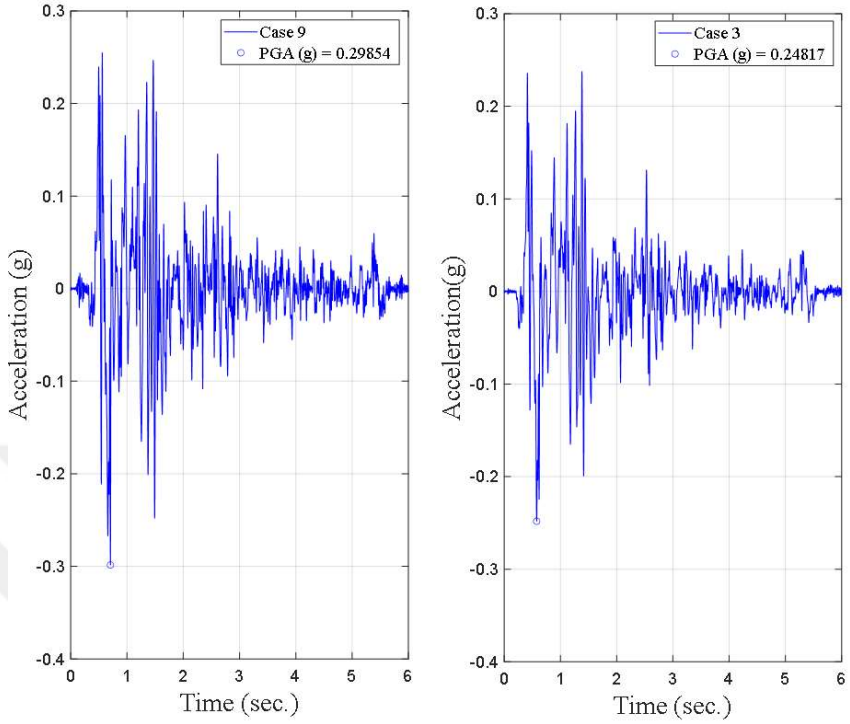

Figure 7.33. The ATH of Case 9 and Case 3 under the near- field Kocaeli Earthquake.

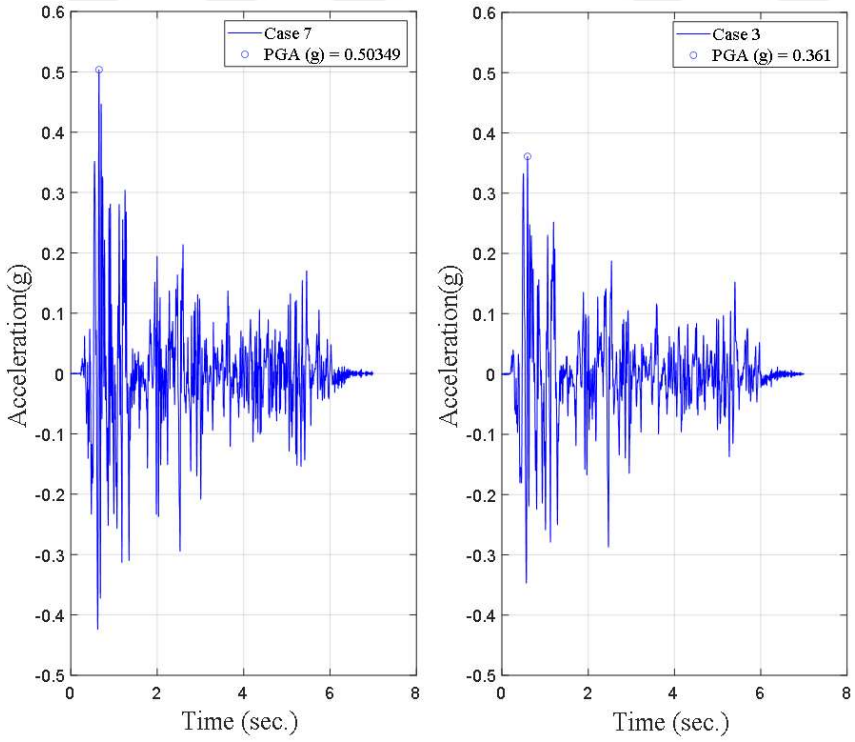

Figure 7.34. The ATH of Case 7 and Case 3 under El-Centro Earthquake.

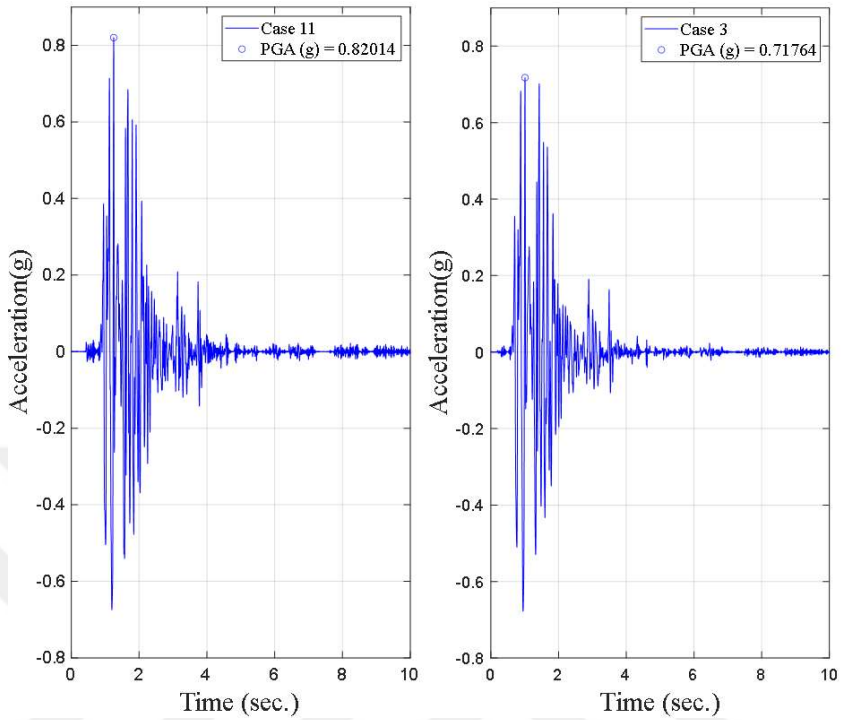

Figure 7.35. The ATH of Case 11 and Case 3 under Kobe Earthquake.

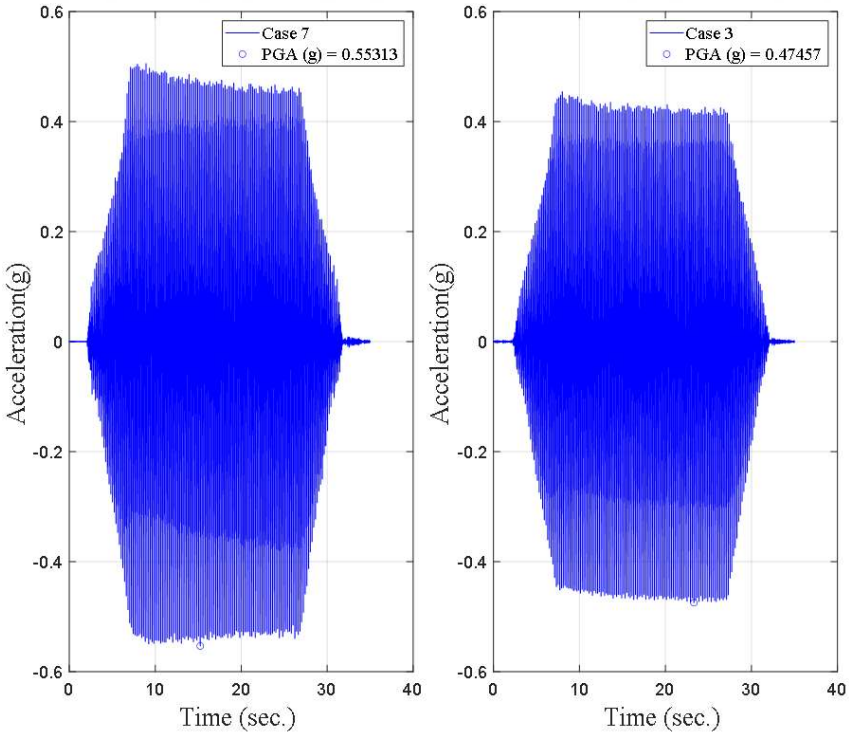

Figure 7.36. The ATH of Case 7 and Case 3 under the sinusoidal motion (0.4g - 5 Hz).

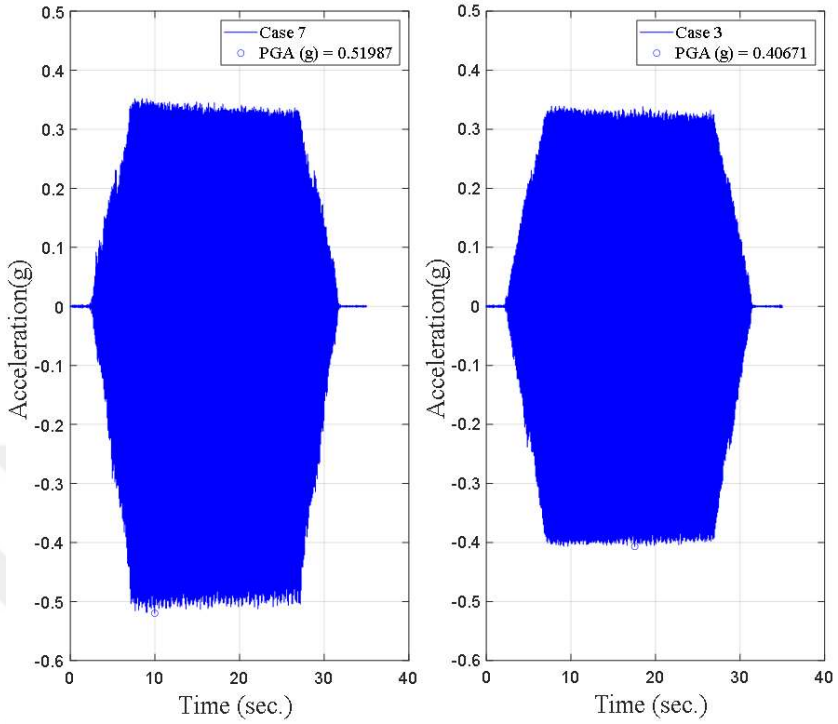

Figure 7.37. The ATH of Case 7 and Case 3 under the sinusoidal motion (0.3g - 10 Hz).

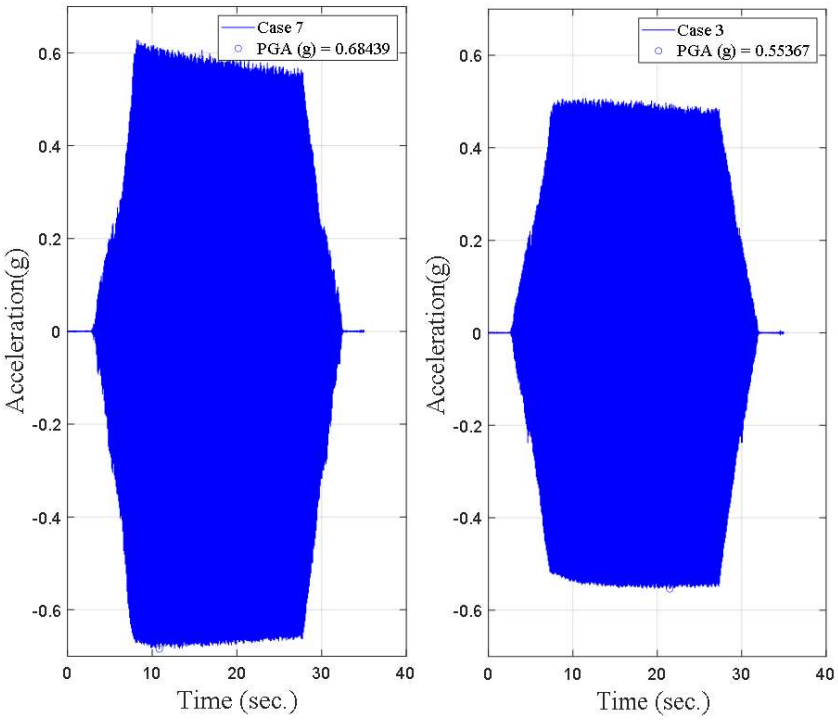

Figure 7.38. The ATH of Case 7 and Case 3 under the sinusoidal motion (0.4g - 10 Hz).

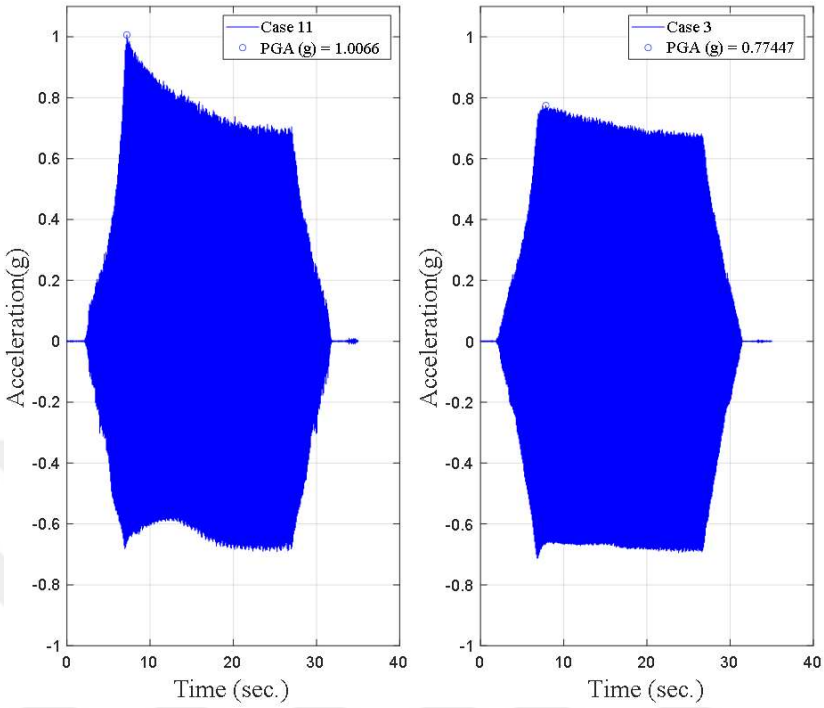

Figure 7.39. The ATH of Case 11 and Case 3 under the sinusoidal motion (0.5g - 10 Hz).

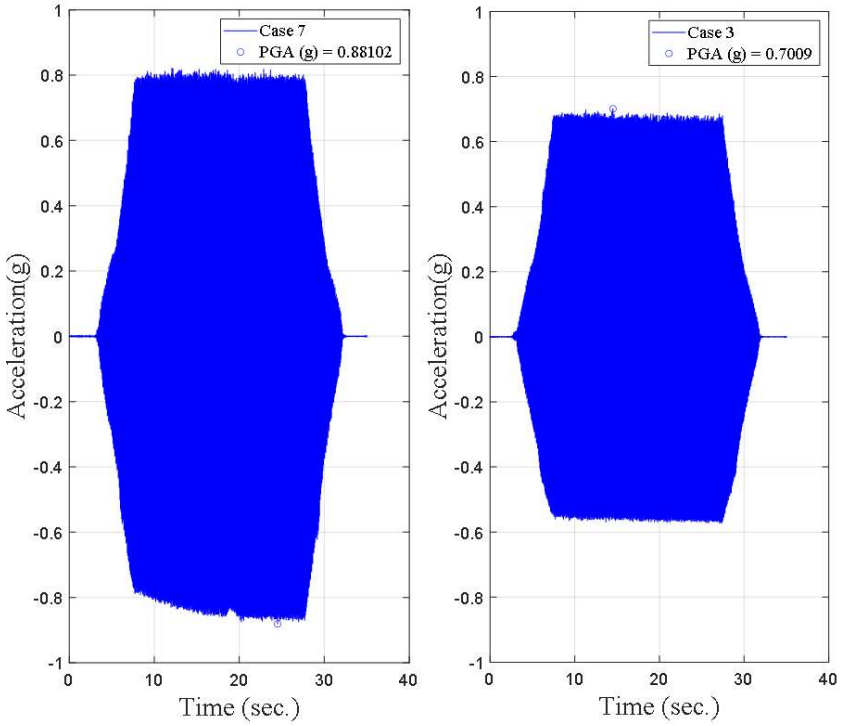

Figure 7.40. The ATH of Case 7 and Case 3 under the sinusoidal motion (0.4g - 15 Hz).

The percentage change in spectral acceleration calculated from the acceleration recordings of A7 is given in Table 7.5. The cushion consisting of EPS geofoam showed better performance than the cushions made of a sand-tire crumb mixture, considering the spectral acceleration changes. Under El-Centro Earthquake, the EPS geofoam cushion caused a 33.5% decrease in spectral acceleration. Nevertheless, under the far-field Kocaeli Earthquake, the effects of cushion on spectral acceleration could not be observed for 4 cm thick cushions. Additionally, the impact of the cushion layer on the seismic performance of the retaining wall was not clear under the sinusoidal motions for Cases 7, 9, and 11.

Table 7.5. The percentage change in SA of A7 (Case 1 to Cases 3, 7, 9, and 11).

Input motion	İzmit-F	İzmir-F	İzmit-N	El-Centro	Kobe	0.4g-5 Hz	0.3g-10 Hz	0.4g-10 Hz	0.5g-10 Hz	0.4g-15 Hz
Case1-3	+7.6	-16.6	-29.3	-33.5	-9.6	+2.3	-3.6	-10.7	-14.6	-20.5
Case1-7	+8.3	+32.6	-12.8	-5.5	+1.4	+8.5	+6.7	+4.7	+1.8	+0.6
Case1-9	+2.7	+17.5	-14.0	-14.1	-2.1	+6.6	+6.8	+2.2	-1.7	-2.7
Case1-11	+2.1	+7.2	-10.9	-12.3	-7.7	+5.9	+9.2	+1.4	-10.1	-7.2

For each input motion, the comparison of the cases in which the reduction in spectral acceleration at the top of the wall was the greatest and lowest is given between Figures 7.41 and 7.50. The improvement in seismic performance due to cushion layer was clear in Figure 7.42.

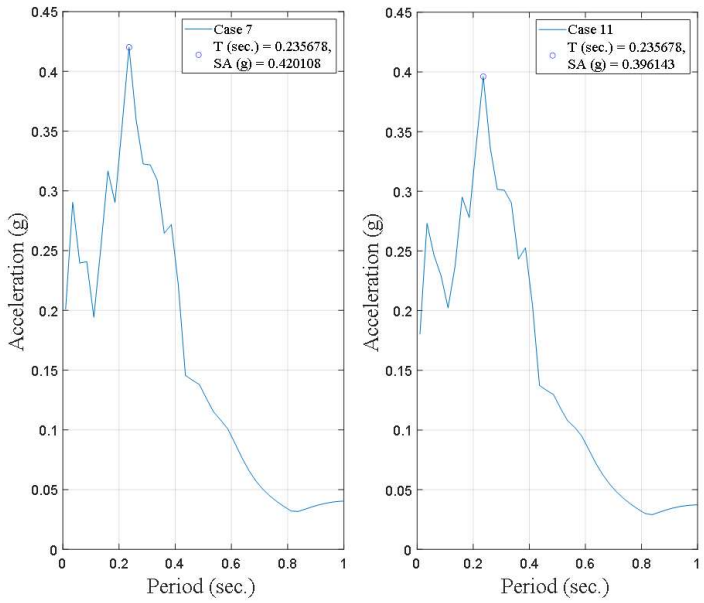

Figure 7.41. The SA of Case 7 and Case 11 under the far- field Kocaeli Earthquake.

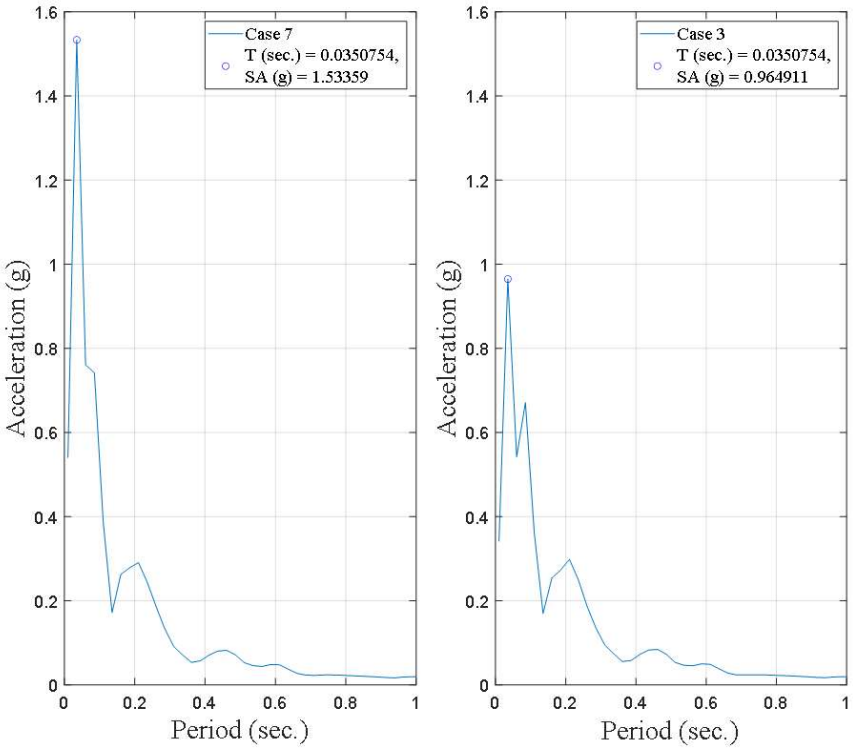

Figure 7.42. The SA of Case 7 and Case 3 under the far- field İzmir Earthquake.

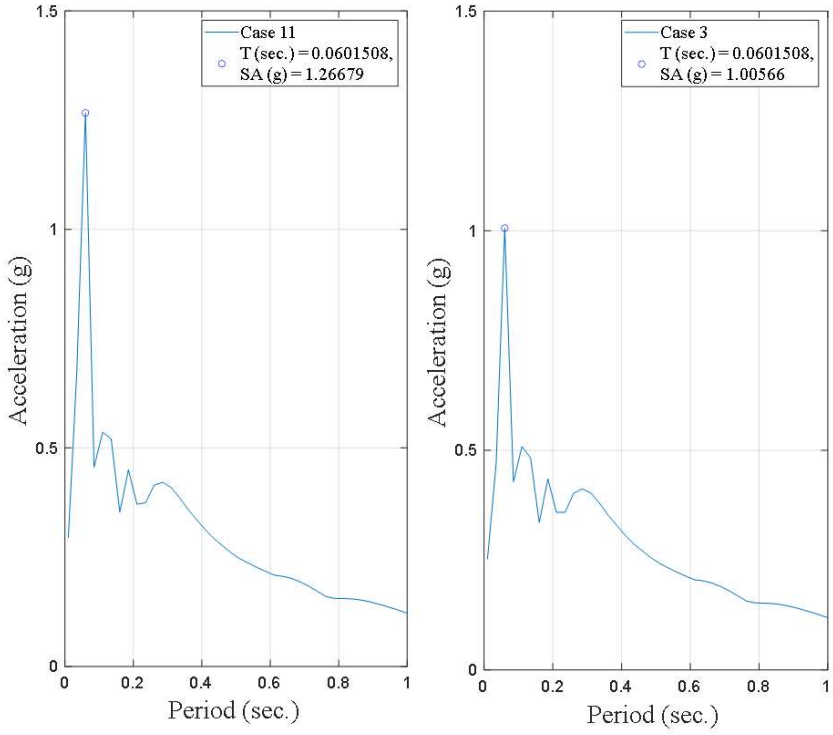

Figure 7.43. The SA of Case 11 and Case 3 under the near- field Kocaeli Earthquake.

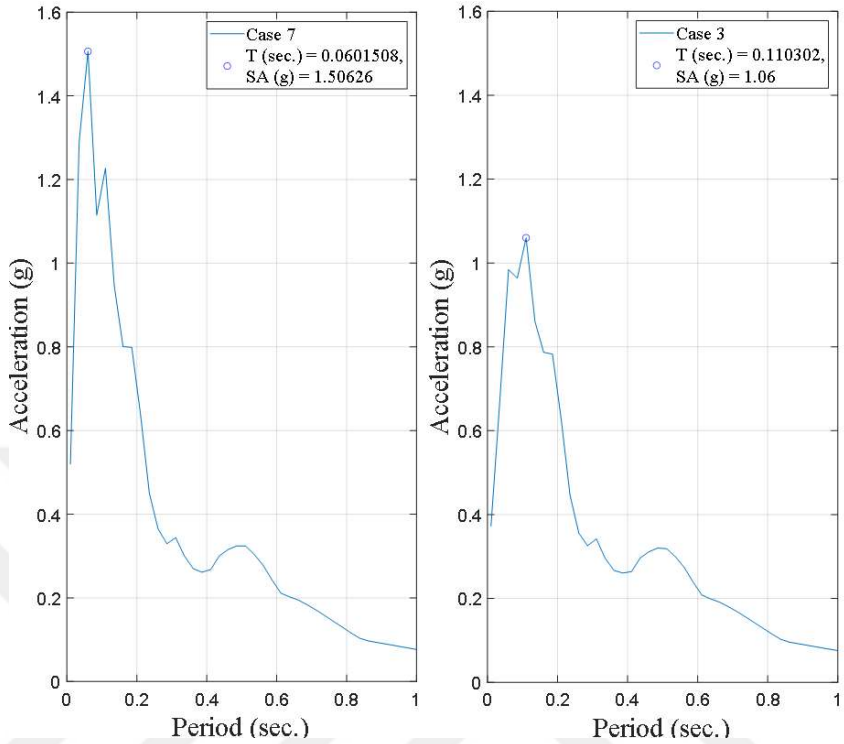

Figure 7.44. The SA of Case 7 and Case 3 under El-Centro Earthquake.

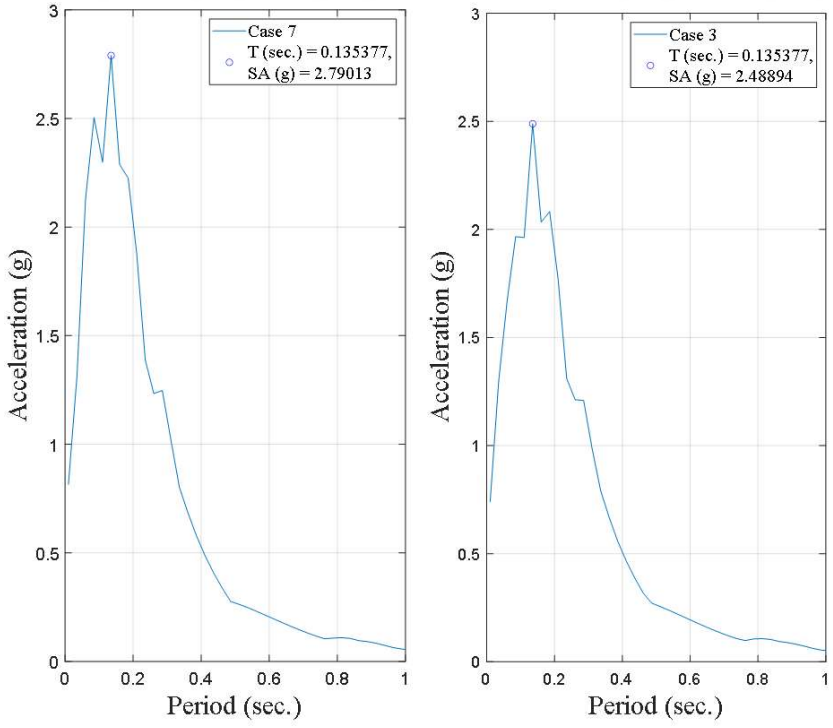

Figure 7.45. The SA of Case 7 and Case 3 under Kobe Earthquake.

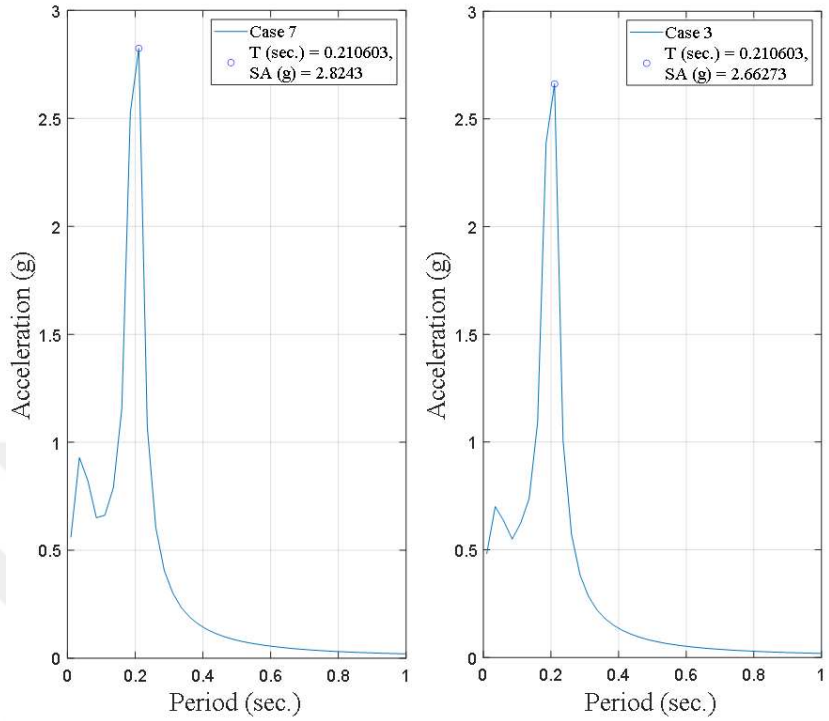

Figure 7.46. The SA of Case 7 and Case 3 under the sinusoidal motion (0.4g - 5 Hz).

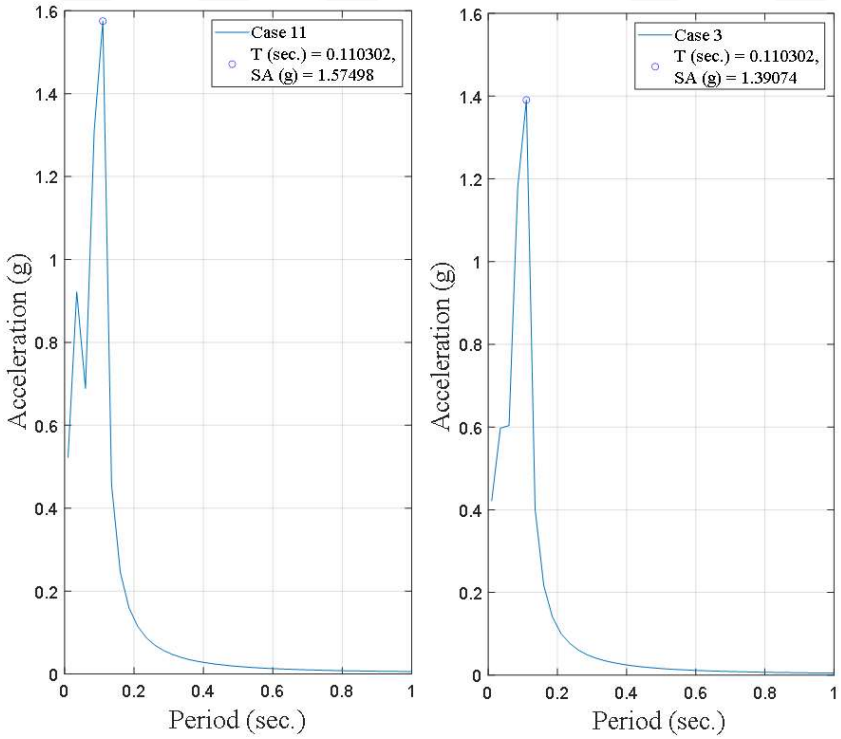

Figure 7.47. The SA of Case 11 and Case 3 under the sinusoidal motion (0.3g - 10 Hz).

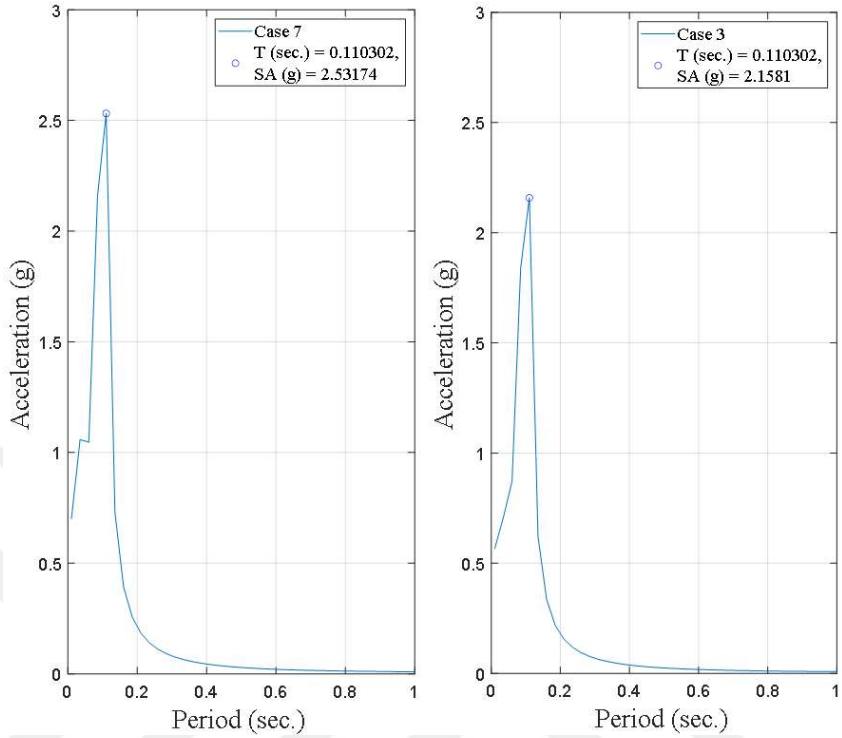

Figure 7.48. The SA of Case 7 and Case 3 under the sinusoidal motion (0.4g - 10 Hz)..

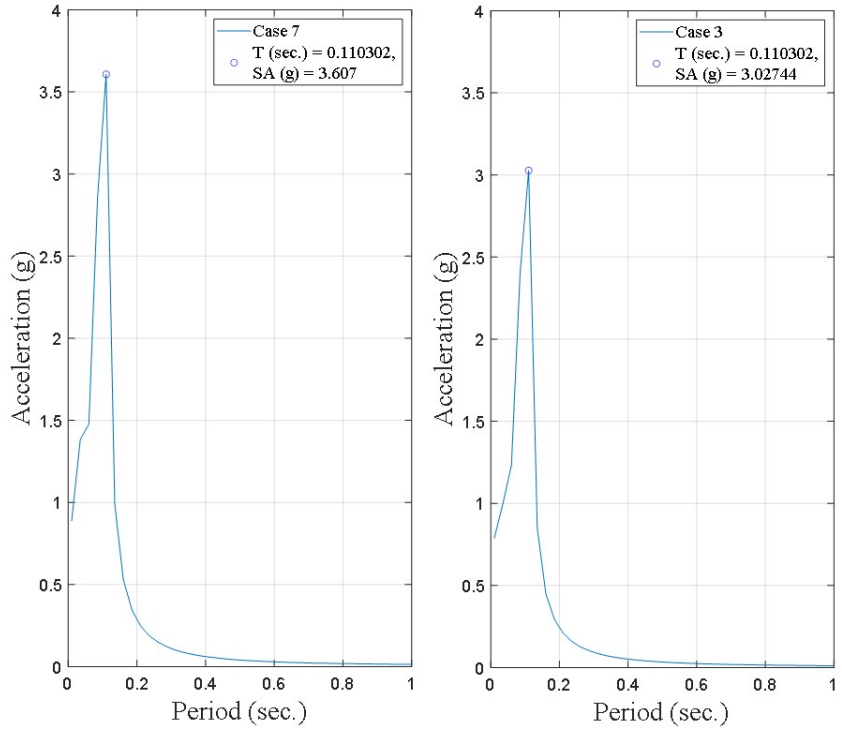

Figure 7.49. The SA of Case 7 and Case 3 under the sinusoidal motion (0.5g - 10 Hz).

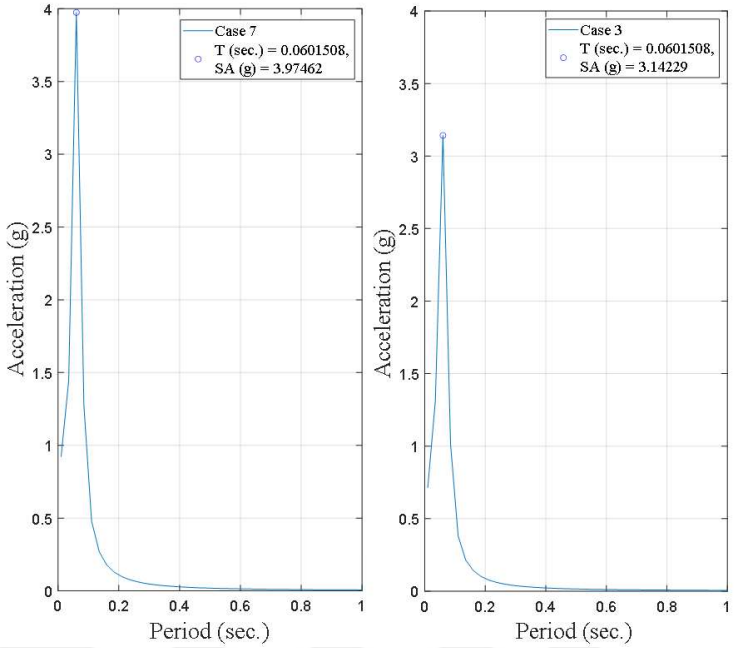

Figure 7.50. The SA of Case 7 and Case 3 under the sinusoidal motion (0.4g - 15 Hz).

The percentage change in displacement recorded by D19 is given in Table 7.6. The EPS geofoam cushion resulted in more reduction in the wall movement than the ones consisting of tire waste-sand mixture. The reduction in displacement due to EPS geofoam reached 46.1%; however, for the cases with tire waste-sand mixture, the reduction amounts were not considerable.

Table 7.6. The percentage change in maximum displacement of D19 (Case 1 to Cases 3, 7, 9, and 11)..

Input motion	İzmit-F	İzmir-F	İzmit-N	El-Centro	Kobe	0.4g-5 Hz	0.3g-10 Hz	0.4g-10 Hz	0.5g-10 Hz	0.4g-15 Hz
Case1-3	-29.4	-46.1	-22.7	-23.3	-19.9	-17.3	-42.0	-7.6	-12.7	-10.7
Case1-7	-2.5	-3.4	-2.5	-4.5	-1.4	-3.6	-10.1	-3.3	-2.0	-5.3
Case1-9	-5.0	-4.5	-3.7	-3.4	-8.5	-4.5	-14.5	-4.3	-4.9	-4.0
Case1-11	-5.0	-3.4	-6.7	-5.7	-13.5	-6.4	-10.1	-6.5	-7.8	-5.3

For each base excitation, the cases that resulted in the greatest and lowest decrease in movement at the top of the wall were compared between Figures 7.51 and 7.60. The improvement in seismic performance due to cushion layer was clear in Figure 7.52.

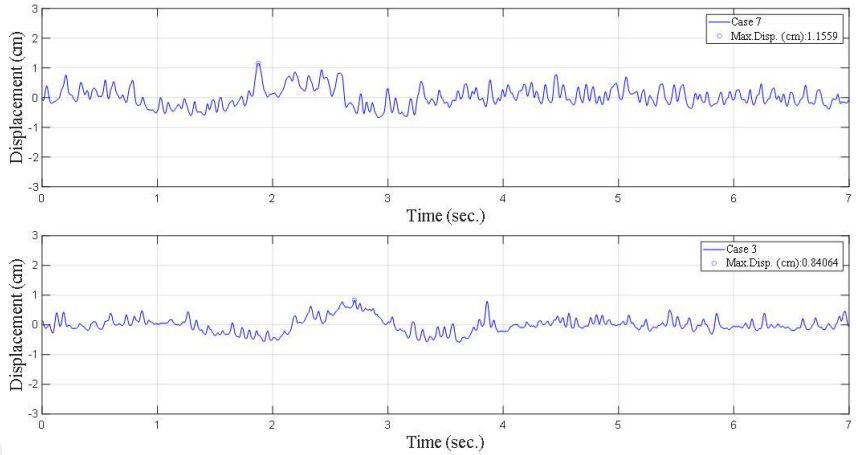

Figure 7.51. The DTH of Case 7 and Case 3 under the far- field Kocaeli Eathquake

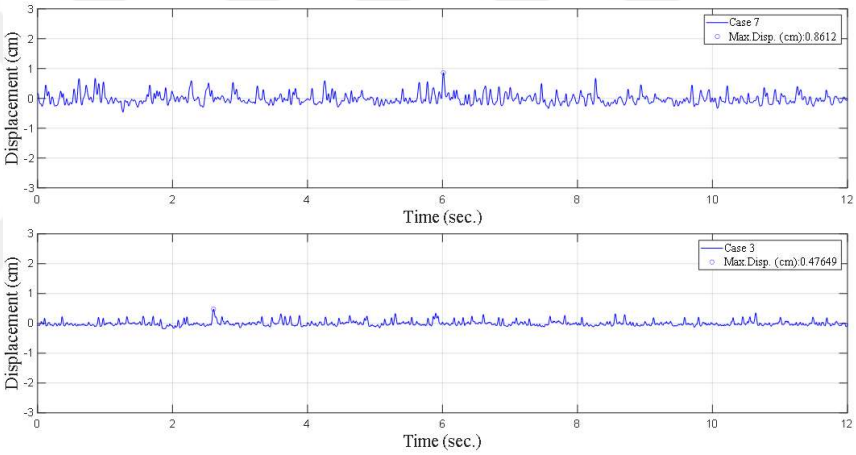

Figure 7.52. The DTH of Case 7 and Case 3 under the far- field İzmir Earthquake.

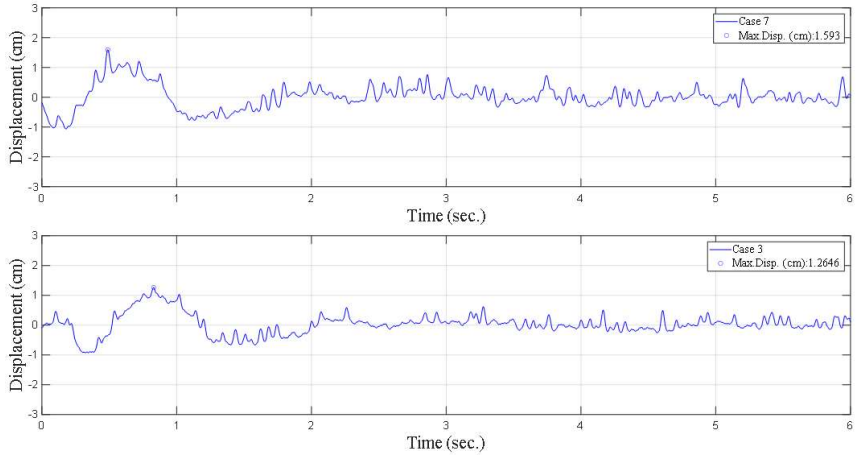

Figure 7.53. The DTH of Case 7 and Case 3 under the near- field Kocaeli Earthquake.

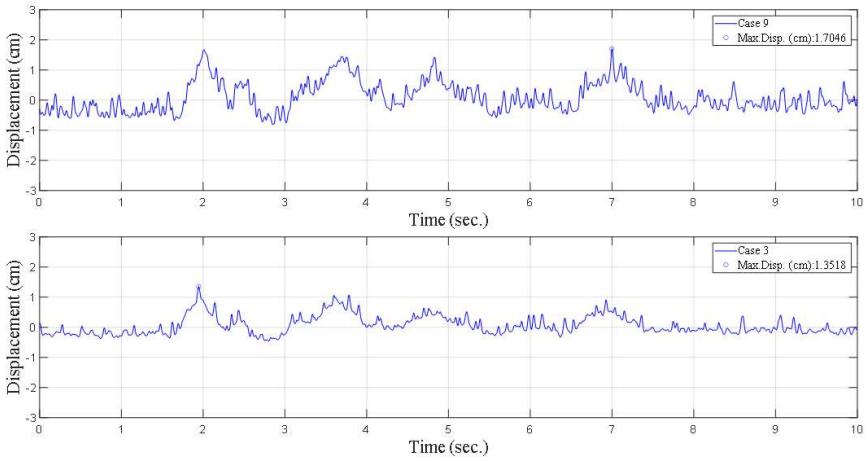

Figure 7.54. The DTH of Case 7 and Case 3 under El-Centro Earthquake.

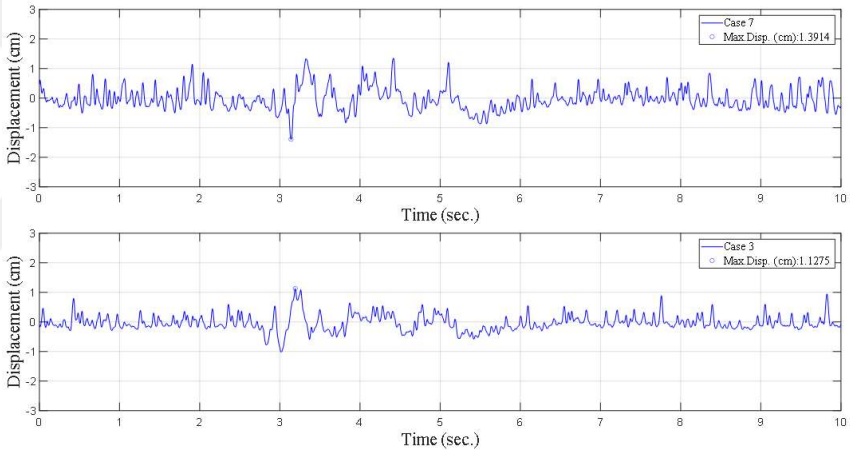

Figure 7.55. The DTH of Case 7 and Case 3 under Kobe Earthquake.

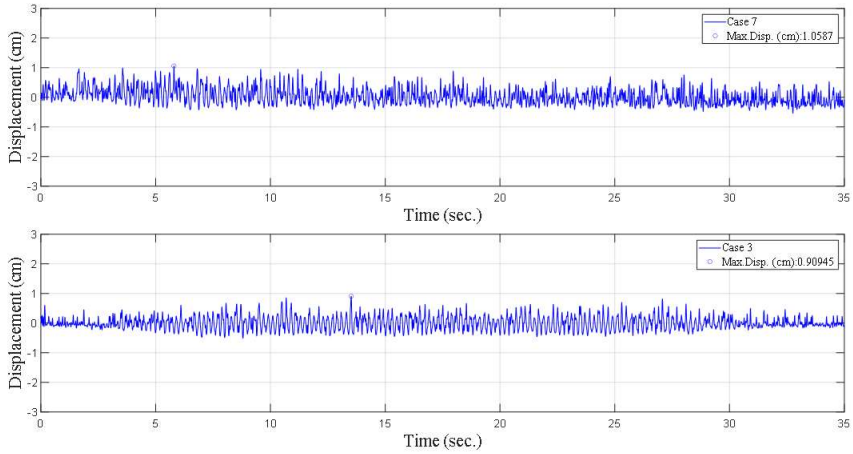

Figure 7.56. The DTH of Case 7 and Case 3 under the sinusoidal motion (0.4g - 5 Hz).

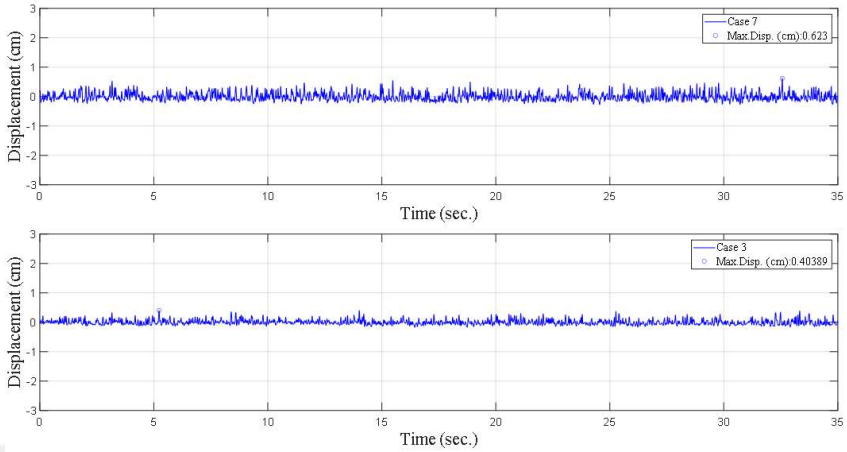

Figure 7.57. The DTH of Case 7 and Case 3 under the sinusoidal motion (0.3g - 10 Hz).

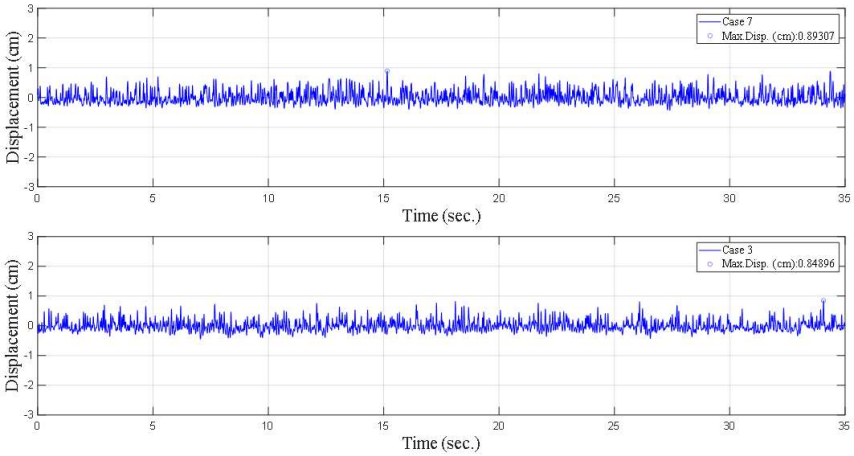

Figure 7.58. The DTH of Case 7 and Case 3 under the sinusoidal motion (0.4g - 10 Hz).

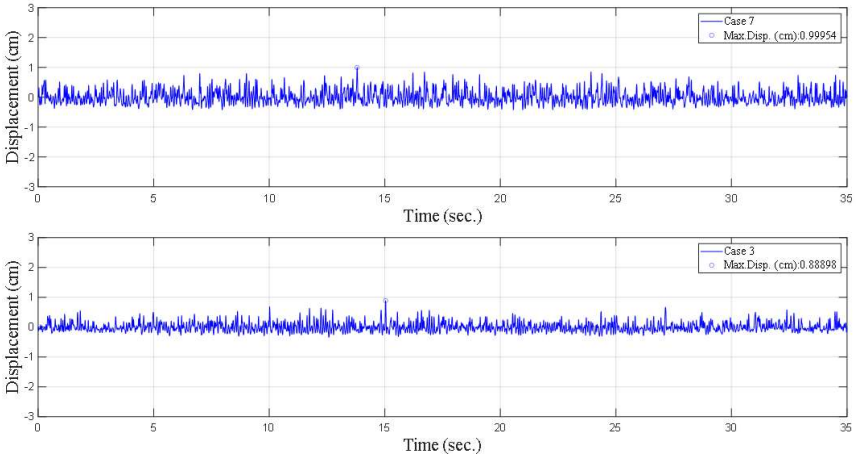

Figure 7.59. The DTH of Case 7 and Case 3 under the sinusoidal motion (0.5g - 10 Hz).

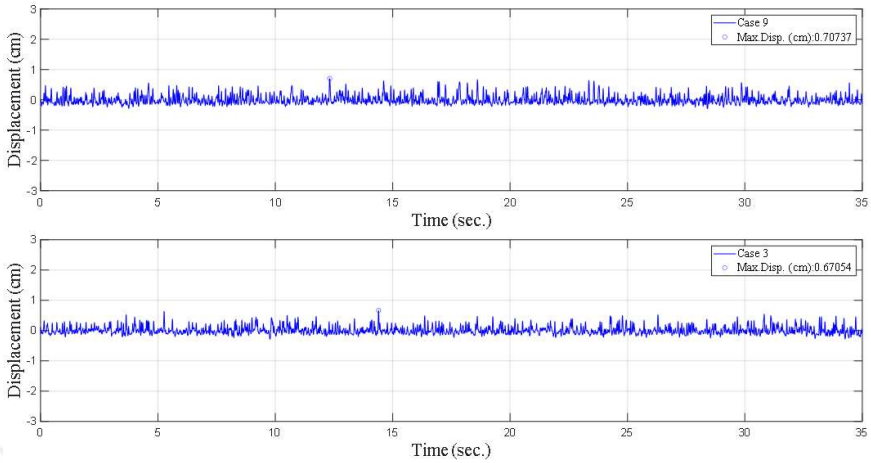

Figure 7.60. The DTH of Case 9 and Case 3 under the sinusoidal motion (0.4g - 15 Hz)..

7.3. The Effects of Cushion Thickness

Four different cushion layers were installed in order to interpret the impact of cushion thickness on the seismic performance of the retaining wall. One of them was an EPS geofoam layer with a density of 10 kg/m^3, and the others were sand-tire crumb mixtures having 10%, 20%, and 30% tire crumb by weight. The cushions designed with two different thicknesses (2 and 4 cm) were chosen. The cases with the cushion layer were compared with the control case. The comparison is made for five different real earthquake motions and five different sinusoidal motions with various amplitudes and frequencies.

7.3.1. EPS10 Geofoam Cushion

In this section, the compressible layer consisting of EPS10 was examined. The thicknesses of the cushions were 2 and 4 cm. The improved cases (Cases 2 and 3) were compared with Case 1 in order to calculate the percentage change due to the inclusion of the EPS10 cushion.

The percentage change in acceleration recorded by A7 is given in Table 7.7. As the thickness of the EPS geofoam cushion increases, the acceleration recorded at the top of the wall model decreases for all input motions. Due to the placement of the EPS10 cushion with 4 cm thickness, the maximum decrease in acceleration at the top of the wall is 34% under El-Centro Earthquake. When the acceleration recordings are taken into account, the 4 cm thick EPS10 cushion layer performed better under El-Centro and İzmir Earthquakes than the other real earthquakes. Moreover, the seismic performance of the EPS10 cushion layer with 4 cm thickness is better under the sinusoidal motion having 0.4g amplitude and 10 Hz frequency than the other sinusoidal motions. Under the far-field Kocaeli Earthquake, the effects of both cushion layers are not significant.

Table 7.7. The percentage change in PGA of A7 (Case 1 to Cases 2 and 3).

Input motion	İzmit-F	İzmir-F	İzmit-N	El-Centro	Kobe	0.4g-5 Hz	0.3g-10 Hz	0.4g-10 Hz	0.5g-10 Hz	0.4g-15 Hz
Case1-2	+0.5	-0.2	-9.9	-9.4	-0.7	-7.3	-7.7	-16.7	-21.8	-14.5
Case1-3	-3.7	-27.1	-20.9	-34.0	-17.6	-11.4	-17.0	-24.5	-22.5	-22.0

The percentage change in spectral acceleration calculated from the acceleration recordings of A7 is given in Table 7.8. The percentage reduction in maximum spectral acceleration increases with the increase in the thickness of the EPS10 cushion under all base excitations. The maximum reduction spectral acceleration caused by the EPS10 cushion with 4 cm thickness is 33.5% at the top of the wall under El-Centro Earthquake. Regarding spectral acceleration, the thicker EPS10 cushion performed better under El-Centro and İzmir Earthquake.

Table 7.8. The percentage change in SA of A7 (Case 1 to Cases 2 and 3)..

Input motion	İzmit-F	İzmir-F	İzmit-N	El-Centro	Kobe	0.4g-5 Hz	0.3g-10 Hz	0.4g-10 Hz	0.5g-10 Hz	0.4g-15 Hz
Case1-2	-0.2	+20.3	-15.4	-10.2	-5.3	+5.8	+2.9	-6.8	-16.4	-12.8
Case1-3	+7.6	-16.6	-29.3	-33.5	-9.6	+2.3	-3.6	-10.7	-14.6	-20.5

The percentage change in displacement recorded by D19 is given in Table 7.9. The increase in thickness of the EPS geofoam cushion results in an increase in the percentage reduction in the displacement at the top of the wall model. The EPS10 cushion with a 4 cm thickness reduced the maximum displacement by 46.1% at the top of the wall. The cushion performed better under İzmir Earthquake and the sinusoidal motion having 0.3g amplitude and 10 Hz frequency.

Table 7.9. The percentage change in maximum displacement of D19 (Case 1 to Cases 2 and 3).

Input motion	İzmit-F	İzmir-F	İzmit-N	El-Centro	Kobe	0.4g-5 Hz	0.3g-10 Hz	0.4g-10 Hz	0.5g-10 Hz	0.4g-15 Hz
Case1-2	-26.9	-38.2	-5.5	-21.6	-17.0	-13.6	-1.4	-4.3	-3.9	-1.3
Case1-3	-29.4	-46.1	-22.7	-23.3	-19.9	-17.3	-42.0	-7.6	-12.7	-10.7

7.3.2. TC10 Cushion

In this section, the cushion layers consisting of TC10 with a thickness of 2 and 4 cm were examined. The improved cases (Cases 6 and 7) were compared with Case 1 in order to calculate the percentage change due to the inclusion of the TC10 cushion.

The percentage change in acceleration recorded by A7 is given in Table 7.10. The increase in thickness of the TC10 cushion results in an increase in acceleration measured at the top of the wall model. This situation is not for sinusoidal motion with 0.4g amplitude and 15 Hz frequency. The TC10 cushion with a 2 cm thickness reduced the maximum acceleration by 25.1% at the top of the wall under El-Centro Earthquake. The TC10 cushion performed better under El-Centro and İzmir Earthquakes when the acceleration recordings are considered.

Table 7.10. The percentage change in PGA of A7 (Case 1 to Cases 6 and 7).

Input motion	İzmit-F	İzmir-F	İzmit-N	El-Centro	Kobe	0.4g-5 Hz	0.3g-10 Hz	0.4g-10 Hz	0.5g-10 Hz	0.4g-15 Hz
Case1-6	-1.0	-16.5	-14.6	-25.1	-10.7	-1.7	-4.2	-10.0	-11.4	+8.2
Case1-7	+9.5	+15.0	-9.9	-8.0	-8.2	+3.3	+6.1	-6.7	-11.9	-2.0

The percentage change in spectral acceleration calculated from the acceleration recordings and A7 are given in Table 7.11. As shown in the table, the spectral acceleration increases with the increase in cushion thickness in general. The TC10 cushion with 2 cm thickness resulted in a reduction in the maximum spectral acceleration at rates of at rates of 23.4% and 27.4% at the top of the wall under İzmir and El-Centro Earthquake, respectively. The effects of thickness on spectral acceleration were not observed clearly under sinusoidal motions.

Table 7.11. The percentage change in SA of A7 (Case 1 to Cases 6 and 7)..

Input motion	İzmit-F	İzmir-F	İzmit-N	El-Centro	Kobe	0.4g-5 Hz	0.3g-10 Hz	0.4g-10 Hz	0.5g-10 Hz	0.4g-15 Hz
Case1-6	+3.9	-9.6	-23.4	-27.4	-3.7	+5.4	+1.7	-3.2	-3.5	-0.6
Case1-7	+8.3	+32.6	-12.8	-5.5	+1.4	+8.5	+6.7	+4.7	+1.8	+0.6

The percentage change in displacement of D19 is given in Table 7.12. The TC10 cushion with 4 cm thickness reduced the maximum displacement by 10.1% at the top of the wall under the sinusoidal motion with an amplitude of 0.3g and a frequency of 10 Hz. In general, the increase in thickness of the cushion results in a decrease in the percentage reduction in the displacement of the model wall. Nevertheless, the percentage changes in displacement were not significantly high enough.

Table 7.12. The percentage change in maximum displacement of D19 (Case 1 to Cases 6 and 7).

Input motion	İzmit-F	İzmir-F	İzmit-N	El-Centro	Kobe	0.4g-5 Hz	0.3g-10 Hz	0.4g-10 Hz	0.5g-10 Hz	0.4g-15 Hz
Case1-6	-7.6	-3.4	-2.5	-7.4	-6.4	-4.5	-7.2	-2.2	-2.0	-8.0
Case1-7	-2.5	-3.4	-2.5	-4.5	-1.4	-3.6	-10.1	-3.3	-2.0	-5.3

7.3.3. TC20 Cushion

In this section, the compressible layer consisted of TC20 with a thickness of 2 and 4 cm. The improved cases (Cases 8 and 9) were compared with Case 1 in order to calculate the percentage change due to the inclusion of the TC20 cushion.

The percentage change in acceleration recorded by A7 is given in Table 7.13. The direct relationship between the thickness of the TC20 cushion and the reduction in acceleration transmitted in front of the wall cannot be developed. The TC20 cushion with a thickness of 2 cm resulted in a reduction in the maximum acceleration at a rate of 13.8% at the top of the wall under the sinusoidal motion having 0.5g amplitude and 10 Hz frequency.

Table 7.13. The percentage change in PGA of A7 (Case 1 to Cases 8 and 9).

Input motion	İzmit-F	İzmir-F	İzmit-N	El-Centro	Kobe	0.4g-5 Hz	0.3g-10 Hz	0.4g-10 Hz	0.5g-10 Hz	0.4g-15 Hz
Case1-8	+13.3	-2.2	-7.4	-7.4	-7.2	-0.1	+1.3	-9.2	-13.8	+2.4
Case1-9	-3.0	+0.9	-4.8	-9.3	-7.0	-0.9	+3.1	-12.3	-5.6	-3.9

The percentage change in spectral acceleration calculated from the acceleration recordings of A7 is given in Table 7.14. The TC20 cushion with a 4 cm thickness reduced the maximum spectral acceleration by 14% and 14.1% at the top of the wall under the near-field Kocaeli and El-Centro Earthquake, respectively. The cushion performed better under El-Centro Earthquake. Under sinusoidal motions, the effects of cushion thickness cannot be considered for the TC20 cushion.

Table 7.14. The percentage change in SA of A7 (Case 1 to Cases 8 and 9).

Input motion	İzmit-F	İzmir-F	İzmit-N	El-Centro	Kobe	0.4g-5 Hz	0.3g-10 Hz	0.4g-10 Hz	0.5g-10 Hz	0.4g-15 Hz
Case1-8	+4.7	+19.1	-13.2	-7.1	-4.1	+6.0	+2.2	-0.4	-2.5	-0.3
Case1-9	+2.7	+17.5	-14.0	-14.1	-2.1	+6.6	+6.8	+2.2	-1.7	-2.7

The percentage change in displacement recorded by D19 is given in Table 7.15. The TC20 cushion with 4 cm thickness reduced the maximum displacement by 14.5% at the top of the wall under 0.3g amplitude and 10 Hz frequency. The change in wall displacement and the thickness of TC20 cushion cannot be correlated.

Table 7.15. The percentage change in maximum displacement of D19 (Case 1 to Cases 8 and 9).

Input motion	İzmit-F	İzmir-F	İzmit-N	El-Centro	Kobe	0.4g-5 Hz	0.3g-10 Hz	0.4g-10 Hz	0.5g-10 Hz	0.4g-15 Hz
Case1-8	-4.2	-11.2	-5.5	-2.3	-5.7	-3.6	-11.6	-2.2	-3.9	-6.7
Case1-9	-5.0	-4.5	-3.7	-3.4	-8.5	-4.5	-14.5	-4.3	-4.9	-4.0

7.3.4. TC30 Cushion

In this section, the TC30 with a thickness of 2 and 4 cm (Cases 10 and 11) were compared with Case 1 in order to calculate the percentage change.

The percentage change in acceleration recorded by A7 is given in Table 7.16. The relationship between the cushion thickness and acceleration reduction cannot be related for the TC30 cushion. However, in general, the decrease in thickness of the TC30 cushion caused an increase in the percentage reduction in peak acceleration. The cushion performed better under El-Centro Earthquake. Due to the inclusion of the 2 cm thick cushion layer, the acceleration decreased at a rate of 16.8% at the top of the wall under El-Centro Earthquake.

Table 7.16. The percentage change in PGA of A7 (Case 1 to Cases 10 and 11).

Input motion	İzmit-F	İzmir-F	İzmit-N	El-Centro	Kobe	0.4g-5 Hz	0.3g-10 Hz	0.4g-10 Hz	0.5g-10 Hz	0.4g-15 Hz
Case1-10	0.0	-4.9	-6.9	-16.8	-9.6	-4.5	-10.4	-11.2	-3.8	-8.9
Case1-11	-1.0	+2.4	-9.9	-10.6	-5.9	-0.8	+2.6	-7.4	+0.8	-9.5

The percentage change in spectral acceleration of A7 is given in Table 7.17. In the table, the TC30 cushion with 2 cm thickness diminished the maximum spectral acceleration by 17.3% at the top of the wall under El-Centro Earthquake. The effects of cushion thickness of TC30 cushion cannot be correlated with the percentage change in spectral acceleration.

Table 7.17. The percentage change in SA of A7 (Case 1 to Cases 10 and 11).

Input motion	İzmit-F	İzmir-F	İzmit-N	El-Centro	Kobe	0.4g-5 Hz	0.3g-10 Hz	0.4g-10 Hz	0.5g-10 Hz	0.4g-15 Hz
Case1-10	+4.0	+10.5	-10.5	-17.3	-8.9	0.0	-3.5	-7.0	-5.0	-2.4
Case1-11	+2.1	+7.2	-10.9	-12.3	-7.7	+5.9	+9.2	+1.4	-10.1	-7.2

The percentage change in displacement of D19 is given in Table 7.18. The TC30 cushion with a 4 cm thickness reduced the maximum displacement by 13.5% at the top of the wall under Kobe Earthquake. The effect of the cushion thickness changes depending on input motion characteristics.

Table 7.18. The percentage change in maximum displacement of D19 (Case 1 to Cases 10 and 11).

Input motion	İzmit-F	İzmir-F	İzmit-N	El-Centro	Kobe	0.4g-5 Hz	0.3g-10 Hz	0.4g-10 Hz	0.5g-10 Hz	0.4g-15 Hz
Case1-10	-6.7	-2.2	-7.4	-6.8	-9.9	-5.5	-5.8	-3.3	-6.9	-4.0
Case1-11	-5.0	-3.4	-6.7	-5.7	-13.5	-6.4	-10.1	-6.5	-7.8	-5.3

7.4. The Effects of EPS Geofoam Cushion Density

EPS geofoam cushions with densities of 10 kg/m^3, 20 kg/m^3, and 30 kg/m^3 were installed behind the model wall with the aim of investigation the impact of EPS density on the seismic performance of the retaining wall system. The EPS geofoam cushion was placed with a thickness of 2 cm. The improved cases (Cases 2, 4, and 5) were compared with Case 1 in order to calculate the percentage change due to the inclusion of EPS geofoam. The comparison is made for five different earthquake recordings and five different sinusoidal motions with various amplitudes and frequencies.

The percentage change in acceleration recorded by A7 is given in Table 7.19. The relationship between EPS geofoam density and acceleration reduction cannot be considered. However, Table 7.19 indicates that the effects of the density change depending on input motion characteristics. The peak acceleration diminished at a rate of 34.4% under El-Centro Earthquake

in Case 4. In Case 5, the cushion reduced the maximum acceleration by 36.3% at the top of the wall under İzmir Earthquake.

Table 7.19. The percentage change in PGA of A7 (Case 1 to Cases 2, 4, and 5).

Input motion	İzmit-F	İzmir-F	İzmit-N	El-Centro	Kobe	0.4g-5 Hz	0.3g-10 Hz	0.4g-10 Hz	0.5g-10 Hz	0.4g-15 Hz
Case1-2	+0.5	-0.2	-9.9	-9.4	-0.7	-7.3	-7.7	-16.7	-21.8	-14.5
Case1-4	-3.7	-28.3	-16.2	-34.4	-8.2	-6.2	-12.9	-19.1	-15.3	-18.9
Case1-5	+2.9	-36.3	-8.7	-16.3	-12.0	-2.9	-8.3	-9.0	-15.4	-9.8

The percentage change in spectral acceleration of A7 is given in Table 7.20. The effects of cushion density relied on the characteristics of base excitation. The highest SA change occurred under the near-field Kocaeli Earthquake. The 2 cm thick EPS20 cushion decreased the maximum spectral acceleration by 34% at the top of the wall.

Table 7.20. The percentage change in SA of A7 (Case 1 to Cases 2, 4, and 5).

Input motion	İzmit-F	İzmir-F	İzmit-N	El-Centro	Kobe	0.4g-5 Hz	0.3g-10 Hz	0.4g-10 Hz	0.5g-10 Hz	0.4g-15 Hz
Case1-2	-0.2	+20.3	-15.4	-10.2	-5.3	+5.8	+2.9	-6.8	-16.4	-12.8
Case1-4	+0.9	-24.9	-34.0	-33.4	-8.9	+2.2	-2.6	-8.5	-11.9	-18.1
Case1-5	+4.4	-33.9	-16.2	-18.4	-4.0	+5.7	-2.3	+12.0	-12.6	-13.5

The percentage change in displacement of D19 is given in Table 7.21. The increase in cushion density resulted in a decrease in wall displacement in general. The 2 cm thick cushion with 10 kg/m^3 density reduced the maximum displacement at a rate of 38.2% at the top of the wall under İzmir Earthquake. The effects of cushion layer observed better under real earthquakes compared to harmonic motions.

Table 7.21. The percentage change in maximum displacement of D19 (Case 1 to Cases 2, 4, and 5).

Input motion	İzmit-F	İzmir-F	İzmit-N	El-Centro	Kobe	0.4g-5 Hz	0.3g-10 Hz	0.4g-10 Hz	0.5g-10 Hz	0.4g-15 Hz
Case1-2	-26.9	-38.2	-5.5	-21.6	-17.0	-13.6	-1.4	-4.3	-3.9	-1.3
Case1-4	-24.4	-32.6	-8.6	-19.9	-18.4	-3.6	-5.8	-1.1	-2.9	-1.3
Case1-5	-20.2	-29.2	-12.9	-14.2	-12.1	-1.8	-11.6	-4.3	-2.9	-2.7

7.5. The Effects of Mixture Ratio of TC

TC10, TC20, and TC30 mixed with the sand were installed behind the model wall in order to investigate the impact of the mixture ratio of sand-tire crumb mixture on the seismic performance of the retaining wall. The cases with the cushion layer were compared with the control case. The effects of the mixture ratio were evaluated for the 2 and 4 cm thick cushion layers. The comparison is made for five different real earthquake recordings and five different sinusoidal motions with various amplitudes and frequencies.

7.5.1. The TC Cushion Layers with a Thickness of 2 cm

In this section, the compressible layer consisted of TC10, TC20, and TC30-sand mixture with a thickness of 2 cm. The improved cases (Cases 6, 8, and 10) were compared with Case 1 in order to calculate the percentage change due to the inclusion of tire waste-sand mixture with 2 cm thickness.

The percentage change in acceleration recorded by A7 is given in Table 7.22. The impact of the sand-tire crumb mixture ratios depends on input motion characteristics, and the direct relationship between mixture ratio and reduction in acceleration cannot be obtained. The 2 cm thick cushion consisting of TC10 material reduced the maximum acceleration by 25.1% at the top of the wall under El-Centro Earthquake.

Table 7.22. The percentage change in PGA of A7 (Case 1 to Cases 6, 8, and 10).

Input motion	İzmit-F	İzmir-F	İzmit-N	El-Centro	Kobe	0.4g-5 Hz	0.3g-10 Hz	0.4g-10 Hz	0.5g-10 Hz	0.4g-15 Hz
Case1-6	-1.0	-16.5	-14.6	-25.1	-10.7	-1.7	-4.2	-10.0	-11.4	+8.2
Case1-8	+13.3	-2.2	-7.4	-7.4	-7.2	-0.1	+1.3	-9.2	-13.8	+2.4
Case1-10	0.0	-4.9	-6.9	-16.8	-9.6	-4.5	-10.4	-11.2	-3.8	-8.9

The percentage change in spectral acceleration of A7 is given in Table 7.23. The 2 cm thick TC10 cushion reduced the maximum spectral acceleration at a rate of 27.4% at the top of the wall under El-Centro Earthquake. Under sinusoidal motions, a significant reduction in maximum spectral acceleration could not be observed.

Table 7.23. The percentage change in SA of A7 (Case 1 to Cases 6, 8, and 10).

Input motion	İzmit-F	İzmir-F	İzmit-N	El-Centro	Kobe	0.4g-5 Hz	0.3g-10 Hz	0.4g-10 Hz	0.5g-10 Hz	0.4g-15 Hz
Case1-6	+3.9	-9.6	-23.4	-27.4	-3.7	+5.4	+1.7	-3.2	-3.5	-0.6
Case1-8	+4.7	+19.1	-13.2	-7.1	-4.1	+6.0	+2.2	-0.4	-2.5	-0.3
Case1-10	+4.0	+10.5	-10.5	-17.3	-8.9	0.0	-3.5	-7.0	-5.0	-2.4

The percentage change in displacement recorded by D19 is given in Table 7.24. The 2 cm thick TC20 cushion reduced the maximum displacement by 11.6% at the top of the wall under the sinusoidal motion with 0.3g amplitude and 10 Hz frequency.

Table 7.24. The percentage change in maximum displacement of D19 (Case 1 to Cases 6, 8, and 10).

Input motion	İzmit-F	İzmir-F	İzmit-N	El-Centro	Kobe	0.4g-5 Hz	0.3g-10 Hz	0.4g-10 Hz	0.5g-10 Hz	0.4g-15 Hz
Case1-6	-7.6	-3.4	-2.5	-7.4	-6.4	-4.5	-7.2	-2.2	-2.0	-8.0
Case1-8	-4.2	-11.2	-5.5	-2.3	-5.7	-3.6	-11.6	-2.2	-3.9	-6.7
Case1-10	-6.7	-2.2	-7.4	-6.8	-9.9	-5.5	-5.8	-3.3	-6.9	-4.0

7.5.2. The TC Cushion Layers with a Thickness of 4 cm

In this section, the cushion layer consisted of TC10, TC20, and TC30-sand mixture with a thickness of 4 cm. The improved cases (Cases 7, 9, and 11) were compared with Case 1 in order to calculate the percentage change due to the inclusion of tire waste-sand mixture with 4 cm thickness.

The percentage change in acceleration recorded by A7 is given in Table 7.25. The 4 cm thick TC20 cushion reduced the maximum acceleration by 12.3% at the top of the wall under the sinusoidal motion with 0.4g amplitude and 10 Hz frequency. The relationship between the mixture ratio and acceleration reduction cannot be established, and the influence of tire crumb content differs depending on the characteristics of input motion.

Table 7.25. The percentage change in PGA of A7 (Case 1 to Cases 7, 9, and 11).

Input motion	İzmit-F	İzmir-F	İzmit-N	El-Centro	Kobe	0.4g-5 Hz	0.3g-10 Hz	0.4g-10 Hz	0.5g-10 Hz	0.4g-15 Hz
Case1-7	+9.5	+15.0	-9.9	-8.0	-8.2	+3.3	+6.1	-6.7	-11.9	-2.0
Case1-9	-3.0	+0.9	-4.8	-9.3	-7.0	-0.9	+3.1	-12.3	-5.6	-3.9
Case1-11	-1.0	+2.4	-9.9	-10.6	-5.9	-0.8	+2.6	-7.4	+0.8	-9.5

The percentage change in spectral acceleration of A7 is given in Table 7.26. The 4 cm thick TC20 cushion reduced the maximum spectral acceleration 14% and 14.1% at the top of the wall under the near-field Kocaeli and El-Centro Earthquakes, respectively. The percentage change in spectral acceleration cannot be correlated with the effect of the mixture ratio.

Table 7.26. The percentage change in SA of A7 (Case 1 to Cases 7, 9, and 11).

Input motion	İzmit-F	İzmir-F	İzmit-N	El-Centro	Kobe	0.4g-5 Hz	0.3g-10 Hz	0.4g-10 Hz	0.5g-10 Hz	0.4g-15 Hz
Case1-7	+8.3	+32.6	-12.8	-5.5	+1.4	+8.5	+6.7	+4.7	+1.8	+0.6
Case1-9	+2.7	+17.5	-14.0	-14.1	-2.1	+6.6	+6.8	+2.2	-1.7	-2.7
Case1-11	+2.1	+7.2	-10.9	-12.3	-7.7	+5.9	+9.2	+1.4	-10.1	-7.2

The percentage change in displacement of D19 is given in Table 7.27. The TC20 cushion with a thickness of 4 cm reduced the maximum displacement by 14.5% at the top of the wall under the sinusoidal motion with 0.3g amplitude and 10 Hz frequency.

Table 7.27. The percentage change in maximum displacement of D19 (Case 1 to Cases 7, 9, and 11).

Input motion	İzmit-F	İzmir-F	İzmit-N	El-Centro	Kobe	0.4g-5 Hz	0.3g-10 Hz	0.4g-10 Hz	0.5g-10 Hz	0.4g-15 Hz
Case1-7	-2.5	-3.4	-2.5	-4.5	-1.4	-3.6	-10.1	-3.3	-2.0	-5.3
Case1-9	-5.0	-4.5	-3.7	-3.4	-8.5	-4.5	-14.5	-4.3	-4.9	-4.0
Case1-11	-5.0	-3.4	-6.7	-5.7	-13.5	-6.4	-10.1	-6.5	-7.8	-5.3

7.6. The Effect of Earthquake Characteristics

The experimental setup was subjected to five different earthquake recordings in order to investigate the impact of earthquake characteristics on the seismic performance of the retaining wall system. The change in acceleration and displacement values were obtained by comparing all improved cases with the unimproved case.

The percentage change in acceleration recorded by A7 is given in Table 7.28. The 2 cm thick cushion consisting of EPS geofoam with a density of 30 kg/m^3 reduced the maximum acceleration by 36.3% at the top of the wall under İzmir Earthquake. Generally, the cushion layers performed better under İzmir and El-Centro Earthquakes. Under the far-field Kocaeli Earthquake, the performance of the cushion layer was not observed clearly.

Table 7.28. The percentage change in PGA of A7 under real earthquake recordings.

Input motion	İzmit-F	İzmir-F	İzmit-N	El-Centro	Kobe
Case1-2	+0.5	-0.2	-9.9	-9.4	-0.7
Case1-3	-3.7	-27.1	-20.9	-34.0	-17.6
Case1-4	-3.7	-28.3	-16.2	-34.4	-8.2
Case1-5	+2.9	-36.3	-8.7	-16.3	-12.0
Case1-6	-1.0	-16.5	-14.6	-25.1	-10.7
Case1-7	+9.5	+15.0	-9.9	-8.0	-8.2
Case1-8	+13.3	-2.2	-7.4	-7.4	-7.2
Case1-9	-3.0	+0.9	-4.8	-9.3	-7.0
Case1-10	0.0	-4.9	-6.9	-16.8	-9.6
Case1-11	-1.0	+2.4	-9.9	-10.6	-5.9

The percentage change in spectral acceleration calculated from the acceleration recordings of A7 is given in Table 7.29. The 2 cm thick cushion consisting of EPS geofoam with a density of 30 kg/m^3 (Case 5) reduced the maximum spectral acceleration at a rate of 33.9% at the top of the wall under İzmir Earthquake. Under Kocaeli Earthquake recorded in İznik Station, the effects of the cushion layer were not clear when the decrease in spectral acceleration is considered. The cushions consisting of EPS geofoam performed better under İzmir, near-field Kocaeli, and El-Centro Earthquakes. The compressible layer composed of sand-tire crumb mixture showed better performance under El-Centro Earthquake.

Table 7.29. The percentage change in SA of A7 under real earthquake recordings.

Input motion	İzmit-F	İzmir-F	İzmit-N	El-Centro	Kobe
Case1-2	-0.2	+20.3	-15.4	-10.2	-5.3
Case1-3	+7.6	-16.6	-29.3	-33.5	-9.6
Case1-4	+0.9	-24.9	-34.0	-33.4	-8.9
Case1-5	+4.4	-33.9	-16.2	-18.4	-4.0
Case1-6	+3.9	-9.6	-23.4	-27.4	-3.7
Case1-7	+8.3	+32.6	-12.8	-5.5	+1.4
Case1-8	+4.7	+19.1	-13.2	-7.1	-4.1
Case1-9	+2.7	+17.5	-14.0	-14.1	-2.1
Case1-10	+4.0	+10.5	-10.5	-17.3	-8.9
Case1-11	+2.1	+7.2	-10.9	-12.3	-7.7

The percentage change in displacement recorded by D19 is given in Table 7.30. When the table is examined, the maximum displacement decreased at a rate of 46.1% at the top of the wall under İzmir Earthquake, owing to the 2 cm thick cushion consisting of EPS geofoam with a density of 10 kg/m^3 (Case 2). In general, the cushions performed better under İzmir Earthquake.

Table 7.30. The percentage change in maximum displacement of D19 under real earthquake recordings.

Input motion	İzmit-F	İzmir-F	İzmit-N	El-Centro	Kobe
Case1-2	-26.9	-38.2	-5.5	-21.6	-17.0
Case1-3	-29.4	-46.1	-22.7	-23.3	-19.9
Case1-4	-24.4	-32.6	-8.6	-19.9	-18.4
Case1-5	-20.2	-29.2	-12.9	-14.2	-12.1
Case1-6	-7.6	-3.4	-2.5	-7.4	-6.4
Case1-7	-2.5	-3.4	-2.5	-4.5	-1.4
Case1-8	-4.2	-11.2	-5.5	-2.3	-5.7
Case1-9	-5.0	-4.5	-3.7	-3.4	-8.5
Case1-10	-6.7	-2.2	-7.4	-6.8	-9.9
Case1-11	-5.0	-3.4	-6.7	-5.7	-13.5

7.7. The Effect of Sinusoidal Motions with Different Frequencies

The experimental setup was subjected to three different sinusoidal base excitations with 0.4g amplitude and various frequencies in order to investigate the effect of the change in the frequency content of sinusoidal motions on the seismic performance of the cushion layer. The

change in acceleration and displacement were obtained by comparing the case with all improved cases with the control case.

The percentage change in acceleration recorded by A7 is given in Table 7.31. When the cases are compared with each other based on the change in acceleration, the best performance has been observed in the case with the EPS10 cushion having 4 cm thickness under the sinusoidal motion with 0.4g amplitude and 10 Hz frequency. The reduction amount in Case 3 was 24.5% at the top of the wall under the sinusoidal motion with 0.4g amplitude and 10 Hz frequency.

Table 7.31. The percentage change in PGA of A7 under the sinusoidal motions with 0.4g amplitude and various frequencies.

Input motion	0.4g - 5 Hz	0.4g - 10 Hz	0.4g - 15 Hz
Case1-2	-7.3	-16.7	-14.5
Case1-3	-11.4	-24.5	-22.0
Case1-4	-6.2	-19.1	-18.9
Case1-5	-2.9	-9.0	-9.8
Case1-6	-1.7	-10.0	+8.2
Case1-7	+3.3	-6.7	-2.0
Case1-8	-0.1	-9.2	2.4
Case1-9	-0.9	-12.3	-3.9
Case1-10	-4.5	-11.2	-8.9
Case1-11	-0.8	-7.4	-9.5

The percentage change in spectral acceleration calculated from the acceleration recordings of A7 is given in Table 7.32. The 4 cm thick cushion consisting of EPS geofoam with a density of 10 kg/m^3 (Case3) reduced the maximum spectral acceleration by 20.5% at the top of the wall under the sinusoidal motion with 0.4g amplitude and 15 Hz frequency. When the comparison is made among eleven cases according to the reduction in spectral acceleration, in general, the cushions showed better performance with an increase in frequency content of harmonic motion.

Table 7.32. The percentage change in SA of A7 under the sinusoidal motions with 0.4g amplitude and various frequencies.

Input motion	0.4g - 5 Hz	0.4g - 10 Hz	0.4g - 15 Hz
Case1-2	+5.8	-6.8	-12.8
Case1-3	+2.3	-10.7	-20.5
Case1-4	+2.2	-8.5	-18.1
Case1-5	+5.7	+12.0	-13.5
Case1-6	+5.4	-3.2	-0.6
Case1-7	+8.5	+4.7	+0.6
Case1-8	+6.0	-0.4	-0.3
Case1-9	+6.6	+2.2	-2.7
Case1-10	0.0	-7.0	-2.4
Case1-11	+5.9	+1.4	-7.2

The percentage change in displacement recorded by D19 is given in Table 7.33. The 4 cm thick cushion consisting of EPS10 (Case 3) reduced the maximum displacement by 17.3% at the top of the wall under the sinusoidal motion with 0.4g amplitude and 5 Hz frequency. However, when the cases are compared with each other on the basis of the reduction in displacement, the relationship between the change in frequency of sinusoidal motion and the performance of the cushion layer could not be obtained.

Table 7.33. The percentage change in maximum displacement of D19 under the sinusoidal motions with 0.4g amplitude and various frequencies.

Input motion	0.4g - 5 Hz	0.4g - 10 Hz	0.4g - 15 Hz
Case1-2	-13.6	-4.3	-1.3
Case1-3	-17.3	-7.6	-10.7
Case1-4	-3.6	-1.1	-1.3
Case1-5	-1.8	-4.3	-2.7
Case1-6	-4.5	-2.2	-8.0
Case1-7	-3.6	-3.3	-5.3
Case1-8	-3.6	-2.2	-6.7
Case1-9	-4.5	-4.3	-4.0
Case1-10	-5.5	-3.3	-4.0
Case1-11	-6.4	-6.5	-5.3

7.8. The Effects of Sinusoidal Motions with Different Amplitudes

The experimental setup was subjected to three different sinusoidal base excitations with 10 Hz frequency and various amplitudes in order to investigate the influence of the change in amplitude of base excitation on the seismic performance of the retaining wall. The change in acceleration and displacement were obtained by comparing the case having the cushion layer with Case 1.

The percentage change in acceleration of A7 is given in Table 7.34. As a result of the comparison among all cases, the EPS10 cushion with 4 cm thickness under the sinusoidal motion with 0.4g amplitude and 10 Hz frequency is shown the best performance behind the wall. In Case 3, the cushion reduced the maximum acceleration by 24.5% at the top of the wall under the sinusoidal motion with 0.4g amplitude and 10 Hz frequency.

Table 7.34. The percentage change in PGA of A7 under the sinusoidal motions with 10 Hz frequency and various amplitudes.

Input motion	0.3g - 10 Hz	0.4g - 10 Hz	0.5g - 10 Hz
Case1-2	-7.7	-16.7	-21.8
Case1-3	-17.0	-24.5	-22.5
Case1-4	-12.9	-19.1	-15.3
Case1-5	-8.3	-9.0	-15.4
Case1-6	-4.2	-10.0	-11.4
Case1-7	+6.1	-6.7	-11.9
Case1-8	+1.3	-9.2	-13.8
Case1-9	+3.1	-12.3	-5.6
Case1-10	-10.4	-11.2	-3.8
Case1-11	+2.6	-7.4	+0.8

The percentage change in spectral acceleration calculated from the acceleration recordings of A7 is given in Table 7.35. The 2 cm thick EPS geofoam cushion with a density of 10 kg/m^3 (Case 2) reduced the maximum spectral acceleration at a rate of 16.4% at the top of the wall under the sinusoidal motion with 0.5g amplitude and 10 Hz frequency. When all cases

are compared with each other based on the reduction in maximum spectral acceleration, the increase in the amplitude of the motion resulted in a decrease in maximum spectral acceleration.

Table 7.35. The percentage change in SA of A7 under the sinusoidal motions with 10 Hz frequency and various amplitudes.

Input motion	0.3g - 10 Hz	0.4g - 10 Hz	0.5g - 10 Hz
Case1-2	+2.9	-6.8	-16.4
Case1-3	-3.6	-10.7	-14.6
Case1-4	-2.6	-8.5	-11.9
Case1-5	-2.3	+12.0	-12.6
Case1-6	+1.7	-3.2	-3.5
Case1-7	+6.7	+4.7	+1.8
Case1-8	+2.2	-0.4	-2.5
Case1-9	+6.8	+2.2	-1.7
Case1-10	-3.5	-7.0	-5.0
Case1-11	+9.2	+1.4	-10.1

The percentage change in displacement recorded by D19 is given in Table 7.36. Due to the application of the 4 cm thick cushion consisting of EPS geofoam with a density of 10 kg/m^3, the maximum displacement diminished at a rate of 42% at the top of the wall under the sinusoidal motion with 0.3g amplitude and 10 Hz frequency. When the reductions in displacement for all cases are compared, the movement of the wall reduces with the decrease in amplitude of the sinusoidal excitation.

Table 7.36. The percentage change in maximum displacement of D19 under the sinusoidal motions with 10 Hz frequency and various amplitudes.

Input motion	0.3g - 10 Hz	0.4g - 10 Hz	0.5g - 10 Hz
Case1-2	-1.4	-4.3	-3.9
Case1-3	-42.0	-7.6	-12.7
Case1-4	-5.8	-1.1	-2.9
Case1-5	-11.6	-4.3	-2.9
Case1-6	-7.2	-2.2	-2.0
Case1-7	-10.1	-3.3	-2.0
Case1-8	-11.6	-2.2	-3.9
Case1-9	-14.5	-4.3	-4.9
Case1-10	-5.8	-3.3	-6.9
Case1-11	-10.1	-6.5	-7.8

8. CONCLUSIONS

The effects of the cushion type on the seismic performance of the retaining wall were investigated by conducting a series of shaking table tests. The shaking table experiments were performed on a 1/25 scaled retaining wall model with the sand backfill. The model was constructed in a rigid-sided plexiglass soil box, and the tests were carried on without/with a cushion layer behind the wall model with the purpose of determining the effects of the cushion layers on the seismic performance of the cantilever retaining wall. The cushion layer was prepared using two different materials with thicknesses of 2 and 4 cm. EPS geofoam with three densities and tire waste-sand mixture with three mixture ratios were used to prepare the cushion. Additionally, the experimental setup was subjected to five real earthquake motions having different characteristics and five sinusoidal motions having various amplitudes and frequencies. As a result, the following conclusions have been obtained:

1. The highest reduction amount in acceleration went up to 36.3% at the top of the wall under İzmir Earthquake for Case 5.

2. Among actual earthquake recordings, the improvement was observed better under El-Centro Earthquake. The best seismic performance of the cushion was observed in Cases 3 and 4. The acceleration reduction amounts at the top of the wall in Case 3 (34%) were virtually identical to Case 4 (34.4%). Case 3 has EPS10 geofoam cushion with 4 cm thickness while Case 4 has EPS20 geofoam cushion with 2 cm thickness.

3. Under far-field Kocaeli Earthquake motion, the reduction in acceleration at the top of the wall was relatively lower than under other earthquake motions.

4. The effect of the cushion layer on the transmitted acceleration was observed more effective under sinusoidal motion with a 0.4g amplitude and 10 Hz frequency. The

maximum reduction in acceleration under input motions was determined as 24.5% at the top of the wall due to the cushion layer consisting of EPS10 geofoam with a thickness of 4 cm.

5. As the thickness of the EPS cushion increases, the performance of the inclusion to reduce acceleration increases. However, the change in density of EPS did not directly affect the seismic performance of the retaining wall. The EPS geofoam cushion with a 10 kg/m^3 density and 4 cm thickness resulted in the greatest reduction in recorded acceleration values.

6. Among the cases with the cushion layer consisting of tire crumb-sand mixture, the cushion showed the best improvement under real earthquake motions (except far-field Kocaeli Earthquake) was the TC10-sand mixture with a thickness of 2 cm. The effects of the cushion layer consisting of sand and tire-crumb mixture were observed clearly under El-Centro Earthquake motion.

7. Among the cases with the TC-sand mixtures, the cushion showed the best performance under sinusoidal motions was the TC20-sand mixture with a thickness of 2 cm. The effects of the change in thickness and tire crumb content relied on the motion characteristics. Therefore, the direct relationship between the cushion performance and the mixture ratio or cushion thickness cannot be found.

8. Among all cushion types, the best improvement has been observed in the case with the EPS geofoam cushion with a 10 kg/m^3 density and 4 cm thickness, regarding the change in recorded acceleration on the wall.

9. The reductions in spectral acceleration went up to 34% at the top of the model wall due to the inclusion of the cushion layer behind the wall under all input motions.

10. The greatest reduction in the maximum spectral acceleration was observed under the near-field Kocaeli Earthquake.

11. Under the far-field Kocaeli Earthquake, the reduction in spectral acceleration was relatively low, and the effects of cushion on spectral acceleration could not be observed clearly.

12. Under sinusoidal motions, generally, the increase in peak acceleration of harmonic motions resulted in a reduction in maximum spectral acceleration. Additionally, the increase in frequency caused the same effect on spectral acceleration.

13. Among the sinusoidal motions, the highest reduction in spectral acceleration was obtained under 0.4g amplitude and 15 Hz frequency.

14. EPS geofoam cushion layer with a 20 kg/m^3 density and 2 cm thickness led to a greater reduction in spectral acceleration compared to other cushion layers. The higher density of EPS geofoam considered in this thesis resulted in more reduction in spectral acceleration. In other words, as the EPS geofoam cushion thickness increased, the calculated spectral acceleration decreased. The effects of the cushion layer consisting of sand and tire crumb mixture were not observed clearly in the spectral acceleration comparison.

15. The reduction in maximum displacement at the top of the model reached 46.1% due to the application of the cushion.

16. Among the real earthquake motions, the highest reduction in the maximum displacement of the model wall was observed under İzmir Earthquake.

17. Among the harmonic motions, the highest reduction in displacement was observed under the sinusoidal motion with 0.3g amplitude and 10 Hz frequency.

18. EPS geofoam cushions resulted in more reduction in displacement compared to tire crumb-sand mixture cushions.

19. The increase in the thickness of the EPS geofoam cushion resulted in a higher reduction in the displacement of the model wall. EPS geofoam cushion with a 10 kg/m^3 density and 4 cm thickness performed better under the considered seismic loadings.

20. The cushions consisting of tire crumb-sand mixture did not significantly affect the amount of wall movement considering the comparison of the improved cases with the control case.

The contributions of this thesis to the literature are given in Table 8.1. Literature studies showed that placing the cushion layer behind the retaining wall can improve the performance of the retaining wall under static and dynamic loads. This study shows that placing a cushion layer behind the retaining wall can improve the seismic performance of the wall by up to 36.3% for acceleration, 36% for spectral acceleration, and 46.1% for displacement of the wall. Also, this study indicated that cushion thickness, cushion density, and characteristics of input motions are very important factors in the seismic performance of the retaining wall. In other words, the seismic behavior of the wall with a cushion is sensitive to the parameters considered in this study. It has been clearly seen that the most important parameter affecting the seismic performance of retaining walls with cushion is the cushion type.

To sum up, the cushion layer consisting of EPS geofoam and sand-tire crumb mixture can result in an improvement in the seismic performance of the retaining wall. The vibration absorption capacity and compressible nature of EPS geofoam and tire crumb material caused a decrease in the transmitted acceleration to the wall, spectral acceleration, and displacement values of the wall. The EPS geofoam layer with a density of 10 kg/m^3 and a thickness of 4 cm showed better improvement performance than the other cases. Similar to the literature studies, this study showed that the inclusion of a cushion layer behind the retaining wall can be used as an improvement method to mitigate earthquake-induced failures.

Table 8.1. The results of this study and comparison with the literature.

Reference	Aim of the Study	Analysis Type	Loading Conditions	Analysis/ Software	Box Type and Dimensions	Wall Type	Wall Dimensions	Parameters	Cushion Material	Input Motion	Results
Karpurapu and Bathurst (1992)	To evaluate preliminary design charts used for the selection of inclusion materials	Numerical	Static	GEOFEM	-	Rigid	Wall with heights of 3, 5, and 10 meters	Thickness of the inclusion layer Wall height Inclusion stiffness Backfill soil with different compaction densities	Mentioned as a compressible layer	-	A preliminary design chart has been proposed to select an appropriate inclusion thickness to reduce lateral earth pressure at a minimum
Ertuğrul and Trandafir (2011)	To evaluate the effects of geofoam layer on lateral pressure	Numerical and Experimental	Static	UWLC	Stiff sand box (2x1x1 m)	Rigid	Wall having a stem with the dimension of 700x980x8 mm and a base with the dimensions of 980x500x8 mm	Thickness of the inclusion layer Wall height EPS stiffness Strength parameters of backfill soil	EPS (15 kg/m^3)	-	As the relative stiffness and thickness of the compressible layer increased, the friction angle of backfill soil increased, and the isolation efficiency of geofoam layer increased.
Ertuğrul et al. (2012)	To evaluate the effects of inclusion properties, wall flexibility on lateral earth pressure	Experimental	Static	-	Stiff sand box (2x1x1 m)	Rigid and flexible	Wall having a stem with the dimension of 700x980x5 mm and a base with the dimensions of 980x500x8 mm	Thickness of the inclusion layer Wall type Strength parameters of backfill soil	EPS (16 kg/m^3)	-	The provided reduction amount by EPS inclusion was greater in forces against rigid walls compared to those against a flexible wall
Ertuğrul and Özkan (2012)	To evaluate the effects of inclusion properties, wall flexibility on lateral earth pressure	Experimental	Static	-	Stiff sand box (2x1x1 m)	Rigid and flexible	Wall having a stem with the dimension of 700x980x (2,4,5 and 8) mm and a base with the dimensions of 980x500x8 mm	Thickness of the inclusion layer Wall flexibility	EPS (15 kg/m^3)	-	The flexibility of the wall increased; the load reduction efficiency of the inclusion decreased. The increase in inclusion thickness resulted in a more attenuating effect on lateral forces.
Ertuğrul and Trandafir (2013)	To evaluate the effects of inclusion properties, wall flexibility on lateral earth pressure	Numerical and Experimental	Static	FLAC 2D	Stiff sand box (2x1x1 m)	Rigid and flexible	Wall having a stem with the dimension of 700x980x(2,4,5 and 8) mm and a base with the dimensions of 980x500x8 mm	Thickness of the inclusion layer Wall height Wall flexibility EPS types and densities (or modulus)	In the experimental study, EPS (15 kg/m^3) and XPS (22 kg/m^3) In the numerical study, EPS (18 and 26 kg/m^3)	-	The reduction in lateral thrust and earth pressure coefficient took place in various amounts depending on the change in inclusion thickness and stiffness, wall flexibility, and strength parameters of the retained soil.
Notash and Dabiri (2018)	To investigate the effects of the geofoam layer on the behavior of the cantilever wall	Numerical	Static	FLAC 2D	-	Yielding and non-yielding	Wall with heights of 3, 6, and 9 meters	Thickness of the inclusion layer Wall height EPS densities (or modulus) Inclusion shape	EPS (15, 20, and 25kg/m^3)	-	The decrease in forces acting on yielding walls was lower than those on non-yielding walls. The decrease in the density of EPS caused a decrease in lateral forces and an increase in lateral displacement
Adelsalam and Azzam (2016)	To generate design charts and correlations to determine the amount of reduction in lateral forces and lateral earth pressure coefficient	Numerical	Static	PLAXIS 2D	-	Rigid and flexible	Wall with a height of 1 meter	Thickness of the inclusion layer	EPS (20 kg/m^3)	-	The amount of reduction in lateral forces against flexible walls was 8% lower than that on rigid walls. For flexible walls, the inclusion thickness, interface, and flexure properties had a significant influence on the lateral forces compared to the geofoam density

Table 8.1. The results of this study and comparison with similar studies. (cont.)

Ertuğrul and Trandafir (2014)	To evaluate the effects of inclusion properties, wall flexibility on lateral earth pressure	Experimental	Dynamic	-	Laminar box (1x1.5x1 m)	Rigid and flexible	Wall having a stem with the dimension of 700x980x(2,4,5 and 8) mm and a base with the dimensions of 980x500x8 mm	Thickness of the inclusion layer Wall flexibility EPS types and densities (or modulus) Input motion frequency and amplitude	EPS (15 kg/m^3) and XPS (22 kg/m^3)	Sinusoidal with frequency varying 4 to 10 Hz and with peak amplitude varying 0.1 to 0.7g	The increase in amplitude and frequency of input motion caused an increase in the horizontal displacement and vertical settlement within retained soil. The compressible layer reduced not only lateral forces against the wall but the amount of flexural movement of the wall stem as well. The load reduction potential of XPS was observed to be slightly lower than those of EPS.
Zarnani et al. (2005)	To examine the reduction influence of geofoam inclusion on the lateral pressure	Experimental	Dynamic	-	Plexiglas box (1.3x1.4x2 m)	Rigid	Wall with a height of 1 meter	EPS densities (or modulus)	EPS (varying 16 to 1.32 kg/m3 - varying 4.7 to 0.32 MPa)	Sinusoidal record (5 Hz - stepped amplitude excessing 0.8g)	A reduction in the density or modulus of EPS geofoam brought about a decrease in lateral forces occurring under seismic shaking. The load reduction amount of seismic buffer reached 60% of the forces acting on the rigid wall without a geofoam panel. Moreover, the compressibility of EPS decreased as the density or modulus increased.
Zarnani and Bathurst (2005)	To examine the reduction influence of geofoam inclusion on the lateral pressure	Numerical	Dynamic	FLAC 2D	-	Rigid	Wall with a height of 1 meter	EPS densities (or modulus)	EPS (12 and 16 kg/m^3)	Sinusoidal record (5 Hz - stepped amplitude up to 0.7g)	A comparison of the results showed good agreement between the predictions made by numerical analysis and the experimental data taken from Zarnani et al. (2005). The reduction in lateral earth thrust has been observed because of geofoam inclusion.
Zarnani and Bathurst (2006)	To examine the reduction influence of geofoam inclusion on the lateral pressure	Numerical	Dynamic	FLAC 2D	-	Rigid	Wall with a height of 1 meter	EPS densities (or modulus)	EPS with densities of 12, 14, and 16 kg/m3 (elastic modulus of 4, 2.8, and 5.4 MPa)	Sinusoidal record (5 Hz - stepped amplitude excessing 0.8g)	The decrease in the elastic modulus of inclusion resulted in higher load reduction. The load reduction amount could exceed 36% of the force acting on the wall without inclusion.
Bathurst et al. (2007)	To examine the reduction influence of geofoam inclusion on the lateral pressure	Experimental	Dynamic	-	Plexiglas box (1.3x1.4x2 m)	Rigid	Wall with a height of 1 meter	EPS densities (or modulus)	EPS (12, 14, and 16 kg/m^3 (elastic modulus of 4, 2.8, and 5.4 MPa))	Sinusoidal record (5 Hz - stepped amplitude up to 0.8g)	The decrease in density and stiffness of buffer material caused an increase in load reduction amount. The greatest reduction in lateral loads was observed as 31% at a maximum acceleration of 0.7g
Zarnani and Bathurst (2007)	To examine the reduction influence of geofoam inclusion on the lateral pressure	Experimental	Dynamic	-	Plexiglas box (1.3x1.4x2 m)	Rigid	Wall with a height of 1 meter	EPS densities (or modulus) Buffer compression Dynamic friction between wall and EPS EPS dynamic elastic modulus Amplification of excitation Stress relaxation and creep	EPS (varying 16 to 1.32 kg/m^3 - varying 4.7 to 0.32 MPa)	Sinusoidal record (5 Hz - stepped amplitude up to 0.8g)	As the density and stiffness of the geofoam increased, the load reduction of the buffer decreased. The seismic buffer with the lowest stiffness reduced the lateral forces by 40%, whereas the one with the highest stiffness led to a 15% reduction in forces against the rigid wall. The cohesive (or adhesive) interface shear strength parameters between retained soil and buffer panel increased with decreasing density and stiffness of EPS

Table 8.1. The results of this study and comparison with similar studies. (cont.)

Zarnani and Bathurst (2009)	To examine the reduction influence of geofoam inclusion on the lateral pressure	Numerical	Dynamic	FLAC 2D	-	Rigid	Wall with heights of 1, 3, 6, and 9 meters	Thickness of EPS Wall Height EPS densities (or modulus) EPS stiffness Excitation frequency	EPS (18.4, 21.6, and 28.9 kg/m^3)	Sinusoidal record with a frequency varying from 7 to 21 Hz and with constant maximum amplitude (0.7g) and duration (17 sec)	The increase in buffer thickness and the decrease in EPS density resulted in an increase in the isolation efficiency of EPS. The total force acting on the wall increased as the frequency of input motion increased. The isolation efficiency decreased as the wall height decreased. Strains occurring on EPS buffer increased with a decrease in the buffer modulus, with an increase in wall height, a reduction in the buffer thickness, and an excitation frequency approaching the fundamental frequency of the wall.
Zarnani and Bathurst (2011)	To examine the reduction influence of geofoam inclusion on the lateral pressure	Numerical	Dynamic	FLAC 2D	-	Rigid	Wall with heights of 1, 3, 6, and 9 meters	Thickness of EPS Wall Height EPS densities (or modulus) EPS stiffness	EPS (18.4, 21.6, and 28.9 kg/m^3)	Sinusoidal record (5 Hz - stepped amplitude up to 0.8g)	The practical range of K was equal to or smaller than 50 MN/m3 for the design of systems using load reduction with EPS installation. The results were demonstrated as design charts.
Wang and Bathurst (2012)	To examine the reduction influence of geofoam inclusion on the lateral pressure	Numerical	Dynamic	ABAQUS	-	Rigid	Wall with a height of 1 meter	EPS densities (or modulus)	EPS (12 and 16 kg/m^3)	Sinusoidal record (5 Hz - stepped amplitude excessing 0.8g)	The decrease in density (also elastic modulus) caused an increase in the compressibility of EPS buffer. Based on the comparison between experimental and numerical results, ABAQUS software can be a successful program for analyzing geofoam buffers.
Hazarika et al. (2001)	To investigate the influence of a lightweight material placed behind the wall instead of conventional backfill	Numerical	Dynamic	Finite Element Modeling	-	Yielding and non-yielding	Wall with a height of 10 meters	Wall type	EPS (20 kg/m^3)	Sinusoidal record (3.5 Hz and 0.2g) – Hyogo-Ken Nanbu earthquake (NS)	The EPS geofoam placed in lieu of retained soil resulted in approximately a 50% - 60% reduction in lateral pressure acting on the wall before the replacement of the lightweight material.
Hazarika (2001)	To assess the effects of EPS geofoam as a seismic buffer behind a retaining wall	Numerical	Dynamic	Finite Element Modeling	-	Yielding and non-yielding	Wall with a height of 10 meters	Wall type	EPS (20 kg/m^3)	Sinusoidal record (3.5 Hz and 0.2g) – Hyogo-Ken Nanbu earthquake (NS)	The reduction in lateral forces has occurred for both non-yielding and yielding conditions. The compressible inclusion gave rise to a decrease exceeding 40% in lateral pressure
Hazarika et al. (2008a)	To determine the enhancement of seismic response of geotechnical structures after placement of cushion layer	Experimental	Dynamic	-	Steel box (4.0x1.25x1.5 m)	Caisson type- quay wall	-	-	Tire chips (average grain size of 20 mm)	Hyogo-Ken Nanbu earthquake (NS)	The buffer layer caused a reduction in both lateral forces and permanent displacement occurring due to excitation. The liquefaction was prevented since the tire chips led to the dissipation of pore water pressure quickly

Table 8.1. The results of this study and comparison with similar studies. (cont.)

Hazarika (2008)	To investigate the effectiveness of the technique called SAFETY	Experimental	Dynamic	-	For the small-scall model; Steel box (0.85x0.36x0.55 m) For large-scale model; Steel box (4.0x1.25x1.5 m)	Caisson type- quay wall	For a small-scale model; a wall with a height of 200 mm For a large-scale model; a wall with a height of 700 mm	-	Tire chips (particle size of 2 mm and 20 mm)	For a small-scale model; Sinusoidal (0.1g to 0.7g) For large-scale model; Hyogo-Ken Nanbu earthquake (NS), Tokachi-oki Earthquake (NS), and a synthetic earthquake	SAFETY techniques. -reduced lateral loads and permanent displacement caused by seismic loading. -reduced wall dimensions by virtue of the decrease in loads. -reduced project cost by virtue of the decrease in wall dimension. -was environmental-friendly due to the use of recycled waste tires. -could be applied not only during construction but also after construction.
Hazarika et al. (2008b)	To investigate whether the reduction in seismic loads was provided by a cushion layer installed between the caisson and the cohesionless backfill	Experimental	Dynamic	-	Steel box (4.0x1.25x1.5 m)	Caisson type- quay wall	Wall with a height of 700 mm	-	Tire chips (grain size of 20 mm)	Hyogo-Ken Nanbu earthquake (NS), Tokachi-oki Earthquake (NS), and a synthetic earthquake	The buffer layer resulted in a reduction in seismic forces, which means that it caused the improvement of the seismic performance of the quay wall. Tire chips cushion helped the porewater pressure to dissipate relatively faster compared to sand backfill without a cushion.
Hazarika et al. (2010)	To explain the use of scrapped tire-derived materials (specifically tire chips and tire shreds)	Experimental	Dynamic	-	Steel box (0.85x0.36x0.55 m)	Caisson type- quay wall	Wall with a height of 200 mm	-	(1) 100% tire chips, (2) 75% tire chips and 25% sand mixture by volume, and (3) 50% tire chips and 50% sand mixture by volume.	Sinusiodal (0.1g to 0.6g)	The cushion layer resulted in not only the residual displacement but also the lateral forces acting on the wall due to the excitation. The seismic cushion with three different mixture percentages approximately resulted in a similar amount of decrease in terms of wall displacement under excitation with increasing amplitude.
Dabiri and Notash (2020)	To investigate the effects of the geofoam layer installed behind the wall on lateral earth pressure	Numerical	Static and Dynamic	FLAC	-	Yielding and non-yielding	Wall with heights of 6 and 9 meters	Thickness of EPS Wall Height EPS unit weight Excitation characteristics	EPS (0.15 and 0.2 kN/m^3)	Loma Prieta Earthquake (far-field), Kocaeli Earthquake (near-field), and the acceleration-scaled version of these two motions	As the thickness of inclusion increased, the relative stiffness decreased. The reduction in stiffness resulted in an increase in the compressibility of geofoam, which decreased lateral forces and increased lateral displacement of soil. The performance of inclusion under static conditions was better than that under dynamic loading. The inclusion layer under near-field earthquake recording showed better performance than under far-field seismic motion. The potential of displacement reduction due to inclusion might exceed 40% for yielding walls
Edinçliler and Toksoy (2018)	To investigate the optimum cushion thickness to improve the seismic performance of the structure	Numerical	Dynamic	PLAXIS 2D	-	Cantilever wall	Wall with heights of 5 and 7 meters	Thickness of tire chips-cushion	30% tire crumbs and 70% sand mixture by weight	Kobe Earthquake	The cushion has enhanced the seismic performance of the wall. t/H ratio should be selected as 0.3 in lieu of 0.4 to increase stability.

Table 8.1. The results of this study and comparison with similar studies. (cont.)

Edinçliler and Toksoy (2017)	To examine the effectiveness of the cushion layer under excitation with different characteristics.	Numerical	Static and dynamic	PLAXIS 2D	-	Cantilever wall	Wall with a height of 7 meters	Excitation characteristics (amplitude and frequency)	Tire crumbs	Kobe and El-Centro Earthquakes	The compressible cushion resulted in a decrease in not only axial stress but also shear stress under both earthquake recordings. The wall performance under static and seismic loadings has been enhanced due to using the installation of tire crumb as a seismic buffer behind the wall.
Athanosopoulos-Zekkos and Athanosopoulos (2012)	To examine the load, displacement, and rotation reduction efficiency of the inclusion layer	Numerical	Dynamic	PLAXIS 2D	-	Yielding	Wall with heights of 4 and 7.5 meters	Thickness of EPS Wall height Excitation characteristics (amplitude and frequency)	EPS (0.2 kN/m^3)	Harmonic record (varying 0.3 to 3 Hz - varying 0.1g to 0.7g)	The presence of a cushion resulted in a decrease in not only static and dynamic earth pressure but also displacement due to earthquake shaking. The isolation potential (for load, displacement, and rotation) of the cushion increased almost linearly for lower thicknesses (t/H=5% - 15%). The isolation potential of the seismic buffer relied on the frequency of the input motion.
In this study	To investigate the effects of the cushion type on the seismic performance of the retaining wall	Experimental	Dynamic	-	Plexiglas soil box (90x40x50 cm)	Cantilever wall	1/25 scaled retaining wall model with a height of 24.5 cm	Thickness of the cushion layer Density of the cushion layer Mixture ratio of sand-tire crumb mixture Excitation characteristics	EPS (10, 20, and 30kg/m^3), Sand-tire crumb mixture (consisting of 10%, 20%, and 30% tire crumb by weight)	Five real earthquake motions and five sinusoidal motions (varying 5 to 15 Hz - varying 0.3g to 0.5g)	The cushion layer resulted in a decrease in the transmitted acceleration, spectral acceleration, and displacement of the model wall. The EPS cushion with a 10 kg/m3 density and 4 cm thickness provided better improvement in the seismic performance of the wall. In this study, the seismic behavior of the wall with a cushion is sensitive to the type of the cushion.

REFERENCES

1. Halabian, A.M., 2015, "Analysis and Design Issues of Geotechnical Systems: Rigid Walls" In *Encyclopedia of Earthquake Engineering*, Springer Berlin Heidelberg. pp. 70–86.

2. Budhu, M., *Foundations and Earth Retaining Structures*, John Wiley & Sons, 2008.

3. Day, R.W., *Geotechnical Earthquake Engineering Handbook,* Second Edition, McGraw Hill Professional, 2012.

4. Das, B.M., *Principals of Foundation Engineering*, Seventh Edition, Cengage Learning, 2011.

5. Teng, W., 1962, *Foundation Design,* Pearson Prentice-Hall, New Jersey.

6. Clayton, C.R.I., R.I. Woods, A.J. Bond, and J. Milititsky, *Earth Pressure and Earth-Retaining Structures*, Third Edition, CRC Press, 2013.

7. Elias, V., B.R. Christopher, and R.R. Berg, *Mechanically Stabilized Earth Walls and Reinforced Soil Slopes Design and Construction Guidelines*, U.S. Department of Transportation Federal, 2001.

8. Brooks, H., *Basics of Retaining Wall Design,* Eighth Edition, HBA Publications, Inc., 2010.

9. Kramer, S.L., 1996, *Geotechnical Earthquake Engineering*, Prentice-Hall, New Jersey.

10. Das, B.M. and G.V. Ramana, *Principles of Soil Dynamics,* Second Edition, Cengage Learning, 2010.

11. Fang, Y.S., Y.C. Yang, and T.J. Chen, 2003, "Retaining Walls Damaged in the Chi-Chi Earthquake", *Canadian Geotechnical Journal*, Vol. 40, No. 6, pp. 1142–1153.

12. Huang, C.C. and Y.H. Chen, 2004, "Seismic Stability of Soil Retaining Walls Situated on Slope" *Journal of Geotechnical and Geoenvironmental Engineering*, Vol. 130, No. 1, pp. 45–57.

13. Binici, H., H. Temiz, C. Kayadelen, H. Kaplan, and M.Y. Durgun, 2010, "Retaining Wall Failure due to Poor Construction and Design Aspects A Case Study", *Electronic Journal of Construction Technologies*, Vol. 6, No. 1, pp. 46–61.

14. Lim, A., 2018, "Lesson Learned from Retaining Wall Failures: A Geotechnical Disaster", in *MATEC Web of Conferences*, France, Vol. 229, pp. 03014.

15. Coduto, D.P., *Foundation Design Principles and Practices,* Second Edition, Prentice Hall, 2001.

16. Das, B.M., *Principles of Geotechnical Engineering,* Fifth Edition, Thompson Learning, 2006.

17. Zarrabi-Kashani, K., 1979, *Sliding of Gravity Retaining Wall During Earthquakes Considering Vertical Acceleration and Changing Inclination of Failure Surface*, M.S. Thesis, Massachusetts Institute of Technology.

18. Whitman, R.V. and S. Liao, 1985, *Seismic Design of Gravity Retaining Walls*. Massachusetts Inst of Tech Cambridge Dept of Civil Engineering, US Army Corps of Engineers, Washington.

19. Seed, H.B. and R.V. Whitman, 1970, "Design of Earth Retaining Structures for Dynamic Loads", in *ASCE Specialty Conference on Lateral Stresses in the Ground and Design of Earth Retaining Structures*, pp. 103–147.

20. Prakash, S., 1981, “Analysis of Rigid Retaining Walls During Earthquakes”, paper presented at the *First International Conferences on Recent Advances in Geotechnical Earthquake Engineering and Soil Dynamics*, Missouri, pp. 993–1020.

21. Puri, V.K., S. Prakash, and R. Widanarti, 2004, “Retaining Walls Under Seismic Loading”, paper presented at the *Fifth International Conference on Case Histories in Geotechnical Engineering*, New York.

22. Das, B.M., and V.K. Puri, 1996, “Static and Dynamic Active Earth Pressure”, *Geotechnical and Geological Engineering*, Vol. 14, No. 4, pp. 353–366.

23. Ghosh, S., 2010, “Pseudo-dynamic Active Force and Pressure Behind Battered Retaining Wall Supporting Inclined Backfill”, *Soil Dynamics and Earthquake Engineering*, Vol. 30, No. 11, pp. 1226–1232.

24. Steedman, R.S. and X. Zeng, 1990, “The Influence of Phase on The Calculation of Pseudo-Static Earth Pressure on A Retaining Wall”, *Geotechnique*, Vol. 40, No. 1, pp. 103–112.

25. Bellezza, I., D. D’Alberto, and R. Fentini, 2012, “Pseudo-dynamic Approach for Active Thrust of Submerged Soils”, *Proceedings of the Institution of Civil Engineers. Geotechnical Engineering*, Vol. 165, No. 5, pp. 321–333.

26. Choudhury, D., and S.S. Nimbalkar, 2006, “Pseudo-dynamic Approach of Seismic Active Earth Pressure Behind Retaining Wall”, *Geotechnical and Geological Engineering*, Vol. 24, No. 5, pp. 1103–1113.

27. Yan, Z., Y. Deng, J. He, Y. Xuan, and W. Wu, 2020, “A Pseudodynamic Approach of Seismic Active Pressure on Retaining Walls Based on a Curved Rupture Surface”, *Mathematical Problems in Engineering*, Vol. 2020.

28. Wood, J.H., 1973, *Earthquake-Induced Soil Pressures on Structures*, Ph.D. Thesis, California Institute of Technology.

29. Building Seismic Safety Council, *NEHRP Recommended Provisions for Seismic Regulations for New Buildings and Other Structures, FEMA P-750,* Washington, DC: Federal Emergency Management Agency, 2009.

30. Ostadan, F. and W.H. White, 1998, "Lateral Seismic Soil Pressure an Updated Approach", paper presented at the *US-Japan SSI Workshop*, California.

31. Scott, R.F., 1973, "Earthquake-induced Earth Pressures on Retaining Walls", paper presented at the *Fifth World Conference on Earthquake Engineering*, Vol. 2, pp. 1611–1620.

32. Veletsos, A.S. and A.H. Younan, 1994a, "Dynamic Soil Pressures on Rigid Vertical Walls", *Earthquake Engineering and Structural Dynamics*, *23*(3), 275–301.

33. Veletsos, A.S. and A.H. Younan, 1994b, "Dynamic Modeling and Response of Soil-Wall Systems", *Journal of Geotechnical Engineering*, Vol. 120, No. 12, pp. 2155–2179.

34. Ostadan, F., 2005, "Seismic Soil Pressure for Building Walls: An Updated Approach", *Soil Dynamics and Earthquake Engineering*, Vol. 25, No. 7–10, pp. 785–793.

35. Elms, D.G., and R. Richards, 1979, "Seismic Design of Gravity Retaining Walls", *Bulletin of the New Zealand Society for Earthquake Engineering*, Vol. 12, No. 2, pp. 114–121.

36. Nadim, F., and R.V. Whitman, 1983, "Seismically Induced Movement of Retaining Walls", *Journal of Geotechnical Engineering*, Vol. 109, No. 7, pp. 915–931.

37. Nadim, F., and R.V. Whitman, 1985, “Coupled Sliding and Tilting of Gravity Retaining Walls During Earthquakes”, *Norwegian Geotechnical Institute Publication*, Vol. 155, 477–484.

38. Wu, Y. and S. Prakash, 2001, “On Seismic Displacements of Rigid Retaining Walls”, *Fourth International Conferences on Recent Advances in Geotechnical Earthquake Engineering and Soil Dynamics,* California.

39. Nicholson, P.G., 2015, *Soil Improvement and Ground Modification Methods*, Butterworth-Heinemann, Elsevier.

40. ASTM D 6270-98, 2004, “Standard Practice for Use of Scrap Tires in Civil Engineering Applications”, *American Society for Testing and Materials*.

41. Humphrey, D.N. and T.C. Sandford, 1993, “Tire Chips as Lightweight Subgrade Fill and Retaining Wall Backfill”, in *Symposium on Recovery and Effective Reuse of Discarded Materials and By-Products for Construction of Highway Facilities*, Denver, Colorado.

42. Humphrey, D.N., T. C. Sandford, M.M. Cribbs, and W.P. Manion, 1993, “Shear Strength and Compressibility of Tire Chips for Use as Retaining Wall Backfill”, *Transportation Research Record*, No. 1422, pp. 29–35.

43. Wu, W.Y., C.C. Benda, and R.F. Cauley, 1997, “Triaxial Determination of Shear Strength of Tire Chips”, *Journal of Geotechnical and Geoenvironmental Engineering*, Vol. 123, No. 5, pp. 479–482.

44. Humphrey, D. N., 1999, “Civil Engineering Application of Tire Shreds”, paper presented at *The Tire Industry Conference,* Hilton Head, South Carolina.

45. Moo-Young, H., K. Sellasie, D. Zeroka, and G. Sabnis, 2003, "Physical and Chemical Properties of Recycled Tire Shreds for Use in Construction", *Journal of Environmental Engineering*, Vol. 129, No. 10, pp. 921–929.

46. Yang, S., R. A. Lohnes, and B.H. Kjartanson, 2002, "Mechanical Properties of Shredded Tires", *Geotechnical Testing Journal*, Vol. 25, No. 1, pp. 44–52.

47. Edil, T.B. and P.J. Bosscher, 1994, "Engineering Properties of Tire Chips and Soil Mixtures", *Geotechnical Testing Journal*, Vol. 17, No. 4, pp. 453–464.

48. Foose, G.J., C.H. Benson, and P.J. Bosscher, 1996, "Sand Reinforced with Shredded Waste Tires", *Journal of Geotechnical Engineering*, Vol. 122, No. 9, pp. 760–767.

49. Ghazavi, M., 2004, "Shear Strength Characteristics of Sand-Mixed with Granular Rubber", *Geotechnical and Geological Engineering*, Vol. 22, No. 3, pp. 401–416.

50. Hyodo, M., S. Yamada, R.P. Orense, M. Okamoto, and H. Hazarika, 2008, "Undrained Cyclic Shear Properties of Tire Chip-Sand Mixtures", in *International Workshop on Scrap Tire Derived Geomaterials - Opportunities and Challenges*, Hazarika, Yasuhara, editors, London, pp. 187–196.

51. Edinçliler, A., 2008, "Using Waste Tire-Soil Mixtures for Embankment Construction", in *International Workshop on Scrap Tire Derived Geomaterials - Opportunities and Challenges,* Hazarika, Yasuhara, editors, London, pp. 319–328.

52. Edinçliler, A., G. Baykal, and A. Saygılı, 2010, "Influence of Different Processing Techniques on The Mechanical Properties of Used Tires in Embankment Construction", *Waste Management*, Vol. 30, No. 6, pp. 1073–1080.

53. ASTM D6817/D6817M-17, 2021, "Standard Specification for Rigid Cellular Polystyrene Geofoam", *American Society for Testing and Materials*.

54. Koerner, R.M., 2005, *Designing with Geosynthetics*, Pearson Prentice-Hall, New Jersey.

55. Elragi, A., D. Negussey, and G. Kyanka, 2001, "Sample Size Effects on the Behavior of EPS Geofoam", *Soft Ground Technology*, Vol. 112, pp. 280–291.

56. Athanasopoulos, G.A., Pelekis, P.C., and V.C. Xenaki, 1999, "Dynamic Properties of EPS Geofoam. An Experimental Investigation", *Geosynthetics International*, Vol. 6, No. 3, pp. 171–194.

57. Preber, T., S. Bang, Y. Chung, and Y. Cho, 1994, "Behavior of Expanded Polystyrene Blocks", *Transportation Research Record*, No. 1462, pp. 36–46.

58. Horvath, J.S., 1994, "Expanded Polystyrene (EPS) Geofoam: An Introduction to Material Behavior", *Geotextiles and Geomembranes*, Vol. 13, No. 4, pp. 263–280.

59. Hazarika, H., 2006, "Stress-strain Modeling of EPS Geofoam for Large-strain Applications", *Geotextiles and Geomembranes*, Vol. 24, No. 2, pp. 79–90.

60. Karpurapu, R. and R.J. Bathurst, 1992, "Numerical investigation of controlled yielding of soil-retaining wall structures", *Geotextiles and Geomembranes*, Vol. 11, No. 2, pp. 115–131.

61. Ertugrul, O.L. and A.C. Trandafir, 2011, "Reduction of Lateral Earth Forces Acting on Rigid Nonyielding Retaining Walls by EPS Geofoam Inclusions", *Journal of Materials in Civil Engineering*, Vol. 23, No. 12, pp. 1711–1718.

62. Ertugrul, O.L., A.C. Trandafir, and M.Y. Ozkan, 2012, "Yanal Zemin Basınçlarının EPS Köpük Kullanımı Vasıtasıyla Azaltılması", *Teknik Dergi/Technical Journal of Turkish Chamber of Civil Engineers*, Vol. 23, No. 2, pp. 5885–5901.

63. Ertugrul, O.L. and M.Y. Ozkan, 2012, “Influence of EPS Geofoam Buffers on the Static Behavior of Cantilever Earth-Retaining Walls”, *Pamukkale University Journal of Engineering Sciences*, Vol. 18, No. 3, pp. 173–181.

64. Ertugrul, O.L. and A.C. Trandafir, 2013, “Lateral Earth Pressures on Flexible Cantilever Retaining Walls with Deformable Geofoam Inclusions”, *Engineering Geology*, Vol. 158, pp. 23–33.

65. Hasanpouri Notash, N. and R. Dabiri, 2018, “Effects of Geofoam Panels on Static Behavior of Cantilever Retaining Wall”, *Advances in Civil Engineering*, Vol. 2018, pp. 1–16.

66. AbdelSalam, S.S. and S.A. Azzam, 2016, “Reduction of Lateral Pressures on Retaining Walls Using Geofoam Inclusion”, *Geosynthetics International*, Vol. 23, No. 6, pp. 395–407.

67. Ertugrul, O.L. and A.C. Trandafir, 2014, “Seismic Earth Pressures on Flexible Cantilever Retaining Walls with Deformable Inclusions”, *Journal of Rock Mechanics and Geotechnical Engineering*, Vol. 6, No. 5, pp. 417–427.

68. Zarnani, S., R.J. Bathurst, and A. Gaskin, 2005, "Experimental Investigation of Geofoam Seismic Buffers Using a Shaking Table”, in *Proceedings of the North American Geosynthetics Society (NAGS)/Geosynthetics Research Institute (GRI) 19 Conference,* Las Vegas.

69. Zarnani, S. and R.J. Bathurst, 2005, “Numerical Investigation of Geofoam Seismic Buffers Using FLAC”, in *Proceedings of the North American Geosynthetics Society (NAGS)/GRI19 Conference,* Las Vegas.

70. Zarnani, S. and R.J. Bathurst, 2006, "Application of EPS Geofoam as A Seismic Buffer: Numerical Study Using FLAC", in *Proceedings of the 59th Canadian Geotechnical Conference,* Vancouver.

71. Bathurst, R.J., S. Zarnani, and A. Gaskin, 2007, "Shaking Table Testing of Geofoam Seismic Buffers", *Soil Dynamics and Earthquake Engineering*, Vol. 27, No. 4, pp. 324–332.

72. Zarnani, S. and R.J. Bathurst, 2007, "Experimental Investigation of EPS geofoam seismic buffers using shaking table tests", *Geosynthetics International*, Vol. 14, No. 3, pp. 165–177.

73. Zarnani, S. and R.J. Bathurst, 2009, "Numerical Parametric Study of Expanded Polystyrene (EPS) Geofoam Seismic Buffers", *Canadian Geotechnical Journal*, Vol. 46, No. 3, pp. 318–338.

74. Zarnani, S. and R.J. Bathurst, 2011, "EPS Seismic Buffers for Earthquake Load Attenuation against Rigid Retaining Walls", in *Geo-Frontiers Congress 2011,* pp. 3166–3176.

75. Wang, D. and R.J. Bathurst, 2012, "Numerical Analysis of Earthquake Load Mitigation on Rigid Retaining Walls Using EPS Geofoam", *The Open Civil Engineering Journal*, Vol. 6, No. 1, pp. 21–25.

76. Hazarika, H., J. Nakazawa, H. Matsuzawa, and D. Negussey, 2001, "On the Seismic Earth Pressure Reduction Against Retaining Structures Using Lightweight Geofoam Fill", paper presented at the *4th International Conferences on Recent Advances in Geotechnical Earthquake Engineering and Soil Dynamics*.

77. Hazarika, H., 2001, "Mitigation of Seismic Hazard on Retaining Structures - A Numerical Experiment", paper presented at the *Eleventh International Offshore and Polar Engineering Conference,* Stavanger, Norway, Vol. 2, pp. 459–464.

78. Hazarika, H., K. Yasuhara, M. Hyodo, A.K. Karmokar, and Y. Mitarai, 2008a, "Mitigation of Earthquake Induced Geotechnical Disasters Using a Smart and Novel Geomaterial", paper presented at the *14th World Conference on Earthquake Engineering*, Beijing, China.

79. Hazarika, H., E. Kohama, and T. Sugano, 2008b, "Underwater Shake Table Tests on Waterfront Structures Protected with Tire Chips Cushion", *Journal of Geotechnical and Geoenvironmental Engineering*, Vol. 134, No. 12, pp. 1706–1719.

80. Hazarika, H., 2008, "Structural Stability and Flexibility During Earthquakes Using Tyres (SAFETY) - A Novel Application for Seismic Disaster Mitigation", in *International Workshop on Scrap Tire Derived Geomaterials - Opportunities and Challenges,* Hazarika, Yasuhara, editors, London, pp. 115–125.

81. Hazarika, H., K. Yasuhara, Y. Kikuchi, A.K. Karmokar, and Y. Mitarai, 2010, "Multifaceted Potentials of Tire-Derived Three Dimensional Geosynthetics in Geotechnical Applications and Their Evaluation", *Geotextiles and Geomembranes*, Vol. 28, No. 3, pp. 303–315.

82. Dabiri, R., and N. Hasanpouri Notash, 2020, "Evaluation of Geofoam Effects on Seismic Response in Cantilever Retaining Wall", *Geotechnical and Geological Engineering*, Vol. 38, No. 2, pp. 2097–2116.

83. Edincliler, A. and Y.S. Toksoy, 2017a, "Effect of Ground Motion Characteristics on the Seismic Performance of Retaining Walls with Tire Waste Cushion", in *16Th World Conference on Earthquake Engineering*, Santiago Chile.

84. Edincliler, A. and Y.S. Toksoy, 2018, “Effects of Dimensions of Tire Waste Cushion on Seismic Performance of Retaining Wall”, *Eurasian Journal of Civil Engineering and Architecture*, Vol. 2, No. 2, pp. 69–78.

85. Athanasopoulos - Zekkos, A., K. Lamote, and G.A. Athanasopoulos, 2012, “Use of EPS Geofoam Compressible Inclusions for Reducing the Earthquake Effects on Yielding Earth Retaining Structures”, *Soil Dynamics and Earthquake Engineering*, Vol. 41, pp. 59–71.

86. Toksoy, Y.S., 2014, *Investigation of The Seismic Performance of Reinforced Highway Embankments,* M.S. Thesis, Boğaziçi University.

87. Edincliler, A. and Y.S. Toksoy, 2017b, “Shake Table Tests to Measure the Dynamic Performance of Geotextile-reinforced Embankment”, *Periodica Polytechnica Civil Engineering*, Vol. 61, No. 4, pp. 803–814.

88. Edincliler, A. and Y.S. Toksoy, 2017c, “Physical Model Study of the Seismic Performance of Highway Embankments with and without Geotextile”, *Journal of Earthquake and Tsunami*, Vol. 11, No. 02, pp. 1750003.

89. Turkish Standard Institute, 1990, “Soil Retaining Structures: Properties and Guidelines for Design (TS 7994)”, *Turkish Standard*, Ankara.

90. Uray, E., Ö. Tan, S. Carbas, and I.H. Erkan, 2021, “Metaheuristics-Based Pre-Design Guide for Cantilever Retaining Walls”, *Teknik Dergi/Technical Journal of Turkish Chamber of Civil Engineers*, Vol. 32, No. 4, pp. 10967–10994.

91. McCormac, J.C. and R.H. Brown, 2015, *Design of Reinforced Concrete,* Tenth Edition, John Wiley & Sons.

92. Azizi, F., *Applied analyses in geotechnics*. CRC Press, 1999.

93. ACI 318, 2014, “Building Code Requirements for Structural Concrete”, *American Concrete Institute*.

94. Iai, S., 1989, “Similitude for Shaking Table Tests on Soil-Structure-Fluid Model in 1g Gravitational Field” *Soils and Foundations*, Vol. 29, No. 1, pp. 105–118.

95. Muir Wood, D., A. Crewe, and C. Taylor, 2002, “Shaking table testing of geotechnical models”, *International Journal of Physical Modelling in Geotechnics*, Vol. 2, No. 1, pp. 1–13.

96. Muir Wood, D., 2004, *Geotechnical Modelling,* Spon Press, London and New York.

97. Hatami, K. and R.J. Bathurst, 2000, “Effect of Structural Design on Fundamental Frequency of Reinforced-Soil Retaining Walls”, *Soil Dynamics and Earthquake Engineering*, Vol. 19, No. 3, pp. 137–157.

98. ASTM D 422-63, 2002, “Standard Test Method for Particle-Size Analysis of Soils”, *American Society for Testing and Materials*.

99. ASTM D6913/D6913-17, 2017, “Standard Test Methods for Particle-Size Distribution (Gradation) of Soils Using Sieve Analysis”, *American Society for Testing and Materials*.

100. Duškov, M., 1997a, “Materials Research on EPS20 and EPS15 Under Representative Conditions in Pavement Structures”, *Geotextiles and Geomembranes*, Vol. 15, No. 1–3, pp. 147–181.

101. Duskov, M., 1997b, *EPS as a Light-weight Sub-base Material in Pavement Structures,* Ph.D. Thesis, Delft University of Technology.

102. Negussey, D. and N. Anasthas, 2001, "Young's Modulus of EPS Geofoam by Simple Bending Test", paper presented at the *3rd International Conference on Geofoam Blocks in Construction Applications*, Salt Lake City, USA.

103. Çağatay, A., 2008, *Investigation of the Effect of Tire Waste Inclusions on Investigation of the Effect of Tire Waste Inclusions on the Shear Strength Parameters of Sand,* M.S. Thesis, Boğaziçi University.

104. Bathurst, R.J. and K. Hatami, 1998, "Seismic Response Analysis of a Geosynthetic-Reinforced Soil Retaining Wall", *Geosynthetics International*, Vol. 5, No. 1–2, pp. 127–166.